

UNIVERSITY OF CALIFORNIA, SAN DIEGO

**The POLARBEAR-2 Cryogenic Receiver for Cosmic Microwave Background
Polarization Science**

A dissertation submitted in partial satisfaction of the
requirements for the degree
Doctor of Philosophy

in

Physics

by

Logan Alfred Howe

Committee in charge:

Professor Brian Keating, Chair
Professor Kam Arnold
Professor William Coles
Professor David Meyer
Professor Thomas Murphy

2019

Copyright
Logan Alfred Howe, 2019
All rights reserved.

The dissertation of Logan Alfred Howe is approved, and
it is acceptable in quality and form for publication on
microfilm and electronically:

Chair

University of California, San Diego

2019

DEDICATION

To Heather.

EPIGRAPH

*Measure what can be measured, and make measurable
what cannot be measured.*

— Galileo Galilei

TABLE OF CONTENTS

Signature Page	iii
Dedication	iv
Epigraph	v
Table of Contents	vi
List of Figures	ix
List of Tables	xiii
Acknowledgements	xiv
Vita	xvi
Abstract of the Dissertation	xxii
Chapter 1 Introduction	1
1.1 The Standard Model of Cosmology	1
1.2 Cosmic Inflation	5
1.3 The Cosmic Microwave Background	8
1.3.1 Temperature Anisotropies	10
1.3.2 Gravitational Waves	17
1.3.3 Inflationary Gravitational Waves	20
1.3.4 Gravitational Lensing	22
1.4 Foregrounds	26
1.4.1 Atmosphere	27
1.4.2 Galactic Synchrotron	29
1.4.3 Thermal Dust	30
1.5 Modern CMB Observations	31
Chapter 2 CMB Detector and Readout Instrumentation	33
2.1 Transition Edge Sensor Bolometers	34
2.1.1 Bolometer Saturation Power	41
2.2 Bolometer Noise	43
2.2.1 Thermal Carrier Noise	45
2.2.2 Johnson-Nyquist Noise	47
2.2.3 Photon Noise	48
2.3 Superconducting Quantum Interference Devices (SQUIDs)	51
2.3.1 SQUID Operation	53
2.3.2 SQUIDs as Transimpedance Preamplifiers	56

2.3.3	SQUID Series Arrays	58
2.3.4	SQUID Tuning	59
2.3.5	SQUID Noise	62
2.4	Multiplexing	63
2.4.1	Digital Frequency Division Multiplexing	66
2.4.2	Cryogenic Circuit	69
2.4.3	Parasitic Impedances	73
2.4.4	DfMUX 300 K Electronics	80
2.4.5	Operating Bolometers with DfMUX	81
2.5	Readout Noise	82
2.5.1	Crosstalk	83
2.5.2	White Noise	87
2.5.3	Current Sharing	89
2.6	Overall System Sensitivity	90
2.7	The Simons Array Experiment	93
2.8	Acknowledgments	95
 Chapter 3	Design and characterization of the POLARBEAR-2b and POLARBEAR-2c cosmic microwave background cryogenic receivers	96
3.1	Introduction	96
3.2	The POLARBEAR-2 Cryogenic Receiver	99
3.2.1	50 K and 4 K Refrigeration	103
3.2.2	Millikelvin Refrigeration	104
3.2.3	Thermal Loading Estimates	112
3.3	Commissioning the POLARBEAR-2b and -2c Backends	121
3.3.1	50 K and 4 K Shell Construction	123
3.3.2	Heatstraps	125
3.3.3	50 K and 4 K Cryogenic Validation	127
3.3.4	Millikelvin Validation	131
3.4	Conclusion	134
3.5	Acknowledgments	135
 Chapter 4	POLARBEAR-2b Readout and Detector Commissioning	136
4.0.1	POLARBEAR-2 Focal Plane and Readout Architecture	137
4.1	Mitigating Current Sharing	138
4.2	SQUID Characterization and Testing	145
4.2.1	Direct Linear Dynamic Range Tests	145
4.2.2	Carrier Bias Amplitude Dependence of Demodulated Noise Levels	149
4.2.3	Frequency Spectrum Effects from Bolometer Biasing	158
4.2.4	Current Sharing Measurements	163
4.2.5	Conclusions and Device Selection	167

Chapter 5	POLARBEAR-2b Full Receiver Integration and Final Commissioning	170
5.1	Backend and Optics Tube Integration	172
5.1.1	Dark Receiver Cryogenic Validation	173
5.1.2	Cryo-optical Receiver Validation	174
5.2	Final Lab Tests and Deployment	181
Chapter 6	Conclusion	182
6.1	Current State of the Field	182
6.2	The Simons Array	183
6.3	Future Experiments	185
6.4	Acknowledgment	186
Bibliography	187

LIST OF FIGURES

Figure 1.1:	CMB spectrum measurement from the COBE FIRAS spectrometer	9
Figure 1.2:	Full-sky maps from the Planck satellite mission observing at nine frequencies between 30 and 857 GHz.	11
Figure 1.3:	CMB temperature anisotropy power spectrum calculated using the CAMB package.	14
Figure 1.4:	Cartoon diagram of CMB polarization due to Compton scattering off an electron surrounded by a quadrupolar temperature anisotropy.	15
Figure 1.5:	CMB E-mode anisotropy power spectrum calculated using the CAMB package.	17
Figure 1.6:	CMB temperature-E-mode correlation power spectrum calculated using the CAMB package.	18
Figure 1.7:	Diagram showing the qualitative effects of the two gravitational wave polarization states.	20
Figure 1.8:	Effects of gravitational lensing on the temperature power spectrum due to neutrino mass.	23
Figure 1.9:	Effects of gravitational lensing on the E-mode power spectrum due to neutrino mass.	24
Figure 1.10:	Pure lensing (i.e. $r = 0$) CMB B-mode power spectrum.	25
Figure 1.11:	Atmospheric transmission model for Cerro Chajnantor, Chile using the <i>am</i> atmospheric model package.	28
Figure 1.12:	Comparison of the temperature, E-mode, and B-mode CMB power spectra.	31
Figure 2.1:	Schematic diagram of a bolometer.	35
Figure 2.2:	Superconducting transition of a POLARBEAR-2 AlMn TES.	37
Figure 2.3:	TES bolometer current-voltage ($I-V$) and resistance-power ($R-P$) relation	38
Figure 2.4:	Circuit diagram of a SQUID.	51
Figure 2.5:	Voltage-flux ($V - \Phi$) relation for a STAR Cryoelectronics AR112EB2 SQUID array.	54
Figure 2.6:	Current-voltage ($I - V$) relation for a STAR Cryoelectronics AR112EB2 SQUID array.	55
Figure 2.7:	Shunt-feedback flux locked loop SQUID configuration diagram.	57
Figure 2.8:	Comparison of the bias points from a high resolution $V - \Phi$ measurement and the DfMUX tuning algorithm.	61
Figure 2.9:	Circuit diagram of the DfMUX FDM system	67
Figure 2.10:	Network analysis of a POLARBEAR-2 LC comb above and below the bolometer superconducting transition temperature of ~ 450 mK.	71
Figure 2.11:	Difference in resonant frequencies $f_{0,i}$ as measured from a network analysis with an LC comb at temperatures of 600 mK and 250 mK.	72
Figure 2.12:	Circuit diagram of the DfMUX FDM system showing Thevenin equivalent parasitic series impedance.	76

Figure 2.13: Measurement of, and correction for, the parasitic impedance of one comb of POLARBEAR-2 bolometers by fitting to each Lorentzian found in the network analysis.	77
Figure 2.14: Measurement of, and correction for, the parasitic impedance for a single POLARBEAR-2 bolometer by fitting to the latched portion of the $I - V$ curve.	78
Figure 2.15: TES bolometer current-voltage ($I - V$) and resistance-power ($R - P$) relation corrected for the Thevenin equivalent series impedance Z_p	79
Figure 2.16: Schematic of the current sharing phenomenon in the DfMUX readout system.	88
Figure 2.17: Current sharing noise enhancement factor as a function of bias frequency for different values of the equivalent SQUID input inductance L	89
Figure 2.18: Photo of the Simons Array site near Cerro Toco in the Atacama Desert, Chile.	93
 Figure 3.1: Section view of the POLARBEAR-2b receiver CAD model.	97
Figure 3.2: Exploded view of the POLARBEAR-2b backend.	100
Figure 3.3: Photo of the POLARBEAR-2b FPT.	101
Figure 3.4: Load curve of the POLARBEAR-2b backend PTC second stage.	103
Figure 3.5: Diagram of the POLARBEAR-2b millikelvin fridges.	105
Figure 3.6: Cycle efficiencies of each stage of the standard He-10 gas light fridge . .	110
Figure 3.7: Hold times and base temperature we measured for the POLARBEAR-2b and -2c He-10 fridges.	110
Figure 3.8: CAD image of the booster He-4 fridge.	112
Figure 3.9: Schematic of the setup for low temperature thermal conductivity measurements with rigid and flexible materials.	121
Figure 3.10: Picture of the POLARBEAR-2b 4 K, 1 K, 350 mK, and 250 mK heatstraps.	125
Figure 3.11: Load curves and thermal conductance measurements of the POLARBEAR-2b 4 K heatstrap during the first cooldown.	128
Figure 3.12: Cooldown plot of the second cooldown of the POLARBEAR-2b backend. .	128
Figure 3.13: [Load curves and thermal conductance measurements of the POLARBEAR-2b 4 K heatstrap during the second cooldown.	129
Figure 3.14: Cooldown plot of run 09b of the POLARBEAR-2b backend with the bare FPT installed (no detector modules).	131
Figure 3.15: Millikelvin fridge recycling and hold times plots for the POLARBEAR-2b receiver.	132
 Figure 4.1: A POLARBEAR-2 “readout quanta” consisting of eight LC resonator combs.	139
Figure 4.2: A POLARBEAR-2 detector module with most of its cold readout assembled.	140
Figure 4.3: A POLARBEAR-2 SQUID mounting PCB, or “SQUID card” and its magnetic shield.	141

Figure 4.4:	The assembled POLARBEAR-2b FPT showing the lenslets arrays of all seven wafer modules.	142
Figure 4.5:	Front view of the complete, assembled POLARBEAR-2b FPT with all seven wafer modules installed.	143
Figure 4.6:	Fully assembled POLARBEAR-2 wafer module.	144
Figure 4.7:	Rear view of the complete, assembled POLARBEAR-2b FPT after installation in the backend cryostat.	145
Figure 4.8:	Direct input coil linear dynamic range test of NIST SA13a and Star Cryoelectronics E2 and F2 SQUID designs.	148
Figure 4.9:	In phase (I) ADN measurement comparing NIST SA13a and Star Cryoelectronics SQUID designs.	150
Figure 4.10:	Quadrature phase (Q) ADN measurement comparing NIST SA13a and Star Cryoelectronics SQUID designs.	151
Figure 4.11:	Mean-of-median ADN noise comparing NIST SA13a and Star Cryoelectronics SQUID designs.	152
Figure 4.12:	SQUID transimpedance during the ADN measurement normalized to the maximum transimpedance Z_t^{max} measured for the SQUID during the bias sweep.	153
Figure 4.13:	Comparison of the low carrier overbias voltage demodulated noise levels for the NIST SA13a and Star Cryoelectronics E2 and F2 SQUIDs. . . .	156
Figure 4.14:	Comparison of the typical carrier overbias voltage demodulated noise levels for the NIST SA13a and Star Cryoelectronics E2 and F2 SQUIDs. . . .	157
Figure 4.15:	Analysis of the SQUID spectrum while overbiasing five bolometers on an SA13a device	160
Figure 4.16:	Analysis of the SQUID spectrum while overbiasing five bolometers on a Star Cryoelectronics E2 device	161
Figure 4.17:	Analysis of the SQUID spectrum while overbiasing five bolometers on a Star Cryoelectronics F2 device	162
Figure 4.18:	Effective SQUID input coil inductance measurement using current sharing noise enhancement with the low amplitude carrier overbias voltage. . . .	164
Figure 4.19:	Comparison of the warm-only and full transfer functions for NIST SA13a and Star Cryoelectronics SQUIDs.	165
Figure 4.20:	Nuller network analysis after correction for the cold transfer function, which is unique to each SQUID.	166
Figure 4.21:	Channel-selected current sharing enhancement measurement via the corrected nuller network analysis.	167
Figure 4.22:	BoloCalc simulations for the POLARBEAR-2b NET and mapping speed as a function of the total readout (current) noise.	168
Figure 5.1:	Section view of the POLARBEAR-2b receiver CAD with labels for key components.	171
Figure 5.2:	Photo of the POLARBEAR-2b receiver during assembly, showing the MLI bridge blankets.	174

Figure 5.3:	Run16b field lens load curve taken using a heater on the outer diameter of the lens.	176
Figure 5.4:	Run16b Lyot load curve taken using a heater on the outer diameter of the nylon disk.	176
Figure 5.5:	BoloCalc simulation of the POLARBEAR-2b sensitivity as a function of various optical element temperatures.	177
Figure 5.6:	Photos of the POLARBEAR-2b field lens on its mounting ring.	177
Figure 5.7:	Cooldown plot of the POLARBEAR-2b backend during the cryo-optical validation run (run17b).	178
Figure 5.8:	Cooldown plot of the POLARBEAR-2b optics tube during the cryo-optical validation run (run17b).	179
Figure 6.1:	Current state of the field of CMB B-mode polarization measurements.	183

LIST OF TABLES

Table 3.1:	Summary of the 50 K and 4 K conductive loads in the POLARBEAR-2b and -2c backends.	114
Table 3.2:	Summary of the values used in the application of the Keller model to the POLARBEAR-2b and -2c backend cryostats.	118
Table 3.3:	MLI contribution to the POLARBEAR-2b backend loading at 50 K and 4 K.	119
Table 3.4:	Projected thermal loads in μW on the fridge intercepts for POLARBEAR-2b (POLARBEAR-2c).	122
Table 3.5:	Base temperatures in K for the POLARBEAR-2b and -2c backends during their 50 K and 4 K validation run.	130
Table 3.6:	Summary of the values used to obtain the millikelvin heatstrap G	133
Table 4.1:	Summary of characteristic properties of various SQUID devices considered for, or used with, the DfMUX readout system.	146
Table 4.2:	Design values for different parameters for the low-power Star Cryoelectronics devices.	146
Table 4.3:	Mean values for the nuller tone dynamic range test shown in Figure 4.8 for each of the three SQUID device types tested. Note that SA13_041.5 is an outlier, most likely due to rf contamination or ground coupling resulting from a short on the device wafer it was connected to. It is excluded from this mean.	147
Table 5.1:	POLARBEAR-2b receiver components corresponding to labels in Figure 5.1.	172
Table 5.2:	Integrated POLARBEAR-2b base temperatures for run16b and run17b.	175

ACKNOWLEDGEMENTS

First off, I would like to thank the members of the POLARBEAR collaboration for their dedication and effort to performing leading-edge science in the CMB field. It is the hard work of many, many people that makes us stand out in the crowded and popular world of CMB science.

I would like to thank my advisor Brian Keating for everything he has done to help me become a successful scientist and physicist, including guidance, useful discussions, networking, and of course, funding. I would also like to thank Kam Arnold, whose expertise, passion, and commitment always provided an invaluable resource.

Special thanks to the UCSD group and its numerous members during my tenure as a grad student: Darcy Barron, Tucker Ellefot, Nick Galitzky, Jen Ito, John Kaufman, David Leon, Lindsay Lowry, Frederick Matsuda, Marty Navaroli, Megan Russel, Max Silva-Feaver, Joe Seibert, Praween Siritanasak, Jake Spisak, Nate Stebor, Grant Teply, Calvin Tsai, Tran Tsan, and Alex Zahn. I couldn't have done it without you.

Finally, thank you to my family and friends whose support and encouragement made the journey possible.

OFFICIAL ACKNOWLEDGEMENTS

Chapter 3 is a reprint in full as it appears in L. Howe, C. Tsai, L. Lowry, K. Arnold, G. Coppi, J. Groh, X. Guo, B. Keating, A. Lee, A. May, L. Piccirillo, N. Stebor, and G. Teply, "Design and characterization of the POLARBEAR-2b and POLARBEAR-2c cosmic microwave background cryogenic receivers," *Millimeter, Submillimeter, and Far-Infrared*

Detectors and Instrumentation for Astronomy IX, vol. 10708, 2018. The dissertation author was the primary investigator and author of this paper.

Figure 2.18 was provided by Praween Siritanasak.

Figure 6.1 was provided by Yuji Chinone.

VITA

2019	Ph. D. Physics, University of California, San Diego
2016	M. S. Physics, University of California, San Diego
2013	B. S. Applied Mathematics <i>cum laude</i> , University of Colorado, Boulder
2013	B. S. Engineering Physics <i>cum laude</i> , University of Colorado, Boulder

PUBLICATIONS

S. Takakura, M. A. O. Aguilar-Faúndez, Y. Akiba, K. Arnold, C. Baccigalupi, D. Barron, D. Beck, F. Bianchini, D. Boettger, J. Borrill, K. Cheung, Y. Chinone, T. Ellefot, J. Errard, G. Fabbian, C. Feng, N. Goeckner-Wald, T. Hamada, M. Hasegawa, M. Hazumi, L. Howe, D. Kaneko, N. Katayama, B. Keating, R. Keskitalo, T. Kisner, N. Krachmalnicoff, A. Kusaka, A. T. Lee, L. N. Lowry, F. T. Matsuda, A. J. May, Y. Minami, M. Navaroli, H. Nishino, L. Piccirillo, D. Poletti, G. Puglisi, C. L. Reichardt, Y. Segawa, M. Silva-Feaver, P. Siritanasak, A. Suzuki, O. Tajima, S. Takatori, D. Tanabe, G. P. Teply, and C. Tsai, “Measurements of tropospheric ice clouds with a ground-based CMB polarization experiment, POLARBEAR,” *arXiv e-prints*, Sep. 2018

L. Howe, C. Tsai, L. Lowry, K. Arnold, G. Coppi, J. Groh, X. Guo, B. Keating, A. Lee, A. May, L. Piccirillo, N. Stebor, and G. Teply, “Design and characterization of the POLARBEAR-2b and POLARBEAR-2c cosmic microwave background cryogenic receivers,” *Millimeter, Submillimeter, and Far-Infrared Detectors and Instrumentation for Astronomy IX*, vol. 10708, 2018

The POLARBEAR Collaboration, D. Barron, K. Arnold, T. Ellefot, J. Groh, D. Kaneko, N. Katayama, A. Lee, L. Lowry, H. Nishino, A. Suzuki, S. Takatori, P. Ade, Y. Akiba, A. Ali, M. Aguilar, A. Anderson, P. Ashton, J. Avva, D. Beck, C. Baccigalupi, S. Beckman, A. Bender, F. Bianchini, D. Boettger, J. Borrill, J. Carron, S. Chapman, Y. Chinone, G. Coppi, K. Crowley, A. Cukierman, T. de Haan, M. Dobbs, R. Dunner, J. Errard, G. Fabbian, S. Feeney, C. Feng, G. Fuller, N. Galitzki, A. Gilbert, N. Goeckner-Wald, T. Hamada, N. Halverson, M. Hasegawa, M. Hazumi, C. Hill, W. Holzapfel, L. Howe, Y. Inoue, J. Ito, G. Jaehnig, O. Jeong, B. Keating, R. Keskitalo, T. Kisner, N. Krachmalnicoff, A. Kusaka, M. Le Jeune, D. Leon, E. Linder, A. Lowitz, A. Madurowicz, D. Mak, F. Matsuda, T. Matsumura, A. May, N. Miller, Y. Minami, J. Montgomery, T. Natoli, M. Navroli, J. Peloton, A. Pham, L. Piccirillo, D. Plambeck, D. Poletti, G. Puglisi, C. Raum, G. Rebeiz, C. Reichardt, P. Richards, H. Roberts, C. Ross, K. Rotermund, M. Silva-Feaver, Y. Segawa, B. Sherwin, P. Siritanasak, L. Steinmetz, R. Stompor, O. Tajima, S. Takakura, D. Tanabe, R. Tat, G. Teply, A. Tikhomirov, T. Tomaru, C. Tsai, C. Verges, B. Westbrook, N. Whitehorn, and A. Zahn, “Electrical characterization and tuning of the integrated POLARBEAR-2a focal plane and readout,” in *Millimeter, Submillimeter, and Far-Infrared Detectors and Instrumentation for Astronomy IX*, vol. 10708, 2018

The POLARBEAR Collaboration, M. Hasegawa, P. Ade, Y. Akiba, A. Ali, M. Aguilar, A. Anderson, K. Arnold, P. Ashton, J. Avva, D. Barron, D. Beck, C. Baccigalupi, S. Beckman, A. Bender, F. Bianchini, D. Boettger, J. Borrill, J. Carron, S. Chapman, Y. Chinone, G. Coppi, K. Crowley, A. Cukierman, T. de Haan, M. Dobbs, R. Dunner, T. Ellefrot, J. Errard, G. Fabbian, S. Feeney, C. Feng, G. Fuller, N. Galitzki, A. Gilbert, J. Goeckner-Wald Groh, N., T. Hamada, N. Halverson, M. Hasegawa, M. Hazumi, C. Hill, W. Holzapfel, L. Howe, Y. Inoue, J. Ito, G. Jaehnig, D. Jeong O. Kaneko, N. Katayama, B. Keating, R. Keskitalo, T. Kisner, N. Krachmalnicoff, A. Kusaka, A. Lee, M. Le Jeune, D. Leon, E. Linder, A. Lowitz, L. Lowry, A. Madurowicz, D. Mak, F. Matsuda, T. Matsumura, A. May, N. Miller, Y. Minami, J. Montgomery, T. Natoli, M. Navroli, H. Nishino, J. Peloton, A. Pham, L. Piccirillo, D. Plambeck, D. Poletti, G. Puglisi, C. Raum, G. Rebeiz, C. Reichardt, P. Richards, H. Roberts, C. Ross, K. Rotermund, M. Silva-Feaver, Y. Segawa, B. Sherwin, P. Siritanasak, L. Steinmetz, R. Stompor, A. Suzuki, O. Tajima, S. Takakura, S. Takatori, D. Tanabe, R. Tat, G. Teply, A. Tikhomirov, T. Tomaru, C. Tsai, C. Verges, B. Westbrook, N. Whitehorn, and A. Zahn, “POLARBEAR-2: A new CMB polarization receiver system for the Simons Array,” in *Millimeter, Submillimeter, and Far-Infrared Detectors and Instrumentation for Astronomy IX*, vol. 10708, 2018, p. 1070 802

P. Ade, J. Aguirre, Z. Ahmed, S. Aiola, A. Ali, D. Alonso, M. A. Alvarez, K. Arnold, P. Ashton, J. Austermann, H. Awan, C. Baccigalupi, T. Baildon, D. Barron, N. Battaglia, R. Battye, E. Baxter, A. Bazarko, J. A. Beall, R. Bean, D. Beck, S. Beckman, B. Beringue, F. Bianchini, S. Boada, D. Boettger, J. R. Bond, J. Borrill, M. L. Brown, S. M. Bruno, S. Bryan, E. Calabrese, V. Calafut, P. Calisse, J. Carron, A. Challinor, G. Chesmore, Y. Chinone, J. Chluba, H. M. S. Cho, S. Choi, G. Coppi, N. F. Cothard, K. Coughlin, D. Crichton, K. D. Crowley, K. T. Crowley, A. Cukierman, J. M. D’Ewart, R. Dünnner, T. De Haan, M. Devlin, S. Dicker, J. Didier, M. Dobbs, B. Dober, C. J. Duell, S. Duff, A. Duivenvoorden, J. Dunkley, J. Dusatko, J. Errard, G. Fabbian, S. Feeney, S. Ferraro, P. Fluxà, K. Freese, J. C. Frisch, A. Frolov, G. Fuller, B. Fuzia, N. Galitzki, P. A. Gallardo, J. T. G. Ghersi, J. Gao, E. Gawiser, M. Gerbino, V. Gluscevic, N. Goeckner-Wald, J. Golec, S. Gordon, M. Gralla, D. Green, A. Grigorian, J. Groh, C. Groppi, Y. Guan, J. E. Gudmundsson, D. Han, P. Hargrave, M. Hasegawa, M. Hasselfield, M. Hattori, V. Haynes, M. Hazumi, Y. He, E. Healy, S. W. Henderson, C. Hervias-Caimapo, C. A. Hill, J. C. Hill, G. Hilton, M. Hilton, A. D. Hincks, G. Hinshaw, R. Hložek, S. Ho, S. P. P. Ho, L. Howe, Z. Huang, J. Hubmayr, K. Huffenberger, J. P. Hughes, A. Iijas, M. Ikape, K. Irwin, A. H. Jaffe, B. Jain, O. Jeong, D. Kaneko, E. D. Karpel, N. Katayama, B. Keating, S. S. Kernasovskiy, R. Keskitalo, T. Kisner, K. Kiuchi, J. Klein, K. Knowles, B. Koopman, A. Kosowsky, N. Krachmalnicoff, S. E. Kuenstner, C. L. Kuo, A. Kusaka, J. Lashner, A. Lee, E. Lee, D. Leon, J. S. Leung, A. Lewis, Y. Li, Z. Li, M. Limon, E. Linder, C. Lopez-Caraballo, T. Louis, L. Lowry, M. Lungu, M. Madhavacheril, D. Mak, F. Maldonado, H. Mani, B. Mates, F. Matsuda, L. Maurin, P. Mauskopf, A. May, N. McCallum, C. McKenney, J. McMahon, P. D. Meerburg, J. Meyers, A. Miller, M. Mirmelstein, K. Moodley, M. Munchmeyer, C. Munson, S. Naess, F. Nati, M. Navaroli, L. Newburgh, H. N. Nguyen, M. Niemack, H. Nishino, J. Orlowski-Scherer, L. Page, B. Partridge, J. Peloton, F. Perrotta, L. Piccirillo,

G. Pisano, D. Poletti, R. Puddu, G. Puglisi, C. Raum, C. L. Reichardt, M. Remazeilles, Y. Rephaeli, D. Riechers, F. Rojas, A. Roy, S. Sadeh, Y. Sakurai, M. Salatino, M. S. Rao, E. Schaan, M. Schmittfull, N. Sehgal, J. Seibert, U. Seljak, B. Sherwin, M. Shimon, C. Sierra, J. Sievers, P. Sikhosana, M. Silva-Feaver, S. M. Simon, A. Sinclair, P. Siritanasak, K. Smith, S. R. Smith, D. Spergel, S. T. Staggs, G. Stein, J. R. Stevens, R. Stompor, A. Suzuki, O. Tajima, S. Takakura, G. Teply, D. B. Thomas, B. Thorne, R. Thornton, H. Trac, C. Tsai, C. Tucker, J. Ullom, S. Vagnozzi, A. V. Engelen, J. V. Lanen, D. D. Winkle, E. M. Vavagiakis, C. Vergès, M. Vissers, K. Wagoner, S. Walker, J. Ward, B. Westbrook, N. Whitehorn, J. Williams, J. Williams, E. J. Wollack, Z. Xu, B. Yu, C. Yu, F. Zago, H. Zhang, and N. Zhu, “The Simons Observatory: Science goals and forecasts,” *Journal of Cosmology and Astroparticle Physics*, vol. 2019, no. 2, 2019

The Simons Observatory Collaboration, N. Galitzki, A. Ali, K. S. Arnold, P. C. Ashton, J. E. Austermann, C. Baccigalupi, T. Baildon, D. Barron, J. A. Beall, S. Beckman, S. M. M. Bruno, S. Bryan, P. G. Calisse, G. E. Chesmore, Y. Chinone, S. K. Choi, G. Coppi, K. D. Crowley, K. T. Crowley, A. Cukierman, M. J. Devlin, S. Dicker, B. Dober, S. M. Duff, J. Dunkley, G. Fabbian, P. A. Gallardo, M. Gerbino, N. Goeckner-Wald, J. E. Golec, J. E. Gudmundsson, E. E. Healy, S. Henderson, C. A. Hill, G. C. Hilton, S.-P. P. Ho, L. A. Howe, J. Hubmayr, O. Jeong, B. Keating, B. J. Koopman, K. Kiuchi, A. Kusaka, J. Lashner, A. T. Lee, Y. Li, M. Limon, M. Lungu, F. Matsuda, P. D. Mauskopf, A. J. May, N. McCallum, J. McMahon, F. Nati, M. D. Niemack, J. L. Orlowski-Scherer, S. C. Parshley, L. Piccirillo, M. Sathyaranayana Rao, C. Raum, M. Salatino, J. S. Seibert, C. Sierra, M. Silva-Feaver, S. M. Simon, S. T. Staggs, J. R. Stevens, A. Suzuki, G. Teply, R. Thornton, C. Tsai, J. N. Ullom, E. M. Vavagiakis, M. R. Vissers, B. Westbrook, E. J. Wollack, Z. Xu, and N. Zhu, “The Simons Observatory: Instrument overview,” in *Millimeter, Submillimeter, and Far-Infrared Detectors and Instrumentation for Astronomy IX*, vol. 10708, Jul. 2018, p. 1070804

T. Ellefot, Y. Akiba, K. Arnold, J. Avva, D. Barron, A. N. Bender, A. Cukierman, T. de Haan, M. Dobbs, J. Groh, M. Hasegawa, M. Hazumi, W. Holzapfel, L. Howe, G. Jaehnig, B. Keating, A. Kusaka, A. T. Lee, L. Lowry, J. Montgomery, H. Nishino, C. Raum, K. M. Rotermund, M. Silva-Feaver, A. Suzuki, B. Westbrook, and N. Whitehorn, “Detector and readout assembly and characterization for the Simons Array,” *Journal of Low Temperature Physics*, vol. 193, no. 5, pp. 1094–1102, 2018

The POLARBEAR Collaboration, B. Westbrook, P. A. R. Ade, M. Aguilar, Y. Akiba, K. Arnold, C. Baccigalupi, D. Barron, D. Beck, S. Beckman, A. N. Bender, F. Bianchini, D. Boettger, J. Borrill, S. Chapman, Y. Chinone, G. Coppi, K. Crowley, A. Cukierman, T. de Haan, R. Dünner, M. Dobbs, T. Ellefot, J. Errard, G. Fabbian, S. M. Feeney, C. Feng, G. Fuller, N. Galitzki, A. Gilbert, N. Goeckner-Wald, J. Groh, N. W. Halverson, T. Hamada, M. Hasegawa, M. Hazumi, C. A. Hill, W. Holzapfel, L. Howe, Y. Inoue, G. Jaehnig, A. Jaffe, O. Jeong, D. Kaneko, N. Katayama, B. Keating, R. Keskitalo, T. Kisner, N. Krachmalnicoff, A. Kusaka, M. Le Jeune, A. T. Lee, D. Leon, E. Linder, L. Lowry, A. Madurowicz, D. Mak, F. Matsuda, A. May, N. J. Miller, Y. Minami, J. Montgomery,

M. Navaroli, H. Nishino, J. Peloton, A. Pham, L. Piccirillo, D. Plambeck, D. Poletti, G. Puglisi, C. Raum, G. Rebeiz, C. L. Reichardt, P. L. Richards, H. Roberts, C. Ross, K. M. Rotermund, Y. Segawa, B. Sherwin, M. Silva-Feaver, P. Siritanasak, R. Stompor, A. Suzuki, O. Tajima, S. Takakura, S. Takatori, D. Tanabe, R. Tat, G. P. Teply, A. Tikhomirov, T. Tomaru, C. Tsai, N. Whitehorn, and A. Zahn, “The POLARBEAR-2 and Simons Array Focal Plane Fabrication Status,” *Journal of Low Temperature Physics*, Sep. 2018

Collaboration, P. A. R. Ade, M. Aguilar, Y. Akiba, K. Arnold, C. Baccigalupi, D. Barron, D. Beck, F. Bianchini, D. Boettger, J. Borrill, S. Chapman, Y. Chinone, K. Crowley, A. Cukierman, R. Dünner, M. Dobbs, A. Ducout, T. Elleflot, J. Errard, G. Fabbian, S. M. Feeney, C. Feng, T. Fujino, N. Galitzki, A. Gilbert, N. Goeckner-Wald, J. C. Groh, G. Hall, N. Halverson, T. Hamada, M. Hasegawa, M. Hazumi, C. A. Hill, L. Howe, Y. Inoue, G. Jaehnig, A. H. Jaffe, O. Jeong, D. Kaneko, N. Katayama, B. Keating, R. Keskitalo, T. Kisner, N. Krachmalnicoff, A. Kusaka, M. Le Jeune, A. T. Lee, E. M. Leitch, D. Leon, E. Linder, L. Lowry, F. Matsuda, T. Matsumura, Y. Minami, J. Montgomery, M. Navaroli, H. Nishino, H. Paar, J. Peloton, A. T. P. Pham, D. Poletti, G. Puglisi, C. L. Reichardt, P. L. Richards, C. Ross, Y. Segawa, B. D. Sherwin, M. Silva-Feaver, P. Siritanasak, N. Stebor, R. Stompor, A. Suzuki, O. Tajima, S. Takakura, S. Takatori, D. Tanabe, G. P. Teply, T. Tomaru, C. Tucker, N. Whitehorn, and A. Zahn, “A Measurement of the Cosmic Microwave Background B-mode Polarization Power Spectrum at Subdegree Scales from Two Years of POLARBEAR Data,” *Astrophysical Journal*, vol. 848, 121, p. 121, Oct. 2017

The POLARBEAR Collaboration, S. Takakura, M. Aguilar, Y. Akiba, K. Arnold, C. Baccigalupi, D. Barron, S. Beckman, D. Boettger, J. Borrill, S. Chapman, Y. Chinone, A. Cukierman, A. Ducout, T. Elleflot, J. Errard, G. Fabbian, T. Fujino, N. Galitzki, N. Goeckner-Wald, N. W. Halverson, M. Hasegawa, K. Hattori, M. Hazumi, C. Hill, L. Howe, Y. Inoue, A. H. Jaffe, O. Jeong, D. Kaneko, N. Katayama, B. Keating, R. Keskitalo, T. Kisner, N. Krachmalnicoff, A. Kusaka, A. T. Lee, D. Leon, L. Lowry, F. Matsuda, T. Matsumura, M. Navaroli, H. Nishino, H. Paar, J. Peloton, D. Poletti, G. Puglisi, C. L. Reichardt, C. Ross, P. Siritanasak, A. Suzuki, O. Tajima, S. Takatori, and G. Teply, “Performance of a continuously rotating half-wave plate on the POLARBEAR telescope,” *Journal of Cosmology and Astroparticle Physics*, vol. 2017, no. 05, p. 008, 2017

The POLARBEAR Collaboration, D. Poletti, G. Fabbian, M. Le Jeune, J. Peloton, K. Arnold, C. Baccigalupi, D. Barron, S. Beckman, J. Borrill, S. Chapman, Y. Chinone, A. Cukierman, A. Ducout, T. Elleflot, J. Errard, S. Feeney, N. Goeckner-Wald, J. Groh, G. Hall, M. Hasegawa, M. Hazumi, C. Hill, L. Howe, Y. Inoue, A. H. Jaffe, O. Jeong, N. Katayama, B. Keating, R. Keskitalo, T. Kisner, A. Kusaka, A. T. Lee, D. Leon, E. Linder, L. Lowry, F. Matsuda, M. Navaroli, H. Paar, G. Puglisi, C. L. Reichardt, C. Ross, P. Siritanasak, N. Stebor, B. Steinbach, R. Stompor, A. Suzuki, O. Tajima, G. Teply, and N. Whitehorn, “Making maps of cosmic microwave background polarization for B-mode studies: the POLARBEAR example,” *Astronomy and Astrophysics*, vol. 600, A60, Apr. 2017

The POLARBEAR Collaboration, Y. Inoue, P. Ade, Y. Akiba, C. Aleman, K. Arnold, C. Baccigalupi, B. Barch, D. Barron, A. Bender, D. Boettger, J. Borrill, S. Chapman, Y. Chinone, A. Cukierman, T. de Haan, M. A. Dobbs, A. Ducout, R. Dünner, T. Elleflot, J. Errard, G. Fabbian, S. Feeney, C. Feng, G. Fuller, A. J. Gilbert, N. Goeckner-Wald, J. Groh, G. Hall, N. Halverson, T. Hamada, M. Hasegawa, K. Hattori, M. Hazumi, C. Hill, W. L. Holzapfel, Y. Hori, L. Howe, F. Irie, G. Jaehnig, A. Jaffe, O. Jeong, N. Katayama, J. P. Kaufman, K. Kazemzadeh, B. G. Keating, Z. Kermish, R. Keskitalo, T. S. Kisner, A. Kusaka, M. Le Jeune, A. T. Lee, D. Leon, E. V. Linder, L. Lowry, F. Matsuda, T. Matsumura, N. Miller, K. Mizukami, J. Montgomery, M. Navaroli, H. Nishino, H. Paar, J. Peloton, D. Poletti, G. Puglisi, C. R. Raum, G. M. Rebeiz, C. L. Reichardt, P. L. Richards, C. Ross, K. M. Rotermund, Y. Segawa, B. D. Sherwin, I. Shirley, P. Siritanasak, N. Stebor, R. Stompor, J. Suzuki, A. Suzuki, O. Tajima, S. Takada, S. Takatori, G. P. Teply, A. Tikhomirov, T. Tomaru, N. Whitehorn, A. Zahn, and O. Zahn, “POLARBEAR-2: an instrument for CMB polarization measurements,” in *Millimeter, Submillimeter, and Far-Infrared Detectors and Instrumentation for Astronomy VIII*, ser. Proceedings of the International Society for Optics and Photonics, vol. 9914, Jul. 2016, p. 99141I

The POLARBEAR Collaboration, N. Stebor, P. Ade, Y. Akiba, C. Aleman, K. Arnold, C. Baccigalupi, B. Barch, D. Barron, S. Beckman, A. Bender, D. Boettger, J. Borrill, S. Chapman, Y. Chinone, A. Cukierman, T. de Haan, M. Dobbs, A. Ducout, R. Dunner, T. Elleflot, J. Errard, G. Fabbian, S. Feeney, C. Feng, T. Fujino, G. Fuller, A. J. Gilbert, N. Goeckner-Wald, J. Groh, G. Hall, N. Halverson, T. Hamada, M. Hasegawa, K. Hattori, M. Hazumi, C. Hill, W. L. Holzapfel, Y. Hori, L. Howe, Y. Inoue, F. Irie, G. Jaehnig, A. Jaffe, O. Jeong, N. Katayama, J. P. Kaufman, K. Kazemzadeh, B. G. Keating, Z. Kermish, R. Keskitalo, T. Kisner, A. Kusaka, M. Le Jeune, A. T. Lee, D. Leon, E. V. Linder, L. Lowry, F. Matsuda, T. Matsumura, N. Miller, J. Montgomery, M. Navaroli, H. Nishino, H. Paar, J. Peloton, D. Poletti, G. Puglisi, C. R. Raum, G. M. Rebeiz, C. L. Reichardt, P. L. Richards, C. Ross, K. M. Rotermund, Y. Segawa, B. D. Sherwin, I. Shirley, P. Siritanasak, L. Steinmetz, R. Stompor, A. Suzuki, O. Tajima, S. Takada, S. Takatori, G. P. Teply, A. Tikhomirov, T. Tomaru, B. Westbrook, N. Whitehorn, A. Zahn, and O. Zahn, “The Simons Array CMB polarization experiment,” in *Millimeter, Submillimeter, and Far-Infrared Detectors and Instrumentation for Astronomy VIII*, ser. Proceedings of the International Society for Optics and Photonics, vol. 9914, Jul. 2016, 99141H

The POLARBEAR Collaboration, A. Suzuki, P. Ade, Y. Akiba, C. Aleman, K. Arnold, C. Baccigalupi, B. Barch, D. Barron, A. Bender, D. Boettger, J. Borrill, S. Chapman, Y. Chinone, A. Cukierman, M. Dobbs, A. Ducout, R. Dunner, T. Elleflot, J. Errard, G. Fabbian, S. Feeney, C. Feng, T. Fujino, G. Fuller, A. Gilbert, N. Goeckner-Wald, J. Groh, T. D. Haan, G. Hall, N. Halverson, T. Hamada, M. Hasegawa, K. Hattori, M. Hazumi, C. Hill, W. Holzapfel, Y. Hori, L. Howe, Y. Inoue, F. Irie, G. Jaehnig, A. Jaffe, O. Jeong, N. Katayama, J. Kaufman, K. Kazemzadeh, B. Keating, Z. Kermish, R. Keskitalo, T. Kisner, A. Kusaka, M. L. Jeune, A. Lee, D. Leon, E. Linder, L. Lowry, F. Matsuda, T. Matsumura, N. Miller, K. Mizukami, J. Montgomery, M. Navaroli, H. Nishino, J. Peloton, D. Poletti, G. Puglisi, G. Rebeiz, C. Raum, C. Reichardt, P. Richards, C. Ross, K. Rotermund,

Y. Segawa, B. Sherwin, I. Shirley, P. Siritanasak, N. Stebor, R. Stompor, J. Suzuki, O. Tajima, S. Takada, S. Takakura, S. Takatori, A. Tikhomirov, T. Tomaru, B. Westbrook, N. Whitehorn, T. Yamashita, A. Zahn, and O. Zahn, “The POLARBEAR-2 and the Simons Array Experiments,” *Journal of Low Temperature Physics*, vol. 184, pp. 805–810, Aug. 2016

S. P. Benz, S. B. Waltman, A. E. Fox, P. D. Dresselhaus, A. Rüfenacht, J. M. Underwood, L. Howe, R. E. Schwall, and C. J. Burroughs, “One-volt Josephson arbitrary waveform synthesizer,” *IEEE Transactions on Applied Superconductivity*, vol. 25, no. 1, pp. 1–8, 2015

L. Howe, A. E. Fox, A. Rüfenacht, C. J. Burroughs, P. D. Dresselhaus, S. P. Benz, and R. E. Schwall, “NIST 10 V programmable Josephson voltage standard system using a low-capacity cryocooler,” *IEEE Transactions on Applied Superconductivity*, vol. 25, no. 3, pp. 1–4, 2015

A. Rüfenacht, L. Howe, A. E. Fox, R. E. Schwall, P. D. Dresselhaus, C. J. Burroughs, and S. P. Benz, “Cryocooled 10 V programmable Josephson voltage standard,” *IEEE Transactions on Instrumentation and Measurement*, vol. 64, no. 6, pp. 1477–1482, 2015

The POLARBEAR Collaboration, P. A. R. Ade, K. Arnold, M. Atlas, C. Baccigalupi, D. Barron, D. Boettger, J. Borrill, S. Chapman, Y. Chinone, A. Cukierman, M. Dobbs, A. Ducout, R. Dunner, T. Elleflot, J. Errard, G. Fabbian, S. Feeney, C. Feng, A. Gilbert, N. Goeckner-Wald, J. Groh, G. Hall, N. W. Halverson, M. Hasegawa, K. Hattori, M. Hazumi, C. Hill, W. L. Holzapfel, Y. Hori, L. Howe, Y. Inoue, G. C. Jaehnig, A. H. Jaffe, O. Jeong, N. Katayama, J. P. Kaufman, B. Keating, Z. Kermish, R. Keskitalo, T. Kisner, A. Kusaka, M. Le Jeune, A. T. Lee, E. M. Leitch, D. Leon, Y. Li, E. Linder, L. Lowry, F. Matsuda, T. Matsumura, N. Miller, J. Montgomery, M. J. Myers, M. Navaroli, H. Nishino, T. Okamura, H. Paar, J. Peloton, L. Pogosian, D. Poletti, G. Puglisi, C. Raum, G. Rebeiz, C. L. Reichardt, P. L. Richards, C. Ross, K. M. Rotermund, D. E. Schenck, B. D. Sherwin, M. Shimon, I. Shirley, P. Siritanasak, G. Smecher, N. Stebor, B. Steinbach, A. Suzuki, J.-i. Suzuki, O. Tajima, S. Takakura, A. Tikhomirov, T. Tomaru, N. Whitehorn, B. Wilson, A. Yadav, A. Zahn, and O. Zahn, “POLARBEAR constraints on cosmic birefringence and primordial magnetic fields,” *Physical Review Letters D*, vol. 92, no. 12, 123509, p. 123 509, Dec. 2015

A. Rüfenacht, L. Howe, A. E. Fox, R. E. Schwall, P. D. Dresselhaus, C. J. Burroughs, and S. P. Benz, “Cryocooled 10 V programmable Josephson voltage standard,” in *Conference on Precision Electromagnetic Measurements*, IEEE, 2014, pp. 458–459

L. Howe, C. J. Burroughs, P. D. Dresselhaus, S. P. Benz, and R. E. Schwall, “Cryogen-free operation of 10 V programmable Josephson voltage standards,” *IEEE Transactions on Applied Superconductivity*, vol. 23, no. 3, pp. 1 300 605–1 300 605, 2013

ABSTRACT OF THE DISSERTATION

The POLARBEAR-2 Cryogenic Receiver for Cosmic Microwave Background Polarization Science

by

Logan Alfred Howe

Doctor of Philosophy in Physics

University of California, San Diego, 2019

Professor Brian Keating, Chair

Measurements of the Cosmic Microwave Background (CMB) have proved pivotal over the last few decades in the development of Λ CDM, the standard model of cosmology. Coupled with the standard model of particle physics, these two theories describe a majority of our observations of the Universe's structure, dynamics, and evolution. Beyond discovering the specifics of how our Universe was formed, remaining open questions regarding our Universe include the masses of neutrino species, the exact nature of dark matter, and the equation of state of dark energy – to name a few. The CMB is imprinted with information

that can help answer all these questions, making measurements of the temperature and polarization field of the CMB at high precision an effective path to increasing our understanding of fundamental physics. The polarization field especially, composed of parity even E-mode and parity odd B-mode patterns, possesses untapped constraining power, at both very large and very small angular scales.

This dissertation describes the design and characterization of cryogenic receivers for the Simons Array CMB polarization experiment. The Simons Array is located at 5200 m elevation in the Atacama desert, Chile and consists of three off-axis Gregorian-Dragone telescopes, each coupled to a POLARBEAR-2 cryogenic receiver. Each receiver's focal plane is comprised of 7,588 transition edge sensor (TES) bolometers cooled to 250 mK and read out using 4 K superconducting quantum interference devices (SQUIDs) using digital frequency division multiplexing (DfMUX). The POLARBEAR-2 receiver cryostat consists of an optics tube and backend cryostat, which are built and tested separately, then integrated for final testing before deployment to the Chilean site. Here we describe fabrication and cryogenic validation of two POLARBEAR-2 backends, and of the complete second POLARBEAR-2 receiver: POLARBEAR-2b. Additionally, we discuss readout and detector integration, including detailed SQUID characterization and TES array measurements, and demonstration of deployment readiness of all selected devices and subcomponents. Finally, we describe efforts and progress towards final lab validation of the POLARBEAR-2b receiver and final demonstrations of deployment readiness.

Chapter 1

Introduction

In the beginning there was nothing, which exploded.

— Terry Pratchett

1.1 The Standard Model of Cosmology

The current best description which agrees with the multitude of both micro and macro physical observations humans have made of our Universe over the past few centuries is known as the Lambda Cold Dark Matter (Λ CDM) model. This model is a specific case of Big Bang cosmology, and uses a cosmological constant Λ general relativity to describe expansion and gravity, and the standard model of particle physics to describe the majority of other dynamics (non-zero neutrino masses are not currently predicted by the standard model of particle physics). In Λ CDM the expansion of the Universe is driven by the cosmological constant Λ (i.e. dark energy) and cold dark matter. The major strengths of Λ CDM are that it accurately describes the expansion of the Universe,

light element abundances, existence of the Cosmic Microwave Background (CMB), and large-scale structure of the Universe [21].

The first step in deriving Λ CDM cosmology is determining expressions which describe the macroscopic evolution of the Universe. Using general relativity and assuming our Universe is homogeneous and isotropic (an assumption we will discuss further in later sections), the metric tensor which exactly solves Einstein's equations

$$G_{ab} = R_{ab} - \frac{1}{2}g_{ab}R = 8\pi GT_{ab} \quad (1.1)$$

is the Friedmann-Lemaître-Robertson-Walker (FLRW) metric

$$ds^2 = g_{ab}x^a x^b = -c^2 dt^2 + a^2(t) \left(\frac{dr^2}{1+kr^2} + r^2 d\theta^2 + r^2 \sin^2 \theta d\phi^2 \right). \quad (1.2)$$

Here R and R_{ab} are the Ricci scalar and tensor, G is Newton's gravitational constant, and G_{ab} and T_{ab} are the Einstein and stress-energy tensors, respectively. The parameter k describes the curvature and can take values of ± 1 or 0 . $a(t)$ is known as the dimensionless “scale factor” which relates the proper distance between two objects at time t . The time derivatives of $a(t)$ describe the evolution of the Universe which can encompass both expansion and contraction depending on the sign of $\dot{a}(t)$.

Our observations of the Universe's history show that $\dot{a}(t)$ is positive for all times

since the Big Bang, in which case we may define the cosmic redshift

$$1+z = \frac{1}{a(t)}. \quad (1.3)$$

The redshift provides a measure of the age of the Universe, and thus size, when light was emitted from a given source ($z=0$ corresponds to the present) [21].

Solving Einstein's equations (i.e. Equation 1.1) using the FLRW metric results in the Friedmann equations, the most ubiquitous formulae in modern cosmology. The time-time Einstein equation yields the first Friedmann equation

$$\left[\frac{\dot{a}(t)}{a(t)} \right]^2 = \frac{8\pi G}{3} \frac{\varepsilon(t)}{c^2} - \frac{c^2 k}{a^2(t)}, \quad (1.4)$$

where $\varepsilon(t)$ is the energy density. We define the Hubble parameter

$$H(a) \equiv \frac{\dot{a}(t)}{a(t)} \quad (1.5)$$

which describes the relative expansion of the Universe as a function of time. As previously mentioned, for much of the history of the Universe $H(a) \sim \text{const}$. If the curvature k in Equation 1.4 is zero then a special value of the energy density is obtained, referred to as the critical energy density:

$$\varepsilon(t)_{cr} = \frac{3c^2}{8\pi G} H^2(t). \quad (1.6)$$

The dimensionless density parameter

$$\Omega(t) = \frac{\varepsilon(t)}{\varepsilon_{cr}(t)} \quad (1.7)$$

is commonly used to describe the energy density and can be used to write Equation 1.4 in terms of the contribution to the total energy density due to each constituent:

$$H^2(a) = H_0^2 \sum_i \frac{\Omega_i}{a^{3(1+w_i)}} - \frac{c^2 k}{a^2}. \quad (1.8)$$

Here H_0 is the value of $H(a)$ at the current time, and $w_i = P/\varepsilon_i$ is the equation of state of the i th energy form.

Using Equation 1.4 in the trace of Equation 1.1 yields the second Friedmann equation relating the Universe's acceleration to both the energy density and pressure P :

$$\frac{\ddot{a}(t)}{a(t)} = \frac{4\pi G}{3c^2}(\varepsilon(t) + 3P). \quad (1.9)$$

$\varepsilon < \varepsilon_{cr}$ yields $k < 0$, corresponding to perpetual and accelerated expansion. $\varepsilon > \varepsilon_{cr}$ yields $k > 0$ and is referred to as a “bounce,” in which the Universe expands until the energy density drops low enough to change the sign of k , and cause contraction. We shall discuss in the following section the implications of the observed value of the energy density, which is very near the critical energy density.

A remarkable feature of Λ CDM is that it describes the majority of the Universe's evolution and large scale structure using only six independent, variable parameters. These

parameters are:

1. Physical baryon density: $\Omega_b h^2$
2. Physical dark matter density: $\Omega_c h^2$
3. Age of the Universe: t_0
4. Scalar perturbation spectral index: n_s
5. Curvature fluctuation amplitude (at reference scale $k_0 = 2 \text{ kpc}^{-1}$): Δ_R^2
6. Optical depth at reionization: τ

1.2 Cosmic Inflation

While the accuracy with which the ΛCDM model can be used to describe the Universe we observe today, it does not provide solutions to what are referred to as the “horizon” and “flatness” problems. In this section we will describe the theory of cosmic inflation [22], proposed as a modification of ΛCDM cosmology in order to provide an elegant and simultaneous solution to both these problems, as well as a potential explanation of the “heavy relic” problem.

The horizon problem refers to difficulties explaining the cosmological principle: that the Universe is statistically homogeneous isotropic on scales larger than $\sim 10^8 \text{ pc}$ (i.e. scales encompassing many galactic clusters). This applies not only to the distribution of ordinary matter and energy in the local Universe, but also to the remarkable uniformity in

the temperature of the CMB. For statistical isotropy there must have been a mechanism allowing interactions between energy and matter which, under a constant or even modestly accelerating Hubble expansion rate [23], remain outside of causal contact over the known age of the Universe (~ 14 Gyr). For reference, the horizon size at the time of formation of the CMB corresponds to roughly 2 degrees on today's sky but we observe a sky temperature of 2.725 K which is uniform to one part in 10^4 across the entire sky. Thus, the cosmological principle mandates a more exotic and rapid expansion at some point early in the lifetime of the Universe in order to allow the space-like separated matter and energy to interact and thermalize to an extraordinary degree.

The flatness problem refers to the fact that observations imply fine-tuning in the value of the energy density. The energy density we observe today Ω_0 is equal to 1 to less than 1% [24]. Using our results from Section 1.1, we can write down a useful expression for $\Omega(t)$:

$$\Omega(t) - 1 = \frac{kc^2}{R_0^2 H^2(t) a^2(t)}, \quad (1.10)$$

where R_0 is the spacetime radius of curvature [25]. Equation 1.10 demonstrates the fine-tuned nature of $\Omega(t)$ equaling 1. Perturbations away from $\Omega = 1$ are amplified over time in a runaway fashion, while $\Omega = 1$ results in $k = 0$ and no evolution (i.e. constant curvature). Thus we arrive at the flatness problem: observations today indicate $\Omega_0 = 1$, therefore we must have $\Omega(t = 0) = 1$ to a very high precision.

Cosmic inflation is the theory by which, in the primordial stages of the Universe (the first $\sim 10^{-35}$ s or so), spacetime underwent an exponential expansion and the size of the

Universe increased by as much as a factor of $\sim 10^{26}$ (60 e-foldings) [26]. This superluminal expansion would have been extremely brief but would solve both the horizon and flatness problems. A simple model for inflation in an FLRW Universe is one which is exactly exponential and where the Hubble parameter remains constant:

$$a(t) = a(0)e^{Ht}. \quad (1.11)$$

In such a model, the horizon size diminishes exponentially during inflation, and once it ends the more prosaic dark-energy-driven expansion resumes and the horizon size grows according to Hubble expansion. Locally significant primordial matter and energy density anisotropies are smoothed out, leading to the cosmological principle and providing a solution to the horizon problem. The flatness problem is similarly solved with cosmic inflation as, if $\Omega(t=0)$ is allowed to take an arbitrary value, then the expansion of the horizon by a factor of $\sim 10^{26}$ takes this initial energy density and reduces $\Omega(t=0) - 1$ to nearly 0.

One example of the heavy relic problem is the complete lack of observation of magnetic monopoles today. The existence of such particles is permitted, and even expected, as they would symmetrize Maxwell's equations (i.e. quantum electrodynamics), but their rest mass would need to be extremely large – potentially above even Grand Unified Theory (GUT) energies of $\gtrsim 10^{15}$ GeV. If the temperature of the Universe was once above the magnetic monopole energy, many such particles would be created, but as the Universe cooled production ceases. Scenarios where monopole production halted before inflation ended would result in a vanishingly dilute concentration today when compared to leptons

and baryons, which continued to be produced for hundreds of seconds after inflation ended. Monopole detection using this model is extremely difficult as a direct result of their low spatial density.

1.3 The Cosmic Microwave Background

Immediately following the Big Bang, the Universe was a hot plasma consisting of fundamental particles (leptons, quarks, gluons, photons etc.). As the Universe cooled in the time following the Big Bang, a series of phase changes corresponding to the formation of composite matter occurred. Initially, within the first second or so, protons and neutrons formed from the quark-gluon plasma. The nucleons then began to fuse and form primordial deuterium and helium nuclei over timescales of a few minutes. After nuclear fusion, the matter in the Universe consists primarily of a proton/electron/nucleon plasma and cooling continues for $\sim 380,000$ years. During this cooling phase the Universe is optically opaque, due to the very short photon mean free path in the plasma. However, once the temperature drops to $\sim 12,000$ K (~ 1 eV), neutral hydrogen is able to form, causing photons to largely decouple from matter and free-stream to us today at $t \sim 14$ Gyr. Radiation from the epoch of decoupling forms a surface, or shell, in the sky beyond which we cannot see (due to the plasma's opacity), making these the photons which Coulomb scattered longest ago. We refer to this as the “surface of last scattering.” Photons from the surface of last scattering make up the Cosmic Microwave Background (CMB) and carry a wealth of information regarding the physics and composition of the early Universe.

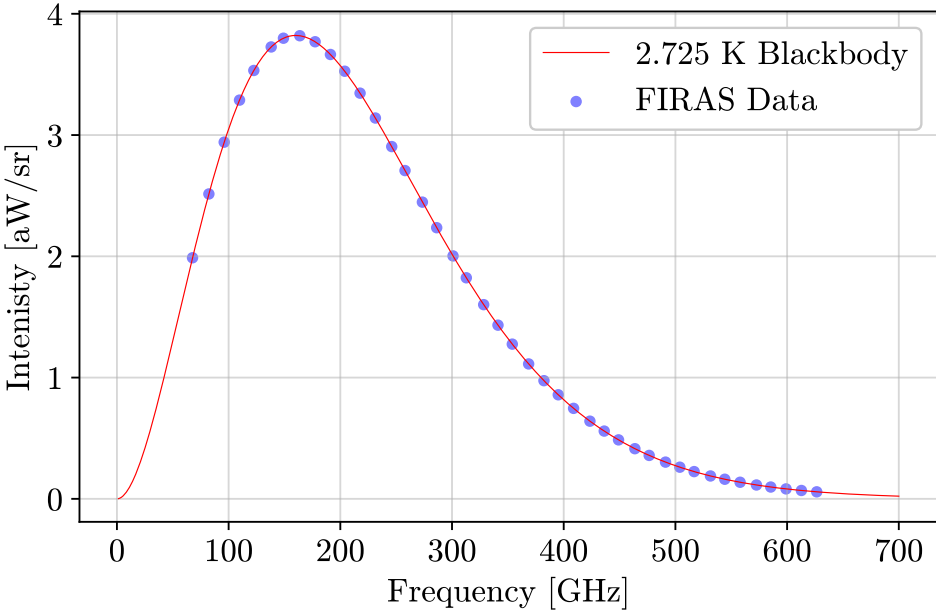


Figure 1.1: CMB spectrum measurement from the COBE FIRAS spectrometer. Traditionally, error bars for these data are magnified by 400 times to become visible around the data points, for this reason they are omitted here. Data from [27].

Any object at temperature T emits electromagnetic radiation with an intensity at frequency ν according to the Planck blackbody distribution:

$$B(\nu, T) = \frac{2h\nu}{c^3} \frac{1}{e^{h\nu/k_B T} - 1} \quad (1.12)$$

Measurements of the intensity spectrum of the CMB reveal that it is extremely well-described by the blackbody equation. The FIRAS measurement gives a temperature as measured today of 2.726 ± 0.010 K (95% confidence level) [27], [28], which means the age of the Universe can be calculated to be 13.8 Gyr [21]. The tight agreement with the blackbody spectrum is demonstrated in Figure 1.1, which shows the measured CMB spectrum from the FIRAS instrument on the COBE satellite [27]. The remarkable agreement with the

blackbody theory of Equation 1.12, and the fact that the FIRAS results contain data for large portions of the sky which indicate temperature uniformity to a single part in 10^4 , imply that prior to the formation of the CMB the Universe was extremely well-thermalized. Here we have direct observational evidence for the cosmological principle: uniformity and isotropy. The CMB’s thermal uniformity implies that at some point, parts of the Universe which are not in causal contact today, i.e separated by a distance greater than the light travel distance for the age of Universe, must have been in contact before the CMB was emitted. In combination with measurements showing nearly scale-invariant scalar fluctuations, and that the Universe’s curvature is very flat [24], we have strong evidence motivating an early inflationary epoch.

Figure 1.1 also demonstrates that experiments hoping to observe the CMB today should choose an observing frequency roughly between 50 and 300 GHz where the spectrum peaks. A number of observational concerns regarding the fidelity of detecting CMB photons, as opposed to those coming from other interactions in the Universe, can influence the exact choice of frequency bands and will be discussed further in Section 1.4. The most common “CMB” observing frequencies are in the range of $\sim 70\text{--}180$ GHz, with other frequencies used to remove spurious signal from final CMB maps. Primary CMB observing frequencies are often chosen with band centers around 90 and 150 GHz.

1.3.1 Temperature Anisotropies

In spite of the extreme uniformity in the average CMB temperature, we also observe anisotropic temperature fluctuations on the order of $\pm 100 \mu\text{K}$ at large scales and across a

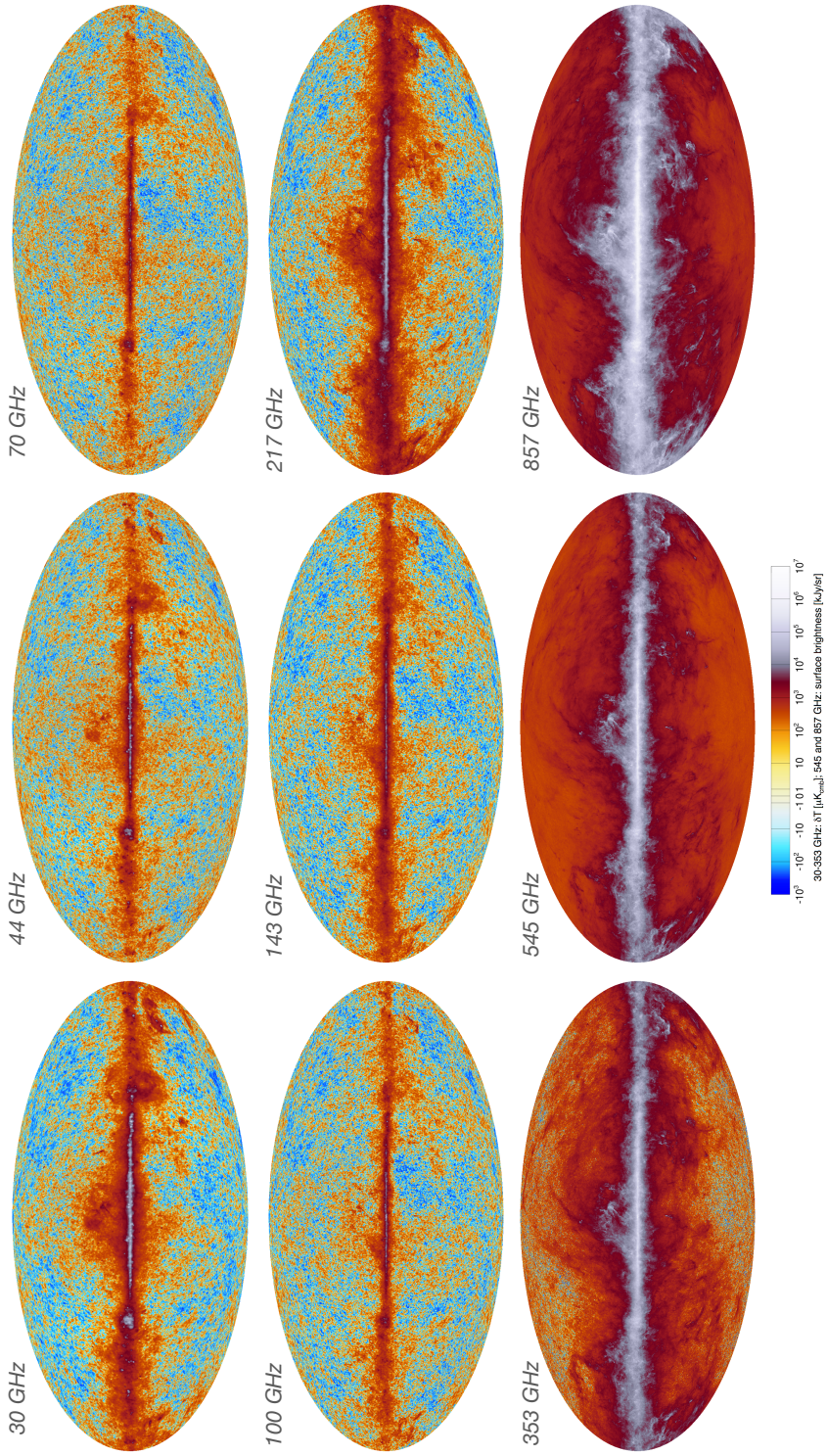


Figure 1.2: Full-sky maps from the Planck satellite mission observing at nine frequencies between 30 and 857 GHz. High temperature/brightness regions near the galactic plane are due to foreground contamination from galactic synchrotron and interstellar dust emission. These regions are often masked during data analysis if foreground removal techniques are deemed inadequate in subtracting the non-CMB signal. Away from the galactic plane and its features, the anisotropies of the CMB are visible and correspond to roughly $\pm 20 \mu\text{K}$. Maps from [29], [30].

wide range of frequencies as can be seen in Figure 1.2. Anisotropies are generated by a variety of phenomena and are separated into both primary and secondary components. The former describes effects generated before decoupling, and the latter refers to effects from interaction between CMB photons and the Universe as they travel towards us from the the surface of last scattering. In this sense, primary anisotropies carry information about the early Universe, where secondary anisotropies carry information about the matter and energy distribution after decoupling.

Temperature anisotropies are typically discussed in terms of an angular power spectrum, which contains statistical information of the fluctuations across a range of scales on the sky. This is done by first decomposing the measured perturbation map at direction \hat{n} into spherical harmonics using the dimensionless temperature

$$\Theta(\hat{n}) = \frac{\Delta T(\hat{n})}{T_0} = \frac{T(\hat{n}) - T_0}{T_0}, \quad (1.13)$$

where T_0 is the mean CMB temperature. We then compute the spherical harmonic coefficients:

$$\Theta_{\ell m} = \int d\Omega \Theta(\hat{n}) Y_{\ell m}^*. \quad (1.14)$$

The power spectrum C_ℓ , as a function of angular multipole moment ℓ , is formed by integrating over all m for each ℓ value

$$\langle \Theta_{\ell m}^* \Theta_{\ell' m'} \rangle = \delta_{\ell\ell'} C_\ell, \quad (1.15)$$

This averaging is performed because we have no knowledge of the specific orientation of the particular $Y_{\ell m}$ which best describes the perturbation at direction \hat{n} . Another common method used in CMB power spectrum analysis is the “flat sky” approximation, which can be made when the patch size on sky under study is small and allows use of a traditional Fourier series in computing the C_ℓ from Equation 1.15. Flat skies may not be assumed for patches more than a few degrees on a side and will result in spurious high angular frequency power in C_ℓ due to ringing of the Fourier modes at the patch edges.

To appropriately scale the power at multipole moment ℓ , the logarithmic power per wave number

$$\Delta T^2 = \frac{\ell(\ell+1)}{2\pi} C_\ell T^2, \quad (1.16)$$

is useful to employ [31]. Figure 1.3 shows the theoretical CMB temperature anisotropy power spectrum, with

$$D_\ell = \frac{\ell(\ell+1)}{2\pi} C_\ell, \quad (1.17)$$

and using the current best-fit values for the six Λ CDM cosmological parameters at the end of Section 1.1.

A fundamental limitation of estimating the power spectrum from cosmological observations arises from the averaging over all $2\ell + 1$ values of m at each multipole. As ℓ decreases the number of components available to average over decreases and uncertainty in the $Y_{\ell m}$ orientation grows. We refer to this as the “cosmic variance” limit, which places a fundamental limit on the precision at which the power spectrum may be measured at large angular scales (small ℓ). The power spectrum error thus depends directly on the number of

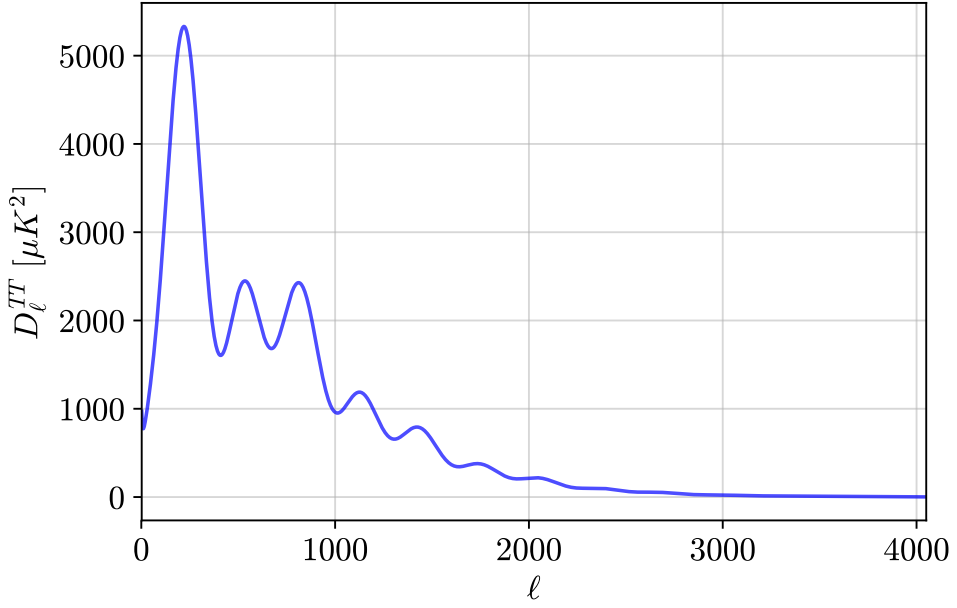


Figure 1.3: CMB temperature anisotropy power spectrum calculated using the CAMB package [32] and the current best fit values for Λ CDM parameters.

available m values:

$$\Delta C_\ell = \sqrt{\frac{2}{2\ell+1}} C_\ell. \quad (1.18)$$

Discussion of the CMB power spectrum in Section 1.3.1 focused on the *temperature* anisotropies of the CMB but, as it happens, the CMB is also weakly polarized. Net polarization arises in a system dominated by Compton scattering when there is inhomogeneity resulting in a quadrupole temperature anisotropy around a central free electron. Figure 1.4 shows a diagram of this effect, where the output net polarization is aligned along the cold axis of the quadrupole (Y_{2m}). The output polarization cross section is

$$\frac{d\sigma}{d\Omega} = \frac{3}{8\pi} |\hat{\varepsilon}' \cdot \hat{\varepsilon}|^2 \sigma_T, \quad (1.19)$$

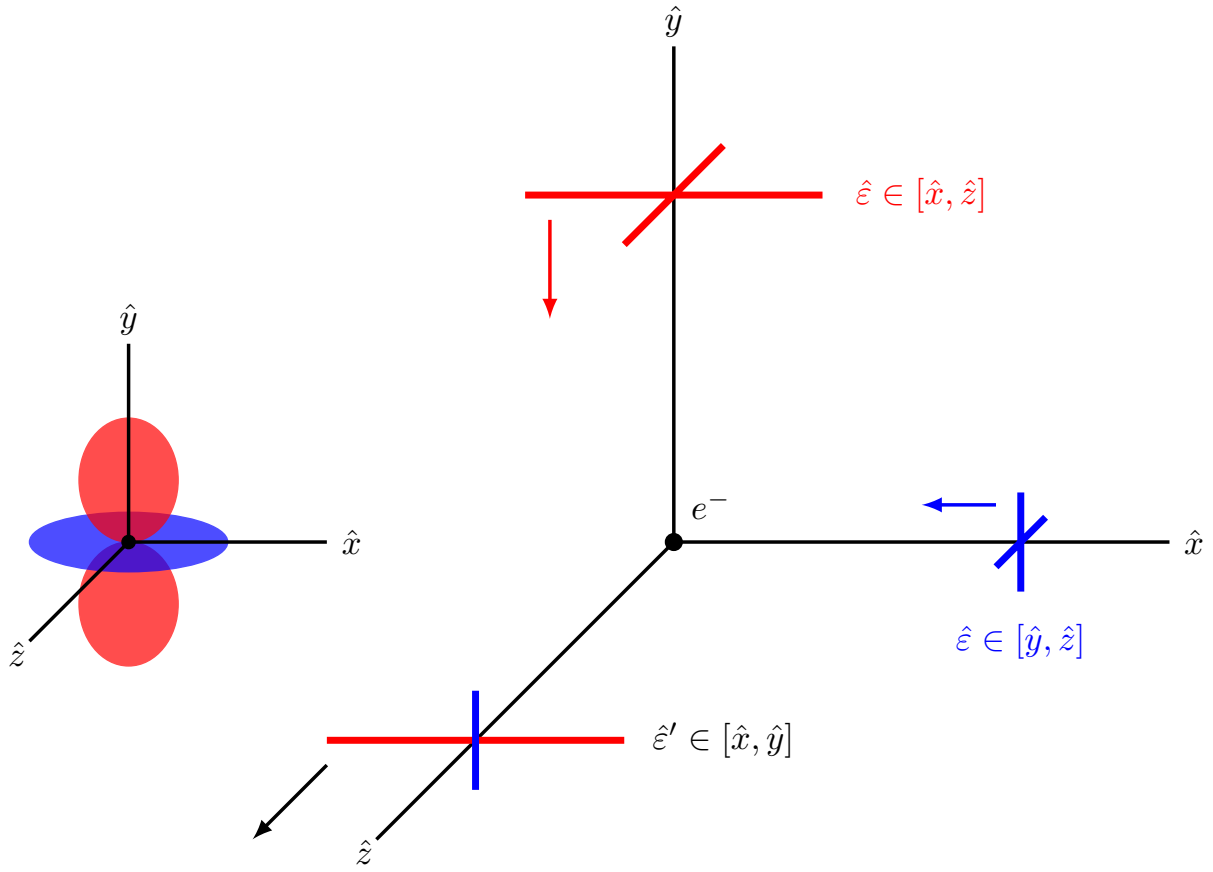


Figure 1.4: Cartoon diagram of CMB polarization due to Thomson scattering off an electron surrounded by a quadrupolar temperature anisotropy. The left depicts the quadrupole temperature anisotropy (red is hot, blue is cold). Radiation with net zero polarization is incident on an electron at the origin from the hot and cold regions. Due to the Thomson scattering cross section's angular dependence, an observer looking along the \hat{z} axis will only see polarization in the xy plane. Finally, since radiation from the hot region is more intense, this polarization dominates, and the observed polarization is thus aligned with the cold axis of the quadrupole.

where σ_T is the Thomson scattering cross section and $\hat{\varepsilon}', \hat{\varepsilon}$ are the incoming and scattered polarization unit vectors. Note that no polarization in the \hat{z} (i.e. the unit normal vector of the last scattering surface) is emitted from quadrupoles with the hot axis aligned with \hat{z} .

Electromagnetic polarization can be fully characterized by the Stokes parameters

$$I = |E_x|^2 + |E_y|^2 \quad (1.20)$$

$$Q = |E_x|^2 - |E_y|^2 \quad (1.21)$$

$$U = 2\text{Re}(E_x E_y^*) \quad (1.22)$$

$$V = -2\text{Im}(E_x E_y^*) \quad (1.23)$$

with the wave traveling in the \hat{z} direction. E_x and E_y are the \hat{x} and \hat{y} components of the electric field. I is the total intensity, Q and U relate to the two linear polarization components, and V is the circular polarization. Since the Stokes parameters depend on a particular choice of coordinate systems it is useful to define new quantities which are coordinate-independent. We call these E-modes and B-modes, where the former carries information of the parity-symmetric (divergence) component and the latter the parity-asymmetric (curl) component of the polarization field. These are constructed using a Helmholtz decomposition.

Once a polarization map is made we can follow the same recipe as laid out in Section 1.3.1 to construct the E-mode and B-mode power spectra C_ℓ^{EE} and C_ℓ^{BB} . In this case we would refer to the power spectrum in Equation 1.15 explicitly as the *temperature* power spectrum: C_ℓ^{TT} . Cross correlation two- and four-point spectra are also routinely used in CMB analysis, i.e. C_ℓ^{EB} , C_ℓ^{EEBB} etc. – where the four-point spectra are constructed as in Equation 1.15 but with four $\Theta_{\ell m}^i$ terms.

Figure 1.5 shows the theoretical E-mode spectrum. As can be seen in Figure 1.6,

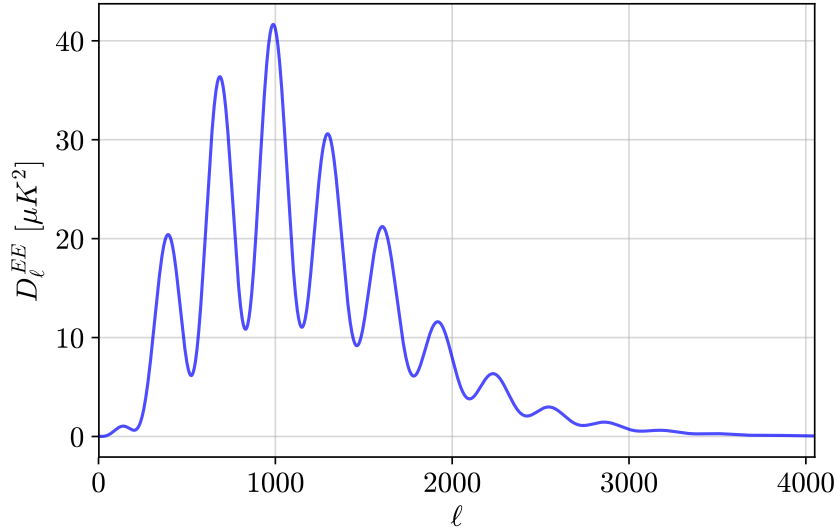


Figure 1.5: CMB E-mode anisotropy power spectrum calculated using the CAMB package [32] and the current best fit values for Λ CDM parameters.

temperature and E-mode anisotropies, in part due to their shared parity symmetry, are correlated. In a spacetime which respects parity conservation, correlations between parity-even and parity odd phenomena such as C_ℓ^{TB} and C_ℓ^{EB} are manifestly vanishing as mandated by the parity symmetry. Nonzero correlations here can be used interchangeably as experimental calibration, or if systematic errors are well-controlled, provide bounds on the degree of parity violation permitted by effects such as cosmic birefringence, defects, axions, or the magnitude of primordial magnetic fields [18].

1.3.2 Gravitational Waves

Early Universe perturbations, modeled as small changes to the primordial metric

tensor g_{ab} , may be decomposed into scalar (density), vector, and tensor components in

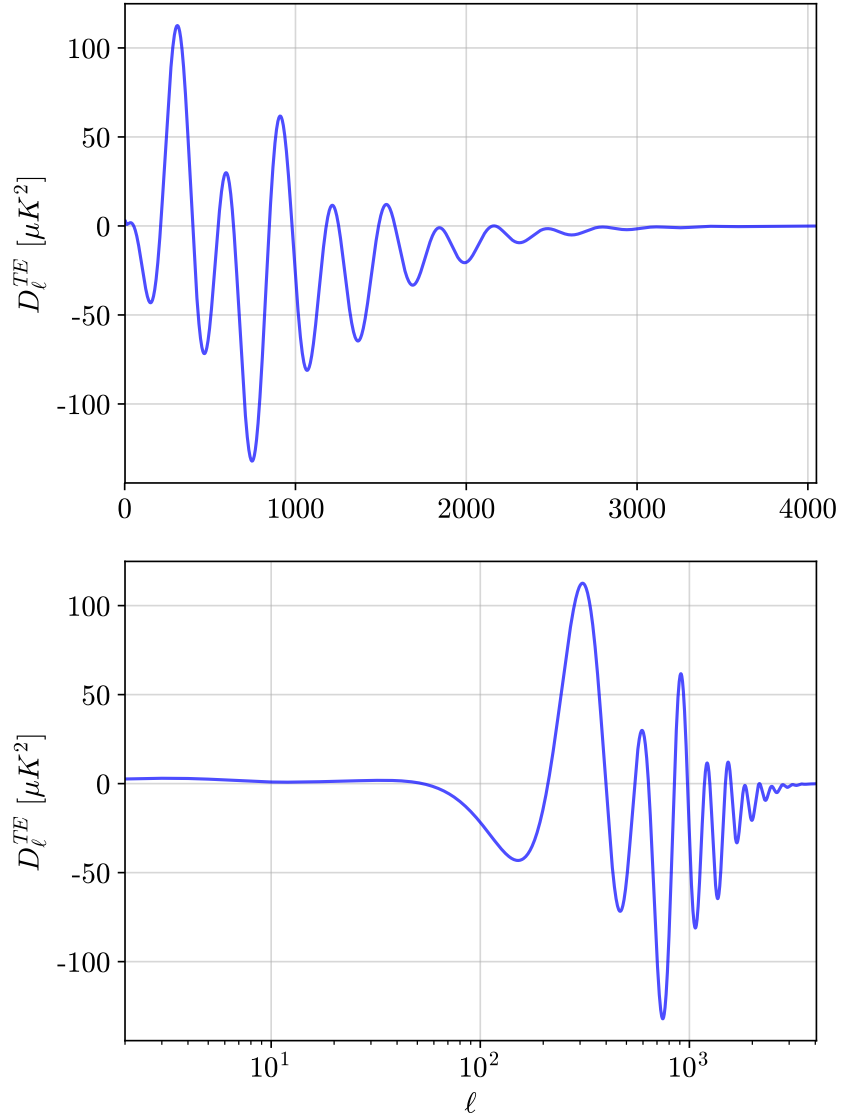


Figure 1.6: CMB temperature-E-mode correlation power spectrum calculated using the CAMB package [32] and the current best fit values for Λ CDM parameters. Both plots show the same curve and, as can be seen from the bottom plot, the TE correlations/anticorrelations peak between $\ell \sim 100$ and $\ell \sim 2000$ — corresponding to relatively small angular scales.

order to separate which component may be affected by different physics [33]:

$$g_{ab} = \eta_{ab} + h_{ab}. \quad (1.24)$$

Here η (g) are the unperturbed (perturbed) metrics, and h is the perturbation tensor.

Working in the transverse-traceless gauge for h_{ab} gives the irreducible decomposition

$$h_{00} = 2\phi \quad (1.25)$$

$$h_{0i} = \beta_i + \partial_i \gamma \quad (1.26)$$

$$h_{ij} = h_{ij}^{\text{TT}} + \frac{1}{3} H \delta_{ij} \partial_{i\varepsilon_j} + \left(\partial_i \partial_j - \frac{1}{3} \delta_{ij} \nabla^2 \right) \lambda. \quad (1.27)$$

Where Equations 1.25, 1.26, and 1.27 are the scalar, vector, and tensor components respectively. The quantities ϕ and γ are free scalar parameters, and β_i and $\partial_i \gamma$ are the transverse and longitudinal components of h_{ti} .

Further insight is gained by enforcing the “no source” constraint by setting the divergence of β_i , ε_i , and h_{ij}^{TT} to zero. h_{ij}^{TT} is also traceless by our choice of gauge, and we enforce the asymptotic boundary conditions that γ , ε_i , λ , and $\nabla^2 \lambda$ vanish as $r \rightarrow \infty$. It can also be shown that h_{ij}^{TT} is gauge invariant and, once Einstein’s equations are solved with an appropriate stress-energy tensor, it is the only component of the metric which satisfies the wave equation:

$$\square h_{ij}^{\text{TT}} = -16\pi \sigma_{ij}, \quad (1.28)$$

with $\square = \partial^a \partial_a$ the d’Alembertian operator. Here we have relaxed the no source condition but in vacuum the right hand side of Equation 1.28 is zero. h_{ij}^{TT} represents the form which gravitational radiation can take, which can be decomposed into two polarization states h_+

and h_x

$$h^{TT} = \begin{bmatrix} 0 & 0 & 0 & 0 \\ 0 & h_+ & h_x & 0 \\ 0 & h_x & h_+ & 0 \\ 0 & 0 & 0 & 0 \end{bmatrix}, \quad (1.29)$$

corresponding to a traveling in the \hat{z} direction. Figure 1.7 schematically demonstrates the effects of a gravitational wave of both polarizations on a test mass ring.

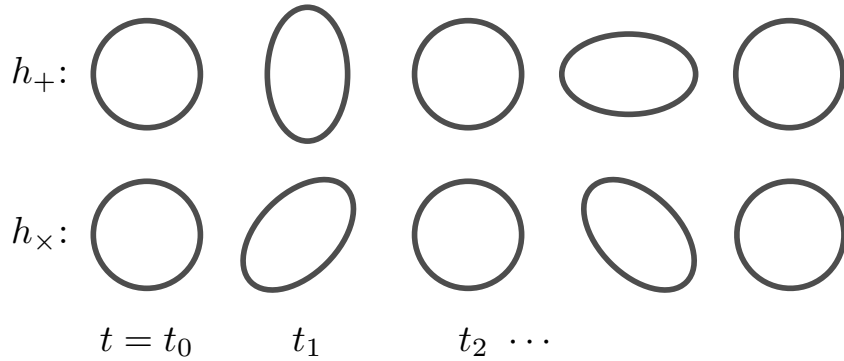


Figure 1.7: Diagram showing the qualitative effects of the two gravitational wave polarization states h_+ and h_x on a test mass ring. The gravitational wave travels in/out of the page ($\pm\hat{z}$ direction).

1.3.3 Inflationary Gravitational Waves

Primordial metric perturbations seed the anisotropies imprinted on the CMB at last scattering and, in some cases, go on to influence the growth of large scale structure seen today. This means primordial metric perturbations seed *primary* anisotropies, the accurate measurement of which allows us to test different physical models of the Universe — such as Λ CDM. One of the most important and popular theories we test using CMB power spectra

are the legion of inflationary models, nearly all of which share a critical common feature in the generation of an almost scale-independent, stochastic, gravitational wave background.

Primordial density perturbations source from dark matter over/under densities which, due to their parity-symmetric (isotropic) nature, manifest in both the temperature and E-mode spectrum only. For this reason there is strong correlation between the temperature and E-mode spectrum ($C_\ell^{TE} \neq 0$). Conversely, the primary B-mode spectrum can only be generated due to parity violating physics, i.e. vector and tensor modes. Vector modes from axions, cosmic defects, heavy relics and other models often contribute weakly and at very small scales as a result of dilution during inflation. Inflation generates all three types of perturbations (again, vector modes are suppressed), but is unique in its ability to generate tensor modes via emission of gravitational waves with nearly scale-invariant power. These primordial gravitational waves are stretched to horizon and super-horizon scales during inflation and leave their signature on the CMB by imprinting parity-odd perturbations at large angular scales. Measuring B-modes with increasing sensitivity and precision means we are able to search for signatures both from cosmic inflation, and other exotic physics depending on the angular scales we observe and models we select.

The energy scale of inflation directly affects the amount of power in the B-mode signal and is typically quantified as the ratio of the amplitudes of the scalar and tensor perturbations (the “tensor-to-scalar ratio”) at a given scale

$$r = \frac{P_t}{P_s}. \quad (1.30)$$

Here the tensor and scalar spectrum is modeled as an amplitude P_t and P_s respectively, with a simple power law dependence and spectral tilt n_t and n_s . Modeling the Universe prior to and during inflation as a quantum mechanical wavefunction traversing a potential V , we have a relation to r and a crude method for measuring the inflationary potential (i.e. energy scale) [21]:

$$V^{1/4} \sim 10^{16} (100 r)^{1/4}, \quad (1.31)$$

where the units of V are in GeV. Typically, constraining r involves measuring the temperature and/or E-mode spectrum to construct the scalar perturbation power spectrum, and measuring the B-mode spectrum to obtain the tensor spectrum. However, to date r has not been detected and the most stringent upper bounds place $r \lesssim 0.06$ [34]. The following sections will discuss limiting factors in constraining r further, and mitigation methods for current and upcoming experiments.

1.3.4 Gravitational Lensing

One challenge in measuring the map of CMB polarization is due to gravitational lensing, i.e the existence of secondary anisotropies. As photons propagate for 14 Gyr between the surface of last scattering and earth today there is ample time for their trajectories to be deflected by gravitational affects from intervening matter/energy. This process is known as weak gravitational lensing, and acts to soften the sharpness of otherwise clearly delineated hot/cold regions (large peaks in the power spectrum) by reducing the fluctuation coherence [35]–[37]. Lensing essentially “remaps” CMB photons around a matter distribution through

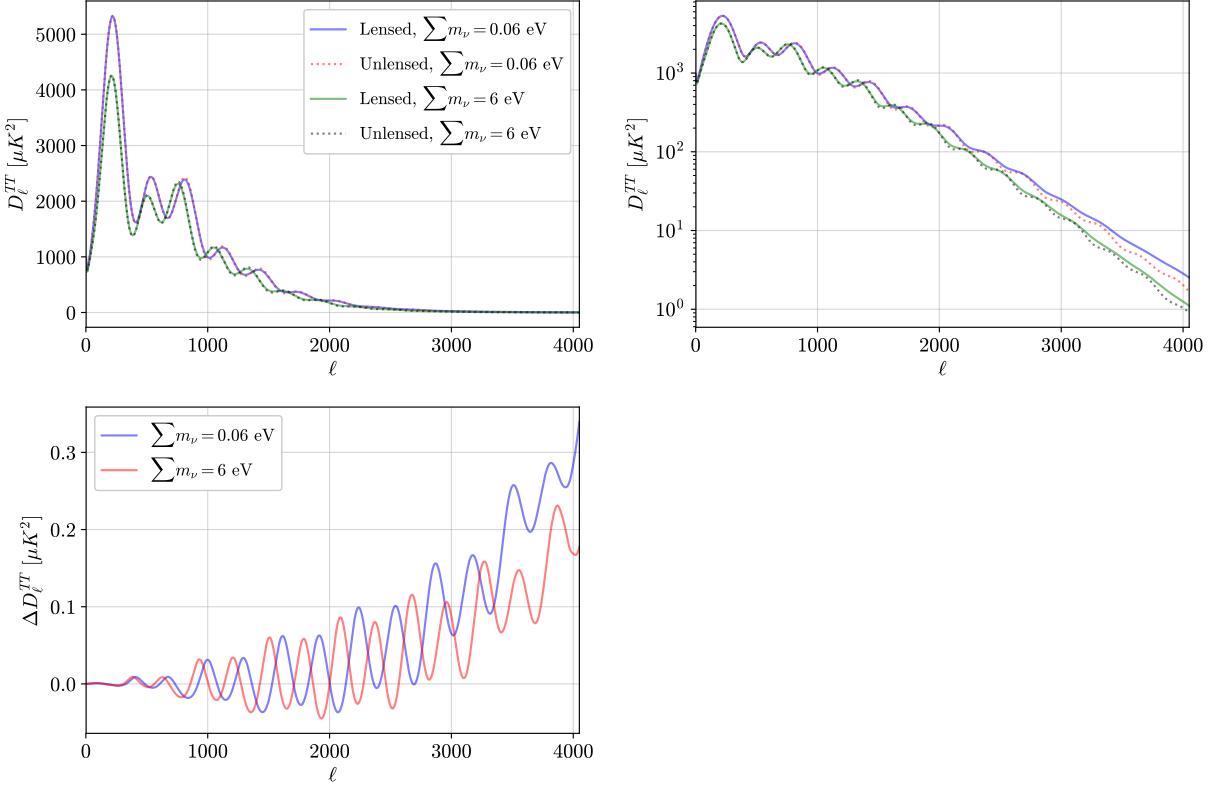


Figure 1.8: Effects of gravitational lensing on the temperature power spectrum due to neutrino mass. The top row shows the temperature power spectrum C_ℓ^{TT} both unlensed, and lensed at two different values of $\sum m_\nu$. $\sum m_\nu = 0.06$ eV is the current best upper bound, and $\sum m_\nu = 6$ eV is used to exaggerate the effects of neutrino mass on lensing of C_ℓ^{TT} . The bottom left plot shows the difference in the power spectra unlensed and lensed, for the two neutrino mass values. Plots made from calculations using the CAMB python package [32].

a deflection which is dependent on the integrated spacetime curvature along the photon trajectory. High- ℓ power in C_ℓ is suppressed on scales smaller than the lensing deflection scale. If photons from a patch of the CMB, which has only an E-mode polarization, travels through a matter-dense region, such as a galaxy cluster, gravitational lensing “converts” some of the E-mode power into B-mode power by remapping the observed polarization. In terms of temperature, lensing reduces the amplitude and shifts the angular scale of

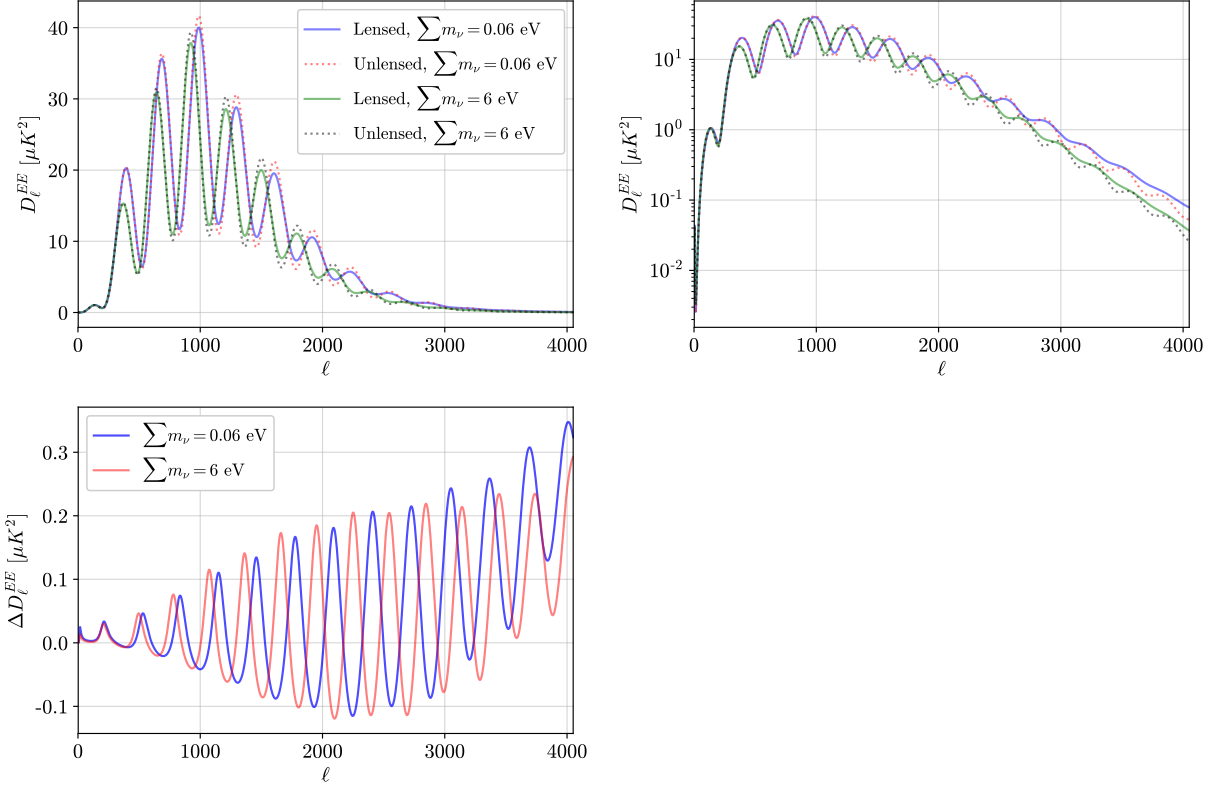


Figure 1.9: Effects of gravitational lensing on the E-mode power spectrum due to neutrino mass. The top row shows the E-mode power spectrum C_ℓ^{EE} both unlensed, and lensed at two different values of $\sum m_\nu$. $\sum m_\nu = 0.06$ eV is the current best upper bound, and $\sum m_\nu = 6$ eV is used to exaggerate the effects of neutrino mass on lensing of C_ℓ^{EE} . The bottom left plot shows the difference in the power spectra unlensed and lensed, for the two neutrino mass values. Plots made from calculations using the CAMB python package [32].

the power spectrum peaks. Both these effects are shown in Figures 1.9 and 1.9, with the neutrino mass the free parameter causing the variation in the degree of lensing.

Gravitational lensing thus traces the matter distribution of the Universe, and because most of the structure has sub-degree angular scales, for the B-mode signal this effect peaks at $\ell \sim 1000$, as can be seen in Figure 1.10. Conversely, the primordial B-mode signal which could be from inflationary gravitational waves peaks at much larger degree scales (ℓ less

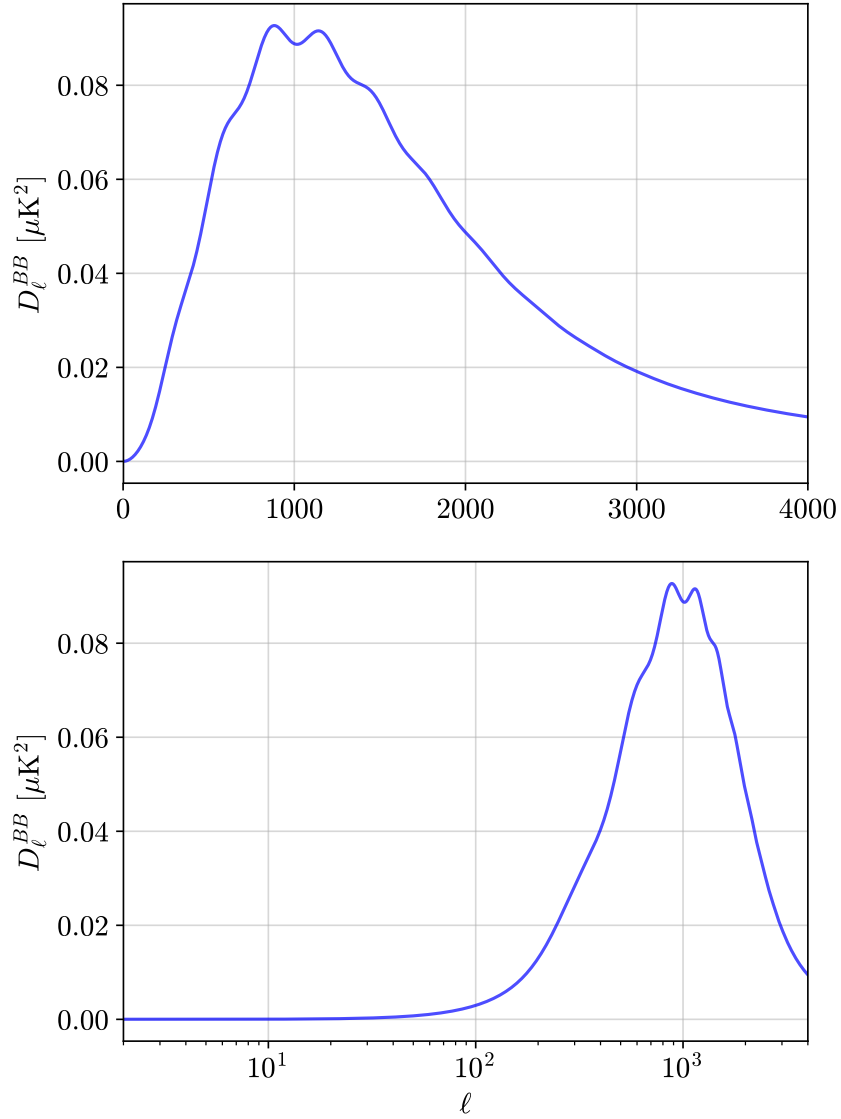


Figure 1.10: Pure lensing (i.e. $r = 0$) CMB B-mode power spectrum. The only contribution to the B-mode power spectrum in this cosmology is due to lensing conversion of E-modes to B-modes. Plots made from calculations using the CAMB python package [32] and the current best fit values for ΛCDM parameters.

than a few hundred). Depending on what the value of r may be, it could be possible to separate these two effects in the B-mode spectrum and independently detect both contributions based on the angular scales at which they dominate. The recent history in

the CMB polarimetry field has progressively lowered the upper bound on r by measuring the lensing B-mode spectrum with increasing precision, and now further bounds on r depend critically on an experiment’s ability to “de-lens” the B-modes and more faithfully reconstruct the CMB polarization map as it was emitted at last scattering. Based on recent measurements of the lensing spectrum amplitude and maximum possible de-lensing capabilities, the lowest r can be while still being detectable is $\sim 2 \times 10^{-4}$ [38].

Since the amount of lensing depends on the distribution of large scale structure, we may use lensing information to compare the observed and expected matter power spectrum [39] to provide constraints on physical parameters which affect structure formation. One such example is the masses of the three neutrino species and their sum $\sum m_\nu$. Lighter neutrinos are able to free-stream and carry more energy out of dark matter potential wells in the early Universe than heavier neutrinos. The degree of suppression of structure formation as compared to Λ CDM models allows us to constrain $\sum m_\nu$ and the effects of $\sum m_\nu$ of different values in the power spectra are demonstrated in Figures 1.9 and 1.9.

1.4 Foregrounds

As we have just discussed, the CMB we observe today is not actually the CMB that was emitted when the Universe was 380,000 years old and is due to the existence of secondary anisotropies. On top of this effect, we also measure spurious signal from a number of other sources which do not involve photons sourced from the last scattering surface. We refer to this effect as “foreground contamination,” which includes emission

from the earth's atmosphere (ground-based experiments only), galactic synchrotron, and polarized thermal dust. When considering foregrounds and their effects it is important to keep in mind whether it is known or expected to be polarized, as the latter has a much more significant effect in the measured B-mode spectrum.

Results from the BICEP/Keck experiment in 2014 reported a measurement of nonzero large scale B-mode signal, indicating the first ever measurement of r and detection of signatures of inflationary gravitational waves [40]. However, later analysis and results from the Planck satellite mission showed that the foreground model used was too simplistic and the B-mode power seen by BICEP was consistent with the thermal emission from interstellar dust in the Milky Way. A joint analysis was conducted [41], ending with an upper bound on r (i.e. a non-detection). These results underscore the importance of accurate foreground removal in the B-mode spectrum for future CMB experiments. As will be discussed in the following sections, the frequency dependence of most foregrounds is key in their measurement and removal, mandating that all future experiments observe at many frequencies.

1.4.1 Atmosphere

Due to the complexity of the atmosphere, its physics is quite rich and results in possible emission in the millimeter from a variety of constituents. Additionally, atmospheric effects are by nature transient (slowly changing) and contribute significantly to low frequency ($1/f$) experimental noise. Water vapor fluctuations are most predominant for CMB experiments. This can be a large hindrance in experiments requiring observation of

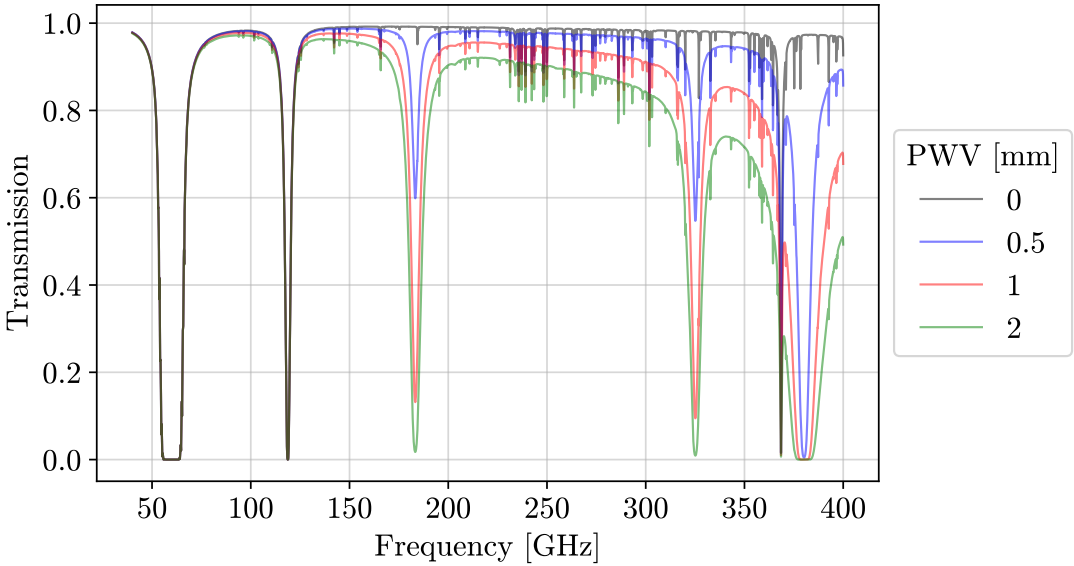


Figure 1.11: Atmospheric transmission model at Cerro Chajnantor using the *am* atmospheric model package [42]. Chajnantor is located at ~ 5200 m in the Atacama Desert, Chile, making it one of the driest places on earth. Year-average PWV calculated from radiometer data at the APEX site near Chajnantor typically falls in the range of $1 - 2$ mm.

large fractions of the sky. Atomic and molecular transitions contribute narrow emission lines, while thermal loading from the thickness/optical depth of the atmosphere results in broadband millimeter wave emission. The most significant contribution to these features is from total water vapor content, quantified as the precipitable water vapor (PWV):

$$\text{PWV} = \frac{1}{\rho g} \int_{p(z)}^0 dp \ x(p). \quad (1.32)$$

Here ρ is the density of water, g is the gravitational acceleration, $p(z)$ is the atmospheric pressure at altitude z , and $x(p)$ is the (dimensionless) gaseous mixing ratio. PWV measures the height per unit area of condensed water for an entire column of atmosphere. Reduction

of PWV, and thus atmospheric loading, is achieved by locating the experiment in a dry location at high altitude. Common choices include the Antarctic plateau (elevation ~ 3000 m), the Chilean Atacama Desert (~ 5000 m) and, more recently, the Tibetan plateau (5000-6000 m) [43], [44]. Further mitigation is possible with balloon-borne or space-based experiments, however, as the atmospheric optical depth decreases signal contamination from dust emission is more significant. Figure 1.11 shows the atmospheric transmission at the site of the Simons Array experiment as a function of PWV. The Simons Array site is located on Cerro Toco (near Chajnantor) in the Atacama desert, Chile at ~ 5200 m.

Emission from the atmosphere is generally taken to be unpolarized, however, recent detection of polarized signals from ice crystals in the lower atmosphere provides evidence that this may be true only of the gaseous constituents [2].

1.4.2 Galactic Synchrotron

A significant source of polarized foreground contamination arises from synchrotron interactions of cosmic ray electrons with the Milky Way magnetic field. The galactic synchrotron spectrum is often modeled as a power law, where the apparent synchrotron temperature is

$$T_{synch} = T_0^{\text{synch}} \nu^{-\beta_{\text{synch}}}, \quad (1.33)$$

with T_0^{synch} the overall amplitude, and $\beta_{\text{synch}} \sim 2 - 3$ dependent on location (magnetic field strength and free electron concentration) and frequency via the cosmic ray energy spectrum [45]. Due to the power law dependence, synchrotron contributes most significantly at low

frequencies and becomes subdominant around 70 GHz. Correlation of an experiment's CMB maps at 90 and 150 GHz with their own maps below 70 GHz, or others such as the Planck 30, 44, and 70 GHz maps, are effective methods currently used to subtract the synchrotron foreground.

1.4.3 Thermal Dust

Interstellar dust in the Milky Way is distributed in a complex manner and, as previously mentioned, can spoil detection of the faint B-mode signal at certain angular scales. If a mechanism exists to preferentially align dust particles in a coherent way then this radiation can also contribute as a significant polarized foreground. Anisotropic dust grains larger than $\sim 10^{-7}$ m in a magnetic field can align their principle axes with the magnetic field via the existence of a “radiative alignment torque” (RAT) [46]. Dust grain emission is also generally polarized along the grain principle axis, so any configuration with sufficient dust and magnetic field density can spuriously contribute to the measured polarization power spectrum. Furthermore, magnetohydrodynamic (MHD) turbulence in the ionized interstellar medium, resulting from the Navier-Stokes MHD component, create odd-parity magnetic field distributions. Coupled with RAT and dust this poses large problems for faithfully measuring CMB B-mode polarization without detailed dust removal methods.

The dust spectrum is modeled analogously to the synchrotron spectrum:

$$T_{dust} = T_0^{\text{dust}} \nu^{\beta_{\text{dust}}}. \quad (1.34)$$

The dust spectrum is relevant for essentially all CMB observing frequencies above 70 GHz, although at very high frequencies the atmospheric opacity attenuates most of this signal. The dust power contribution also depends on the portion of the Milky Way being observed, and can be dominant even if observations are performed away from the galactic plane. Scaling the Planck 353 GHz map using $\beta_{\text{dust}} \sim 2$ in Equation 1.34 to reach typical CMB observing frequencies of 90 or 150 GHz is a common practice to estimate the B-mode contribution from dust. Similarly to synchrotron contamination, simultaneous observation at frequencies above 150 GHz provide a means to subtract some of the dust signal.

1.5 Modern CMB Observations

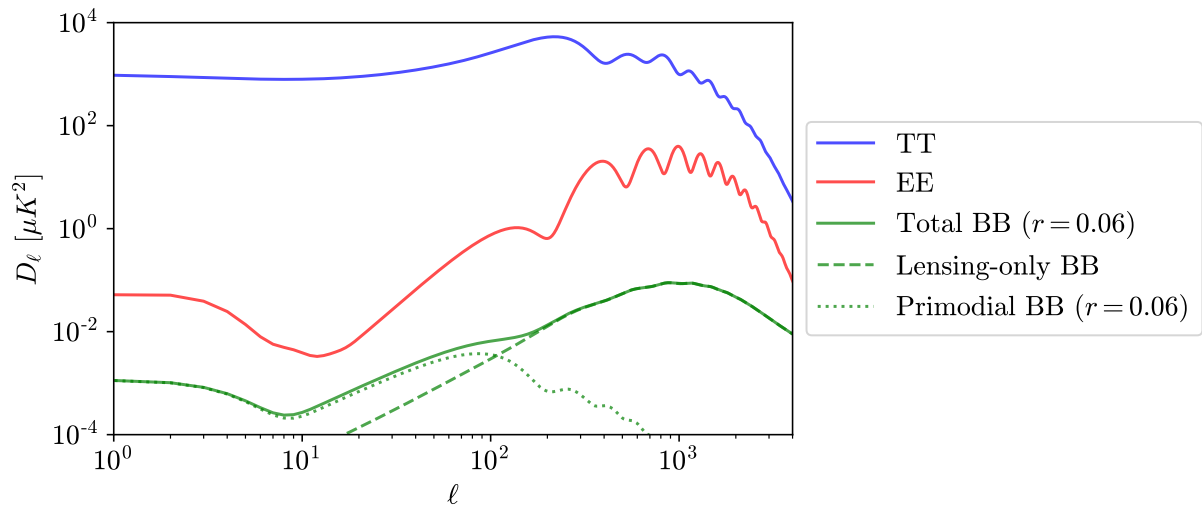


Figure 1.12: Comparison of the temperature, E-mode, and B-mode CMB power spectra using the current best upper bound on r of 0.06.

In Section 1.3 we covered the basic features and observations of the CMB, its radiation spectrum, and the power spectra of temperature and polarization anisotropies.

Due to the complicated nature of foregrounds, the effects of gravitational lensing, the faintness of the B-mode signal in general (see Figure 1.12 for a comparison of all power spectra), and the tight constraints bounding r to be small, modern CMB experiments hoping to measure the B-mode spectrum with increasing precision must implement a number of techniques and capabilities to increase their sensitivity. In combination with the routine use of detector technology whose inherent noise levels are subdominant to noise in the CMB photons themselves (discussed further in Chapter 2), the landscape is this: increasing B-mode sensitivity requires an experiment observing at multiple frequencies, in dry locations, and often for hundreds or thousands of detector hours. Only in the last few years have CMB experiments been able to detect the lensed B-mode spectrum, with the POLARBEAR-1 collaboration the first to do so in 2014 using CMB data only [47]. Since then, other experiments including the ACT, BICEP/Keck, and SPT collaborations have also detected the lensing B-mode signal. Many technical efforts now focus on increasing telescope sensitivity and foreground removal capabilities by increasing the number of detectors in a single receiver and the number of observation frequencies, respectively — as well as enhancing delensing capabilities.

Chapter 2

CMB Detector and Readout

Instrumentation

*I chose to pursue a career in physics
because there the truth isn't so easily bent.*
— Angela Merkel

In the previous Section we discussed the fundamentals and basic theory of the Universe, its cosmology, and how we may measure and constrain various physical parameters using the CMB to gain a better understanding of the Universe's constituents and evolution. In this Chapter we will cover the basics of instrumentation, specifically the detector and readout technologies, which enable so-called “quantum-limited” CMB observations where the noise spectral density of the detector signal (i.e. sensitivity) is dominated by intrinsic properties of the detected radiation itself. Therefore, it is not possible to increase a CMB instrument’s sensitivity by implementing lower noise detector technologies, rather we must rely on approaches in increasing the number of detectors – which gives an ideal $1/\sqrt{N}$

reduction in the overall instrument noise level. This feature, along with the need for simultaneous observation at multiple frequencies, has been and is one of the major driving design goals of current and future CMB polarization experiments.

2.1 Transition Edge Sensor Bolometers

The main technology responsible for quantum-limited observations of the CMB is the transition edge sensor (TES) bolometer. A bolometer is a device which measures the intensity of radiation incident by means of detecting the radiative heat deposited on an absorber, a schematic of which is shown in Figure 2.1.

A bolometer consists of a thermistor $R_{TES}(T)$ which is located on an **absorbing island** at temperature T and possessing heat capacity C . The island is weakly connected to a thermal bath of temperature T_{bath} via the thermal conductance G_{bath} . During operation the bolometer is electrically biased into a favorable regime using V_{bias} . Background radiation P_{opt} and radiation from a source of interest $\delta P_{opt} \ll P_{opt}$ is incident on the absorbing island which, along with the bias power $P_{bias} = I_{TES}V_{bias}$, raises the island temperature by $\Delta T = (P_{opt} + \delta P_{opt} + P_{bias})/G_{bath}$ and is measured using the thermistor. This heat dissipates through the weak link to the bath with a characteristic time constant $\tau = C/G_{bath}$.

In the case of millimeter-wave astronomy, the most sensitive bolometers use thermistors formed from a superconducting film which is biased into its superconducting-normal transition; a so-called transition edge sensor (TES) bolometer. TES bolometer sensitivity is large due to the steepness of the transition from the normal resistive state to that

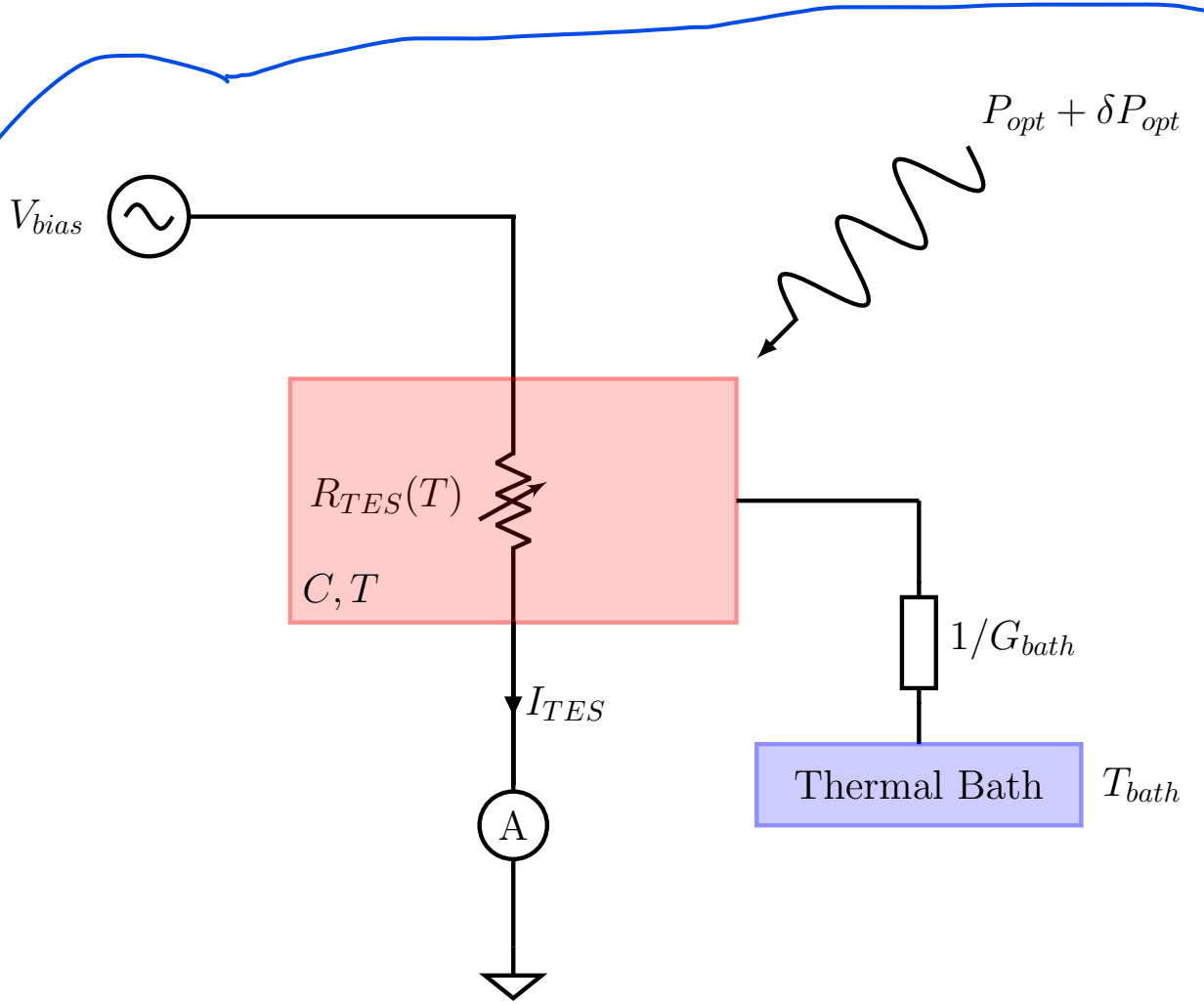


Figure 2.1: Schematic diagram of a bolometer showing the bolometer island (red) which is thermally connected to the thermal bath (blue) by conductance G_{bath} . A TES thermistor possessing a variable resistance R_{TES} that is a steep function of temperature is located on the bolometer island and voltage biased by V_{bias} . The island temperature T , and thus R_{TES} and I_{TES} , is modulated by δP_{opt} . The current measured by a low-noise ammeter, and the variation of electrical power dissipated on the island provides a measurement of δP_{opt} .

of the zero resistance superconducting state, which occurs when the temperature of the superconducting film is lowered below its critical temperature T_c . dR/dT is nonnegative for all T , i.e. TESs are positive temperature-coefficient devices, therefore in order to achieve a stable bias point in the transition TESs must be voltage biased during operation. Because $dR/dT \geq 0$, TESs possess an additional benefit when voltage biased: the power dissipated

on the island remains constant on time scales faster than τ , enabling measurements of quickly-varying signals. This phenomenon is referred to as electrothermal feedback (ETF). When the optical power incident on the bolometer increases, the temperature of the TES increases and the resistance of the film increases, which in turn lowers the bias power $P_{bias} = V_{bias}^2/R_{TES}$; cooling the film and restoring it to its original temperature.

If $T_{bath} < T_c$, decreasing V lowers the bolometer temperature and begins to drop the TES into its superconducting transition (R decreases rapidly), at which point I_{TES} increases, as is shown in the $I - V$ curve in Figure 2.3. The point in the $I - V$ curve (I_{turn} , V_{turn}) at which $dI/dV = 0$ is called the “turnaround” point, after which ETF begins to turn on and the TES’s sensitivity increases dramatically. The TES relation between resistance $R = V/I$ and power $P = IV$ is also shown in Figure 2.3. From these curves it is evident that above P_{turn} the TES responsivity is significantly reduced since even large changes in power only change R by a small amount.

The strength of the ETF determines the TES’s responsivity to power fluctuations and is parameterized by α , the logarithmic derivative of resistance with respect to temperature

$$\alpha = \frac{\delta \log R}{\delta \log T} = \frac{T}{R} \frac{\delta R}{\delta T}. \quad (2.1)$$

For materials with a narrow superconducting transition, as can be seen for a POLARBEAR-2 TES in Figure 2.2, α can be as large as 10^3 .

The role of α becomes apparent after balancing the power flowing through the

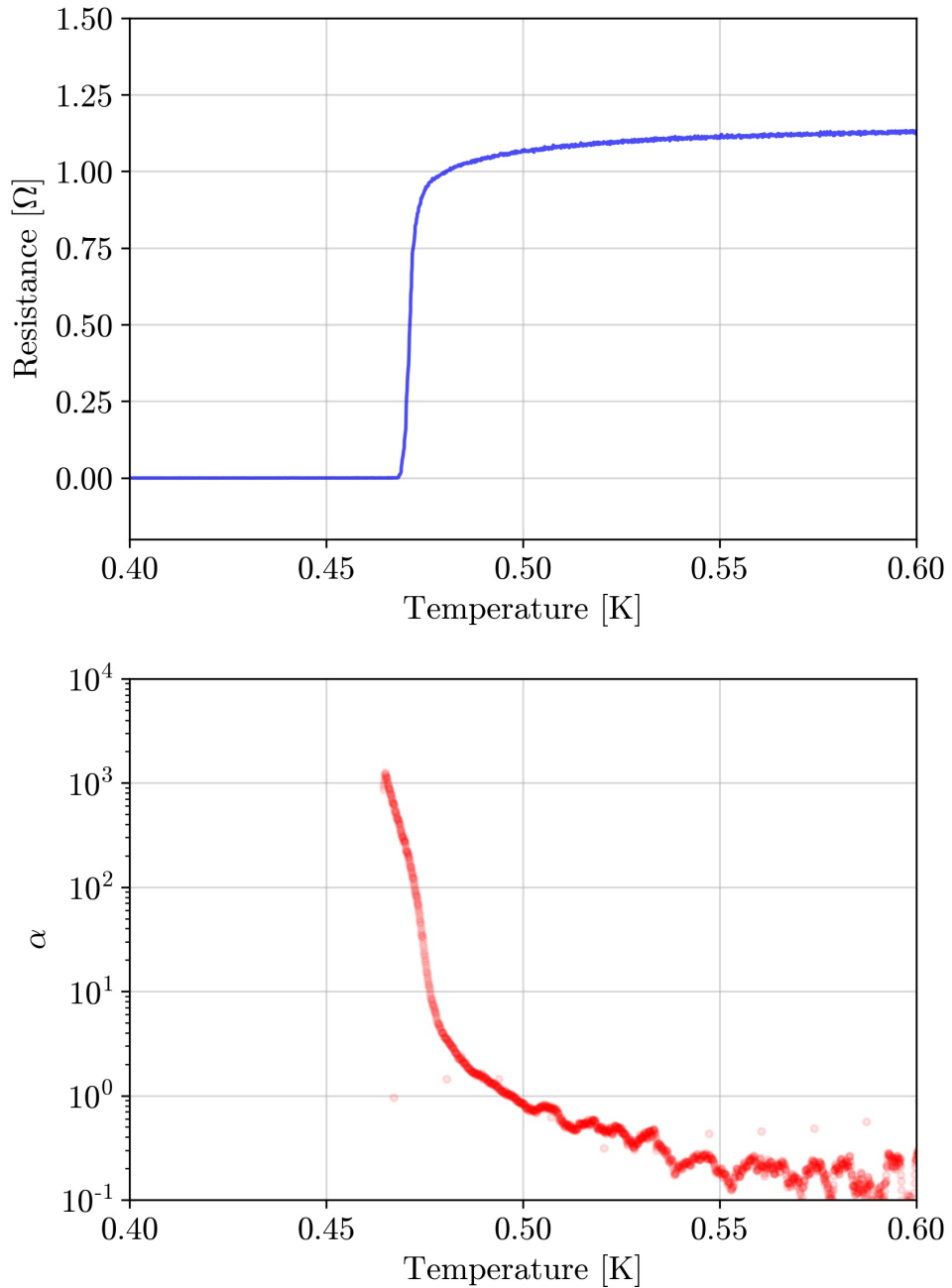


Figure 2.2: Resistance (*top*) and $\alpha = \delta \log R / \delta \log T$ (*bottom*) as a function of temperature for a POLARBEAR-2 AlMn TES as it enters the superconducting state. The transition critical temperature T_c for this device is 0.473 K. Data are noisy and not shown for α once the TES resistance is fully superconducting ($R \lesssim 0.1 \Omega$).

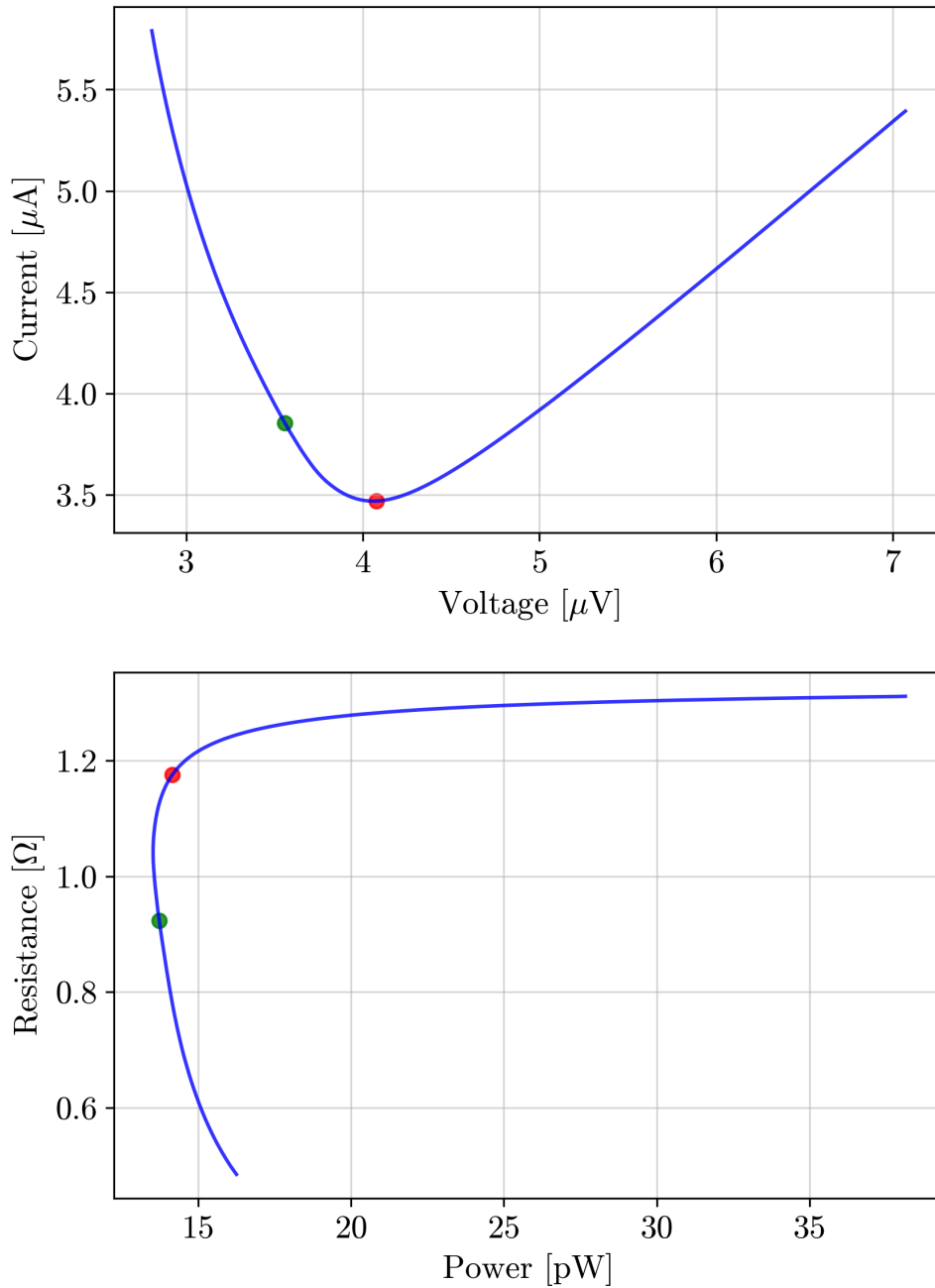


Figure 2.3: (*Top*) The current-voltage or I - V relation of a dark POLARBEAR-2 bolometer as V_{bias} is lowered to allow the TES to drop into the transition. (*Bottom*) Corresponding resistance-power or R - P relation. In both plots the red point indicates where $dI/dV = 0$, which also corresponds to $\mathcal{L} = 1$, and the green point indicates the operating point at $R_{frac} = R/R_N = 0.7$, where POLARBEAR-2 bolometers have demonstrated $\mathcal{L} \gtrsim 10$. Stray impedances in the readout circuit have not been corrected for in either plot.

bolometer [48]

$$P_{opt} + \delta P_{opt} e^{i\omega t} + \frac{V_{bias}^2}{R} \left(1 - \frac{\delta R}{\delta T} \delta T e^{i\omega t} \right) = \bar{G}(T - T_{bath}) + (G + i\omega C) \delta T e^{i\omega t} \quad (2.2)$$

where δP_{opt} is the small signal power characterized by frequency ω , causing time-varying island temperature δT . $T \gg \delta T$ and R are the steady-state temperature and resistance of the bolometer. $\bar{G} = P_{avg}/(T_c - T_{bath})$ and $G = \delta P/\delta T$ are the time-averaged and differential thermal conductances. Power flows through the bolometer to the bath of temperature T_{bath} according to the complex thermal conductance which is modified by ETF

$$G_{eff} = \left(\frac{\alpha P_{bias}}{T} + G + i\omega C \right) \delta T e^{i\omega t}, \quad (2.3)$$

where we have used our result from Equation (2.1).

ETF decreases the operational bolometer time constant τ according to

$$\tau = \frac{\tau_0}{\alpha P_{bias}/GT + 1} \quad (2.4)$$

with $\tau_0 \equiv C/G$. The system loopgain \mathcal{L} is defined as the ratio of the change in bias power to the change in the total power

$$\mathcal{L} = \frac{\alpha P_{bias}}{GT}. \quad (2.5)$$

The frequency-dependent ETF loopgain is then

$$\mathcal{L}(\omega) = -\frac{\delta P_{bias}}{\delta P_{total}} = \frac{\alpha P_{bias}}{GT(1+i\omega\tau_0)} = \frac{\mathcal{L}}{1+i\omega\tau_0}, \quad (2.6)$$

which leads to

$$\tau = \frac{\tau_0}{\mathcal{L}+1}. \quad (2.7)$$

For a TES it is often difficult to directly measure G and/or G_{eff} so, in order to characterize a detector through measurements of τ (and/or $\mathcal{L}(\omega)$) the response of the TES is determined as a function of ω by providing an optical signal which is chopped at ω . This can then be fit to a single-pole thermal filter model

$$A(\omega) = \frac{A_0}{\sqrt{(\omega\tau)^2 + 1}} \quad (2.8)$$

with A_0 an overall normalization factor.

Holding a stiff voltage bias V_{bias} on a TES allows determination of incident power not due to V_{bias} , i.e. the modulated optical power δP_{opt} , by measuring the TES current I . Modulating the bolometer temperature, δP_{opt} in turn modulates the TES resistance and thus the TES current δI . The relationship between δP_{opt} and δI is the current responsivity S_I [49]:

$$S_I = \frac{\delta I}{\delta P_{opt}} = -\frac{1}{V_{bias}} \frac{\mathcal{L}}{\mathcal{L}+1} \frac{1}{1+i\omega\tau}. \quad (2.9)$$

If $\mathcal{L} \gg 1$ then for low-frequency signals ($\omega \ll 1/\tau$) the responsivity reduces to

$S_I = -1/V_{bias}$ and, without compromising the linearity of the TES response, can be increased by decreasing V_{bias} . Decreasing V_{bias} lowers the TES further into the transition and increases the loopgain up to the point of instability, at which point the voltage bias is longer able to prevent the TES from superconducting. This is referred to as “latching” a TES, which occurs due to multiple factors including stray impedances in the bias circuit, as well as the limit imposed by the electrical time constant of the readout electronics (most often limited by the input inductance of the TES pre-amplifiers).

2.1.1 Bolometer Saturation Power

The linear response of a TES we have just discussed is valid only while the TES remains biased in the superconducting transition, i.e. in the small-signal limit. In the steady state, with $P_{oper} = P_{bias} + P_{opt}$,

$$\bar{G} = \frac{P_{oper}}{T_c - T_{bath}} \quad (2.10)$$

the power balance is

$$P_{bias} + P_{opt} = \bar{G}(T - T_{bath}). \quad (2.11)$$

The point at which TES linearity is no longer preserved is when $P = P_{bias} + P_{opt} = P_{turn}$. Any additional power exceeding P_{turn} raises the bolometer temperature and forces the TES fully out of the transition and into the normal metal state. In the case of large optical loading this may occur regardless of P_{bias} so, while characterizing a particular device,

it is important to ensure that during a P_{turn} measurement, the bolometer is truly dark ($P_{opt} = 0$).

Measuring P_{turn} contains information about the properties of the thermal link and allows us to quantify the power delivered to the bath P_{bath} in terms of the properties of the thermal link. The conductance of the link is

$$G(T) = \frac{A}{L}\kappa(T) \quad (2.12)$$

where A is the cross-sectional area, L is the length, and $\kappa(T) = \kappa_0 T^n$ is the temperature-dependent thermal conductivity of the link material. Nearly all bolometers, including those used in the POLARBEAR-2 receivers, possess links composed of electrical insulating low-stress silicon nitride and silicon dioxide, and superconducting niobium. The expected thermal conductivity index for such a link is $n = 3$ due to the fact that both insulators and superconductors only have contributions to their thermal conductivities from phonon interactions ($n = 3$). It has been shown that links produced for the POLARBEAR-1 and POLARBEAR-2 receivers have $n \approx 2.7$ [50].

The power conducted to the bath through the link is

$$P_{bath} = \int_{T_{bath}}^{T_c} \frac{A}{L}\kappa(T) dT = \frac{A}{L} \frac{\kappa_0}{n+1} (T_c^{n+1} - T_{bath}^{n+1}) = \frac{A\kappa_0}{4L} (T_c^4 - T_{bath}^4), \quad (2.13)$$

where the bolometer is at temperature $T = T_c$.

Equation 2.13 allows us to define the bolometer's optical saturation power P_{sat} at

each bias point in the TES transition, which is simply the value of $P_{opt} + \delta P_{opt}$ that may be incident on the bolometer without exceeding P_{sat} (P_{bias} is turned down to zero as the optical power approaches P_{sat}) [51]:

$$P_{sat} = (1 - R_{frac})P_{bath}(T_c). \quad (2.14)$$

Here $R_{frac} = R/R_N$ is the fractional resistance at the TES bias point, with R_N the TES normal state resistance. $P_{bath}(T_c)$ is from Equation 2.13.

Experiment design plays a crucial role in determining what value of P_{sat} to choose during detector fabrication (i.e. tuning G and P_{bath}) as increasing G also adds noise to the detector. P_{sat} must be selected carefully based on loading not just from the CMB, but also from loading from the radiative environment of the receiver and, for ground-based experiments, the atmosphere.

2.2 Bolometer Noise

When observing the CMB, TES bolometers are used as power sensors so the noise in the detector is most usefully quantified in terms of the noise equivalent power (NEP), which describes the spectral response of the bolometer in the noise-dominated regime, typically in $\text{W}/\sqrt{\text{Hz}}$. A convenient way of defining the NEP is the power required to achieve a signal-to-noise ratio (SNR) of 1 over 1 second of integration. Often it is useful to characterize noise sources as being Gaussian (i.e. “white”), in which case the NEP is

related to the power variance σ_p by

$$\sigma_p^2 = \int_0^{f_{max}} |\text{NEP}|^2 df \quad (2.15)$$

where $f_{max} = f_{Nyquist}/2$ and $f_{Nyquist}$ is the Nyquist frequency for a digitally sampled signal.

A further useful observation is that integration over the bandwidth is not necessary [52] as all samples (characterized by variance σ_i^2) are independent, so the mean variance $\langle \sigma_p^2 \rangle$ is

$$\langle \sigma_p^2 \rangle = \frac{\langle \sigma_i^2 \rangle}{f_{Nyquist}} = \frac{\langle \sigma_i^2 \rangle}{2f_{max}} = \frac{|\text{NEP}|^2}{2}. \quad (2.16)$$

The NEP associated with a timestream, NEP_t , is related to the actual NEP by the square root of the mean variance – i.e. $\sqrt{\langle \sigma_p^2 \rangle}$, which is the root-mean-square (RMS) of the NEP – so we have

$$\text{NEP}_t = \frac{\text{NEP}}{\sqrt{2}}. \quad (2.17)$$

The fundamental noise contributions to TES bolometers in CMB applications are:

- Thermal carrier (“phonon”) noise: NEP_g
- Johnson-Nyquist (“electronic”) noise: NEP_J
- Photon noise: NEP_γ

All noise sources are again assumed to be white and uncorrelated so the total noise, NEP_{total}

is the quadrature sum of each individual contribution:

$$\text{NEP}_{\text{total}} = \sqrt{\text{NEP}_g^2 + \text{NEP}_J^2 + \text{NEP}_\gamma^2}. \quad (2.18)$$

2.2.1 Thermal Carrier Noise

Phonon noise arises from the fluctuations in the energy $\langle \sigma_E \rangle$ of any macroscopic thermodynamic system and can be expressed in terms of its heat capacity C_v [53]:

$$\langle \sigma_E^2 \rangle = k_B T^2 C_v. \quad (2.19)$$

If two identical systems at the same temperature T are thermally connected by conductance g then the corresponding power fluctuations are:

$$\langle \sigma_{P,g}^2 \rangle = k_B T^2 C_v \frac{g^2}{C_v^2} = \frac{k_B T^2 g^2}{C_v}. \quad (2.20)$$

Thermal power transferred across the link is attenuated at high frequencies by the single-pole thermal filter created by C_v and g with a 3 dB frequency of $f_0 = g/2\pi C_v$. Below f_0 the power spectral density (PSD) of the thermal fluctuations is white so we can use Equations 2.15 and 2.20 to calculate NEP_g :

$$\langle \sigma_{P,g}^2 \rangle = \int_0^\infty \frac{\text{NEP}_g^2}{1 + \left(\frac{f}{f_0}\right)^2} df = \frac{k_B T^2 g^2}{C_v}, \quad (2.21)$$

which simplifies to

$$\text{NEP}_g = \sqrt{4k_B T^2 g}. \quad (2.22)$$

For the incorrect case of $T_c \approx T_{bath}$

$$\text{NEP}_g = \sqrt{4k_B T_c^2 g} \quad (2.23)$$

and using Equation 2.10 and setting $g = \bar{G}$ (also incorrect for a bolometer operating with appreciable \mathcal{L}) we have

$$\text{NEP}_g = \sqrt{4k_B \frac{T_c^2}{T_c - T_{bath}}}. \quad (2.24)$$

This is instructive as it provides an example of how tuning apparatus parameters (such as T_c and T_{bath}) can minimize independent noise terms. While T_{bath} is typically set by cryogenic limitations, T_c can be taken as freely tunable. Minimizing NEP_g according to Equation 2.24 yields $T_c = 2T_{bath}$ so our assumption that $T_c \approx T_{bath}$ is not valid if we want to minimize NEP_g by tuning T_c .

A more general treatment requires using a temperature-dependent expression for g :

$$g = \frac{dP}{dT_c} \quad (2.25)$$

in the region $T \in [T_{bath}, T_c]$. We parameterize the link conductance in this temperature range using

$$\Gamma = \frac{\int_{T_{bath}}^{T_c} \left(\frac{T\kappa(T)}{T_c\kappa(T_c)} \right)^2 dT}{\int_{T_{bath}}^{T_c} \frac{\kappa(T)}{\kappa(T_c)} dT} = \frac{1}{T_c^2 \kappa(T_c)} \frac{\int_{T_{bath}}^{T_c} (T\kappa(T))^2 dT}{\int_{T_{bath}}^{T_c} \kappa(T) dT}, \quad (2.26)$$

and if we again assume the link conductivity model of $\kappa(T) = \kappa_0 T^n$ this reduces to

$$\Gamma = \frac{n+1}{2n+3} \frac{1 - (T_{bath}/T_c)^{2n+3}}{1 - (T_{bath}/T_c)^{n+1}}. \quad (2.27)$$

Now we can write NEP_g in terms of only T_c , T_{bath} , and P_{bath} :

$$\text{NEP}_g = \sqrt{4k_B P_{bath} T_{bath}} \sqrt{\frac{(n+1)^2}{2n+3} \frac{(T_c/T_{bath})^{2n+3} - 1}{((T_c/T_{bath})^{n+1} - 1)^2}}. \quad (2.28)$$

As previously mentioned, phonon contributions to $\kappa(T)$ have $n = 3$, which for POLARBEAR-2 with $T_{bath} \sim 0.27$ K means the minimal value of Γ (and thus NEP_g) is $\Gamma \sim 2$ is achieved at $T_c/T_{bath} \sim 1.7$. In principle NEP_g can be further minimized if we have freedom to choose n , but this would require changing the fabrication procedure to introduce a dominantly electronic thermal link and could also raise issues in biasing and operating bolometers using the POLARBEAR-2 readout system.

2.2.2 Johnson-Nyquist Noise

Charge-carrier noise, also known as Johnson-Nyquist noise, is also present in TES bolometers due to the finite operating resistance R . Modeling the TES as a single lumped element of resistance R at temperature T_c , the Johnson noise contribution is suppressed by the loopgain, which we first write as a noise equivalent current (NEI):

$$\text{NEI}_J = \frac{1}{\mathcal{L}} \sqrt{\frac{4k_B T_c}{R}}. \quad (2.29)$$

The contribution in terms of NEP is obtained using the above, Equation 2.9 (while setting $\tau = 0$), and using $P_{bias} = V_{bias}^2/R$:

$$\text{NEP}_J = \frac{\mathcal{L} + 1}{\mathcal{L}^2} \sqrt{4k_B T_c P_{bias}}. \quad (2.30)$$

It is useful to note that for $\mathcal{L} \gg 1$ a dark POLARBEAR-2 bolometer's noise is dominated by NEP_g .

2.2.3 Photon Noise

The final contribution to the intrinsic noise of TES bolometers arises when the bolometer is made optical, i.e. when observing the CMB, and is due to photon quantum mechanics. Since the photon noise contribution NEP_γ is a property of the source and cannot be altered, it is standard practice to design TES bolometers such that their overall noise is dominated by NEP_γ , which we refer to as a *photon noise-limited detector*.

Recall the thermal blackbody intensity relation of Equation 1.12:

$$B(\nu, T) = \frac{2h\nu^3}{c^2} \frac{1}{e^{h\nu/k_B T} - 1}, \quad (2.31)$$

where we can define the Boltzmann photon occupation number as

$$n_{occ} = \frac{1}{e^{h\nu/k_B T} - 1}. \quad (2.32)$$

The total optical power deposited on a detector with area A , whose beam subtends solid

angle Ω , and frequency-dependent optical efficiency $\eta(\nu)$ is

$$P_{opt} = A\Omega \int_0^\infty \eta(\nu)B(\nu, T) d\nu. \quad (2.33)$$

Using the throughput $\lambda^2 = c^2/\nu^2 = A\Omega$ we have

$$P_{opt} = \int_0^\infty n_{occ}\eta(\nu)h\nu d\nu. \quad (2.34)$$

If the detector bandwidth $\Delta\nu$ is small and we approximate the detector efficiency as a constant over frequency range $\Delta\nu$ centered at ν_0 gives

$$P_{opt} \approx \eta n_{occ} h\nu_0 \Delta\nu. \quad (2.35)$$

The variance of radiative power fluctuations from a thermal source incident on a detector and integrated over time τ is [54]:

$$\langle \sigma_{opt}^2 \rangle = \frac{1}{\tau} \int (h\nu)^2 \eta n_{occ} (1 + \eta n_{occ}) d\nu. \quad (2.36)$$

The first term in the integral of Equation 2.36 which is proportional to ηn_{occ} is referred to as “photon bunching noise.” The second term proportional to $(\eta n_{occ})^2$ is the photon shot noise. Photon bunching and shot noise dominate for different temperatures and frequencies. In the $h\nu \gg k_B T$ (optical) limit, $n_{occ} \ll 1$ and power fluctuations are dominated by photon arrival times with $\langle \sigma_{opt}^2 \rangle \sim \sqrt{N}$ – where N is the total number of photons collected in time

τ . At radio frequencies, where most CMB observations are performed, $n_{occ} \sim 0.2$ so both terms must be considered in evaluating NEP_γ . It should also be noted that for a noiseless detector observing at radio frequencies, both signal and noise scale linearly with signal power, so SNR cannot be improved by increasing the power received by the detector (i.e. by increasing the size of the detector or optical efficiency). Increasing $\Delta\nu$ increases SNR for a TES bolometer, but not for a detector fully in the radio limit, which leads to the common practice of making ground-based observing bands as wide as permitted by certain atmospheric windows.

The NEP at the bolometer input due to the optical fluctuations of Equation 2.36 is obtained using the result of Equation 2.16:

$$NEP_\gamma = \sqrt{2 \int (h\nu)^2 \eta n_{occ} (1 + \eta n_{occ}) d\nu}. \quad (2.37)$$

Employing our earlier simplification that the detector bandwidth $\Delta\nu$ is narrow and sharply peaked around frequency ν_0 , the noise is dependent only on the intensity of the source for GHz frequency CMB observations:

$$NEP_\gamma \approx \sqrt{2P_{opt} \left(h\nu_0 + \frac{P_{opt}}{\Delta\nu} \right)}. \quad (2.38)$$

This approximation breaks down when $n_{occ} \gtrsim 10$, i.e. for high temperature ($T \gtrsim 10$ K) and low frequency ($\nu \lesssim 10$ GHz) sources.

In the Rayleigh-Jeans limit of $h\nu \ll k_B T$ the emitted power for a source at temper-

ature T_{RJ} is

$$P_{opt} = \eta\Delta\nu k_B T_{RJ}. \quad (2.39)$$

We use this to simplify Equation 2.38 and obtain the detector's NEP γ :

$$\text{NEP}_\gamma \approx \sqrt{2\eta\Delta\nu k_B T_{RJ}(h\nu_0 + \eta k_B T_{RJ})}. \quad (2.40)$$

2.3 Superconducting Quantum Interference Devices (SQUIDs)

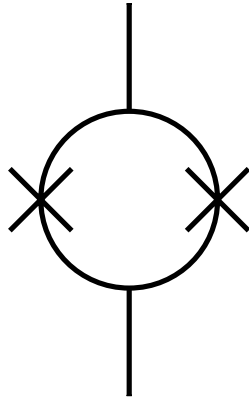


Figure 2.4: Circuit diagram of a SQUID, formed from a superconducting loop broken by two Josephson junctions (denoted as an “x”). Magnetic flux incident on the loop results in the formation of screening current which act to null the field interior to the loop due to the Meissner effect. The magnetic collecting area of SQUIDs fabricated using photolithography is often too small to be practical and an input inductor L_{in} is often patterned in close proximity (or completely over) the SQUID loop to increase the field collected by the SQUID.

Due to the low impedance of typical TES bolometers ($R \sim 1 \Omega$), and small changes in current ($\delta I \sim 1 - 10 \mu\text{A}$), a low-noise preamplifier with a low input impedance is necessary

to preserve the low-noise properties of the TES. The device used in nearly all modern CMB experiments to achieve this is the superconducting quantum interference device (SQUID) [55]. In fact, much of the motivation for use of TES detectors lies in their low input impedance. Many neutron transmutation doped (NTD) germanium detectors can achieve comparable performance but at much higher impedances – making them significantly more susceptible to environmental variations [56].

SQUIDs are extremely sensitive magnetometers created by a loop of superconducting wire and two Josephson junctions (JJs). A JJ is formed when two superconductors are brought near each other with a “weak-link” between them, which can either be a normal metal or an insulator. A circuit diagram if a SQUID is shown in Figure 2.4. The individual JJ critical current is $I_{c,JJ}$, thus the SQUID critical current is $I_c = 2I_{c,JJ}$. Cooper pairs of electrons [57] on one side of the superconductor utilize the dc Josephson effect to tunnel across the potential barrier formed by the weak link to the other superconductor. This allows for the creation of circulating “screening” currents (I_s) in the SQUID loop which, due the Meissner effect [58], are created whenever a magnetic field is incident on the SQUID, and act to null the magnetic field in the loop.

The Meissner effect allows integer units of the magnetic flux quantum $\Phi_0 = h/2e$, where h is Planck’s constant and e is the elementary charge, to exist interior to a superconductor (depending on the superconductor type) or superconducting loop. As the external field is increased, I_s also increases until it exceeds $I_{c,JJ}$. Once $I_s \sim I_{c,JJ}$ the JJs transition briefly to the normal state and allow integer Φ_0 to thread the loop, at which point I_s reverses sign (same magnitude) and begins to increase again. This is referred to

as “flux-jumping,” which can, but does not always, deleteriously affect the operation of a SQUID. Typically SQUIDs are biased into operation soon after transitioning into the superconducting state after being heated to $T > T_c$ in order to take the number of quanta threading the loop as small. After the superconducting transition, a negative feedback loop is commonly implemented which helps prevent flux-jumping and also increases the linear dynamic range (discussed in Section 2.4.1).

2.3.1 SQUID Operation

For $I_s < I_{c,JJ}$, the SQUID remains purely superconducting and no output voltage develops. In order to use a SQUID as a transimpedance amplifier it must first be biased into a regime where V_{out} is nonzero due to small changes in a current I . The first step is to apply a bias current $I_b = I_c$ directly across the SQUID JJs. Often, I_c is defined as the current required to observe V_{out} above some threshold or noise floor.

Second, a flux bias must be applied to the input coil which linearizes the SQUID. For a given current through the input coil I_{in} , the resulting magnetic flux incident on the SQUID is given by

$$\Phi_{in} = M_{in} I_{in}, \quad (2.41)$$

where M_{in} is the mutual inductance of the SQUID flux input coil and the SQUID loop. The current required to present a field of Φ_0 to the loop is then

$$I_{\Phi_0} = \frac{\Phi_0}{M_{in}}. \quad (2.42)$$

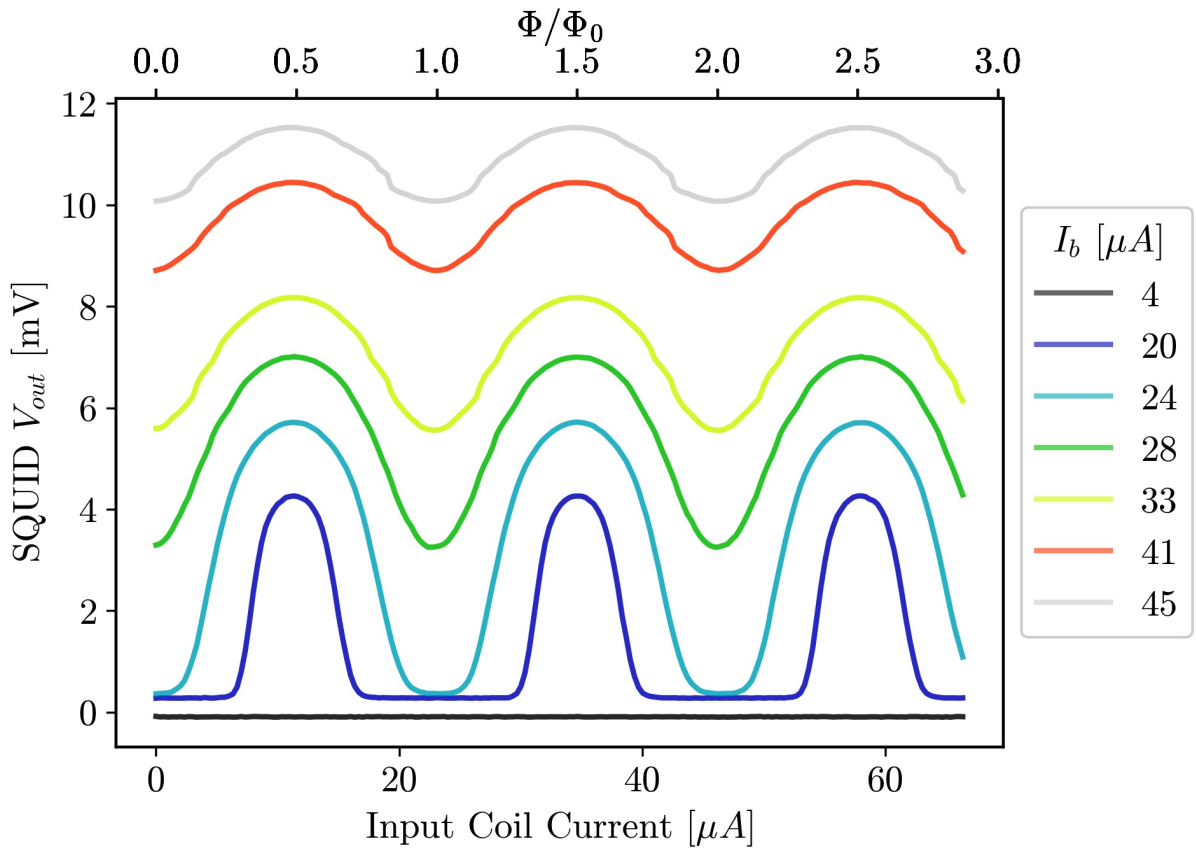


Figure 2.5: Voltage-flux ($V - \Phi$) relation for a STAR Cryoelectronics SQUID array used in the POLARBEAR-2b receiver. A SQUID current bias (I_b) is chosen and then the input coil current (I_{in}) is swept to create each family of curves.

An example of the output voltage-flux relation ($V - \Phi$ curve) is shown in Figure 2.5 for multiple values of I_b . After setting $I_b \geq I_c$, ramping the flux bias results in oscillations of V_{out} with Φ_0 periodicity. This is because Φ_{in} causes the SQUID to oscillate between two $I - V$ curves of Figure 2.6. The $V - \Phi$ oscillations are approximately sinusoidal for $I_b \gtrsim I_c$

$$V_{out} \approx V_{pp} \sin(2\pi I_{in}/I_{\Phi_0}), \quad (2.43)$$

where V_{pp} is the peak-to-peak voltage swing.

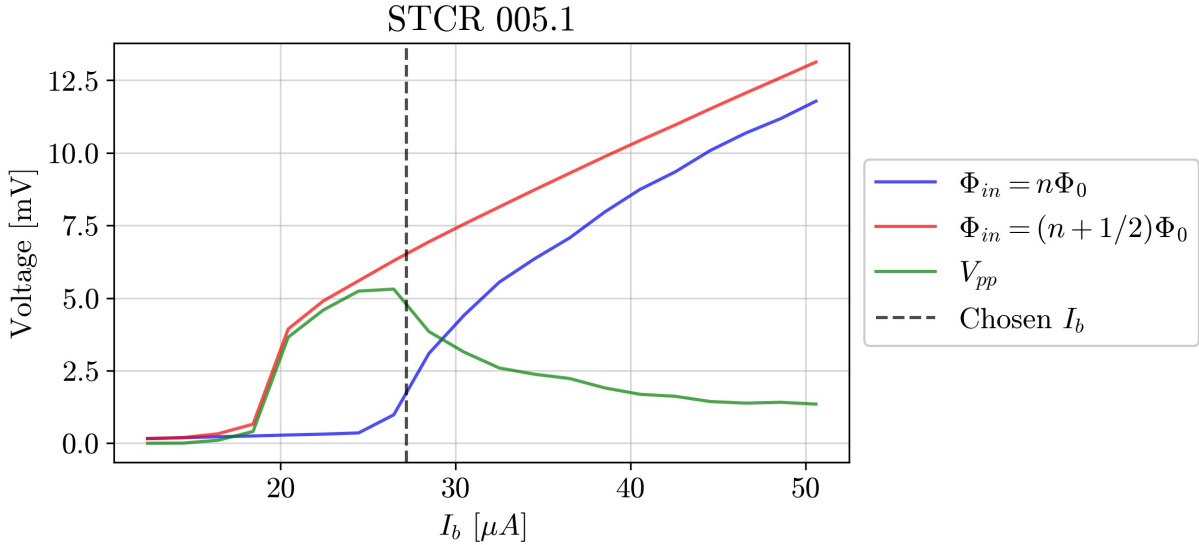


Figure 2.6: Current-voltage ($I - V$) relation for a STAR Cryoelectronics SQUID array used in the POLARBEAR-2b receiver for two different flux biases. Also shown is the maximum peak-to-peak output voltage of the SQUID at each current bias.

Small changes in flux $\delta\Phi_{in}$ cause the output voltage to change:

$$\delta V_\Phi = \frac{\delta V_{out}}{\delta\Phi_{in}}, \quad (2.44)$$

where δV_Φ is the voltage-flux transfer coefficient, or gain of the SQUID [51]. This quantity is maximized, as can be seen in Figure 2.5 and Equation 2.43, at quarter integer flux quanta

$$\Phi_{V_{pp},max} = \Phi_0 \frac{2n+1}{4}. \quad (2.45)$$

As can be seen in Figure 2.6, the JJs undergo the superconducting-normal transition at different values of I_b depending on the flux bias. Thus, the purest measurement of I_c and $I_{c,JJ}$ is with integer Φ_0 flux bias applied.

2.3.2 SQUIDs as Transimpedance Preamplifiers

Using a SQUID as a preamplifier for measuring TES bolometer current modulations, i.e. as a transimpedance amplifier, requires biasing the SQUID into regime of maximal sensitivity and linearity, referred to as “tuning” the SQUID [59]. Maximizing the SQUID sensitivity amounts to maximizing the transimpedance

$$Z_t = M_{in} \frac{\delta V_{out}}{\delta \Phi_{in}} = \frac{\delta V_{out}}{\delta I_{in}}, \quad (2.46)$$

which is achieved by first sweeping I_b to determine I_c . Then I_{in} is swept to trace out one member of the family of $V - \Phi$ curves shown in Figure 2.5. I_b which yields in the maximal V_{pp} is then selected and I_{in} is again swept to determine the flux bias value leading to the largest Z_t , resulting in maximal SQUID sensitivity. For POLARBEAR-2 we choose to bias on the descending portion of the $V - \Phi$ curve in order to maintain inverting feedback for the first stage warm amplifier, enabling implementation of a “low-frequency” analog feedback loop with $\mathcal{O}(10^2)$ Hz bandwidth. The SQUID output impedance is

$$Z_{out} = \frac{\delta V_{out}}{\delta I_b}. \quad (2.47)$$

Once the SQUID is tuned, the output voltage is carried to room temperature to the input of a traditional low-noise semiconductor amplifier which is configured to provide inverting feedback to the SQUID input coil. This is called the “flux-locked loop” (FLL) configuration, which keeps departures in Φ_{in} due to modulations of the input coil current –

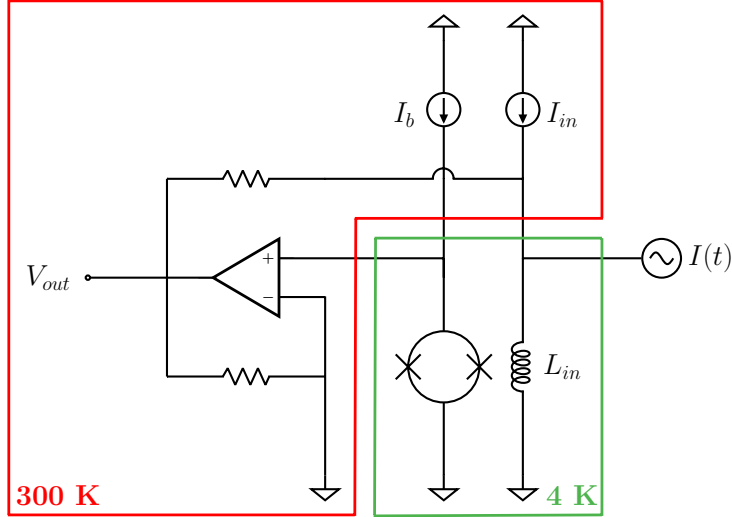


Figure 2.7: Shunt-feedback flux locked loop SQUID configuration diagram. DC current (I_b) and flux (I_{in}) biases are provided by 300 K electronics and the signal of interest – i.e. from modulated bolometer currents at 250 mK – $I(t)$ is coupled to the SQUID input coil. Inverting feedback I_{fb} (also applied by 300 K electronics) extends the SQUID dynamic range by keeping departures in Φ_{in} small, which also helps to suppress flux-jumping. In this configuration the error signal due to $I(t)$ is the signal of interest.

i.e. from performing a CMB scan – small, in a process often referred to as “nulling.” Nulling plays the extremely important role of extending the SQUID’s dynamic range and keeping its input impedance low so it matches the TES impedance. An example configuration of an FLL system is shown in Figure 2.7 depicting the shunt-feedback FLL used in the POLARBEAR-1 readout system. The discriminating feature here is that the flux feedback is applied directly to the SQUID input coil L_{in} , rather than the flux feedback coil. A proper FLL implementation has the benefit of lowering the SQUID input impedance to $\lesssim 100 \text{ m}\Omega$ if $R_{FB} = 10 \text{ k}\Omega$, and can apply a nulling signal across the entire system bandwidth of a few MHz [60].

The primary limitation of a shunt-feedback FLL is its limited bandwidth when compared to the potential SQUID bandwidth of $\sim 100 \text{ MHz}$. The reason for this limitation

is signal delay in the feedback signal due to the fact that a finite wiring length is needed to connect the cold (4 K) SQUIDs to the room temperature electronics. A theoretical upper bound for the FLL with a 1 m wiring length is \sim 20 MHz [61]. Of course a real-world system may experience significantly lower bandwidths due to nonidealities in the warm electronics beyond simple phase/timing delays, such as component variation and undesired resonances in the cold circuit. For example, the POLARBEAR-1 readout system demonstrated only a 1.3 MHz bandwidth using wiring lengths of \sim 20 cm and multiplexing 8 TESs per SQUID [60]. Increasing the number of TESs that can be read out on a single SQUID was a major design goal for the POLARBEAR-2 readout system and was achieved by replacing the shunt-feedback circuit with digital baseband feedback – i.e. application of narrowband ($\mathcal{O}(10^2)$ Hz) feedback using a set of discrete tones. For POLARBEAR-2 this extends the system bandwidth to \sim 10 MHz, which will be discussed in Section 2.4.1.

2.3.3 SQUID Series Arrays

For a single SQUID the maximal V_{out} is typically too small to be useful (tens of μ V), so it is common practice to assemble many individual SQUIDs in series. These are often referred to as “SQUID series arrays” (SSAs) which, if properly fabricated and phased (i.e. if JJ I_c and the Φ_{in} applied to each loop is uniform), can be treated as a single SQUID with the aggregate properties of all individual SQUID loops in the array. In later sections we will refer to SSAs as “SQUIDs” and will emphasize when behavior is applicable only to a single SQUID loop in the array.

Configuring SQUIDs in arrays comes at a cost: while the SSA output voltage and

transimpedance scale as the number of SQUIDs in series (the “array factor”) N_{SQ} , the voltage noise also increases. However, this only increases by the factor of $\sqrt{N_{SQ}}$. Array factors of ~ 100 are typical in order to achieve both mV level peak-to-peak voltages and transimpedances of a few hundred Ohms. For these SSAs, typical current noise levels at 4 K are less than $10 \text{ pA}/\sqrt{\text{Hz}}$ [55]. The SSAs used in the POLARBEAR-2b receiver from Star Cryoelectronics have an array factor of 112. Due to the increased size of an SSA (hundreds of mm^2) when compared to that of an individual SQUID (tens of μm^2) care must be taken to eliminate gradients in the magnetic field across the SSA chip. Traditional solutions include encompassing the SSA in a high-permeability (“ μ -metal”) or superconducting shield to attenuate magnetic fields and thus minimize cross-chip gradients. Recent SSA mask designs from NIST and other institutions incorporate first or second order gradiometric input coils which drastically reduce the SSA sensitivity to both static and time-varying external magnetic fields [62], [63].

2.3.4 SQUID Tuning

Following the discussion in Section 2.3.1, a suitable array current and flux bias must be chosen in order to provide transimpedance amplification. A number of considerations are important in selecting the bias point, which we refer to as “tuning” the SQUID, the most notable of which are balancing linearity, gain, and tuning speed. The DfMUX tuning algorithm balances the speed at which hundreds of SQUIDs may be tuned in parallel, since SQUID tuning occurs frequently during observation, with choosing the exact optimal bias point for each device. The tuning procedure, starting with all SQUID and detector biases

already zeroed, is roughly summarized below:

1. Determine the input coil current bias required for integer ($I_{in,1}$) and half-integer ($I_{in,2}$) flux bias. This is done by taking a $V - \Phi$ curve using a reference SQUID current bias which is guaranteed to produce voltage modulation as the flux bias is swept. The reference current is user-specified and most commonly corresponds to a value close to optimal in terms of V_{pp} .
2. Find the maximum voltage modulation. **Dither** I_b to determine the value yielding the maximum voltage modulation V_{pp}^{max} , i.e. I_b^{max} . V_{pp} is calculated by measuring V_{out} using $I_{in,1}$, $I_{in,2}$, and two points on either side of each. A parabola is fitted to each peak and trough and the difference in the vertices is taken as V_{pp} .
3. Set the current bias. Increase I_b above I_b^{max} and continue measuring V_{pp} until $V_{pp} = 0.9V_{pp}^{max}$.
4. Set the flux bias. Measure a “final” $V - \Phi$ curve and re-compute $I_{in,1}$ and $I_{in,2}$. Set the flux bias to the midpoint of $I_{in,1}$ and $I_{in,2}$.
5. Measure and record Z_t using a 50 kHz (i.e. \sim dc) tone. This measurement of the SQUID gain is typically used as a proxy for SQUID “health” during stress testing.

The factor of 0.9 in step (3) above is arbitrary and was determined empirically using the NIST SA4 SSA design. The purpose of this “detuning” is to avoid choosing a current bias where the JJs remain fully superconducting at integer Φ_0 flux bias, corresponding to the minimum screening current in the SQUID loop. It is not clear that such a choice

deterministically results in the best tuning point in terms of balancing gain and linear range for all SQUID designs.

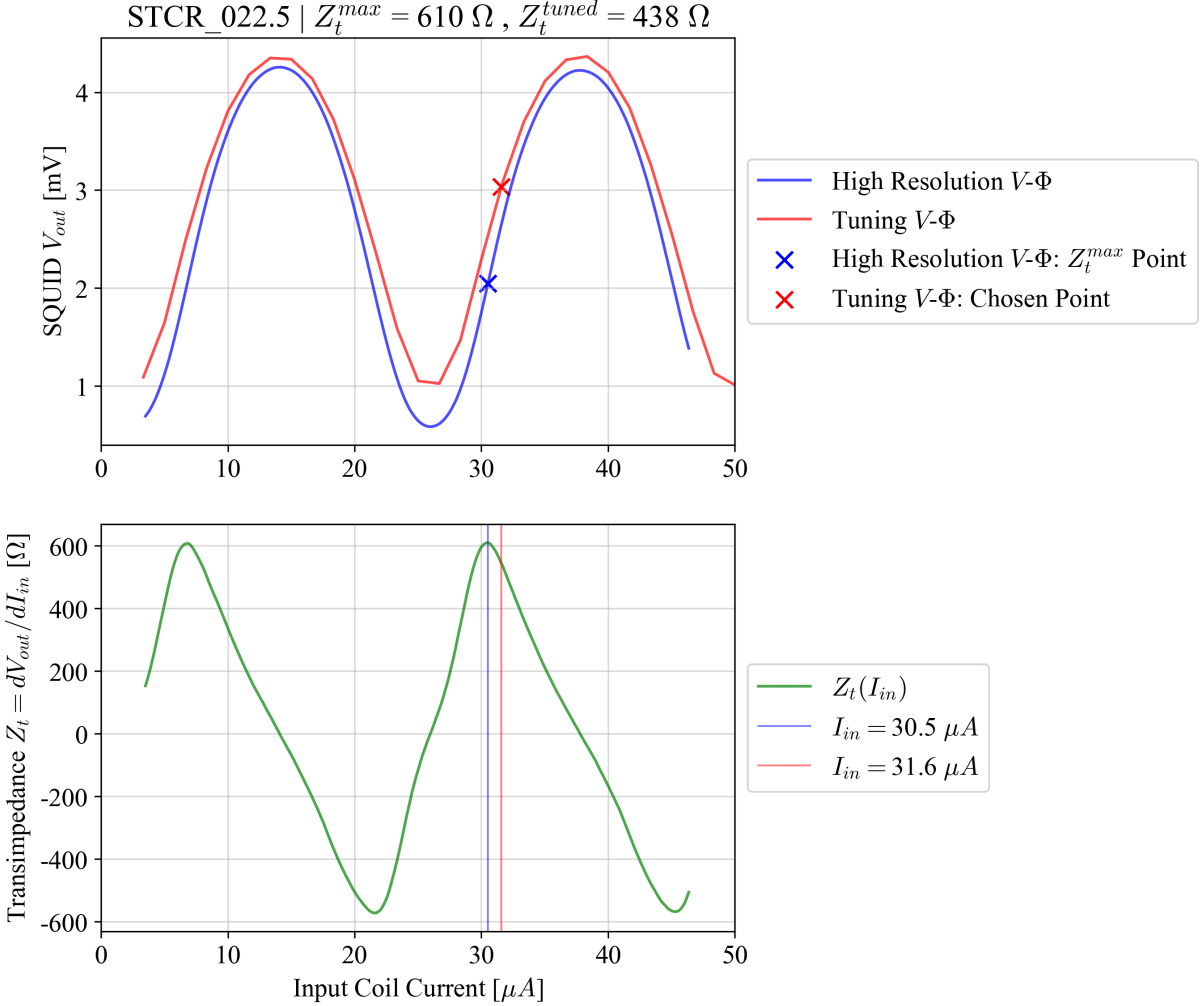


Figure 2.8: Comparison of the bias points from a high resolution $V - \Phi$ measurement and the DfMUX tuning algorithm. (*Top*) demonstration of the deliberate increase in I_b above the value yielding V_{pp}^{max} and comparison between the selected tuning point and maximal gain bias point measured with a high resolution $V - \Phi$ curve. (*Bottom*) Z_t calculated at every point in the high resolution $V - \Phi$ curve.

This choice of flux bias actually helps to increase the linearity and dynamic range while detector biases are active. All un-nullled currents flowing through the input coil manifest as an RMS current, pushing the mean bias away from the tuned bias point (in

the positive direction). The reason for this is that the flux bias point chosen via tuning is a few μA discrepant with the bias corresponding to the maximum Z_t , as can be seen in Figure 2.8.

2.3.5 SQUID Noise

As mentioned in Section 2.2, CMB experiments pay careful attention to individual noise contributions in the system and go to great lengths to ensure the overall system noise is dominated by CMB photon noise. We shall now determine expressions for the SQUID's contribution to the system noise. Using a SQUID as an ammeter for measuring TES bolometer currents means the SQUID contributes a noise equivalent current NEI_{SQ} which, when referenced to the bolometer input, becomes a noise equivalent power NEP_{SQ} if the bolometer is operating at high loopgain and responsivity. Equation 2.9 gives

$$\text{NEP}_{SQ} = \frac{\text{NEI}_{SQ}}{(\delta I / \delta P_{opt})} = \frac{\text{NEI}_{SQ}}{S_I} \approx V_{bias} \text{NEI}_{SQ}. \quad (2.48)$$

Additionally, there is a voltage noise contribution from the first stage warm amplifier used to measure the SQUID's output. The SQUID transimpedance converts this to a noise equivalent current referenced to the SQUID input and we again reference this as an NEP at the bolometer input using the responsivity. The contribution from the first stage amplifier is

$$\text{NEP}_{amp} \approx \frac{V_{bias} E_n}{Z_t}, \quad (2.49)$$

where E_n is the amplitude of the (white) power spectral density voltage noise of the amplifier.

In the POLARBEAR-2 receivers, NEP_{SQ} and NEP_{amp} can be significant and nearly equal to NEP_γ . Since both these terms depend on bolometer voltage bias, one of the more effective ways of minimizing the SQUID and first stage amplifier contribution to the system noise is to devise strategies for operating at a lower V_{bias} . This can be done by tuning the bolometer geometry so that P_{bath} is at most a small multiple of P_{opt} , reducing the electrical power required to remain in the superconducting transition. Additionally, lowering the operating R_{frac} by lowering V_{bias} is beneficial, with the caveat that for bolometer stability R_{frac} cannot be set arbitrarily low.

2.4 Multiplexing

Due to the faintness of the B -mode signal, and the fact that all modern CMB experiments are engineered so the system is CMB photon noise-limited, the primary path towards increasing the sensitivity of such an experiment is by increasing the number of detectors. Current experiments employ thousands of TES bolometers which must all be simultaneously read out for observation times of a few thousand hours. If every TES was read out using one pair of wires the parasitic heat load delivered to the cold stages would quickly become intractable for even a few hundred bolometers. Cooling capacities of most millikelvin refrigeration technologies are on the order of tens to hundreds of μW , which is easily overwhelmed even if small gauge, low thermal conductivity cryogenic wiring is

implemented. Instead of reading out a single bolometer per pair of wires we now employ multiplexing methods allowing many detectors to be read out on a single pair. The number of bolometers read out per pair of wires is the multiplexing factor N_{mux} , which reduces the number of wires needed by N_{mux}^{-1} . Modern multiplexing factors of 10-100 are quite common, with certain configurations showing promise of factors in the thousands [64], [65].

Other motivations for implementing multiplexing besides mitigation of thermal loads include cost, the amount of space physically available in the cryostat, and system complexity. Many readout components, such as SQUIDs, FPGAs, and tone generators are quite expensive, so reducing the number needed greatly improves the sensitivity of a receiver for a fixed cost. Additionally, space within the anterior portion of the cryogenic receiver is often at a premium and dominated by efforts to maximize the detector count. Thus multiplexing also plays a key role in extending sensitivity beyond what would be possible otherwise given the amount of physical space available for the cold readout components.

Multiplexing schemes come in two varieties: time-division multiplexing (TDM) and frequency-division multiplexing (FDM). Each technology takes advantage of the fact that the SQUID (or any amplifier for that matter) bandwidth is often tens or hundreds of MHz – much larger than the $\mathcal{O}(10^2)$ Hz bandwidth required to readout the CMB signal while a telescope is scanning the sky [66]. Both these technologies have demonstrated success in deployed instruments [67]–[70], with TDM occupying the older more established position. In TDM, each TES is coupled to a first-stage SQUID, often located on the millikelvin detector stage, which act as switches and are controlled by a row address boxcar signal which sequentially selects each TES in the row (much the same way information is read out

of computer memory). Outputs of the first stage SQUIDs are then summed along a row and fed into a second-stage SQUID at ~ 4 K. TDM suffers from one primary limitation: for $N_{mux} = N_{row}$ TESs in each row, each TES can only be read out for a fraction $1/N_{row}$ of the time. This means that (1) the SQUID noise bandwidth is N_{row} times larger than the Nyquist sampling frequency – which requires addition of “Nyquist inductors” to properly limit bandwidths and the effects of this “TDM multiplex disadvantage,” and (2) because the multiplexing factor depends on the switching speed of the first stage SQUID, there is a practical limit to N_{mux} . Recent efforts at NIST have achieved $N_{row} = 32$ [71] but extending the multiplexing factor beyond this by more than a few multiples will be difficult. Code-division multiplexing (CDM) is a new technology currently under development [72] which modifies the manner in which the boxcar row address waveform is generated and samples each TES according to a Walsh matrix of dimension N_{mux} . Applying the inverse Walsh matrix then de-multiplexes the signal for each row. CDM has the ability to increase the multiplexing factor by as much as $N_{mux}^{1/3}$, where N_{mux} is the traditional TDM multiplexing factor.

The second variety of multiplexing for TES bolometers, FDM, relies on the orthogonality of sinusoidal bias tones to increase the number of TESs that can be read out on a single wire pair. In FDM, each TES is connected in series to a distinct channel-defining inductor-capacitor (LC) resonator, allowing each TES to be biased or read out using a unique carrier tone. Within FDM there are two major delineations. The first, referred to as the digital frequency division multiplexing (DfMUX) system [60], operates at lower resonator frequencies in the MHz range, supplied the detector bias solely using the sinu-

soidal bias tone, and uses only a single dc ~ 4 K SSA to read out one comb of detectors. The second, referred to as the microwave multiplexing (μ mux) system [65], supplies a common dc detector bias to an entire TES comb and achieves individual detector read out using low-amplitude probe tones in the GHz range (corresponding to the LC resonator frequencies). The TES comb signals are preamplified using a front-end rf SQUID for every TES and a single low-noise coherent amplifier for reading out each comb.

The DfMUX system, is used in the POLARBEAR-1 and SPTpol receivers, as well as the APEX-SZ and SPT-SZ experiments. A continuation of the DfMUX system is what is used in the POLARBEAR-2 and SPT-3G receivers which increases the bias frequencies from just around 1 MHz, to $\sim 1.5 - 4.5$ MHz and multiplexing factors from 8 to ~ 100 [73]. The μ mux system has only recently been deployed for systems using microwave kinetic inductance detector (MKID) arrays [74] and is currently undergoing development for deployment with TES detectors for the Simons Observatory [6], [75] and BICEP collaborations, with indications that N_{mux} can routinely be in the range of $\mathcal{O}(10^2 - 10^3)$.

2.4.1 Digital Frequency Division Multiplexing

The DfMUX readout system used in the POLARBEAR-1 and SPTpol experiments (DfMUX) which has a bandwidth of 1.3 MHz and $N_{\text{mux}} = 8$ [59]. A diagram of the DfMUX system is shown in Figure 2.9. This system has undergone modifications to extend the bandwidth to ~ 10 MHz, enabling N_{mux} as high as 128 currently, which is primarily achieved by replacing the shunt-feedback FLL with digital baseband feedback in a narrow band around each bias frequency. This is referred to as “digital active nulling” (DAN). As

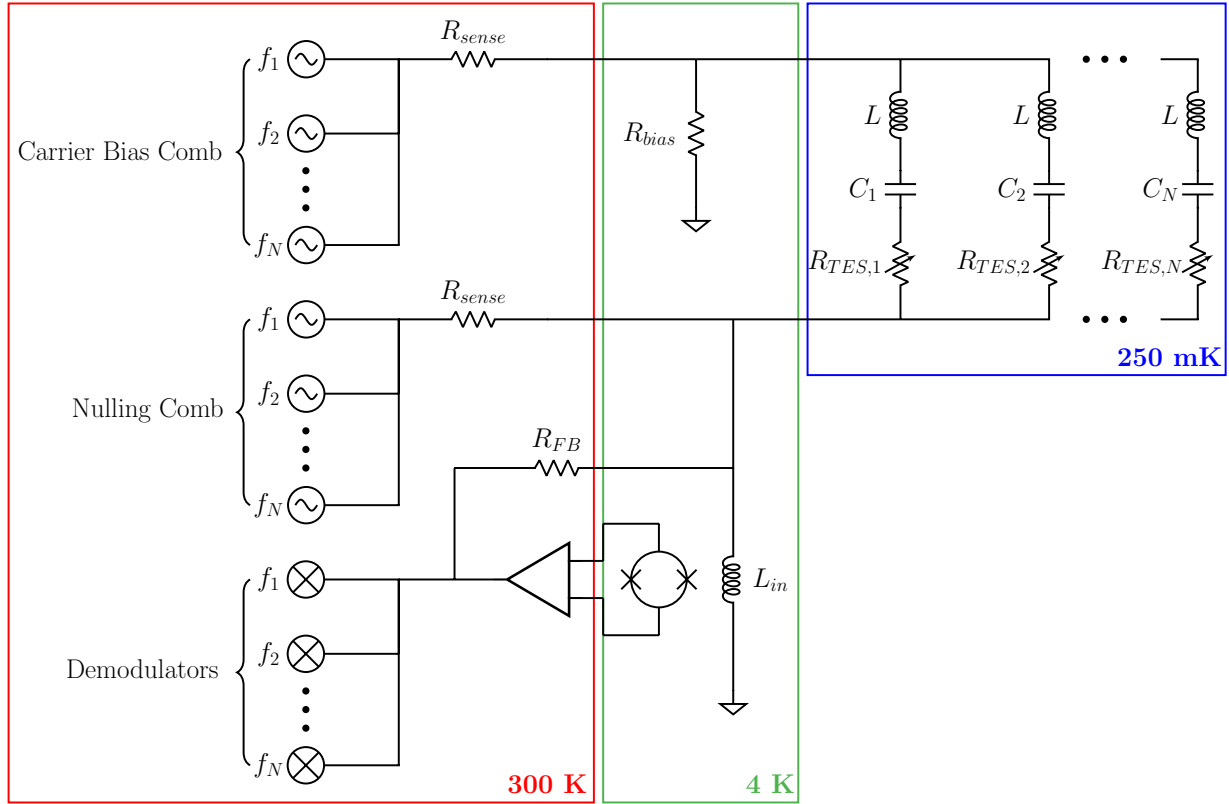


Figure 2.9: Circuit diagram of the DfMUX system with the approximate stage temperatures of each component. TESs are denoted as variable resistors connected to their respective channel-defining LC filter.

mentioned in Section 2.4, each TES (modeled as a variable resistor R) in the DfMUX system is wired in series to an LC resonator of frequency

$$f_0 = \frac{2\pi}{\sqrt{LC}}. \quad (2.50)$$

The full width at half maximum (FWHM) bandwidth of each LCR resonator is

$$\Delta f = \frac{2\pi R}{L}, \quad (2.51)$$

where R is the total effective series impedance of one LCR resonator, i.e. this includes any stray or parasitic impedances present in the circuit. Similar to the FWHM, the quality factor describes the “sharpness” of the resonance by relating the resonant frequency to the bandwidth:

$$Q = \frac{f_0}{\Delta f} \frac{2\pi}{f_0 R C}. \quad (2.52)$$

The readout time constant is the inverse of the resonator bandwidth

$$\tau_{readout} = \frac{2\pi L}{R}, \quad (2.53)$$

and to maintain stability in the TES transition we require $\tau_{bolo} > 5.8\tau_{readout}$ [51]. The bolometer time constant is determined by its thermal time constant and electrothermal loopgain (see Section 2.1) which must be fast enough to resolve the science signal. During a typical CMB scan, and using a continuous polarization modulator operating at ~ 2 Hz, the science signal is < 100 Hz; therefore the readout bandwidth must be of order 100 Hz at each resonator tone. As can be seen in Equation 2.53, for a fixed TES resistance the readout time constant is determined solely by the inductance. To implement DfMUX, we choose a fixed L and vary C with each resonator to ensure the readout bandwidth is constant for all channels.

The inductance also plays a role in determining the electrical bias power dissipated

on the bolometer island at bias frequency ($\omega_0 = 2\pi f_0$)

$$P_{avg}(\omega) = \frac{V_{bias,rms}^2 \omega^2 R}{\omega^2 R^2 + L^2(\omega^2 - \omega_0^2)}. \quad (2.54)$$

At $\omega = \omega_0$, Equation 2.54 reduces to $P_{avg} = V_{bias,rms}^2 / R$. This illustrates a need for tightly controlling all inductances in the system, especially stray/parasitic inductances, due to their ability to spoil TES stability by increasing the readout time constant and broadening the LC resonances – especially if bias tones used are not exactly at each f_0 .

In addition to the readout time constant and the resonator inductance, care must be taken in determining the frequency spacing of each resonator in order to minimize off-resonance induced currents (i.e. crosstalk) between neighboring channels. Increasing the channel spacing with increasing bias frequency is commonly implemented in order to mitigate this effect. This also has the added benefit of reducing the amount of Johnson-Nyquist noise that is able to crosstalk and refer to the bolometer. For the frequency spacing used in the POLARBEAR-2 receivers this is sufficient to ensure that this effect (on paper) is less than 1% [51].

2.4.2 Cryogenic Circuit

In FDM, the primary component in the circuit which defines the multiplexing factor is the bank of parallel LC filters connected to the input coil of the SQUID. These are referred to as an LC “comb” (blue portion of Figure 2.9), each of which is connected in series to its own bolometer. To extend the multiplexing factor one simply needs to add more LC

resonators to the comb and accordingly attach a bolometer to each. If care is taken in the design of other system components to eliminate crosstalk, stray impedances, and unwanted resonances, the response of the comb due to a swept carrier bias tone, called a “network analysis”, is simply the linear combination of every resonator. Due to the existence of stray impedances and temperature dependence in the inductance, network analyses are routinely taken to empirically determine f_0 for each resonator in each configuration of the system. The admittance Y of a comb at frequency ω for an N -channel comb with fixed inductance L , capacitance C_j , and resonant frequencies $\omega_{0,j} = 1/\sqrt{LC_j}$, is simply a sum of Lorentzians

$$Y(\omega) = \sum_{j=1}^N \left[i\omega L + i\frac{1}{\omega C_j} \right]^{-1} = \sum_{j=1}^N \left[iL \left(\frac{\omega^2 - \omega_{0,j}^2}{\omega} \right) \right]^{-1}. \quad (2.55)$$

Figure 2.10 shows an example network analysis of a POLARBEAR-2 comb with 36 out of a maximum of 40 connected channels over the readout band of approximately 1.5-4.5 MHz. Figure 2.11 shows the difference in the resonant frequencies as measured using a network analysis. At MHz frequencies $f_{bias} \gg \tau_{TES}^{-1}$ (τ_{TES} is the bolometer time constant) so the bolometers always see this bias tone as an average electrical power. Due to the complexity of the cold circuitry, lack of redundancy, and difficulty in verifying assembly of the LC combs used in the POLARBEAR-2 receivers before cooldown, yield loss is a common concern as a single connection failure between the SQUID and bolometer results in inoperable detectors which cannot be repaired while the receiver is cold (i.e. during testing/observation).

Mounted at 4 K is a low resistance bias resistor with $R_{bias} \ll R_{TES}$ which creates a voltage bias across the comb even at very low TES operating resistance; although the

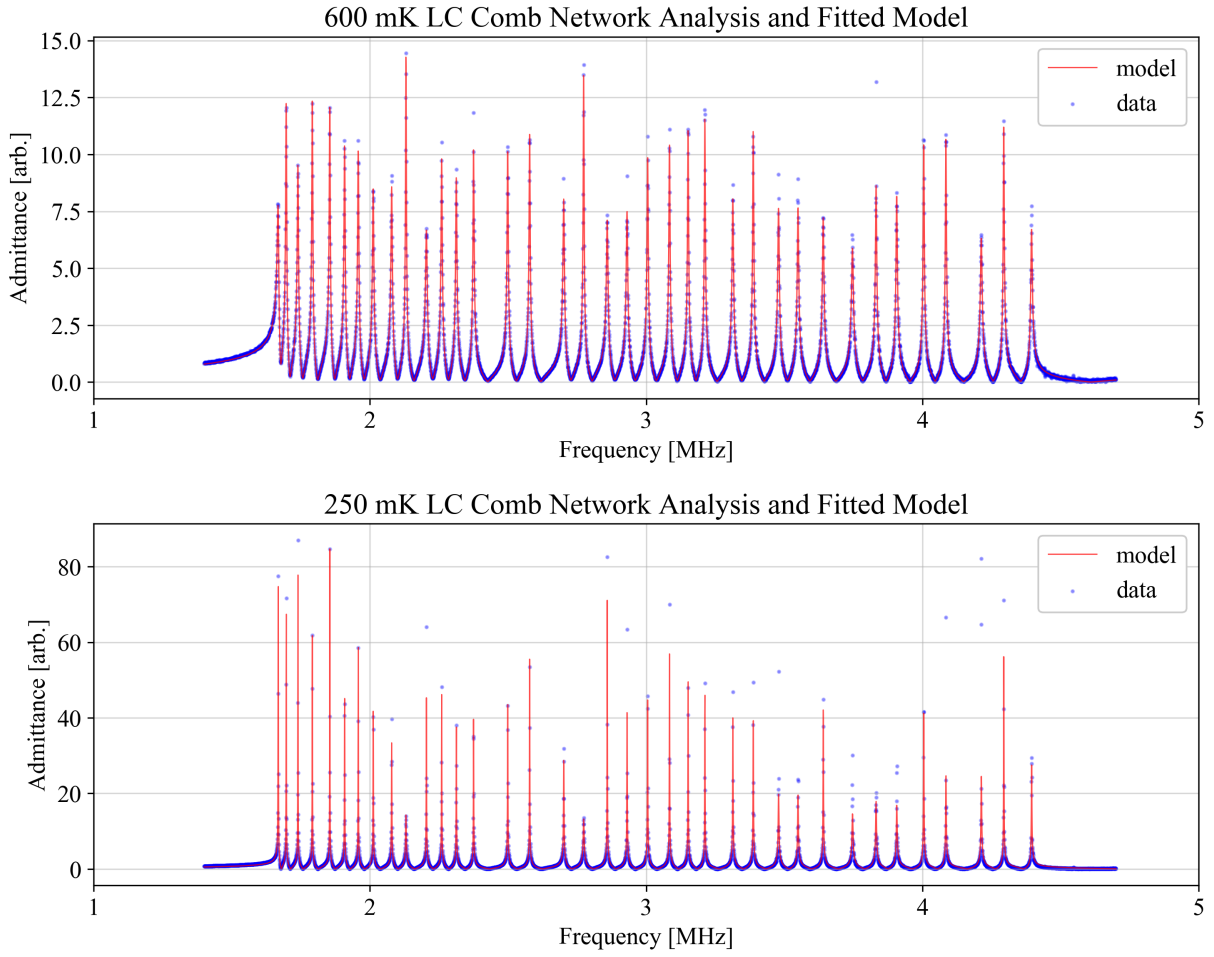


Figure 2.10: Network analysis of a POLARBEAR-2 LC comb with 36 connected channels above (*top*) and below (*bottom*) the TES superconducting transition temperature of ~ 450 mK. Clearly visible is the effect on the resonator quality factor due to the fact that at 600 mK $R_{TES} \sim 1 \Omega$ and at 250 mK $R_{TES} = 0$. The frequency spacing increases logarithmically with frequency to help minimize neighboring channel crosstalk. Imperfections during fabrication and stray impedances do, however, result in some scatter in the actual resonant frequencies away from the design values – contributing to crosstalk.

stiffness of this voltage bias can be spoiled by stray impedances present after the bias resistor and before the SQUID input coil (discussed in Section 2.4.3). Additionally, a precision resistor is used for sensing the current output by both the carrier and nuller tones in order to precisely measure the voltage bias across each leg in the LC comb. While

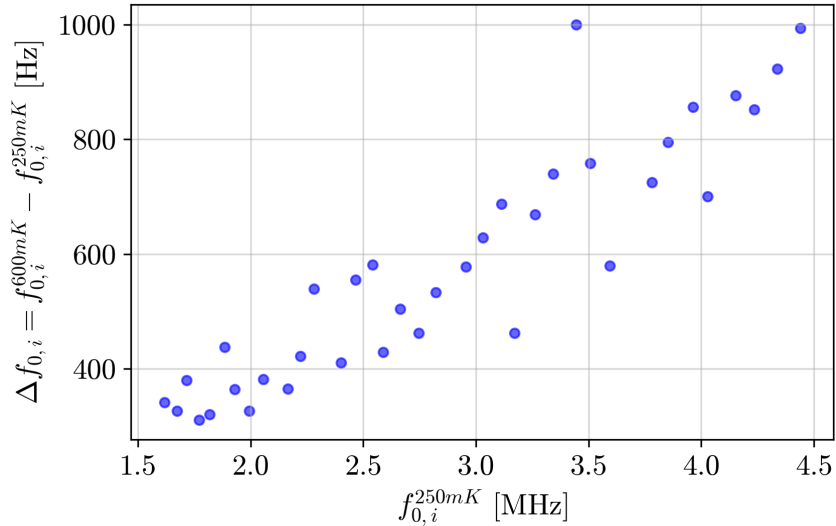


Figure 2.11: Difference in resonant frequencies $f_{0,i}$ as measured from a network analysis with an LC comb at temperatures of 600 mK and 250 mK. A typical resonance has a ~ 1 kHz FWHM so these shifts are significant enough that separate bias frequencies must be used if the bolometer stage temperature is raised and if effects of biasing off-resonance need be eliminated.

operating at 4 K the power dissipation in the bias resistor is negligible compared to the cooling power of the 4 K mechanical refrigerator, however if this component were moved to the millikelvin stage, where cooling powers are many orders of magnitude lower, this would result in unacceptably high heat loads. This would also require a bias resistor for every detector, which would occupy a large amount of physical space on the focal plane. Moving the bias resistor to a colder section of the cryostat does have the advantage of reducing its Johnson-Nyquist noise contribution to the overall system noise. However, even at 4 K, this noise is not a significant contribution to the readout noise in DfMUX. Investigations into architectures locating a “front-end” SQUID at millikelvin temperatures with the bolometer arrays in order to reduce the effects of parasitic impedances and increase multiplexing factors are currently underway [76].

Preamplification of the bolometer plus LC comb is achieved using an SSA, which is also mounted at 4 K and tuned to a regime of maximal linearity as described in Section 2.3.2. All current through the LC comb is summed and passed into the SQUID input coil, producing a modulated output voltage. This output voltage is amplified at 300 K and the error signal, i.e. the un-nullled current through L_{in} , is determined and injected using inverting feedback in order to null I_{in} . The error signal typically contains contributions from dc up to a few hundred Hz, and at each bias frequency (corresponding to the LC resonant frequencies $f_{0,i}$). It is also possible for intermodulation distortion (IMD) products, which arise from mixing between two or more bias tones that are transmitted on the same wire pair, to exist in the error signal. Nulling these contributions to the error signal is often difficult and/or impossible if the feedback circuit is not designed to operate over the entire bandwidth, as in the case of DAN. Nulling is critically important in extending the dynamic range of the SQUID and ensuring its input impedance is well matched to the $\sim 1\Omega$ bolometers it is being used to readout. In Chapter 4 will discuss in detail how imperfect nulling can affect the SQUID dynamic range and noise performance.

2.4.3 Parasitic Impedances

A major requirement for successful FDM systems is that the parasitic (or “stray”) impedances due to lossy conductors, circuit board trace inductances, and interconnects are all effectively minimized so the LCR resonators’ behavior is dominated by the nominal design values of the resonator inductor and capacitor. If R_{TES} is not the dominant resistance, the resonator peaks broaden, increasing crosstalk, and the voltage drop across the TES

becomes less certain and can lead to instability, especially if the other resistive contribution is an unknown stray. In order to ensure R_{TES} dominates the resistive contribution in each leg of the comb, low-loss inductors and capacitors must be used. Superconducting resonators made from lithographed niobium or aluminum spiral inductors and interdigitated capacitors are excellent choices for this. Stray inductance can affect not only the readout time constant, but also crosstalk and will be discussed in Section 2.5.1. To enforce a uniform readout time constant the resonator L is chosen to be much larger than the strays, which are often on the order of nH. In the case of channel-dependent stray inductances, this results in variations in bolometer stability. Minimizing the stray inductance is more difficult as cable runs from the 4 K bias resistor, to the 250 mK focal plane, and back to the SQUID input coil can be 100–200 cm in total. A twisted pair using typical cryogenic wire gauges ($L_p \sim 3$ nH/cm) results in parasitic inductances of 300–600 nH. Within the bias frequency range of 1.5–4.5 MHz, the parasitic reactance due to this stray inductance is in the range of $1.4 - 8.5 \Omega$, which is clearly too high for bolometers with normal resistances of $\sim 1 \Omega$. Instead, broadside-coupled NbTi striplines are used in POLARBEAR-2 DfMUX to reduce this parasitic to ~ 60 nH. Additional measures to reduce strays include the use of superconducting materials wherever possible, high purity copper with high residual-resistance-ratio (RRR), superconducting tin-lead eutectic solder joints and plated traces, and connectors with low contact resistance and inductance. Note that the stray inductance of the bias resistor, which can be ~ 1 nH, can result in stray reactances on the order of 1Ω at 4.5 MHz, which can reduce the stability of bolometers with higher bias frequencies.

Another complication due to the existence of parasitic impedances is that the actual

TES RMS voltage bias is not what is commanded by the tone generators, even after taking into account the known/measured warm-to-cold transfer function composed of cable loss, bandwidth-limiting filters, and impedance mismatches. Generally, each channel has its own unique parasitic impedance which causes some variation in the TES bias voltage. For a given channel we model this as a Thevenin equivalent series impedance Z_p [7]. The true voltage bias V'_{bias} of the TES is then obtained using a voltage divider

$$V'_{bias} = V_{bias} \frac{R_{TES}}{R_{TES} + Z_p}, \quad (2.56)$$

where R_{TES} is the operating resistance of the TES and V_{bias} is the RMS voltage bias across the 4 K bias resistor at $f_{bias} = f_{0,i}$. Figure 2.12 shows the DfMUX system with each channel's unique parasitic impedance $Z_{p,i}$ (in actuality these are complex, but our Thevenin equivalent model assumes a purely resistive stray). This model does not include parasitic-induced crosstalk and, in reality, there is a network of parasitic impedances bridging all bolometer legs in a comb. We assume these affects are small when compared to the voltage drop across $Z_{p,i}$.

Fortunately, there are multiple methods for measuring $Z_{p,i}$. Taking a network analysis with the bolometers in the superconducting state allows us to measure the parasitic impedance due to the fact that $R_{TES} = 0$. The LC resonator bandwidth is then determined purely by the stray impedance and the total series inductance:

$$\Delta f_p = \frac{2\pi R_p}{L + L_p} \rightarrow \frac{2\pi Z_p}{L}. \quad (2.57)$$

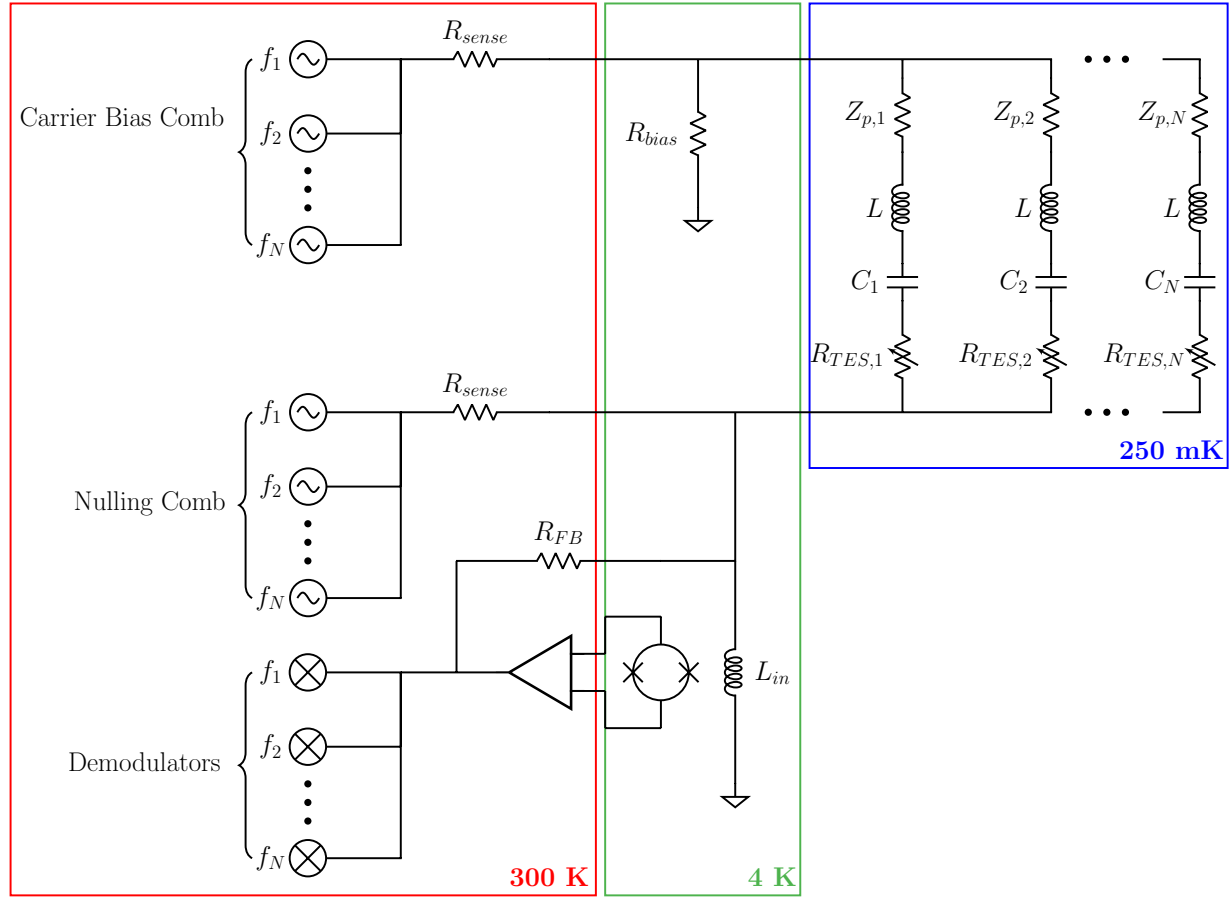


Figure 2.12: Circuit diagram of the DfMUX FDM system showing Thevenin equivalent parasitic series impedances for each channel $Z_{p,i}$. Generally, each $Z_{p,i}$ is distinct.

Again, we stress that in actuality the impedance on resonance is complex and affected by parasitic-induced bias leakage from the rest of the comb, but due to the complexity of this model we choose the aforementioned simplification. Taking a network analysis above the TES T_c and fitting the resonator bandwidths then provides a measurement of the total resistance present in one channel $R = R_{TES} + Z_p$. Obtaining R_{TES} is then a simple matter of subtracting the parasitic. An example of this correction is shown for one comb of POLARBEAR-2 bolometers in Figure 2.13. The network analyses corresponding to these measurements are those shown in Figure 2.10. This method of stray-correction

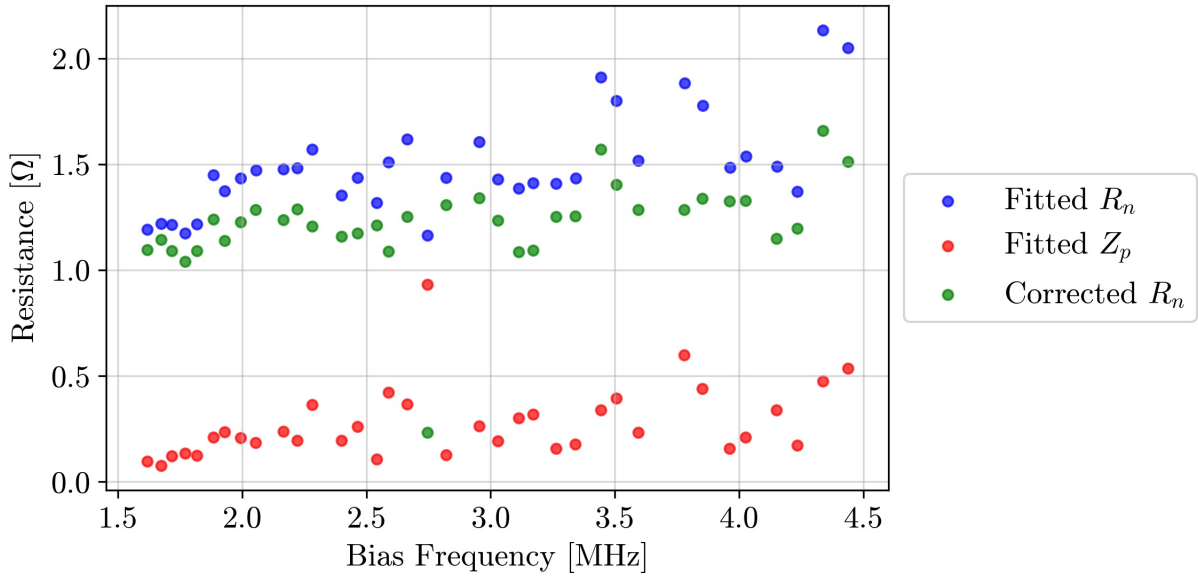


Figure 2.13: Measurement of, and correction for, the parasitic impedance for one comb of POLARBEAR-2 bolometers by fitting to each Lorentzian found in the network analysis with the stage at 600 mK. Based on geometric measurements of the AlMn TES after fabrication, these bolometers are expected to have $R_n \sim 1.5 \Omega$. The corrected TES normal resistance is simply $R'_n = R_n - Z_p$.

does rely heavily on knowing a-priori actual values for the inductance of the spiral inductor and typical values for the mean parasitic inductance which is present on all channels for all combs. In the POLARBEAR-2 receivers these correspond to $59.7 \mu\text{H}$ and $\sim 60 \text{ nH}$, respectively.

A second method for measuring the parasitic impedance is by taking $I - V$ curves of a bolometer at voltage biases below the point where it becomes unstable and latches. Once the bolometer has latched, the $I - V$ curve traces out the behavior due to the presence of Z_p , i.e. it will be linear with a slope of $Z_p = dV/dI$. An example of this measurement is shown in Figure 2.14. In this measurement, the voltage bias is set to a large value ($\gtrsim 5 \mu\text{V}_{rms}$) with the bolometer thermal stage above T_c . The stage is then cooled to 250 mK and

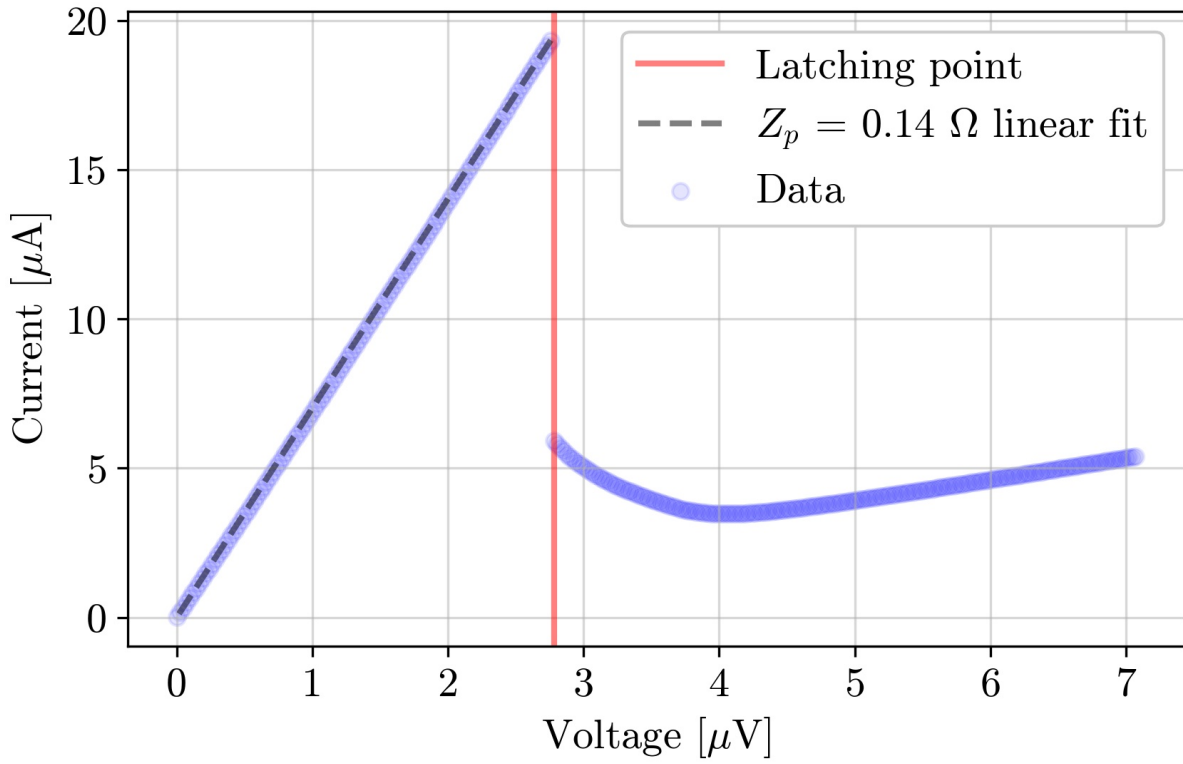


Figure 2.14: Measurement of, and correction for, the parasitic impedance for a single POLARBEAR-2 bolometer by fitting to the latched portion of the $I - V$ curve. When the bolometer latches, a large jump in current occurs due to the sudden decrease in the total channel resistance. Below this point the behavior is dominated by the stray impedance.

the $I - V$ curve is measured by iteratively lowering the voltage bias to zero amplitude. Typically in this measurement the voltage bias for entire combs of bolometers is adjusted simultaneously, which can cause anomalies in the latched portion of the $I - V$ curve, such as nonlinearity due to crosstalk between channels. Performing the measurement serially, i.e. adjusting V_{bias} for a single bolometer on a comb at a time, helps mitigate the effects of crosstalk. This measurement may also be performed serially with the bolometer beginning in the latched state with the stage at 250 mK, which also helps minimize crosstalk and improve the accuracy of the parasitic measurement.

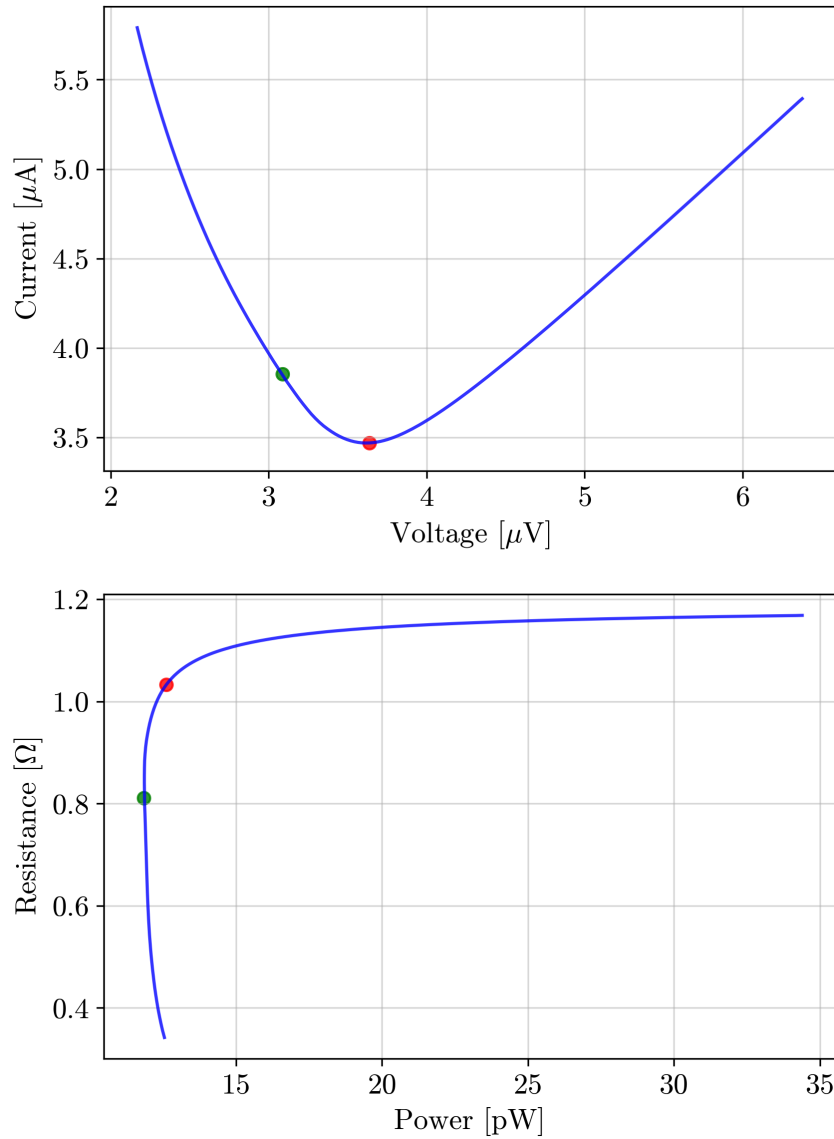


Figure 2.15: TES bolometer current-voltage ($I - V$) and resistance-power ($R - P$) relation corrected for the Thevenin equivalent series impedance Z_p . Here the voltage shown is the actual voltage across the TES, as opposed to simply the voltage output by the carrier tone generator at 300 K. Comparing to Figure 2.3 we can see the effects Z_p has on the measured voltage and power. This is most evident in how the power does not begin to increase significantly at low voltage bias, corresponding to the bolometer operating in “constant” (total) power mode. Curvature towards higher power below 0.4Ω is from the onset of instability due to the parasitic.

Figure 2.15 shows the effects of removal of Z_p on the $I - V$ and $R - P$ curves for the same bolometer shown in Figure 2.3 where parasitics are not accounted for.

2.4.4 DfMUX 300 K Electronics

The custom room temperature (300 K) electronics responsible for biasing and controlling the cold circuit described in Section 2.4.1 is part of the “ICE” electronics system developed by McGill University [59], [60], [73], [77], [78]. Beginning at the far left of Figure 2.9, there are three banks of sinusoidal tone generators operating at their respective channel’s resonant frequency $f_{0,i}$, each of which are also referred to as combs. The carrier comb is responsible for providing the voltage bias for each LCR channel and is only changed when a change in the bolometer’s operating resistance is desired. Each tone here is summed and dropped across the bias resistor to create a voltage bias across the bolometer comb.

The nulling tone is responsible for zeroing the current (i.e. the error signal) present at the junction where the nulling comb, bolometer comb, and SQUID input coil meet – creating a virtual ground at this point. In the absence of a sky signal this is simply the inverse of the current due to the carrier comb, however, when a sky signal is present ($f_{sky} \sim 100$ Hz) the error signal contains content not only at $f_{0,i}$ but also in the sidebands $(f_{0,i} \pm f_{sky})$. In order to null this portion of the error signal, the SQUID output is mixed with a comb of demodulators (also with tones at $f_{0,i}$) to determine the sideband signal. The nulling comb then applies inverting feedback with content at each $f_{0,i}$ that has a slow modulation envelope corresponding to f_{sky} . This process of baseband feedback only around the LC channel resonant frequencies is referred to as Digital Active Nulling (DAN), which

can be configured to have an effective bandwidth about $f_{0,i}$ of up to a few hundred Hz.

Measurements of the bolometer current are performed using I/Q mixing techniques which contain the amplitude component I, and the phase Q. In this system the science signal is almost entirely present in the I component of the bias frequency sidebands.

2.4.5 Operating Bolometers with DfMUX

A general procedure for operating bolometer combs using DfMUX (see Section 2.4.1) entails first raising the detector stage above the bolometer T_c , typically 500–600 mK. SQUIDs are then tuned and the carrier, nuller, and demodulator combs are turned on (i.e. DAN is enabled) for each bolometer comb (one comb per SQUID). This is referred to as “overbiasing.” The stage is then cooled to \sim 250 mK. Carrier voltages of $\sim 5 - 10 \mu\text{V}_{rms}$ are typical in order to ensure Joule heating is sufficient to keep the bolometer island above T_c despite the fact the substrate is colder. “Tuning” a bolometer, i.e. biasing it to a specific R_{frac} , simply involves reducing the Joule heating (P_{elec}) by lowering the carrier amplitude. This drops the TES into the superconducting transition. At high carrier bias the TES is in the normal state with normal resistance $R_n \sim 1 \Omega$ for POLARBEAR-2 .

As the carrier amplitude is lowered bolometers may abruptly transition into the superconducting state, which is referred to as “latching.” At this point, further operation of the detector must be abandoned because the 300 K bias electronics do not possess sufficient dynamic range to exceed the TES critical current and bring the bolometer island back to or above T_c . The most common reasons for latching detectors are noise, feedback latency, and instability due to softening of the TES voltage bias. Noise leads to latching by

causing DAN to apply improper nulling signals, which may momentarily drop P_{elec} below the threshold required to remain in the transition. Softening of the voltage bias primarily stems from parasitics. When the TES operating resistance is low enough to be nearly equal to the parasitic, only \sim half of the bias voltage is actually dropped across the TES. Proper feedback in this regime is difficult without explicitly compensating for Z_p .

For routine CMB observations the TES operating point is set based on two main parameters discussed in Section 2.1: τ and P_{sat} . Both may be increased by choosing a lower R_{frac} , which lowers the electrical power dissipated on the bolometer island (and thus operating resistance) and allows a larger δP_{opt} before the TES is pushed fully out of the transition. In terms of τ , ETF increases after the turnaround is reached, up to an effective saturation point – set by stray impedances, the readout time constant, and the island heat capacity – which correspondingly increases τ . Moving the operating point deeper into the transition must be balanced by latching effects. For POLARBEAR-2 bolometers, the optimal bias point is $R_{frac} \sim 0.7$ where $\tau \lesssim 5$ ms and the “tuning yield,” the number of overbiased channels that do not latch before the target R_{frac} is reached, can be higher than 90%.

2.5 Readout Noise

One of the major technical difficulties in implementation of the DfMUX system is maintaining the SQUID dynamic range and linearity by effectively nulling all current through the input coil. This can be difficult due to the fact that the nulling feedback is baseband with DAN as opposed to broadband with a traditional FLL. Spurious signals

outside the baseband feedback bandwidth from rf contamination are major contributors to limiting the SQUID dynamic range as all un-nulled signals present through the input coil. If the SQUID is pushed into a non-linear regime, large signals through the input coil at the bias frequencies are distorted after amplification by the SQUID. These large signals can, in principle, experience a shift in frequency which is sufficient to push them outside of the DAN bandwidth and leaving them un-nulled, – quickly reducing the SQUID dynamic range. Signal crosstalk is a final concern as any error signal measured after demodulation in a channel on one comb can include crosstalk from channels on other combs. In this case the nulling signal for the original channels/comb includes content which does not correspond to a physical bolometer current and cannot cancel, leading to an overall increase in system noise . Additionally, so-called “optical” crosstalk may be present due to imperfections in the optical design resulting in reflections of the sky signal, and from signal correlation due to tightly packed detectors and the mm-wavelength CMB photons being observed. This maps the sky signal erroneously to focal plane position and for POLARBEAR-2 receivers is expected to be on the order of 1%. Thus, measures are taken to attempt to reduce the signal (i.e. electrical) crosstalk to less than the 1% expected optical crosstalk.

2.5.1 Crosstalk

Crosstalk between channels comes from three main sources: (1) channel-to-channel inductive coupling, (2) thermal effects in neighboring detectors due to nonzero impedances in the SQUID or wiring, and (3) bias tone leakage [59]. For (1), the crosstalk magnitude results in coupling between the inductors in the LC resonators and depends on the mutual

inductance between two channels i and j

$$M_{i,j} = k_{ij} L_i L_j, \quad (2.58)$$

where k_{ij} is the coupling coefficient of the two channels' inductors. Current modulations in one channel I_i lead to voltage modulations in another channel

$$V_j = \omega_i M_{i,j} I_i. \quad (2.59)$$

In DfMUX implementations, LC combs are installed in close proximity (a few mm chip-to-chip typically) but it is possible to reduce this contribution by shuffling the physical position on-chip of each resonator so the closest LC pairs between chips are separated by many factors of the channel spacing $\Delta\omega$, which in turn reduces k_{ij} to approximately 0.01 or less.

Nonzero SQUID input impedance and wiring parasitics $Z_{p,wiring}$ between the SQUID and the LC resonators causes a discrepancy in the commanded voltage bias and the actual voltage bias $V'_{bias} = V_{bias} - V_p$ where V_p is the voltage drop due to Z_{in} and $Z_{p,wiring}$. Typically the reactive portion of Z_{in} and $Z_{p,wiring}$ is dominated by inductive contributions. The majority of the current $I_i^{\omega_i}$ in channel i at resonant frequency ω_i flows through the i th LC channel but some is split and flows through the parasitics. For a small current $\delta I_i^{\omega_i}$

voltage bias discrepancy is

$$\delta V'_{bias} = \delta V_{bias} - \delta V_p = -\delta I_i^{\omega_i} Z_p \approx -i \delta I_i^{\omega_i} \omega_i L_p. \quad (2.60)$$

The corresponding current fluctuation in nearest-neighbor channels is

$$\delta I_{i\pm 1}^{\omega_i} = \frac{\delta V'_{bias}}{Z_{i\pm 1}} \approx \frac{-\delta I_i^{\omega_i} \omega_i L_p}{2\Delta\omega L}, \quad (2.61)$$

where $Z_{i\pm 1}$ is the impedance of the nearest-neighbor LCR circuit with resonant frequency $\omega_{i\pm 1}$. The resultant power fluctuation in channel $i \pm 1$ is

$$\delta P_{i\pm 1}^{\omega_i} \approx 2R_{TES,i\pm 1} I_{i\pm 1}^{\omega_i} \delta I_{i\pm 1}^{\omega_i}. \quad (2.62)$$

Comparing with the actual signal in channel i ,

$$\delta P_i^{\omega_i} = \delta I_i^{\omega_i} V'_{bias}, \quad (2.63)$$

gives the nearest-neighbor crosstalk level for crosstalk source (2):

$$\frac{\delta P_{i\pm 1}^{\omega_i}}{\delta P_i^{\omega_i}} \approx -\frac{I_{i\pm 1}^{\omega_i}}{I_i^{\omega_i}} \frac{\omega_i}{\Delta\omega} \frac{L_p}{L}. \quad (2.64)$$

For POLARBEAR-2 receivers this contribution is well below 1%.

The third and final crosstalk contribution, bias tone leakage, is the most significant.

Qualitatively, this term arises from overlap in the Lorentzians of neighboring resonators. The current induced in nearest-neighbor channels due to current $I_i^{\omega_i}$ in channel i at resonant frequency ω_i is

$$I_{i\pm 1}^{\omega_i} = \frac{V_{bias}^{\omega_i}}{R_{TES,i} + i\omega_i L + (i\omega_i C_{i\pm 1})^{-1}} \approx -i \frac{V_{bias}^{\omega_i}}{2\Delta\omega L} \left(1 + i \frac{R_{TES,i}}{2\Delta\omega L} \right). \quad (2.65)$$

The crosstalk contribution for this term arises from modulations of the bolometer resistance for channel i which induce nearest-neighbor current modulations $\delta I_{i\pm 1}^{\omega_i}$

$$\frac{\delta I_{i\pm 1}^{\omega_i}}{\delta R_{TES,i}} \approx \frac{V_{bias}^{\omega_i}}{(2\Delta\omega L)^2}. \quad (2.66)$$

Comparing to the signal current modulation in channel i

$$\frac{\delta I_i^{\omega_i}}{\delta R_{TES,i}} \approx \frac{V_{bias}^{\omega_i}}{R_{TES,i}^2} \quad (2.67)$$

gives the crosstalk contribution due to bias tone leakage

$$\frac{\delta I_{i\pm 1}^{\omega_i}}{\delta I_i^{\omega_i}} \approx \left| \frac{R_{TES,i}}{2\Delta\omega L} \right|^2. \quad (2.68)$$

Again, using POLARBEAR-2 values for quantities in Equation 2.68, we obtain a crosstalk contribution of $\sim 2.7\%$.

2.5.2 White Noise

In general the readout noise has many contributions, one of which is NEI_{SQUID} and was discussed in Section 2.3.5. Other significant contributions include current and/or voltage noise from amplifiers in the 300 K electronics, and Johnson noise from the 4 K bias resistor. Johnson NEI from resistors in the 300 K electronics and the 4 K bias resistor is not suppressed by ETF like the bolometer NEI. The bias resistor Johnson noise contribution is

$$\text{NEI}_{Johnson,bias} = \frac{\sqrt{k_B T R_{bias}}}{R_{loop}}, \quad (2.69)$$

where R_{loop} is the round-trip series resistance. For POLARBEAR-2 DfMUX $R_{bias} = 30 \text{ m}\Omega$ and $R_{loop} \sim 1.2 \Omega$, yielding $\text{NEI}_{Johnson,bias} = 1.07 \text{ pa}/\sqrt{\text{Hz}}$.

The carrier and noller synthesizers noise contribution is from Johnson, amplifier, DAC, and quantization (i.e. digitization) noise. DAC noise often contains unique spectral content or can be more pink than white over a large band. However, for the DfMUX bandwidth of a few MHz this can be well-approximated as white. Special care has been taken in designing the DfMUX warm electronics to ensure quantization noise is as white as possible by using as much of the ADC's dynamic range as possible in the observation configuration. The NEI referred to the SQUID input coil for the noller chain is simplest, due to the fact that it directly drives current through the input coil, and comes to $4.79 \text{ pA}/\sqrt{\text{Hz}}$. The carrier chain refers a voltage noise (as opposed to a current noise for the noller) across the comb to the SQUID input coil, therefore the NEI of the carrier is dependent on specific circuit values such as the ESR at $f_{0,i}$ and Z_t . On resonance, for 1Ω bolometers, combs

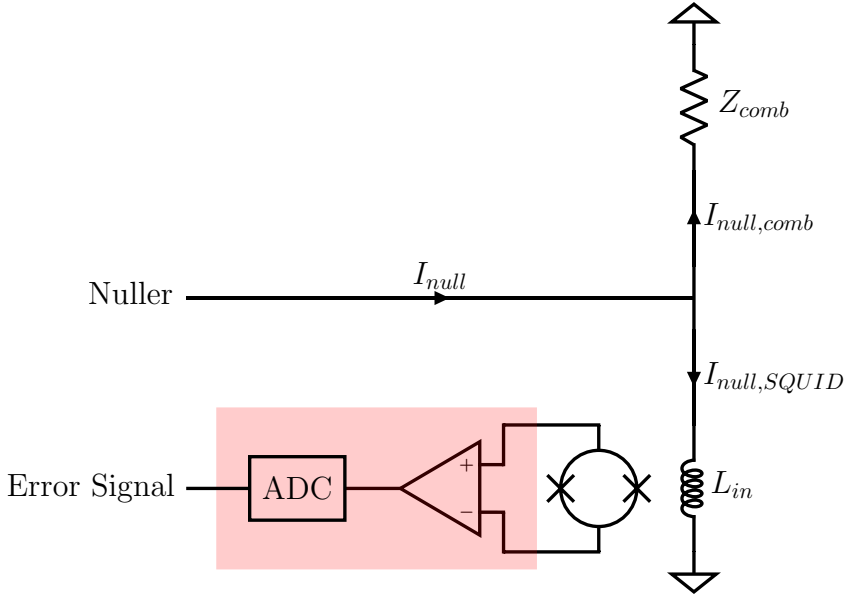


Figure 2.16: Schematic of the current sharing phenomenon in the DfMUX readout system. Any contribution to the error signal as measured by the demodulators which does not correspond to physical currents in the bolometer comb (i.e. due to pickup in the red shaded region) is fed back by DAN and does not cancel with a physical current. This current is then split between the comb and the SQUID input coil, increasing the overall system noise by increasing the bolometer NEI.

with ESR = 0.25 Ω , and a SQUID with $Z_t = 500 \Omega$, the carrier NEI is $4.19 \text{ pA}/\sqrt{\text{Hz}}$ [79].

A final contribution from the warm electronics to the NEI is that of the demodulation chain, which is dominated by the noise of the first stage amplifier. Including the contributions from Johnson and quantization noise for the demodulators results in an NEI (again for a SQUID with $Z_t = 500 \Omega$) of $3.84 \text{ pA}/\sqrt{\text{Hz}}$ [79]. The values for the carrier, nuller, and demodulator noise contribution correspond to the NEI present at the output of the warm electronics, i.e. they do not take into account the transfer function of the cryogenic circuit or any filtering at the cryostat input.

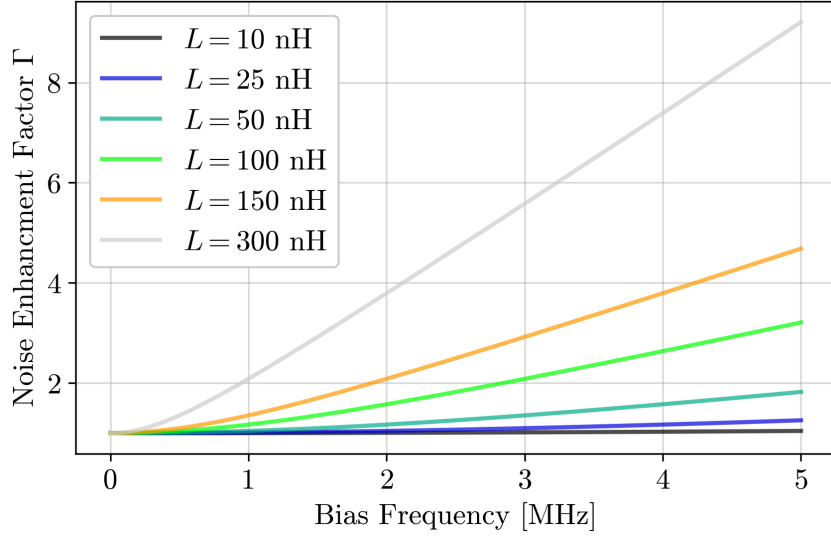


Figure 2.17: Current sharing noise enhancement factor as a function of bias frequency for different values of the equivalent SQUID input inductance L .

2.5.3 Current Sharing

A final significant contribution to the DfMUX noise is due a phenomenon referred to as “current sharing,” in which the error signal measured by the demodulators does not exactly match the real currents flowing through each channel in the comb [80]. The primary mechanism for this discrepancy is due to noise pickup after the SQUID, which is added to the physical error signal. DAN, in an effort to null the measured error signal, then injects the noise signal which cannot cancel with physical currents in the comb. This then splits the injected noise signal between the SQUID input coil and the comb. A simplified schematic of current sharing is shown in Figure 2.16, for which the noise enhancement factor Γ is

$$\Gamma = \frac{\text{NEI}_{eff}}{\text{NEI}} = \frac{|R_{TES} + R_{bias} + i\omega L_{in}^{eff}|}{R_{TES} + R_{bias}}, \quad (2.70)$$

where NEI_{eff} is the enhanced NEI due to current sharing. Here the total equivalent series inductance of the SQUID input coil contains contributions from the traces on the SQUID mounting PCB, i.e. $L_{in}^{eff} = L_{in} + L_{PCB}$. Figure 2.17 shows the value of Γ over the DfMUX bandwidth for different relevant values of L .

Original design of the POLARBEAR-2 DfMUX system implemented the SA4 SQUID design from NIST, which has $L_{in} \sim 300$ nH. Γ ranges from three, to nearly eight across the 1.5 – 4.5 MHz readout band with this device, resulting in unacceptably high readout noise levels when referred to the bolometer input. In Chapter 4 we will discuss efforts to minimize Γ by integrating replacement SQUID designs with much lower L_{in} .

2.6 Overall System Sensitivity

Now, with a proper accounting of all known noise sources, it is possible to estimate the overall sensitivity of a CMB instrument with respect to some key design parameters [51]. The total noise level is a quadrature sum of each individual contribution

$$\text{NEP}_{total}^2 = \text{NEP}_g^2 + \text{NEP}_\gamma^2 + \text{NEP}_{Johnson}^2 + \text{NEP}_{readout}^2 + \text{NEP}_{excess}^2 \quad (2.71)$$

where NEP_{excess} is used to encompass any noise term which is not accounted for in the preceding terms. A variety of phenomena can contribute to NEP_{excess} , including optical loading fluctuations due to changing atmospheric conditions [2], [81], gain variation due to thermal fluctuations both in the warm electronics and at the focal plane, and any

scan-synchronous signals. As discussed in Section 2.2.3, the sensitivity of a well-designed CMB experiment using TES bolometers is dominated by photon noise and scales with the number of detectors.

The most useful expression for the sensitivity of a CMB instrument is not the NEP, rather it is the noise equivalent *temperature* of the CMB (NET_{CMB}) as measured by the instrument. NET_{CMB} essentially describes the variation in on-sky temperature the instrument is able to detect with an SNR of one after integrating for one second. The NET_{CMB} is related to the NEP by

$$\text{NET}_{CMB} = \frac{1}{\sqrt{2}} \frac{\text{NEP}}{dP/dT}. \quad (2.72)$$

dP/dT is calculated from Equation 2.35:

$$\frac{dP_{opt}}{dT_{CMB}} = \eta \Delta\nu k_B \left(\frac{h\nu}{k_B T} \right)^2 n_{occ}^2 e^{h\nu/k_B T}. \quad (2.73)$$

However, as in Section 2.2.3, the Rayleigh-Jeans limit for the CMB allows us to simplify this expression to

$$\frac{dP_{opt}}{dT_{CMB}} \approx \frac{d}{dT_{RJ}} (\eta \Delta\nu k_B T_{RJ}) = \eta \Delta\nu k_B. \quad (2.74)$$

The Rayleigh-Jeans NET (NET_{RJ}) of a CMB instrument observing at a single frequency is then

$$\text{NET}_{RJ} = \frac{\text{NEP}}{2\sqrt{2}k_B\eta\Delta\nu}. \quad (2.75)$$

For an experiment observing at multiple frequencies we must simply calculate the NET_{RJ} of each frequency channel

$$\text{NET}_{RJ} = \sqrt{\sum_i^{n_\nu} \text{NET}_{RJ,i}^2} = \frac{1}{2\sqrt{2}k_B} \sqrt{\sum_i^{n_\nu} \left(\frac{\text{NEP}_i}{\eta_i \Delta\nu_i} \right)^2}, \quad (2.76)$$

where n_ν is the number of observation frequencies and η_i , $\Delta\nu_i$ are the optical efficiency and bandwidth of the i th frequency. This shows that instrument sensitivity increases with the number of observational frequencies (really just the familiar detector-count scaling), optical efficiency η , and optical bandwidth $\Delta\nu$. For truly photon-noise-limited instruments these are the primary avenues for increasing sensitivity as the instrument NEP is bounded below by NEP_γ .

A final quantity of interest in discussing instrumental sensitivity is the mapping speed

$$\text{MS} = \frac{1}{\text{NET}^2}, \quad (2.77)$$

which has units of $\text{K}^2\text{-s}^{-1}$. Where NET applies to an instrument's sensitivity in the map domain, MS instead applies in the C_ℓ power spectrum domain and quantifies the integration time required to measure a power spectrum at a given intensity (e.g. in μK^2). The quadratic dependence on NET should be noted, as small changes in NET can have larger impacts on an experiment's MS and final science products stemming from the C_ℓ which can be measured.

2.7 The Simons Array Experiment



Figure 2.18: Photo of the Simons Array site near Cerro Toco in the Atacama Desert, Chile. The left and right telescopes are the POLARBEAR-2a and -2b instruments respectively. The central telescope currently houses the POLARBEAR-1 instrument and will be retrofitted with the POLARBEAR-2c receiver in 2020. Photo courtesy of Praween Siritanasak.

The current generation of ground-based CMB polarimetry experiments, so-called “third-generation,” are now deploying and beginning routine science observations with $\mathcal{O}(10^4)$ TES bolometers per camera and multi-chroic capabilities. Armed with foreground subtraction and gravitational delensing techniques, the field is poised to impose new, tighter constraints on various cosmological parameters with forthcoming data sets – among them r and $\sum m_\nu$. The Simons Array is one such experiment and is located at 5200 m elevation

in the Chilean Atacama desert. The main science goals of the Simons Array are to place 95% confidence level upper bounds on r being less than 4×10^{-3} and on $\sum m_\nu < 40$ meV. Figure 2.18 shows a picture of the Simons Array site with all three telescopes at the Atacama site.

The Simons Array consists of three off-axis Gregorian-Dragone telescopes (see [51] for a picture) coupled to a POLARBEAR-2 cryogenic receiver. The telescopes have a 2.5 m monolithic primary mirror with a comoving ground shield and continuously rotating half waveplate (HWP) polarization modulators. We refer to the telescopes/receivers as the POLARBEAR-2a (first), -2b (second), and -2c (third) telescope/receivers – all three of which are largely similar to each other in design and construction – with a few key differences/upgrades. The HWP for the POLARBEAR-2a instrument operates at ambient temperature (~ 280 K) and is located directly in front of the receiver window [82], while for POLARBEAR-2b and -2c the HWP is located within the receiver near the Gregorian focus and operates at ~ 50 K to increase the instrument sensitivity [83]. Each of the POLARBEAR-2 receivers are constructed from an “optics tube” and “backend” cryostat. The optics tube contains three reimaging lenses, IR blocking filters, the cryogenic HWP, and a 4 K aperture (lyot) stop. The backend is where the millikelvin refrigerator, focal plane array – constructed from 7,588 optically active TES bolometers operating at 250 mK – and 4 K SQUID pre-amplifiers are housed. Each cryostat has two stages which are cooled to ~ 50 K (primarily a radiation shield stage) and ~ 4 K by their own PT415 mechanical cryocooler.

Currently, POLARBEAR-2a has been deployed to the site and is undergoing system

characterization and calibration before beginning routine CMB science observations. Overall, the system is working well and serves as an excellent proof-of-concept for the optical design of both the POLARBEAR-2 receiver and telescopes. Concurrently, the POLARBEAR-2b receiver is poised to complete lab commissioning testing and will be deployed to the site by the end of 2019. As will be discussed in Section 3, the POLARBEAR-2c backend cryogenic commissioning is complete, and work is underway at the University of California, Berkeley to construct and validate the optics tube for this receiver. Deployment for this third and final Simons Array receiver is expected to occur in 2020.

2.8 Acknowledgments

Figure 2.18 was provided by Praween Siritanasak.

Chapter 3

Design and characterization of the Polarbear-2b and Polarbear-2c cosmic microwave background cryogenic receivers

All of physics is either impossible or trivial.

It is impossible until you understand it

and then it becomes trivial.

— Ernest Rutherford

3.1 Introduction

The current accepted model of our Universe is built on precision measurements of the temperature and polarization anisotropies in the cosmic microwave background (CMB) that

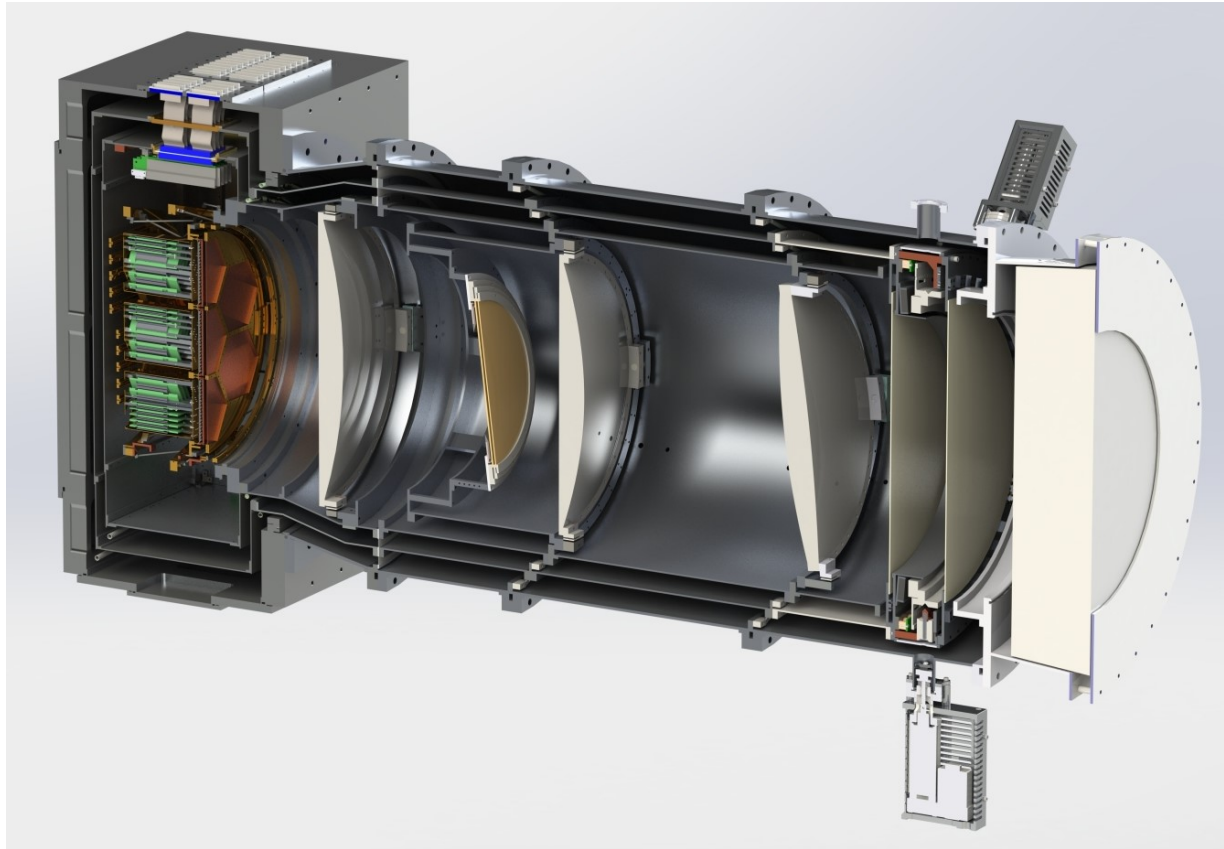


Figure 3.1: Section view of the POLARBEAR-2b receiver CAD model. The optics tube + backend are 2 m long and the diameter of the optics tube 300 K (outermost) shell is 0.75 m. The focal plane tower (FPT) and detector modules (hexagonal structures) are located on the far left inside the rectangular backend. The SQUID pre-amplifiers and wiring harnesses are located just above the focal plane. The optics tube consists of three reimaging lenses (gray, convex circular structures), a cold aperture (yellow circular structure), a vacuum window (thick white, circular structure on far right), IR absorbing filters (thin grey flat circular structures) and a cryogenic half waveplate (between vacuum window and first lens). The protruding elements near the vacuum window are mechanical grippers for the half waveplate sapphire (not shown). Cryogenic refrigerators are not shown.

have been made in the last 30 years. These measurements have revealed that our Universe is both spatially flat and currently Dark Energy-dominated, however the exact physics governing evolution during the earliest times remains a mystery. Measurement of the

polarization properties of the CMB may shed light on the quantum nature of the primordial Universe, and constrain other fundamental parameters responsible for the creation of the large scale structure observed today.

It is commonly held that in order to create our Universe, which is both uniform and isotropic on scales larger than the Hubble time, there must have been a period of exponential expansion driven by a scalar field immediately following the Big Bang. This period of superluminal expansion is called *cosmic inflation* and to date there is no direct evidence that this phenomenon occurred. Cosmic inflation is unique in that it would generate a stochastic background of gravitational waves at large (degree) scales whose amplitudes are proportional to the energy scale of inflation. Recent results in studies of CMB anisotropies [84], [85] have revealed that *B*-mode measurements are critically dependent on foreground subtraction and gravitational de-lensing, especially in efforts to measure the temperature-to-scalar ratio r . Current bounds set $r < 0.06$ [34], indicating the energy scale of inflation is as high as $\sim 10^{16}$ GeV. Detection of inflationary gravitational waves could provide windows into ultra-high energy physics, including grand unified theories.

The Simons Array [13], [86] is a next-generation CMB polarization experiment which upgrades and expands the previous generation POLARBEAR-1 (POLARBEAR-1) experiment [67] to an array of three POLARBEAR-2 receivers – POLARBEAR-2a , -2b, and -2c – mounted on three 2.5 m off-axis Gregorian-Dragone telescopes, each with larger cryogenic receivers and numbers of detectors at multiple observing frequencies. Expanding the number of detectors and observing frequencies – 95 GHz and 150 GHz for POLARBEAR-2a and -2b, and 220 GHz and 270 GHz for -2c – increases sensitivity and enables precise foreground

subtraction and gravitational de-lensing, which are imperative to detect the very low amplitude inflationary B -mode signal. After performing cross-correlations with Planck, the Simons Array will place an upper bound of $r < 4 \times 10^{-3}$ (95% CL).

Both Big Bang Nucleosynthesis and the standard model of particle physics contain neutrinos as critical components but very little is known about their masses. Additionally, Big Bang relic neutrinos are believed to be responsible for the formation of the large-scale gravitational structure in the Universe. By combining measurements of the CMB polarization with the DESI Baryon Acoustic Oscillation (BAO) experiment [87] the Simons Array will constrain the sum of the neutrino masses to $\sum m_\nu \leq 40$ meV (95% CL) and determine if the mass hierarchy is inverted.

3.2 The Polarbear-2 Cryogenic Receiver

Increasing the number of detectors per receiver generally requires increasing the size of the cryostat. While the POLARBEAR-1 receiver consists of a single cryostat for the focal plane, SQUID pre-amplifiers, re-imaging optics, and IR filters, each of the Simons Array's POLARBEAR-2 receivers are constructed from two separate cryostats: the backend and the optics tube. These are fabricated and cryogenically validated separately before integration. A CAD drawing of the full POLARBEAR-2b receiver is shown in Figure 3.1.

Both the backend and the optics tube consist of a 300 K vacuum shell, a 50 K shell, and a 4 K shell, their namesake being derived from their approximate operating temperatures. For both cryostats, the 50 K stage is used to intercept radiative loading

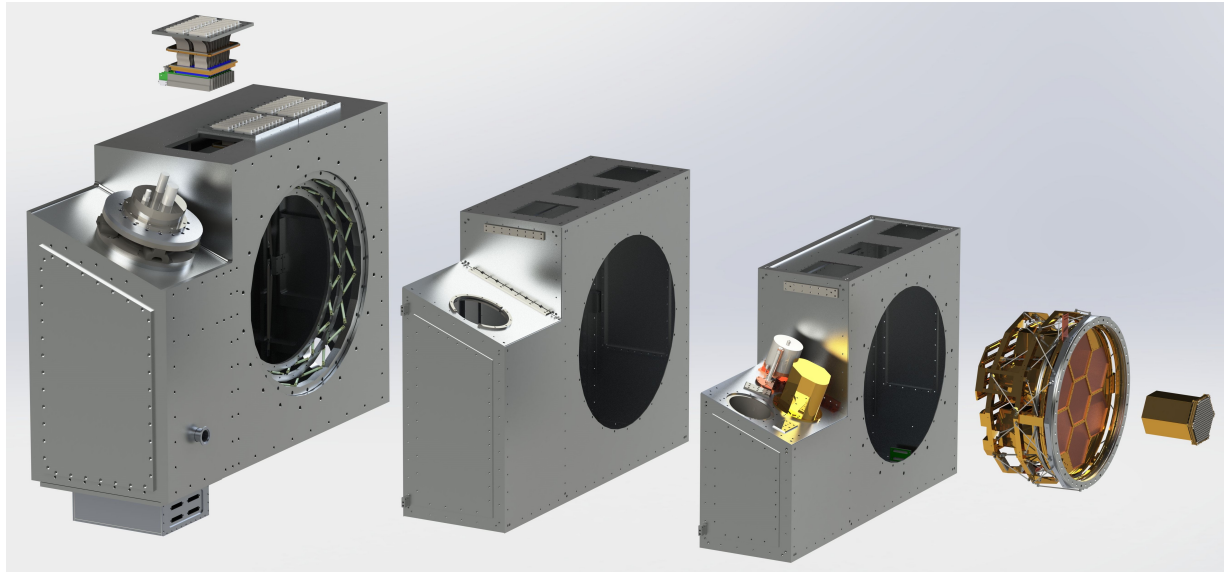


Figure 3.2: Exploded view of the POLARBEAR-2b backend showing (from left to right) the 300 K shell, 50 K shell, 4 K shell, focal plane tower, and one detector module. Also shown exploded from the 300 K shell is one wiring harness. The pulse tube cryocooler is mounted to an anti-vibration bellows on the 300 K shell and the millikelvin refrigerators are mounted to the 4 K shell mainplate (angled portion).

from room temperature. The backend 4 K shell is used to cool the SQUID pre-amplifiers and provide a stage for condensation of helium-4 (He-4), which is essential for reaching millikelvin temperatures, and the optics tube 4 K shell is used to cool the reimaging lenses and cold aperture to reduce optical loading of the TES bolometers (enhancing sensitivity). Cooling of the 50 K and 4 K shells in each cryostat is achieved with two PT415 two-stage mechanical pulse tube cryocoolers (PTCs) from Cryomech Inc.¹ (one each for the backend and optics tube). In addition to the PTC and the 300 K, 50 K, and 4 K shells, the POLARBEAR-2 backend cryostat also contains the detector modules, focal plane tower (FPT), cold readout components, SQUID pre-amplifiers, cryogenic wiring

¹<http://www.cryomech.com/cryorefrigerators/pulse-tube/pt415/>

for detector readout and housekeeping, and millikelvin refrigerator. An exploded view of the POLARBEAR-2b backend is shown in Figure 3.2. The main function of the backend is to create a \sim 250 mK temperature stage where the detector thermal carrier noise is subdominant to the CMB photon noise. It is also important to create a \sim 4 K SQUID stage but this is achieved as a by-product of the cryogenics required to reach millikelvin temperatures (He-4 condensation in the millikelvin refrigerator).

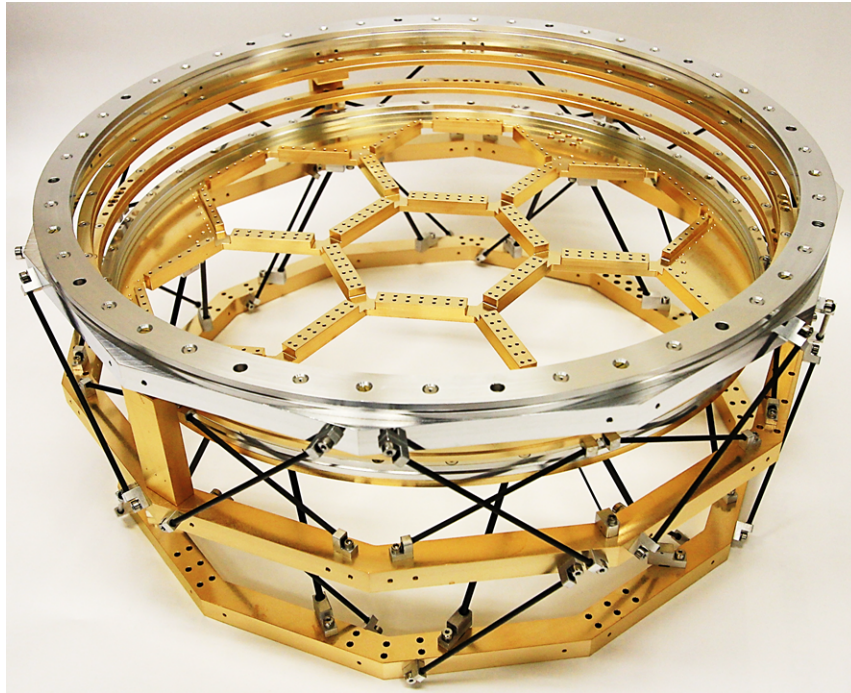


Figure 3.3: Photo of the POLARBEAR-2b FPT which is designed around the He-10 gas light fridge and consists of four thermal stages: 4 K (top silver dodecagonal ring), 1 K (middle gold dodecagonal ring), 350 mK (bottom dodecagonal ring), and 250 mK bolometer stage (circular plate with hexagonal cutouts). The circular rings are the rf shield thermal intercepts. Not shown is the 350 mK MMF stage which is located directly above the detector modules.

The focal plane tower (FPT), shown in Figure 3.3, is a multi-stage thermal isolation structure which is thermally anchored to each substage of the millikelvin fridge and provides

thermal intercepts for the detector wiring and a radio frequency (rf) shield at 4 K, 1 K, 350 mK, and 250 mK. Additionally, there is a 350 mK stage where the final IR low-pass metal mesh filters (MMFs) are located [88]. Thermal isolation of each stage is provided by carbon fiber rods which are epoxied to aluminum 6061 (Al6061) alloy feet using Stycast 2850ft ². The 1 K ring and 350 mK rings are made of Al6061 as opposed to copper to minimize weight and thermal mass while maintaining structural strength. The bolometer stage (250 mK) is made from copper 101 (C101) alloy. The majority of all metal parts, excluding the Al6061 carbon fiber feet, is plated with gold to a thickness of 1.27 μm to reduce emissivity and increase the contact conductance of the heatstraps anchoring each FPT stage to its corresponding millikelvin fridge substage.

Design of the FPT was motivated not only thermally based on results from detailed testing of the POLARBEAR-2b millikelvin refrigerator (Section 3.2.2), but also from a desire to avoid coupling vibrations to the cold stages which can cause microphonic heating during observations. The FPT was designed to be a high-pass filter with its cutoff above that of the backend, which acts as a low-pass filter. This minimizes the vibrational coupling to the FPT millikelvin stages. Lab testing has shown the FPT does behave as a high-pass filter with its cutoff frequency of \sim 80 Hz, while the backend does not perform exactly as a low-pass filter. Rather, the backend has demonstrated broadband vibration rejection excepting 120 Hz (along the receiver z-axis), and 75 Hz (x-axis), although the latter is suspected to be a mode excited in the receiver mounting cart. Microphonic heating has not been observed in laboratory testing near these frequencies with an electromechanical

²<http://na.henkel-adhesives.com/product-search-1554.htm?nodeid=8802688008193>

shaker using vibration amplitudes expected during observation.

3.2.1 50 K and 4 K Refrigeration

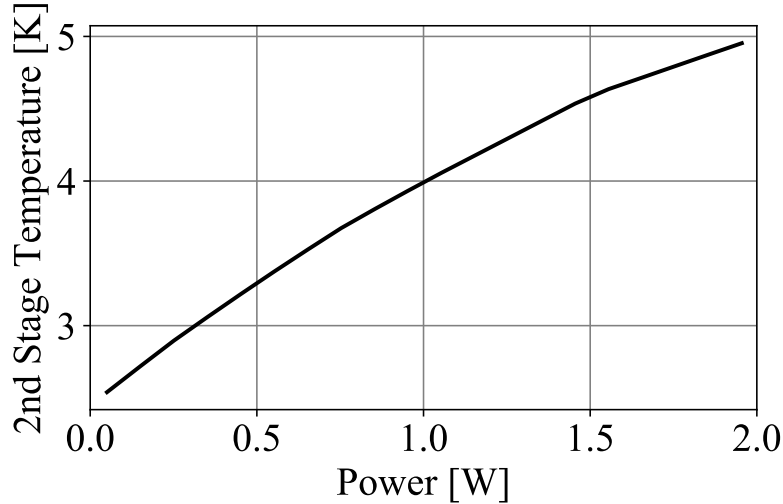


Figure 3.4: Load curve of the POLARBEAR-2b backend PTC second stage with care taken to fully minimize conduction parasitics and radiative loads. The base temperature (0 W applied power) is 2.54 K. All increases in temperature above this zero load configuration are due to increased loading to the coldhead and can be measured absolutely using this curve.

For all cryocoolers there is a relation between the maximum heat load that they can dissipate and their operating temperature, known as a *load curve*, or in a two-parameter space, a *capacity map*. The nominal cooling power of a PT415 is 50 W at 50 K on the first stage coldhead, and 1.5 W at 4 K on the second stage coldhead. Heat loads above (below) these operating points results in higher (lower) system temperatures as can be seen in the load curve of the POLARBEAR-2b backend PT415 second stage shown in Figure 3.4. A measurement of the base temperatures of the PTC stages allows for precise determination of

the loading present. Measurement of the load curve of a PT415 first stage is more difficult but less variable from unit-to-unit, and has been done to high temperatures [89]. Generally, minimizing loading between stages is crucial for basic functionality of the cryostat, while precise optimization of the cryogenics is critically important for creating a high duty cycle receiver with minimal complications in readout and biasing of the detectors. The lowest temperature reached by each stage of the PTC is referred to as the *base temperature*, which is a balance of the PTC cooling capacity and the parasitic loading. For CMB cryogenic receivers the most important base temperature is typically the second stage (for POLARBEAR-2b and -2c this is the 4 K shell), where operation near 3 K is preferred. The primary driver for this target is the He-4 condensation efficiency in the millikelvin refrigerator, which will be discussed in later sections.

3.2.2 Millikelvin Refrigeration

Cooling below 4 K can be achieved using a variety of techniques, including adiabatic demagnetization refrigerators (ADRs), He-3/He-4 dilution refrigerators (DRs), or helium adsorption refrigerators. ADRs are generally avoided in applications requiring SQUIDs due to the strong magnetic fields created by the salt pill. For POLARBEAR-2b and -2c we have opted to use an helium adsorption refrigerator over a DR due to the fact they are an order of magnitude lower in cost, smaller scale, and easier to integrate, maintain, and operate – especially at the high altitude, remote site where the Simons Array is located. The POLARBEAR-2b and -2c adsorption refrigerators are so-called *He-10 gas light* fridges from

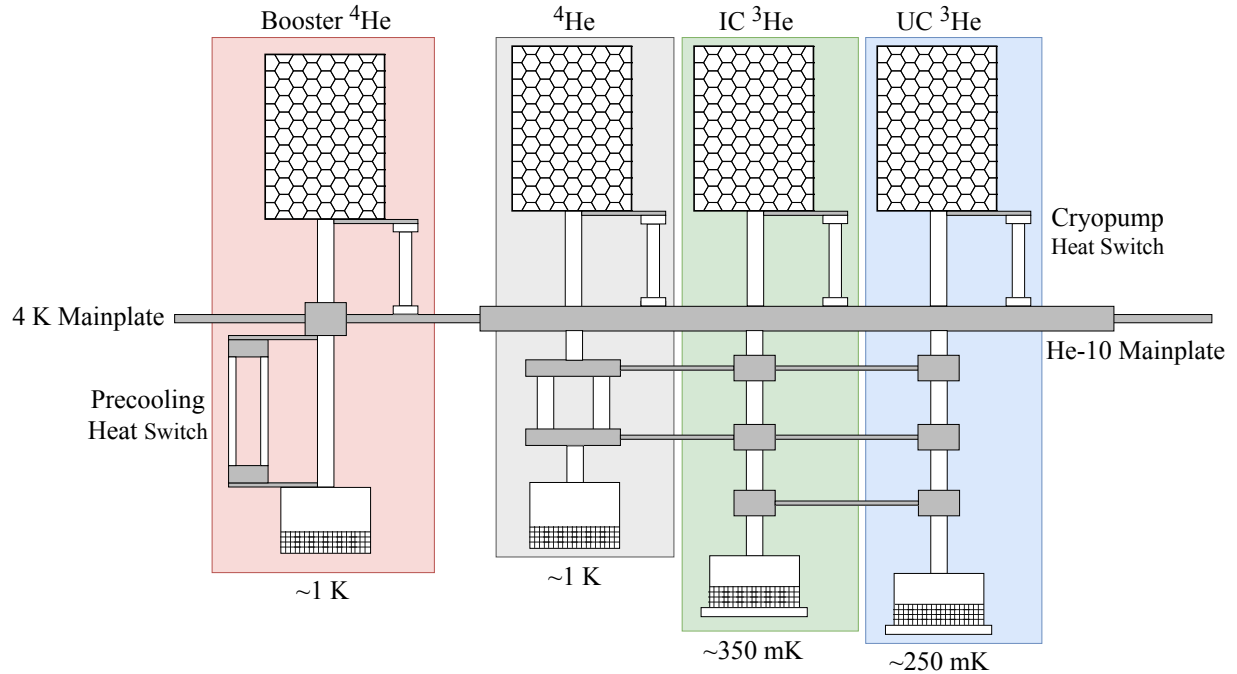


Figure 3.5: Diagram of the POLARBEAR-2b millikelvin fridges. The He-10 gas light is comprised of the gray shaded He-4 stage, the green-shaded *Intercold* (IC) He-3 stage, and blue-shaded *Ultracold* (UC) He-3 stage. These stages share a copper mainplate which is in turn bolted to the mainplate of the 4 K shell. The booster He-4 (red shaded stage) is a standalone fridge used to increase the POLARBEAR-2b hold time. Dark grey shaded components are copper for thermal connections, hexagonal-fill boxes denote the activated charcoal adsorption pumps, and the hatched region on each fridge head denotes the region where liquefied He exists. The He-4 stage of the gas light fridge employs a double-tube architecture which allows convection to more rapidly cool the head and mass attached to it. For the booster He-4 we have employed a similar technology using an external, He-3-charged convective *precooling* heat switch.

Chase Research Cryogenics³, which are comprised of one He-4, and two He-3 adsorption refrigerator stages ($4 + 3 + 3 = 10$), which reach approximate base temperatures of 1 K, 350 mK, and 250 mK respectively. The enabling physics of all adsorption refrigerators is that of evaporative cooling, which relies on liquefying a quantity of He in the evaporator (or *head*) and then pumping on the liquid to facilitate boil-off and lower the bath temperature.

³<http://www.chasecryogenics.com/>

Adsorption refrigerators not only exhibit load curve behavior in relation to their base temperatures, but are also non-continuous (*single-shot*). When the He reservoir expires (i.e. has completely evaporated) the evaporative cooling ceases, at which point the head temperature of the expired stage increases and the He must be re-liquefied (*recycled*). We define the *hold time* of a stage as the time interval during which the fridge operates below a target temperature without expiring. The configuration of the He-10 gas light, shown in Figure 3.5, is such that the coldest stage – the UC head – cannot operate at sufficiently low and constant temperature (i.e. 250 mK) if one of the warmer stages expires first. Thus the practical hold time of a He-10 is determined by the substage with the shortest hold time. For the long exposure observations that Simons Array will conduct [13], [86], it is important to have a hold time which allows for continuous observation for multiple days. The specification for POLARBEAR-2b and -2c is for the sum of the recycling time t_{cycle} and the hold time t_{ht} to be $t_{tot} = t_{cycle} + t_{ht} \geq 72$ hrs (i.e. a three sidereal day schedule). The maximum observation duty cycle from a cryogenic perspective is then t_{ht}/t_{tot} which, for POLARBEAR-2b and -2c, we are targeting >90%. For reference, POLARBEAR-1 demonstrated a typical cryogenic duty cycle of $\sim 70\%$ while operating on a two sidereal day schedule.

Increasing the duty cycle and hold times beyond that of POLARBEAR-1 is challenging due to the fact the POLARBEAR-2 receivers are larger with more detectors and wiring, which increases loading to the fridges. Careful consideration and accurate estimation of these loads is important not only in designing the FPT, but also in determining the amount of He required in each stage to reach the desired hold times and duty cycle. In the following

sections we describe our work towards characterizing the overall recycling efficiency of the POLARBEAR-2b and -2c fridges and their hold times which motivates some of the design of the FPT.

Fridge Cycle Efficiency and Characterization

Cycling an adsorption refrigerator stage is achieved by first applying electrical power and heating the charcoal cryopump to ~ 40 K, at which point all He is desorbed. This allows the gas to come in contact with a cold source (the 4 K mainplate) and condense into the evaporator. Initially the gas will be quite hot in comparison to the mainplate and will initially raise the evaporator temperature above that of the mainplate. As the amount of residual gas in the stage being cycled decreases due to condensation, the evaporator temperature can cool to the mainplate temperature. Once the evaporator is sufficiently cold the cryopump is activated: power is turned off and the heat switch linking the cryopump to the mainplate is energized to cool the cryopump, allowing the He bath to evaporatively cool as the boil-off is collected in the cryopump. We define the condensation point T_{cond} as the temperature of the evaporator before cryopumping is initiated. The amount of He that is liquefied is a function of T_{cond} , which impacts the stage hold time. We define the cycle efficiency, η , of a stage as the fraction of the total He charge which remains liquefied in the evaporator once at base temperature, which is just the condensation efficiency while taking into account the self-cooling loss when cooling to base temperature. The cycle efficiency is thus a function of the mass attached to the fridge and can be computed for each configuration. For the purposes of discussing the performance of the He-10 only we

neglect this correction.

The two isotopes of He condense at different temperatures: 4.23 K for He-4 and 3.19 K for He-3 [90], which is sufficiently cold that it is necessary to use an He-4 stage to condense the gas in an He-3 stage so that η_{He-3} is near unity. Thus, cycling an He-10 gas light fridge first requires cycling the He-4 stage to condense the He-3 in the IC and UC stage, after which the IC and UC cryopumps are cooled. A typical He-10 gas light cycle is shown in Figure 3.15.

A model for η as a function of cryopump temperature T_{CP} and T_{cond} can be developed by treating He as an ideal gas in liquid-vapor equilibrium at every point in the stage [91]. The total number of moles of He the stage has been filled with is

$$n = n_l + n_e + n_t + n_{CP} \quad (3.1)$$

where n_l is the number of moles of liquid, and n_e , n_t , and n_{CP} the number of gaseous moles in the evaporator, tube and cryopump respectively. Applying the ideal gas law gives

$$n_l = \frac{n - n_t - \frac{p}{R} \left(\frac{V_e}{T_e} + \frac{V_{CP}}{T_{CP}} \right)}{1 - (p\tilde{V}/RT_e)} \quad (3.2)$$

with subscripts as in Equation (3.1), p the overall system pressure (constant everywhere in the stage), R the ideal gas constant, V_i the volumes corresponding to subscripts i , and \tilde{V} the He molar volume. Due to the gradient at location z along the tube between the

evaporator and the cryopump, the number of moles in the tube is

$$n_t = \frac{p}{R} \pi r^2 \int_0^L \frac{dz}{T(z)} \quad (3.3)$$

where r is the tube radius and $T(z)$ is the temperature in the tube at location z . For our fridges, the volume of the tubes is small and we find that n_t/n is less than 0.5% so we can neglect this in calculating η . To cool n moles of liquid a temperature dT requires evaporation of dn moles, i.e.

$$nC(T)dT = L(T)dn, \quad (3.4)$$

where $C(T)$ and $L(T)$ are the specific heat and latent heat of the liquid at temperature T . The final number of moles of liquid remaining n , after starting with n_0 initial moles and cooling the head from temperatures $T_{cond} = T_e$ to T_{base} is

$$n = n_0 \exp \int_{T_e}^{T_{base}} \frac{C(T)}{L(T)} dT. \quad (3.5)$$

Although η predicted by this model is insensitive to pump temperatures over ~ 20 K during condensation, in the laboratory it is necessary to heat the pumps to 45 K before any effect on η is negligible. Results of this model are shown in Figure 3.6 for the standard He-10 gas light. It is evident that achieving $\eta_{He-3} \sim 100\%$ is relatively easy given a typical condensation point of 1.2 K, while a typical η_{He-4} will be 70% in the POLARBEAR-2b and -2c backends due to the fact that the condensation temperature is bounded below by the

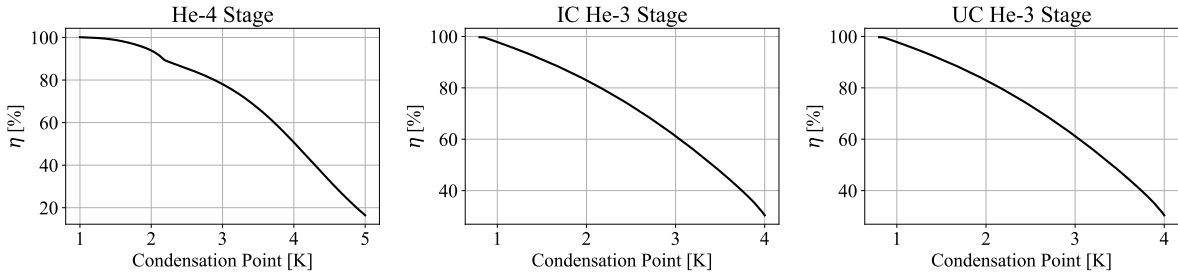


Figure 3.6: Cycle efficiencies of each stage of the standard He-10 gas light fridge for stage operating base temperatures of 850 mK (He-4), 350 mK (IC He-3), and 250 mK (UC He-3). As the condensation temperature nears the stage base temperature the self-cooling loss becomes negligible and η approaches 100%.

4 K mainplate temperature of $3.2 - 3.3$ K.

Millikelvin Fridge Characterization

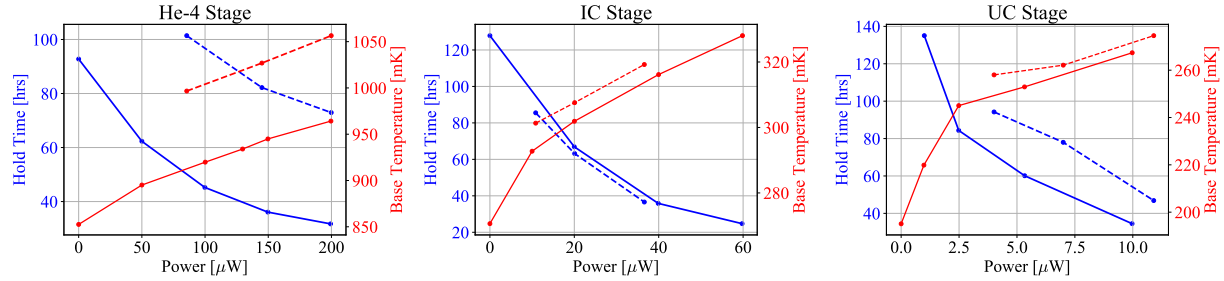


Figure 3.7: Hold times and base temperatures for the POLARBEAR-2b (solid lines) and -2c (dashed lines) He-10 fridges. These results indicate that – for the loading specification of 150 μW , 20 μW , and 5 μW on the He-4, IC, and UC stages respectively – the expected hold times of POLARBEAR-2b (-2c) are 36 (81), 63 (61), and 67 (78) hrs for the He-4, IC, and UC stages respectively. These specifications are over-estimated and we expect to be able to reduce the IC and UC loading sufficiently to allow a 72 hr cycle for POLARBEAR-2b . The POLARBEAR-2c gas light is similarly limited by the IC stage to 61 hrs but reduction of the load to this stage quickly allows t_{ht} to exceed 72 hrs.

For POLARBEAR-2b we chose to purchase the standard model He-10 gas light before millikelvin hardware was finalized so detailed thermal loading estimates did not yet exist. As a rough baseline the specifications for the POLARBEAR-2b millikelvin loads were defined

to be $150 \mu\text{W}$ to the 1 K (He-4) stage, $20 \mu\text{W}$ to the 350 mK (IC) stage, and $5 \mu\text{W}$ to the 250 mK (UC) stage. In order to help inform the design of the FPT we fully characterized this fridge by measuring the load curve and hold times of each stage with no mass attached and no optical loading, as shown in Figure 3.7. With $150 \mu\text{W}$, $20 \mu\text{W}$, and $5 \mu\text{W}$ of loading to the He-4, IC, and UC stages the hold times are 36 hrs, 67 hrs, and 63 hrs – i.e. the practical hold time is 36 hrs and limited by the He-4 stage, which is far below our three sidereal day requirement. Our solution is to install a second standalone He-4 *booster fridge* which meets the hold time requirement. A CAD rendering of the booster fridge is shown in Figure 3.8. In the new POLARBEAR-2b configuration the gas light He-4 stage is left unattached to the FPT and is used only as a buffer for the IC and UC stages, which reduces its loading to less than $1 \mu\text{W}$ from radiation. Instead, the booster fridge is used to intercept all of the loading incident on the 1 K FPT stage. Owing to the fact that the hold time of the booster fridge is designed to be multiple days, we chose only to verify that it met specifications before integrating in the POLARBEAR-2b backend so detailed load curve and hold time measurements have not been made.

The booster fridge is charged with 1.3 moles of He-4, has an operating temperature of 936 mK with $150 \mu\text{W}$ of loading applied, and demonstrated a hold time of 73 hrs when cycled with a condensation point of 3.7 K in a bare, dark environment. For POLARBEAR-2c, because the fridge had not already been purchased, we used the He-10 and booster characterization to inform design and fabrication of a custom super gas light (SGL) He-10 from Chase Research Cryogenics. The SGL is an oversized version of the standard gas light He-10 with a larger amount of He-4 and UC He-3 in order to bring the hold time up to

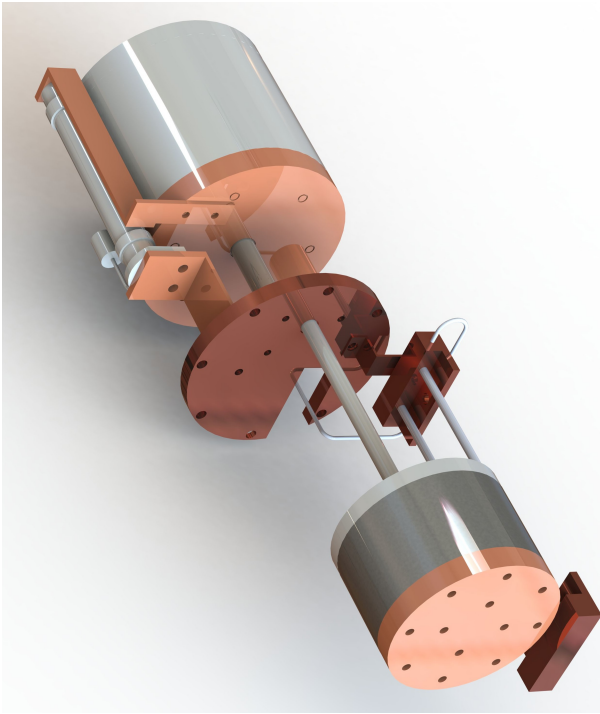


Figure 3.8: CAD image of the booster He-4 fridge with the cryopump in the upper left corner and the head in the lower right. The precooling heatswitch can be seen to the right of the booster head.

72 hrs in a single fridge. Results from the characterization of the POLARBEAR-2c SGL are shown in Figure 3.7.

3.2.3 Thermal Loading Estimates

50 K and 4 K Loading

Modeling thermal loading is important for cryostat design and validation to ensure proper functionality in reaching desired base temperatures. After evacuating the cryostat to $\sim 10^{-8}$ Bar there is only conductive loading – from the mechanical G-10CR shell supports and wiring – and radiative loading. The heat load \dot{Q} on stage 1 due to stage 2 via conduction

of one element is

$$\dot{Q}_c = \frac{A}{l} \int_{T_1}^{T_2} \kappa(T) \, dT, \quad (3.6)$$

where T_1 and T_2 are the temperatures of the stages, and A is the cross-sectional area, l the length, and $\kappa(T)$ the thermal conductivity of the element connecting the stages.

Table 3.1 details the source and contribution of each load to the 50 K and 4 K stages in the POLARBEAR-2b and -2c backends. Readout and housekeeping wiring from 300 K to 4 K is polyimide-clad, 127 μm diameter manganin alloy. Housekeeping wiring from 4 K to 250 mK is polyimide-clad, 127 μm diameter niobium-titanium (NbTi) alloy. Readout wiring from 4 K to 250 mK is a polyimide-NbTi superconducting stripline specially developed for the readout system employed in the POLARBEAR-2 and SPT-3G receivers [92], which will be discussed in Section 3.2.3.

The radiative heat transfer between two bodies at temperatures T_1 and T_2 with areas A_1 and A_2 , and emissivities ϵ_1 and ϵ_2 is

$$\dot{Q}_{rad} = \frac{\sigma(T_1^4 - T_2^4)}{(1 - \epsilon_1)/(A_1 \epsilon_1) + 1/(A_1 F_{1 \rightarrow 2}) + (1 - \epsilon_2)/(A_2 \epsilon_2)} \quad (3.7)$$

where $F_{1 \rightarrow 2}$ is the *viewing factor* for body 1 and 2 [93]. For two large parallel plates, as in the backend cryostats, $F_{1 \rightarrow 2} = 1$. Using Equation (3.7) we can quickly calculate for the POLARBEAR-2 backend cryostats (with $A_{300\text{ K}} = 3.67\text{ m}^2$, $A_{50\text{ K}} = 2.81\text{ m}^2$) which are made from unpolished aluminum with $\epsilon_1 = \epsilon_2 = 0.12$, the radiation load to 50 K is in excess of 85 W. This would overwhelm the cooling capacity of the PT415 first stage, which necessitates mitigation of the radiative load. While the calculation for the second stage

Table 3.1: Summary of the 50 K and 4 K conductive loads in the POLARBEAR-2b and -2c backends. A is the cross sectional area of one loading component. N is the number of components of each type at each stage. The integrated conductivities are calculated using interpolants of available measured data for each material.

Stage	Load Source	N	A [m 2]	$\int \kappa(T) dT$ [W·m]	l [m]	Load [W]
50 K	Long G-10 Supports	6	2.68×10^{-5}	97	0.22	0.07
50 K	Short G-10 Supports	24	1.18×10^{-5}	97	0.047	0.59
50 K	Readout Wiring	2160	1.27×10^{-8}	3950	0.057	1.9
50 K	Housekeeping Wiring	102	1.27×10^{-8}	3950	0.10	0.051
4 K	Long G-10 Supports	6	2.68×10^{-5}	8.6	0.22	0.0053
4 K	Short G-10 Supports	24	1.18×10^{-5}	8.6	0.047	0.11
4 K	Readout Wiring	2160	1.27×10^{-8}	258	0.049	0.14
4 K	Housekeeping Wiring	102	1.27×10^{-8}	258	0.070	0.0044
50 K Total						2.6
4 K Total						0.26

yields 0.056 W and is within the second stage capacity, it is beneficial to reduce loading as much as possible. This further lowers the 4 K mainplate and assists in the endeavor of maximizing η_{He-4} .

Mitigation of radiative loading can be achieved by wrapping the 50 K and 4 K shells in multilayer insulation (MLI) blankets which reduces the effective emissivity of the shells. For POLARBEAR-2b and -2c we chose the Coolcat 2 NW MLI from Ruag⁴, which is constructed from many sheets of double-sided, aluminized (40 nm aluminum thickness on each side) polyester foil with non-woven polyester spacers between adjacent layers (used to reduce conduction between adjacent layers). The full blankets are comprised of multiple stacks of 10-layer blankets which are cut precisely using a laser. The cutting process also bonds each stack by melting the polyester spacers along the laser path. For POLARBEAR-2b and -2c there are 50 layers at 50 K and 20 layers at 4 K.

MLI reduces radiative loading due to the fact that each internal layer of MLI acts roughly as an isolated radiation shield in radiative equilibrium with its neighbors, with the innermost layer isothermal with the shell it encloses. This would suggest that MLI reduces loading by a factor that is proportional to the inverse of the number of layers. However, this does not take into account conduction between layers or from the interstitial gas, and other nonidealities. Depending on the configuration, i.e. how many edges and seams are required and whether the MLI layers are tightly constrained or allowed to expand, the actual performance of the MLI can be multiple orders of magnitude worse

⁴<https://www.ruag.com/en/products-services/space/spacecraft/thermal-systems/cryogenic-thermal-insulation-coolcat>

than expected from models built from first principles. To address this, numerous empirical models have been developed to account for these nonidealities [94]. Of these we have chosen the commonly-used Keller model [95], which gives the heat load per unit area as a sum of the radiative flux

$$\dot{Q}_{rad} = \frac{AC_r\epsilon}{N_l}(T_h - T_c), \quad (3.8)$$

the contact conduction between layers

$$\dot{Q}_{c,MLI} = \frac{AC_s\tilde{N}_l^{n_s}T_m}{N_l + 1}(T_h - T_c), \quad (3.9)$$

and conduction from the interstitial gas

$$\dot{Q}_{gas} = \frac{AC_g p_{int}(T_h^{m+1} - T_c^{m+1})}{N_l}. \quad (3.10)$$

A is the area of the cold shell, N_l is the number of layers, \tilde{N}_l is the layer density, $T_m = (T_h - T_c)/2$, and p_{int} is the interstitial gas pressure. C_r , C_s , and n_s , are parameters dependent on the material and construction of the blankets, and C_g and m are parameters that depend on which gases are present. For our modeling we will consider two contributions of the interstitial mode between 300 K and 50 K: He and N₂. The POLARBEAR-2b and -2c MLI layers have perforations, with a total open area of 0.5-1%, to help minimize p_{int} . In more complicated geometries with many edges and seams, p_{int} can still be multiple orders of magnitude larger than the vacuum vessel pressure and thus \dot{Q}_{gas} can be significant. The interstitial pressures in Table 3.2 reflect the POLARBEAR-2b best-fit values after cryogenic

validation from the residual load determined from the PTC capacity map after subtracting \dot{Q}_c (Table 3.1), \dot{Q}_{rad} and $\dot{Q}_{c,MLI}$. We will discuss this further in Section 3.3.3.

Millikelvin Loading

As with the thermal loads on the PTC thermal intercepts, the loads on the millikelvin refrigerator may be divided into conductive loads and radiative loads. Three components contribute to the millikelvin conductive loading: the mechanical supports in the FPT, the readout cables, and the rf shield. By design, thermal radiation from elements internal to the cryostat is negligible, but radiation from the atmosphere that passes through the telescope optical chain is incident on various millikelvin components and contributes non-negligible loading.

The supports of the FPT are a combination of pultruded carbon fiber tubes manufactured by vDijk Pultrusion Products^{* 5} (DPP) and rods of the commonly used Graphlite pultruded carbon fiber. The cryogenic thermal conductivity of Graphlite has been well-measured [96], [97], but that of DPP was not known at the time of design. To verify this material, measurements of thermal conductivity along the tube axis were performed in the desired temperature range. Known amounts of power P_{app} were applied to one end of a sample and the resulting equilibrium temperature T_{high} was measured, while the other end was fixed at a base temperature T_{low} (see Figure 3.9 for a schematic). The thermal

⁵<http://www.dpp-pultrusion.com/>

Table 3.2: Summary of the values used in the application of the Keller model to the POLARBEAR-2b and -2c backend cryostats. The units of all parameters are such that the final units of each \dot{Q} are [W]. Values not in parentheses are for He and in parenthesis are for N_2 .

	A [m^2]	N_l	$C_r \times 10^{10}$	$C_s \times 10^8$	\tilde{N}_l [cm^{-1}]	n_s	$C_g \times 10^{-4}$	m	p_{int} [mBar]
50 K	2.81	50	7.07	7.30	25	2.63	4.89 (1.40)	-0.74 (-0.48)	2.6×10^{-5}
4 K	2.19	20	7.07	7.30	20	2.63	4.89 (1.46)	-0.74 (-0.48)	1.2×10^{-8}

Table 3.3: MLI contribution to the POLARBEAR-2b backend loading at 50 K and 4 K. This is the effective radiation load in the presence of the POLARBEAR-2b MLI. The sum of \dot{Q}_{rad} , $\dot{Q}_{c,MLI}$, and \dot{Q}_{gas} provides the effective radiative load after installing the MLI.

	\dot{Q}_{rad} [W]	$\dot{Q}_{c,MLI}$ [W]	\dot{Q}_{gas} [W]
50 K	1.58	0.564	36.1
4 K	7.98×10^{-4}	2.12×10^{-2}	1.88×10^{-2}

conductivity of DPP was found to be well approximated by a power law

$$\kappa(T) = \alpha T^\beta, \quad (3.11)$$

and the coefficient α and index β were obtained by fitting to Equation (3.6). Due to cooling power limitations of the adsorption fridge used for testing, measurements were performed with $T_{low} \sim 300$ mK from a single-shot He-3 adsorption refrigerator, and separately with $T_{low} \sim 1.2$ K from pumped liquid He-4. The best fit in the 0.25 K–2 K range is $\kappa_{DPP}(T) = 4.17 T^{1.21}$ mW/m·K, and the best fit in the 1.4 K–4.5 K range is $\kappa_{DPP}(T) = 7.59 T^{0.61}$ mW/m·K.

The readout cables are fabricated from a custom stack-up of polyimide, superconducting NbTi, photoresist, and adhesive layers. Although cryogenic thermal conductivities of polyimides and NbTi have been measured [98], [99], building an accurate thermal model of the combined cable is subject to large errors due to uncertainty in the properties of the remaining materials. Thus, a measurement of the cryogenic thermal conductivity of the readout cables was performed in a manner similar to that described above. Since the cables

are flexible, they were held taut and clamped on opposite sides at T_{low} , while a central clamp with a heater and thermometer was used to apply power (see Figure 3.9). As the cross-sectional area of the cables is fixed but the distance between thermal intercepts in the POLARBEAR-2 backends is not, the relevant quantity of interest is the thermal conductance per unit length, G/L . The best fit in the 0.25 K–1.5 K range is $G/L = 7.1 T^{1.79} \mu\text{W}/\text{mm}\cdot\text{K}$, and the best fit in the 1.4 K–6 K range is $G/L = 9.3 T^{1.05} \mu\text{W}\cdot\text{mm}/\text{K}$.

The rf shield is comprised of 300 Å of aluminum deposited on a 6.35 μm sheet of polyethylene terephthalate. The strong dependence of the cryogenic thermal conductivity of aluminum films on their purity motivated a measurement of a sample of the rf shield in a manner similar to that of the readout cables. Due to the sample’s long time constant for equilibration and fridge hold time limitations, measurements were only performed in the 1.4 K–6 K range. Since the thermal conductivity will decrease more strongly below the critical temperature of the aluminum film, extrapolating measurements from this range provides an overly pessimistic estimate of the thermal loads at colder temperatures. Moreover, as the rf shield extends radially as well as vertically away from the focal plane, the relevant quantity of interest is the thermal conductance multiplied by the thickness d of the shield, κd . The measured best fit is $\kappa d = 33.5 T^{1.41} \text{nW}/\text{K}$.

Optical loads which contribute to the thermal loading of the adsorption fridge include out-of-band radiation absorbed by the 350 mK metal mesh filter and in-band radiation absorbed by emissive lenslets on the focal plane. The particular estimation of these loads depends on the specifics of the optical design (and therefore differ for POLARBEAR-2b and -2c), which will be detailed in an upcoming publication. For the purposes of estimating the

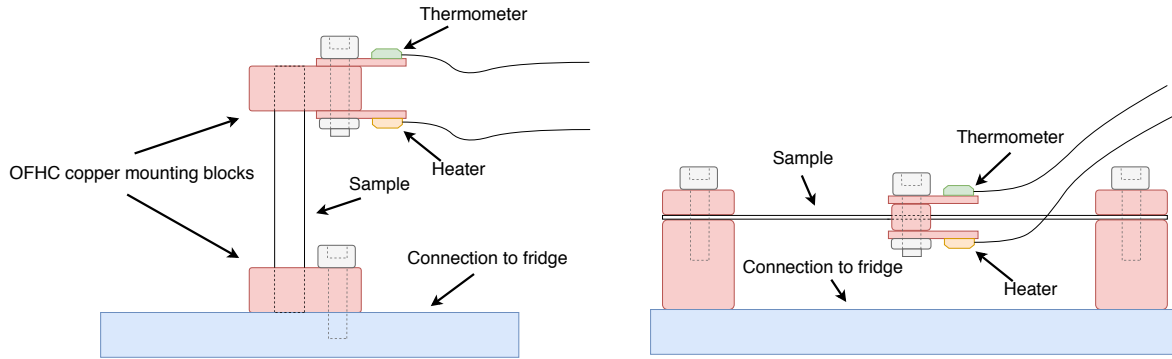


Figure 3.9: Schematic of the setup for low temperature thermal conductivity measurements with rigid (*left*) and flexible (*right*) materials. When necessary to reduce parasitic thermal loads on the sample, samples were also enclosed in a radiation shield.

thermal budget, conservative upper limits are quoted here.

A summary of the expected thermal loads on the He-10 fridge substages is given in Table 3.4. All conductive loads were calculated according to Equation (3.6) with known geometries and with temperatures measured from a cooldown with realistic thermal loads applied to each fridge intercept via resistive heaters.

3.3 Commissioning the Polarbear-2b and -2c Backends

We chose to construct and validate the POLARBEAR-2b and -2c backends in series with essentially no changes in design or construction, excepting the SGL He-10 fridge specifically designed to have increased hold times beyond that of the POLARBEAR-2b standard gas light He-10. Apart from this, cryogenic performance for the two backends is similar so the majority of the data shown in the following sections is only for the

Table 3.4: Projected thermal loads in μW on the fridge intercepts for POLARBEAR-2b
 (POLARBEAR-2c).

	Mechanical supports	Readout cables	rf shield	Radiation	Total
He-4 stage	13.8	40.6	21.3	0 (0)	76.1 (76.1)
IC stage	0.8	1.8	0.9	<4.8 (<6.7)	<8.3 (<10.2)
UC stage	0.3	0.1	0.1	<1.7 (<3.5)	<2.0 (<3.8)

POLARBEAR-2b backend.

3.3.1 50 K and 4 K Shell Construction

The POLARBEAR-2b and -2c 50 K and 4 K shells are constructed from aluminum 1100 (Al1100) alloy panels which are 3 mm and 4 mm thick respectively. These panels are bolted to an Al6061 alloy frame with Apiezon N grease between the panels and the frame at 4 K (no interface material exists at 50 K). This is an acceptable construction at 4 K in the limit that the only load that needs to be transferred to the PTC is the relatively small radiative load. In order to both minimize thermal gradients across the panels and preserve a lightweight construction, the conductance of the panels was augmented with very high purity metal ribbons.

Aluminum is a good choice for both 50 K and 4 K temperature ranges due to the fact that its thermal conductivity can be $\sim 10^4$ W/m·K or higher [100]. 75 mm \times 0.5 mm 99.9998% purity (6N) aluminum ribbons were annealed in an N₂ environment at 300 °C for 8 hours and were attached to the panels using Stycast 2850ft epoxy. For the front, rear, and bottom panels we placed ribbons only along the edges on one side. For the top, mainplate, and trapezoidal panel (seen in Figure 3.2 between the mainplate and top panels) we chose to cover the entire surface of both sides in 6N ribbons. Initial stress testing via rapid thermal cycling from 300 K to 77 K revealed that surface preparation is critical to ensure a robust, high quality thermal connection between the Al1100 panel and the 6N aluminum. In order to create the best quality interface, both the panels and ribbons were

first roughened using 60-grit sandpaper, then a toluene-based epoxy adhesion-promoter⁶ was applied, after which the epoxy (prepared with catalyst 9⁷) was applied to the panel, and then the 6N ribbon.

We chose to use an initially thick layer of epoxy (~ 2 mm) and apply an even pressure of ~ 10 kPa along the ribbon to ensure complete coverage and adhesion while keeping the epoxy layer thin by forcing out the excess. These epoxy interfaces were cured at room temperature for 24 hrs with the 10 kPa pressure applied, after which the final epoxy thickness is consistently 0.5 mm. Attaching 6N aluminum ribbons lowers thermal gradients across the shell panels to their practical minima for the geometries in the POLARBEAR-2b and -2c backends. The remaining gradients between the coldheads and shell sections are subsequently dominated by the thermal interface resistance between the panels, and the Al6061 frame and its lower conductivity. However, the small radiation and G-10CR conduction heat loads, and large parallel heat path at these interfaces means these gradients are typically about 0.5 K or less.

For the large conductive load from the SQUID wiring harnesses it is necessary to implement a more carefully engineered solution with special consideration given to the interfaces between perpendicular panels. This is especially important because the performance of the SQUID pre-amplifiers is highly temperature dependent. Avoiding local hotspots due to the wiring harness load and creating the coldest stage possible minimizes complications in readout of the focal plane and increases mapping speed. In order to more

⁶<https://www.lord.com/products-and-solutions/chemlok-ap-134-primer>

⁷<http://na.henkel-adhesives.com/product-search-1554.htm?nodeid=8797863247873>

effectively transmit the wiring harness load across the two shell interfaces between the top panels and the shell mainplates, we completely covered these panels on both sides in the 6N aluminum ribbons and have added extra length. These lengths are then clamped to the adjacent panel using stainless steel M5 screws, washer/nut plates, and split ring lock washers. Screws are tightened to $\sim 80\%$ their yield stress. At the interface between the 4 K mainplate and the trapezoid panel there is not enough space to accommodate this solution so we have implemented a C101 L-bracket instead of the clamped overhanging 6N ribbons.

3.3.2 Heatstraps

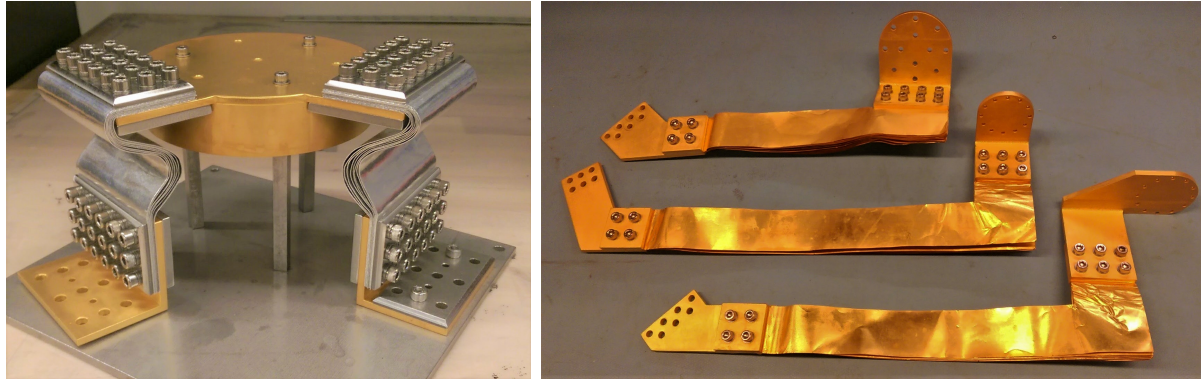


Figure 3.10: (*Left*) The POLARBEAR-2b mainplate-coldhead heatstrap consists of two sets of eight 75 mm \times 160 mm 6N aluminum ribbons which are clamped to gold-plated C101 adapters on each end. Each clamped interface uses 24 M5 stainless steel screws and split-ring lock washers with stainless steel pressure-spreading *washer plates* and *nut plates*, and no thermal interface material. (*Right*) The POLARBEAR-2b millikelvin heatstraps after gold-plating. Pressure is applied to the FPT stages using 10-32 screws and the same washer and nut plate method as the 4 K mainplate-coldhead heatstrap, and to the millikelvin fridge heads using brass 4-40 screws with serrated Belleville washers.

One of the most important components of any large cryostat is the heatstrap connecting the PTC to the mainplates because it must pass the entire stage's loading.

It is rarely possible to directly mount critical components to the coldheads so the lowest temperature presented to the He-10 fridge and SQUIDs is correspondingly above the PTC base temperature. For the POLARBEAR-2b and -2c backends the 50 K mainplate-coldhead heatstrap is less critical because the main function of the 50 K shell is as a radiation buffer and an adequate base temperature of the 4 K shell is relatively insensitive to a mean 50 K shell temperature drift of ± 10 K. The 50 K mainplate-coldhead heatstrap is simply constructed of six stacks of eight 20 mm \times 80 mm pieces of 6N aluminum ribbons which are clamped to the PTC coldhead and 50 K mainplate. This implementation does not optimize the surface area or interfaces of the thermal connection. The 4 K mainplate-coldhead heatstrap (Figure 3.10) is more carefully designed in order to minimize the thermal contact resistance between the coldhead and mainplate. While using 6N aluminum is advantageous due to its high bulk conductivity at 4 K (higher than that of C101 when the 6N is annealed), there is significant concern in accessing this due to the robust aluminum oxide which rapidly forms at room temperature in atmospheric conditions [101]. This problem is exacerbated when multiple 6N-6N interfaces are present. Our solution is to prepare the joints with very high bolt force in order to fracture the oxide and to deform the soft 6N aluminum (enhances the effective cross sectional area of the joint). We do not disassemble these interfaces so as to avoid re-oxidation. Rather, the interface which is disassembled is the gold-plated copper interface to the coldhead and mainplate.

Due to the fact that the thermal interface (Kapitza) resistance [102] scales as T^{-3} we have paid special attention to optimizing the conductance of the millikelvin heatstraps by minimizing the number of bolted interfaces [103], [104]. Of additional concern is the

potential for vibrations coupling to millikelvin stages which can cause microphonic heating and is deleterious to the millikelvin base temperatures. The POLARBEAR-2b and -2c millikelvin heatstraps are constructed from C101 feet, that bolt to the fridge heads and FPT stages and have 15 layers of 0.1 mm thick C101 copper ribbons bolted between C101 pressure plates and the feet. These ribbons are then welded along the edges so there is a bulk thermal connection to the feet in addition to the contact interface of each ribbon. A picture of the POLARBEAR-2b millikelvin heatstraps is shown in Figure 3.10. As will be mentioned in Section 3.3.4, we have reason to believe the conductance of these heatstraps is limited by the thermal interface resistance between the feet and the FPT and He-10 stages.

3.3.3 50 K and 4 K Cryogenic Validation

To first-order, cryogenic validation of the POLARBEAR-2b and -2c backend 50 K and 4 K stages simply entails ensuring that an acceptable base temperature is reached; i.e. ~ 50 K and ~ 3.5 K. However, encompassed in this is a careful accounting of the observed thermal loads and a comparison with the model to ensure significant spurious loads are not observed. Additionally we require that thermal time constants are low enough that egregiously long cooldown times are not observed, but this is generally solved in tandem with the optimization of thermal gradients as $\tau_{thermal} \sim G^{-1/2}$ where G is the thermal conductance linking a body to the cold source.

For the POLARBEAR-2b backend, cryogenic validation was done in two cooldowns. The first cooldown (run01b) was started on August 23rd, 2016, without any of the three wiring harnesses in order to measure the 4 K load curve, 50 K base temperature, and

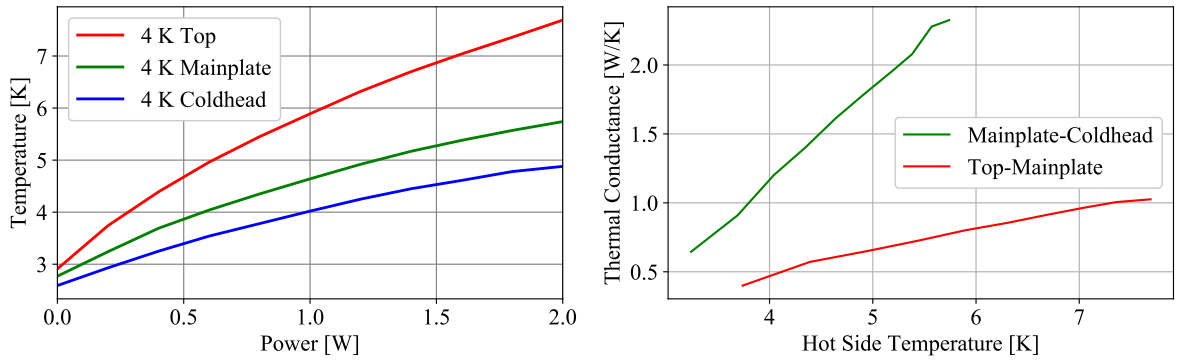


Figure 3.11: (Left) Load curve taken in the first run of the POLARBEAR-2b backend using a heater on the top panel. (Right) Measured thermal conductance of the mainplate-coldhead and the top-mainplate heatstrap.

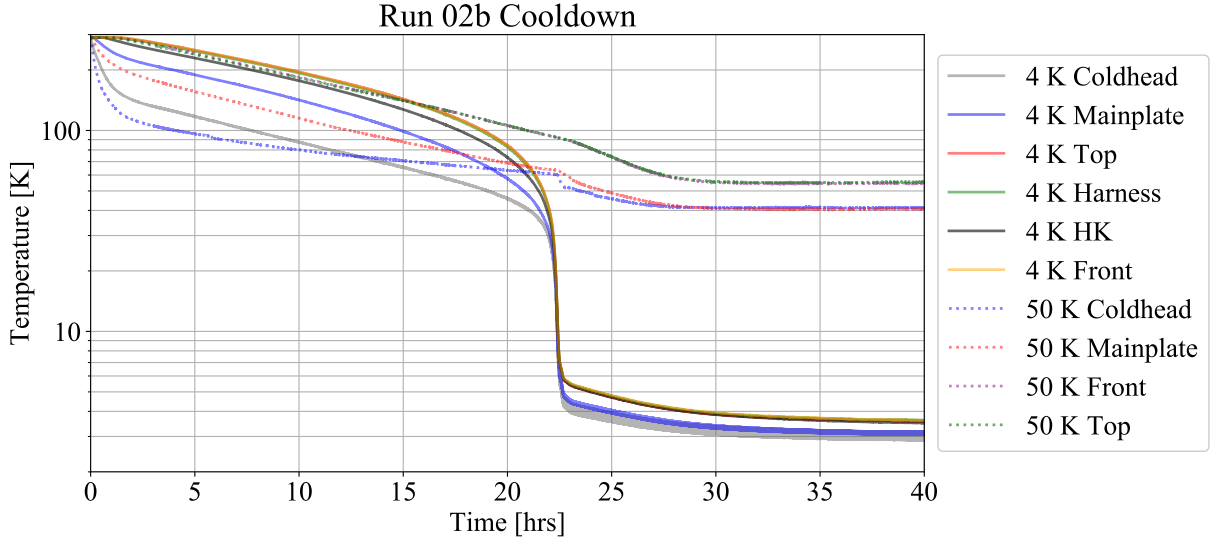


Figure 3.12: Cooldown plot of the second cooldown of the POLARBEAR-2b backend. Base temperature is reached in ~ 35 hrs.

evaluate the performance of all heatstraps and thermal interfaces. Measurement of the 4 K load curve and 50 K base temperature with no harnesses installed allows us to precisely measure the loading due to the harnesses after installation and evaluate whether their thermal performance is acceptable. Figure 3.11 shows the PTC second stage load curve

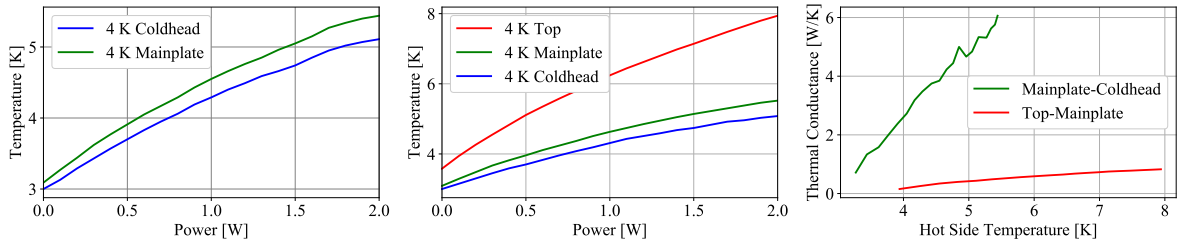


Figure 3.13: (Left) Run 02b load curve taken using a heater on the 4 K mainplate. This is a more accurate measure of the mainplate-coldhead heatstrap G . (Center) Run 02b load curve taken using a heater on the 4 K top panel. (Right) Heatstrap thermal conductances as a function of the hot side temperature.

taken using a heater on the top panel of the 4 K shell and the resultant thermal conductance G for the thermal connection between the mainplate and the coldhead, and between the top panel and the mainplate.

Figure 3.12 shows the second cooldown (run 02b), which began October 28th, 2016, of the POLARBEAR-2b backend after installing the three wiring harnesses and re-mating the mainplate-coldhead and top-mainplate heatstraps at higher screw torques and using Apiezon N grease as a thermal interface material. Load curves and the corresponding G for the two heatstraps in run 02b are shown in Figure 3.13. From this we see that the both the mainplate-coldhead G and the top-mainplate G have been improved, although the increase is more significant in the former. We estimate that recycling the He-10 fridge adds ~ 150 mW of loading ($\Delta T_{MP} \sim 100$ mK) to the 4 K mainplate so all efforts in minimizing the mainplate-coldhead gradient will aid in maximizing η . The POLARBEAR-2c 50 K and 4 K validation was also achieved on the second run (run 02c). Base temperatures for both 50 K and 4 K validation runs on POLARBEAR-2b and -2c are shown in Table 3.6.

Base temperatures for run 02b and run 02c are listed in Table 3.6. From these

Table 3.5: Base temperatures in K for the POLARBEAR-2b and -2c backends during their 50 K and 4 K validation run.

Location	POLARBEAR-2b	POLARBEAR-2c
4 K Coldhead	3.00	2.81
4 K Mainplate	3.09	3.05
4 K Top	3.55	3.47
4 K Front	3.57	3.55
4 K Bottom	—	3.47
4 K Harness	3.59	—
50 K Coldhead	40.9	32.6
50 K Mainplate	41.1	39.3
50 K Top	56.1	50.1
50 K Front	55.4	50.4

values and the PTC capacity map [89] and load curve in Figure 3.4 it is evident that the 50 K loading for POLARBEAR-2b (-2c) is ~ 40 W (~ 20 W) and the 4 K loading is ~ 0.30 W (~ 0.25 W). Our modeling of the conductive loads in Section 3.2.3 is consistent with these values, and the discrepancy between the two backends can be attributed to more thorough pumping out of the POLARBEAR-2c backend than POLARBEAR-2b for their respective runs.

If we attribute the remainder of the observed loads to the gas conduction (\dot{Q}_{gas}) and assume the pressures for He and N₂ are equal, we can obtain rough estimates for the interstitial gas pressure during the cooldown of each cryostat. For run 02b (run 02c) we have at 50 K $p_{int} \sim 2.6 \times 10^{-5}$ ($\sim 1.1 \times 10^{-6}$) mBar and at 4 K $p_{int} \sim 1.2 \times 10^{-8}$ ($\sim 5.0 \times 10^{-9}$) mBar. For reference the vacuum vessel pressure gauge typically reads $10^{-5} - 10^{-6}$ mBar so these numbers are consistent at 50 K. The interstitial pressures for 4 K are unphysically low, most

likely due to uncertainties in the thermal loading model of other components. Regardless, no large spurious loads or gradients were observed during run 02b and run 02c. This, in conjunction with the verification that the 4 K mainplate in both cryostats will reach a low enough base temperature such that $\eta_{He-4} \sim 70\%$, completes the 50 K and 4 K validation of the POLARBEAR-2b and -2c backends.

3.3.4 Millikelvin Validation

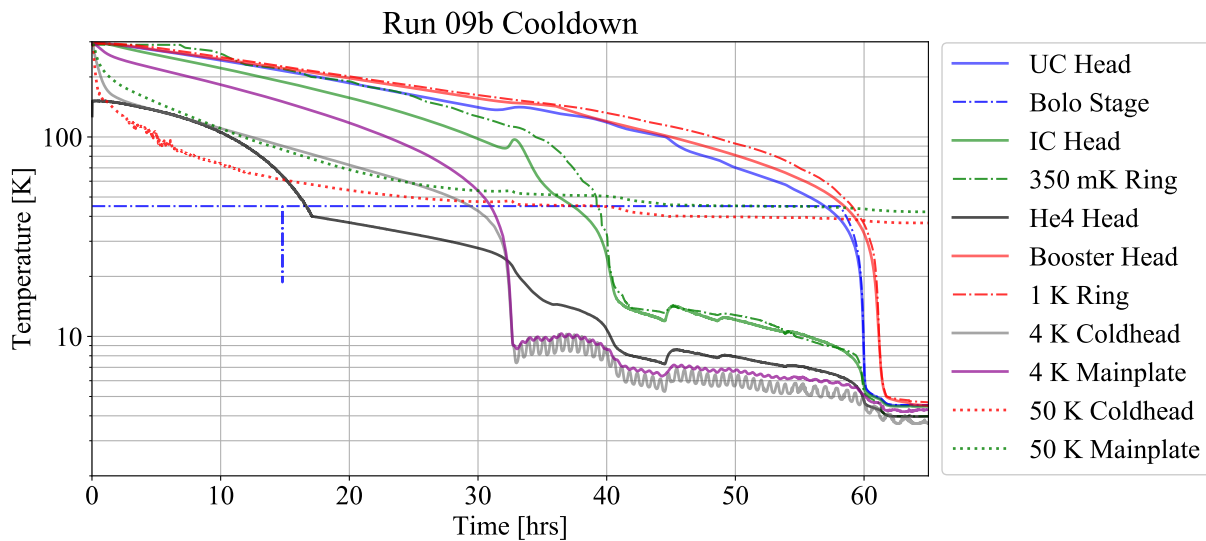


Figure 3.14: Cooldown plot of run 09b of the POLARBEAR-2b backend with the bare FPT installed (no detector modules). Base temperature is reached in ~ 65 hrs.

Once the 50 K and 4 K validation is complete we begin integration of the millikelvin fridges and FPT. It is advantageous to integrate the bare (no attached mass) millikelvin refrigerators in order to identify any stray loading (such as light leaks) that may be present, and to diagnose any deleterious thermal gradients between the 4 K mainplate and the fridge condensers. This required multiple cooldowns for the POLARBEAR-2b backend due

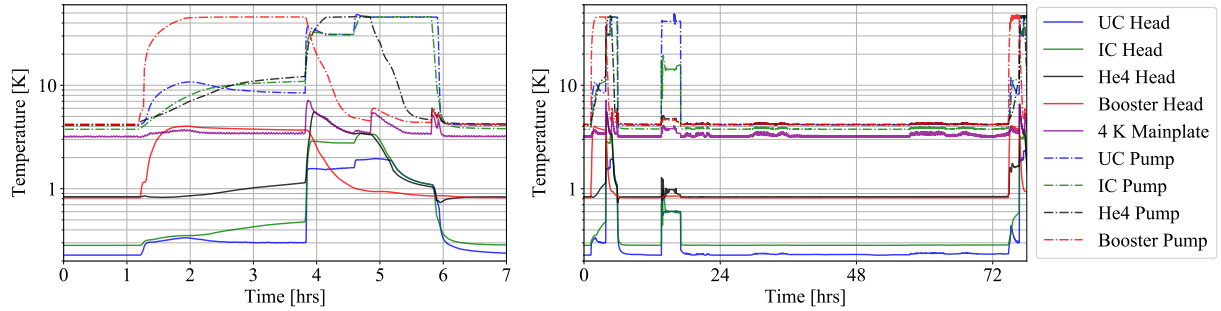


Figure 3.15: (Left) Plot showing POLARBEAR-2b He-10 fridge recycling which takes 6 hrs to reach a condensation point low enough that t_{tot} is in excess of 72 hrs. The booster fridge is cycled before the He-10 in order to keep the 4 K mainplate temperature as cold as possible so η_{He-4} is maximized. (Right) Fridge cycle and hold time plot during initial focal plane integration demonstrating that t_{tot} of the POLARBEAR-2b fridge is ≥ 72 hrs with $\sim 75, 0, 6$, and $1.5 \mu\text{W}$ of loading to the booster, He-4, IC, and UC stages. The portion of the plot between 14 and 20 hrs is deliberate heating of the stage which is performed during various detector and readout commissioning tests. The fridge cycle was started before expiration of any fridge stages so the hold time is actually longer than shown here.

to large gradients between the booster condenser and the 4 K mainplate, and long recycling times due to improper thermal anchoring of the precooling switch. Figure 3.14 shows the cooldown for run 09b (started on June 9th, 2017) in which the millikelvin validation was completed. This run contained only the mechanical structure of the FPT, i.e. no detector modules, MMFs, or rf shields were installed. For the POLARBEAR-2b and -2c backends, millikelvin validation entails demonstrating acceptable base temperatures (and identifying spurious loads), fridge hold time, and fridge recycling time. Hold times and recycling times are validated by applying the loads expected at each FPT stage after integration of the entire focal plane and optics tube using heaters. Figure 3.15 shows a typical millikelvin fridge cycle in a later run of the POLARBEAR-2b backend with $t_{cycle} = 6$ hrs and $t_{ht} > 68$ hrs which demonstrates that t_{tot} falls within a three sidereal day observation cycle. The loading

Table 3.6: Summary of the values used to obtain the millikelvin heatstrap G . ΔT refers to the temperature gradient from the fridge head to the corresponding FPT stage. In this way G is a measurement of the combination of the thermal contact interfaces on both ends of each heatstrap, as well as the bulk properties.

Heatstrap	ΔT [mK]	Power [μW]	G [$\mu\text{W}/\text{mK}$]
Booster	52	68	1.3
IC	21	18	0.85
UC	3	3.8	1.26

for this cycle is less than the full loading after integration, however, we still expect to achieve 72 hrs.

Additionally, we obtain a measurement of the conductance of the millikelvin heatstraps, summarized in Table 3.6, by observing the temperature gradient from the FPT stages to the He-10 heads and inferring the heat load from the He-10 load curves (Figure 3.7). Due to the strong temperature dependence of the Kapitza resistance below 1 K [95], [105], these values are somewhat variable depending on how the joint is prepared and the force applied [106], [107]. This indicates that neither the cross-sectional area of the C101 foils, nor the bulk conductivity is limiting G , rather it is the thermal interface resistance. While these values do vary from cooldown to cooldown, the numbers reported here are representative of the distribution of values of observed.

3.4 Conclusion

The Simons Array is a next generation CMB polarization experiment consisting of three POLARBEAR-2 telescopes and cryogenic receivers and will observe at 95 GHz, 150 GHz, 220 GHz, and 270 GHz. Each receiver consists of two meter-scale cryostats – the backend and the optics tube – each employing PT415 cryocoolers to reach approximate temperatures of 50 K and 4 K. The backends use three-stage helium adsorption refrigerators to provide a 250 mK TES bolometer stage. In this work we have discussed the design, construction, and cryogenic validation of the POLARBEAR-2b and -2c backend cryostats, which is focused on the desire for a three sidereal day observation cycle. In order to realize this goal, for POLARBEAR-2b we have extensively characterized an *off-the-shelf* He-10 fridge and modeled its condensation efficiency. This, along with thermal conductivity measurements of materials contributing loading to the millikelvin stages, motivates the design of this structure so we may lower loads and enable the fridge to achieve a three day cycle. We find that for our requirements the standard model He-10 gas light fridge from Chase Research Cryogenics has an undercharged He-4 stage which requires addition of the standalone booster He-4 fridge to meet this goal. For POLARBEAR-2c we purchased an overcharged super gas light He-10 which meets the three day hold time requirement in the dark configuration with no attached mass. As of spring 2018, the POLARBEAR-2b backend is undergoing detector integration and readout commissioning before integration with its optics tube.

3.5 Acknowledgments

Chapter 3 is a reprint of material, with minor edits to improve clarity, as it appears in: L. Howe, C. Tsai, L. Lowry, K. Arnold, G. Coppi, J. Groh, X. Guo, B. Keating, A. Lee, A. May, L. Piccirillo, N. Stebor, and G. Teply, “Design and characterization of the POLARBEAR-2b and POLARBEAR-2c cosmic microwave background cryogenic receivers,” *Millimeter, Submillimeter, and Far-Infrared Detectors and Instrumentation for Astronomy IX*, vol. 10708, 2018. The dissertation author was the primary author of this paper.

Chapter 4

Polarbear-2b Readout and Detector Commissioning

*Everything we call real is made of things
which cannot be regarded as real.*

— Niels Bohr

After cryogenic fabrication and validation for the POLARBEAR-2b backend is complete, cryogenic readout and detector array integration and testing is possible. In this section we will discuss specifics of the layout and architecture of the POLARBEAR-2 focal planes and cryogenic readout components, as well as efforts towards integration and scalability to the complete POLARBEAR-2b focal plane and readout. Much of this work focused on noise mitigation, predominantly current sharing noise (Section 2.5.3), by selection of an appropriate SQUID design. Designs under consideration for the Simons Array receivers were the NIST SA13a and two designs from Star Cryoelectronics. Due to the vetted and demonstrated SA13a design (deployed in the BICEP-2 and BICEP-3 instruments), this

design was selected for the POLARBEAR-2a (and SPT3G) receivers. For POLARBEAR-2b and -2c a more careful evaluation and comparison of the SA13a and Star Cryoelectronics designs was considered.

4.0.1 Polarbear-2 Focal Plane and Readout Architecture

As previously mentioned, a POLARBEAR-2 focal plane consists of 7,588 optical TES bolometers which are cooled to 250 mK. These are spread across 1,897 pixels such that each pixel is simultaneously sensitive to two frequencies and both polarization states. In addition, there are a number of non-optically-coupled (“dark”) detectors for calibration purposes. The full array is constructed from seven TES subarrays fabricated on 15 cm silicon wafers with 271 pixels each. These “device wafers” are packaged in an invar mechanical holder underneath a lenslet array consisting of 271 hemispherical, two-layer anti-reflection coated silicon lenslets [108] (one for each pixel) to focus CMB photons onto each pixel on the device wafer [8].

The LC resonator combs (see Figure 4.1) are mounted in pairs to PCBs, which are fastened to a copper backplate on the underside of the invar holder, shown in Figure 4.2. 30 combs are required to read out a full device wafer. Each comb is read out by a single SQUID located at 4 K, so a full focal plane requires 210 SQUIDs. SQUIDs are arranged in groups of eight devices on a PCB package shown in Figure 4.3. A completely assembled device wafer, with its lenslet array and set of 30 LC combs is referred to as a “detector module,” which is shown in Figure 4.6. These are installed in the FPT (Figure 3.3), the readout striplines are heatsunk, and an RF shield and final stage of band-defining optical filters

are mounted on the skyward side of the detectors. Figure 4.4 shows the POLARBEAR-2b FPT with all seven detector modules before installation of the 350 mK band-defining metal mesh filters and the FPT RF shield. The fully assembled POLARBEAR-2b FPT is shown in Figure 4.5, which is then installed as a unit into the receiver backend and the final connections between the readout quanta and the SQUID cards are made (Figure 4.7).

4.1 Mitigating Current Sharing

The primary means of reducing the current sharing noise enhancement (see Section 2.5.3) is to reduce the inductance of the SQUID input coil. Reducing series inductances from parasitics on the SQUID PCBs is also beneficial but only amounts to a few nH. This lowers the impedance of the input coil relative to the bolometer comb impedance and allows more of the nulling current to pass through the input coil rather than the bolometer comb. While beneficial in terms of lowering the noise referred to the TES array, this can have significant impacts on SQUID operation by limiting linear dynamic range. Along with the fact that nonzero noise currents are injected at a higher degree through the input coil, a lower L_{in} also makes the SQUID more susceptible to RF interference. Modification of the filtering circuit on the 300 K DfMUX electronics to provide a steeper cutoff just above the readout band (\sim 4.5 MHz) was implemented to alleviate RF SQUID loading.

Replacing the SA4 SQUID design originally chosen for DfMUX requires a number of considerations, including the L_{in} , Z_t , and Z_{out} of the new design. Readily available and demonstrated low- L_{in} SSAs from fabrication facilities with sufficient yield are not common.

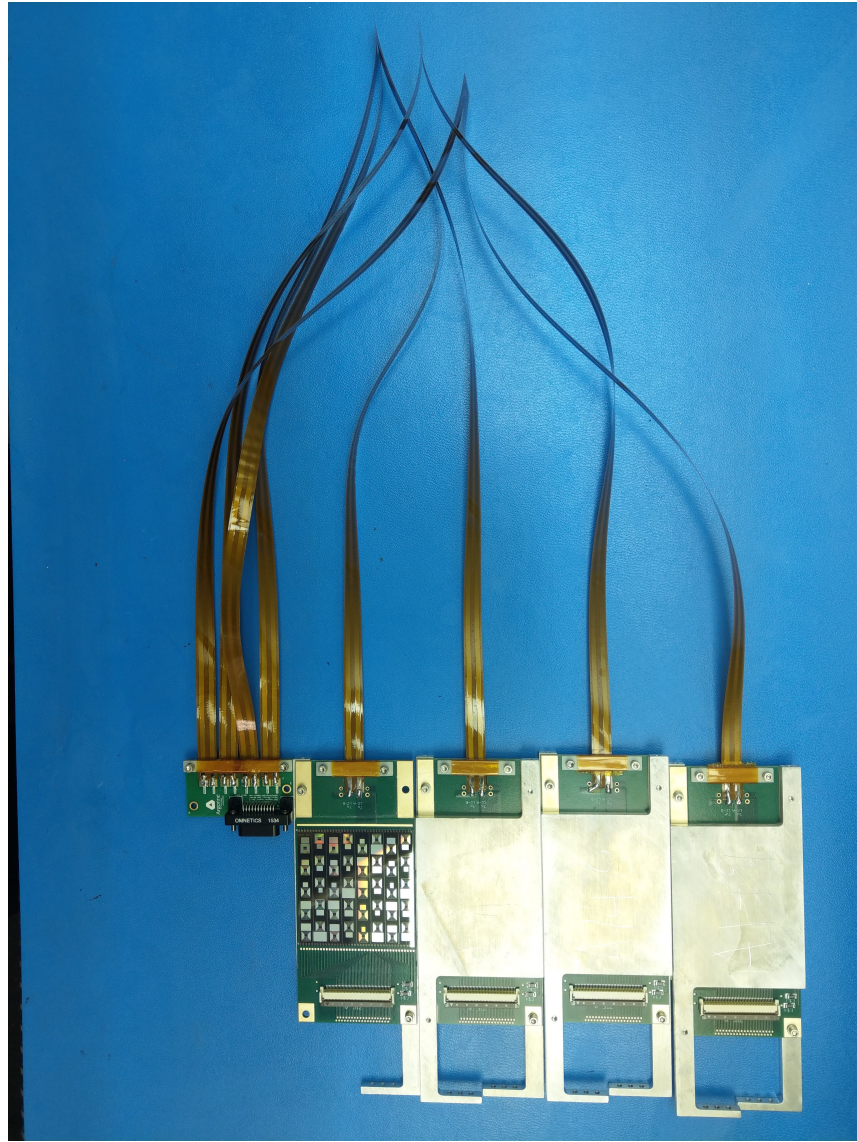


Figure 4.1: A POLARBEAR-2 “readout quanta” consisting of eight LC resonator combs. Each LC comb consists of a silicon die containing a planar lithographed array of 40 spiral inductor and interdigitated capacitor pairs. There are two LC combs per PCB (one each on the front and back). On one end of the PCB, using ultrasonic soldering techniques [7], the polyimide-NbTi readout striplines are attached to each LC board, bundled in groups of three or four LC PCBs and connected to an “adapter” PCB. This board consists mainly of a micro-D connector that plugs directly into a POLARBEAR-2 SQUID card. On the other end a zero insertion force (ZIF) connector mates with the flex wiring circuit fanout from the TES array device wafer. Packages consisting of three (four) PCBs are referred to as a “small” (“large”) readout quanta.” The left-most PCB has its aluminum shield removed to display the LC comb die.

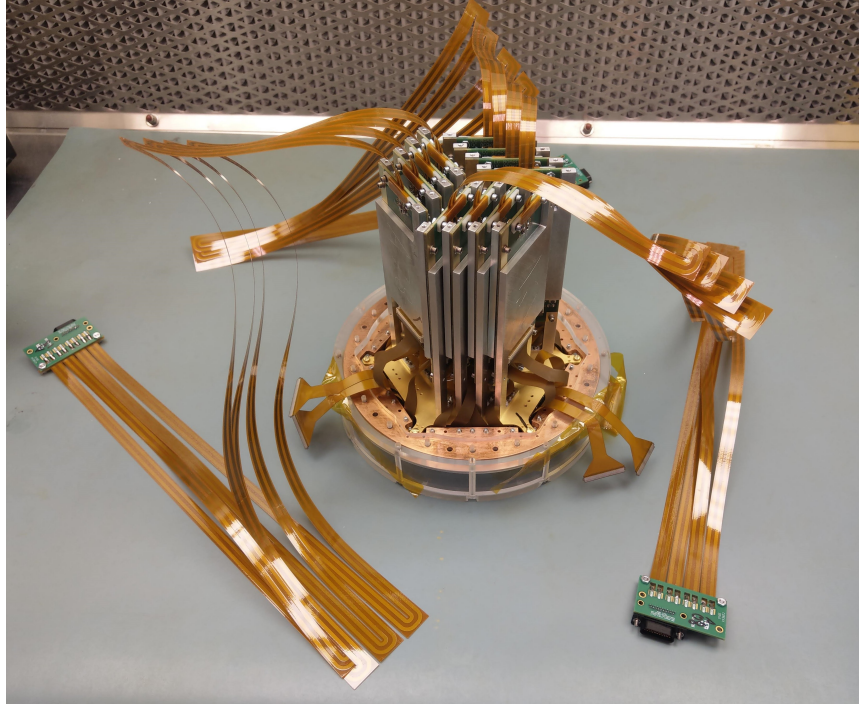


Figure 4.2: A POLARBEAR-2 detector module with most of its cold readout assembled. PCBs housing the LC resonator combs (two per PCB) are bolted to the detector module wafer backplate, directly behind the device wafer. A total of 30 combs (three large and one small readout quanta) are needed to read out a complete POLARBEAR-2 detector wafer. This results in a maximum of 1200 channels per module which can be read out, however not all of these are read out. Additionally, some read out bolometers are not wired to antennae (“dark”) for calibration purposes.

Essentially only three designs from two manufacturers were considered for expediency’s sake: the SA13aa design from NIST [71], and the AR112-EB2 (referred to as the “E2” type/design) and AR112-FB2 (“F2”) from Star Cryoelectronics (STCR) [109]. The main difference between the E2 and F2 designs is the JJ shunt resistance. Typical values for parameters of interest in relation to applications in the DfMUX system are summarized in Table 4.1. The SA4 SSA is a 100 SQUID array with 8-turn input coils for each SQUID loop. Both the Star Cryoelectronics and SA13aa devices use first-order gradiometric input coils[62], which both reduces the total coil inductance, as well as the susceptibility of the

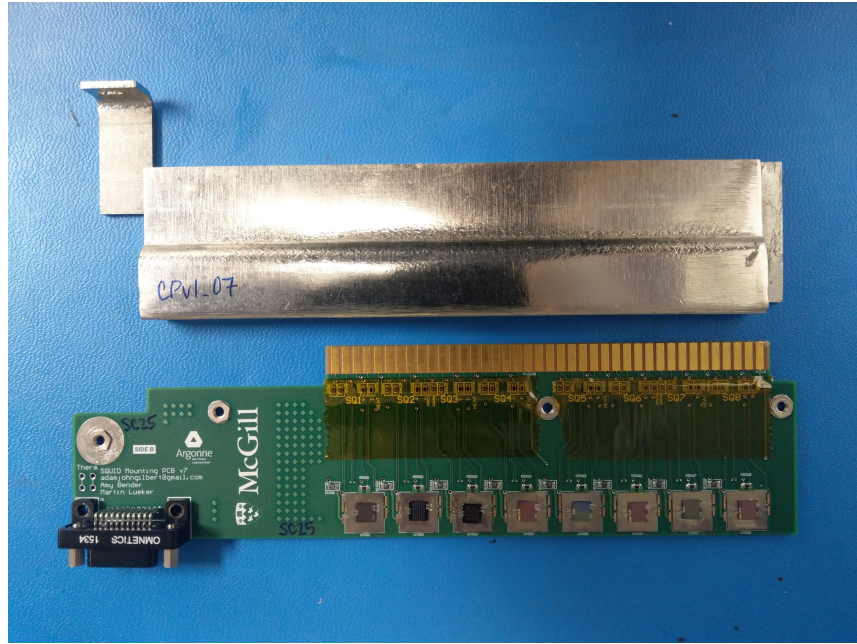


Figure 4.3: A POLARBEAR-2 SQUID mounting PCB, or “SQUID card” and its magnetic shield. A total of eight SQUID series array amplifiers may be located on a single SQUID card. Each die is mounted on top of a niobium foil ground shield using rubber cement. Electrical interconnection is done via aluminum wirebonds to bare copper PCB bond pads. The entire card (*bottom*) is inserted into a high permeability “cryoperm” shield to magnetically shield the SQUIDs. The micro-D connector mates a single SQUID card to a single readout quanta.

array to external magnetic fields. The SA13aa SQUID array is constructed from six banks of 64 individual SQUIDs, with two banks in parallel and three banks in series with one unused – i.e. this is a 192 element series array [110]. The Star Cryoelectronics devices are 112 element series arrays originally optimized for low-power millikelvin operation.

Typical values for design parameters of interest from the original low-power Star Cryoelectronics devices can be found in Table 4.2. Adaptations for 4 K operation in the POLARBEAR-2 DfMUX architecture primarily involved increasing I_c to achieve sufficient transimpedance and dynamic range, which will clearly affect many of the values in Table 4.2. For reference, we discovered from testing that a lower bound of $I_c = 2I_{JJ} \gtrsim 28 \mu\text{A}$ is

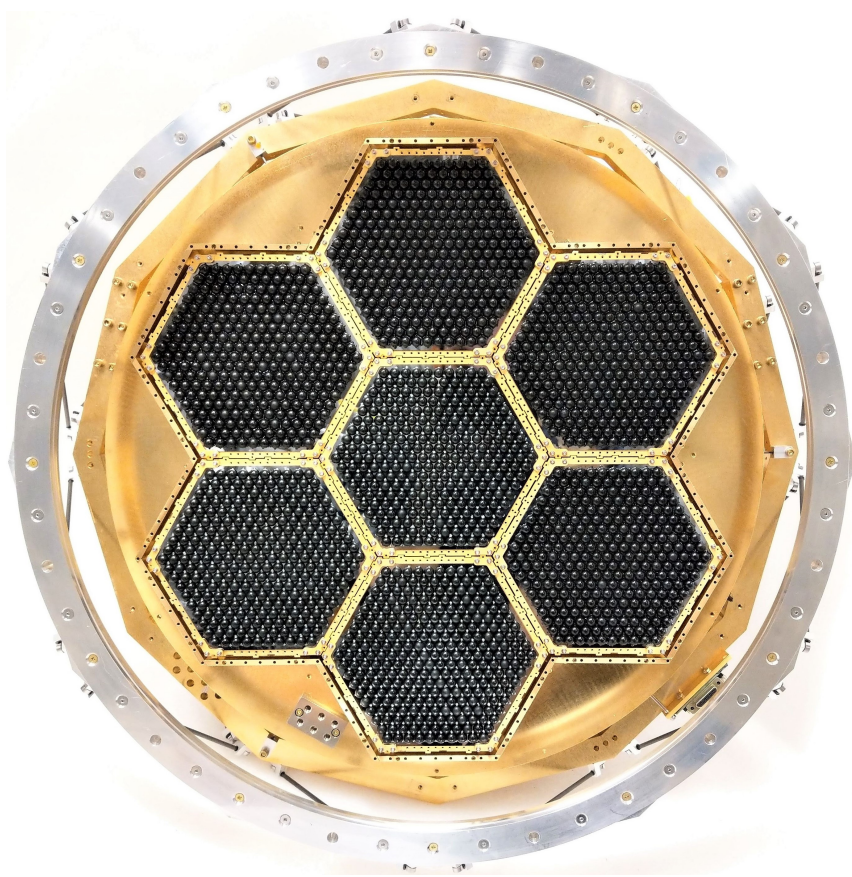


Figure 4.4: The assembled POLARBEAR-2b FPT showing the lenslets arrays of all seven wafer modules. The final stage of assembly involves mounting the final stage of band-defining metal mesh filters on the 350 mK stage and the FPT RF shields consisting of (a) the $50 \mu\text{m}$ aluminum sheet forming the inter-wafer shield, and (b) the $6.27 \mu\text{m}$ polyethylene sheet with double-sided 15 nm aluminization.

required for these arrays to surpass our minimum transimpedance threshold of $\sim \Omega$. This is motivated primarily from the fact that the first-stage semiconductor amplifier in the 300 K DfMUX electronics is (current) noise matched for $Z_t \sim 600 \Omega$. Detailed noise estimates for configurations assuming $Z_t = 500 \Omega$ have already been calculated [79], thus setting a requirement that the transimpedance must exceed 600Ω ensures the POLARBEAR-2b readout system will perform as similarly as possible to the configuration in this previous study.

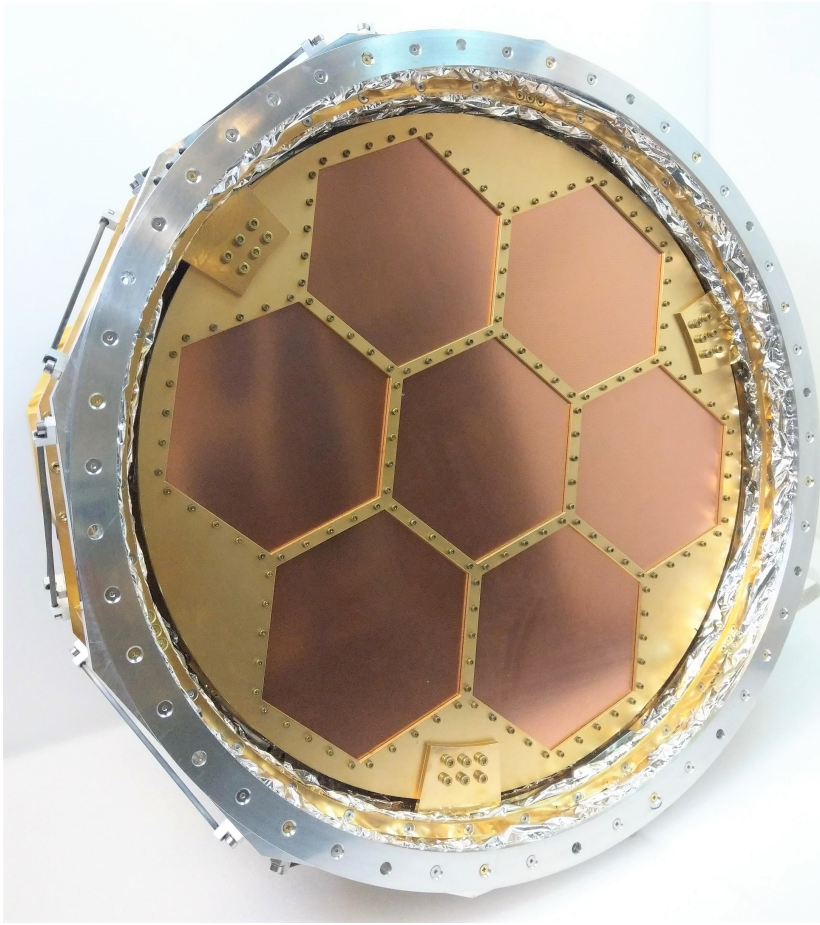


Figure 4.5: Front view of the complete, assembled POLARBEAR-2b FPT with all seven wafer modules installed. The wafer modules are located behind the final 350 mK band-defining optical filters (copper hexagons), known as metal mesh filters. Also visible is the RF shield (aluminized sheet running between rings) which completes the Faraday cage protecting the 4 K SQUID amplifiers, located behind and above the FPT, from RF interference.

It is important to note that the replacement SQUID design must maintain sufficient gain, linearity, and demodulated noise levels while operating a 40-channel POLARBEAR-2 bolometer comb. The limited DAN bandwidth of $\mathcal{O}(10^2)$ Hz around each bias frequency (spaced by $\mathcal{O}(10)^4$ Hz) means inter-channel currents cannot be nulled effectively and will load the SQUID. Inter-channel currents arise both from noise, which can be white – or

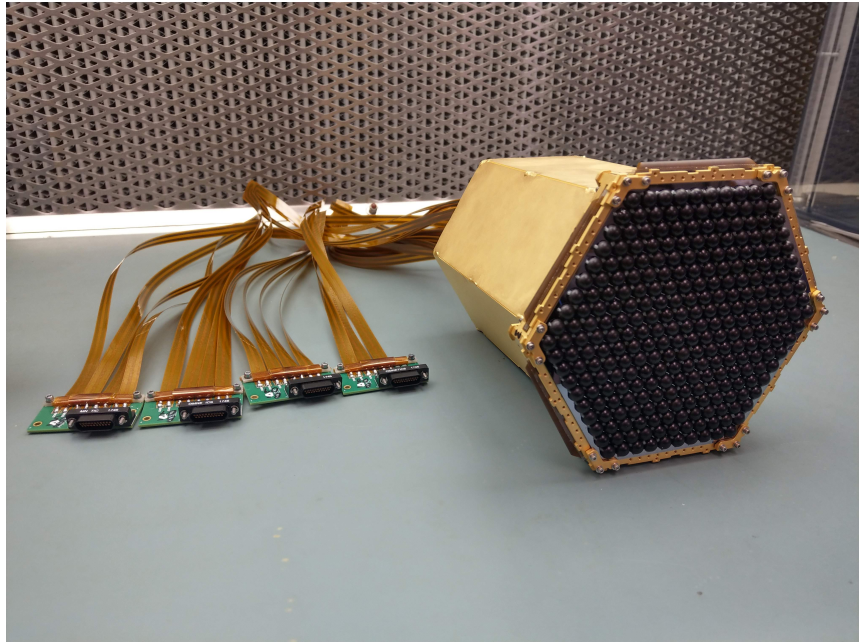


Figure 4.6: Fully assembled POLARBEAR-2 wafer module. The readout quanta are mechanically stabilized using a gold-plated copper can, which also serves to block some of the radiative load to the 250 mK stage.

aliased from higher frequencies and featureful – crosstalk, and intermodulation distortion (IMD) products. IMD products can arise both from mixing of tones within a single comb and from mixing with crosstalked tones between combs. The most common effect that an appreciable amount of RMS un-nulled input coil current has on SQUID operation is to shift the flux bias point. In order to evaluate and compare SQUID designs and performance in a deployment-like system, two assembled detector modules with partial cold readout were attached to a set of eight each SA13a and Star Cryoelectronics E2 and F2 SQUIDs. For this testing, not all SQUIDs were actively able to bias bolometer combs due to broken readout cable connections or issues in tuning the SQUID. Results from various performance metrics will be summarized in the following sections.

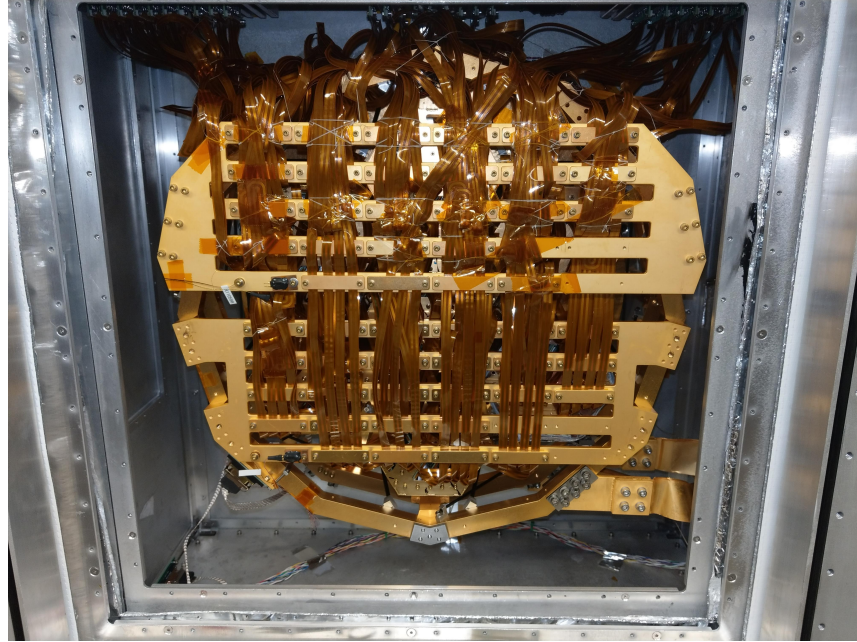


Figure 4.7: Rear view of the complete, assembled POLARBEAR-2b FPT after installation in the backend cryostat. The superconducting NbTi detector readout striplines (orange strips bundled in groups of three and four cables) can be seen. These travel from the bolometer stage (250 mK) near the front of the FPT, and connect to the 4 K SQUID amplifiers located at the top of the backend cryostat. Heatsinking is achieved by clamping the striplines to gold-plated aluminum bars at temperatures of 350 mK (bottom slotted plate) and 1 K (top slotted plate).

4.2 SQUID Characterization and Testing

4.2.1 Direct Linear Dynamic Range Tests

First, given that the main quantity of interest is the bolometer comb current and whether typical operating comb currents are acceptable with respect to SQUID performance, we assume the SQUID dynamic range is primarily a function of the magnitude of un-nulled current in its input coil. One of the most pure measurements for the SQUID dynamic range with respect to un-nulled input coil current is realized by applying a tone at increasing amplitude after tuning the SQUID and tracking how the SQUID performance evolves.

Table 4.1: Summary of characteristic properties of various SQUID devices considered for, or used with, the DfMUX readout system. The input inductance values reported here are the design values. Transimpedance, output impedance, and SQUID critical current measurements reported here were performed at an array temperature of 3.4–3.8 K in the POLARBEAR-2b backend.

SQUID	L_{in} [nH]	Z_t [Ω]	Z_{out} [Ω]	I_c [μA]
SA4	300	300 – 600	75 – 150	~ 150
SA13a	50	400 – 700	500 – 650	~ 30
E2	11	750 – 850	550 – 650	~ 30
F2	11	750 – 1000	550 – 750	~ 30

Table 4.2: Design values for different parameters for the low-power Star Cryoelectronics devices. Values taken from a poster presented at the 2017 Low-temperature Detectors Conference in Magome, Japan [109].

Parameter	Value	Units
N_{SQ}	112	–
Input/feedback-SQUID loop mutual inductance: $1/M_{in}$	23.6	$\mu\text{A}/\Phi_0$
SQUID normal resistance: $R_{N,JJ}/2$	2.6	Ω
SQUID critical current: $2I_{c,JJ}$	11.5	μA
Screening parameter: $\beta_L = 2LI_{c,JJ}/\Phi_0$	0.56	–
Stewart-McCumber parameter: $\beta_c = 2\pi R_{N,JJ}^2 C_{JJ}/\Phi_0$	0.28	–
Array voltage-flux transfer coefficient: $\partial V_{out}/\partial\Phi$	9.4	mV/Φ_0
Array flux noise spectral density: $\sqrt{S_F}$ ($f > 100$ Hz)	250	$\text{n}\Phi_0/\sqrt{\text{Hz}}$

Specifically, we can measure Z_t as the RMS un-nulled current increases. Deviations from the initial transimpedance indicate movement through the $V - \Phi$ curve away from the dc bias point (see Figure 2.8). The linear range depends on the shape of the $V - \Phi$ curve local to the dc bias point, which can be quantitatively described via a polynomial Taylor expansion about each point in the $V - \Phi$ curve. The second and third order Talyor expansion coefficients are a direct measure of the nonlinearity at each bias point. Following [110],

appreciable nonlinearity appears approximately when the transimpedance has degraded by $\sim 10\%$ of the tuned value. At the onset of significant nonlinearity, the SQUID begins to mix and synthesize crosstalked and IMD tones at a much larger degree – few or none of which DAN can effectively null – and the flux burden and demodulated noise levels increase dramatically.

Table 4.3: Mean values for the nullder tone dynamic range test shown in Figure 4.8 for each of the three SQUID device types tested. Note that SA13_041.5 is an outlier, most likely due to rf contamination or ground coupling resulting from a short on the device wafer it was connected to. It is excluded from this mean.

SQUID	Linear Dynamic Range [μA_{rms}]
SA13a	0.74
E2	0.85
F2	0.81

Figure 4.8 shows this measurement for a subset of the evaluation SQUIDs, and the mean values for each of the three designs are reported in Table 4.3. These results show there is a preference towards the Star Cryoelectronics E2 design. This test serves to directly measure the amount of free input coil current the SQUID can tolerate during bolometer operation. Quantifying the amount of un-nulled current while biasing full bolometer combs can be difficult, but attempts will be made to do so in the following section.

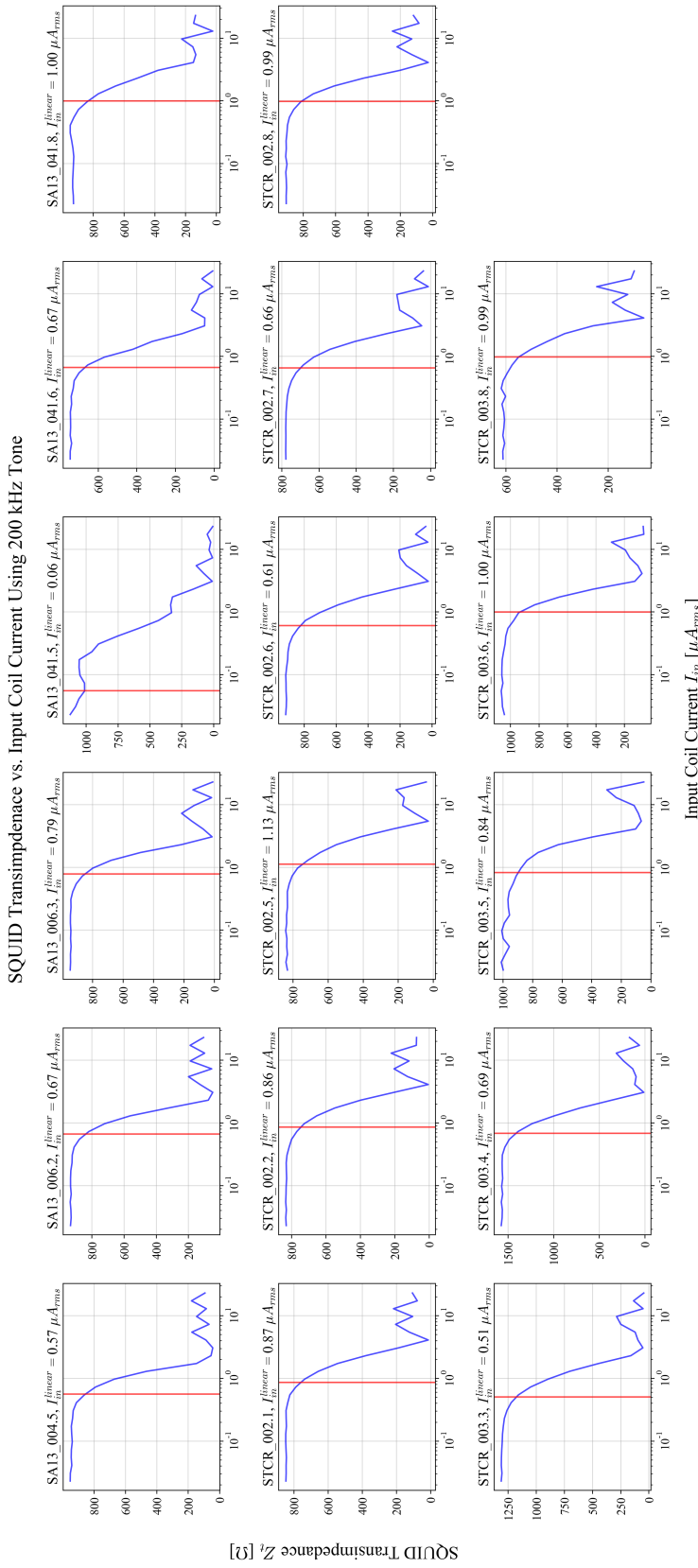


Figure 4.8: Direct input coil linear dynamic range test of NIST SA13a and Star Cryoelectronics E2 and F2 SQUID designs. SQUIDs are first tuned, then a 200 kHz tone through the input coil is turned on and ramped in amplitude while measuring the transimpedance with a low amplitude 50 kHz tone. 200 kHz is chosen to avoid interaction between the primary tone, and the first few harmonics, with the LC comb (peaks in $\sim 1.5 - 4.5$ MHz). Tests were repeated at different primary tone frequencies up to 1.4 MHz, both with and without LC combs present, and no dependence on primary tone frequency was found.

4.2.2 Carrier Bias Amplitude Dependence of Demodulated Noise Levels

A less pure metric, although one which is perhaps more relevant for the DfMUX-specific POLARBEAR-2 receivers, is to simply measure and determine whether a SQUID can support biasing a complete 40-channel detector comb under the expected comb current loads without serious increases in the demodulated detector noise levels. Based on the $I - V$ curve shown in Figure 2.3, where the highest voltage corresponds to the overbiased voltage, it is clear that only deep in the transition does the bolometer current exceed that which is typical during overbiasing. A useful proxy then, in assessing a SQUID’s ability to operate a bolometer comb across the range of parameters subjected to it during observation, is a measurement of the bolometer white noise level at different carrier overbias voltages. We refer to this as the carrier amplitude-dependent noise (ADN) measurement. In the event the SQUID bias point shifts significantly – either continuously due to a gradual increase in the RMS flux burden from incomplete nulling, or from a flux jump – noise levels can also increase due to reduced linearity. The SQUID pseudo white noise floor is determined by taking the median value of a bolometer timestream spectrum between 10 and 40 Hz to avoid $1/f$ effects. Finally, since this is an overbiased measurement, the stage must be heated to ~ 600 mK (above bolometer T_c), and as demonstrated in Figure 2.11, use of bias frequencies measured at 600 mK is important. Otherwise the carrier bias is slightly (or even completely) off-resonance, and can enhance variations in the I-phase timestreams and manifest as an additional noise contribution.

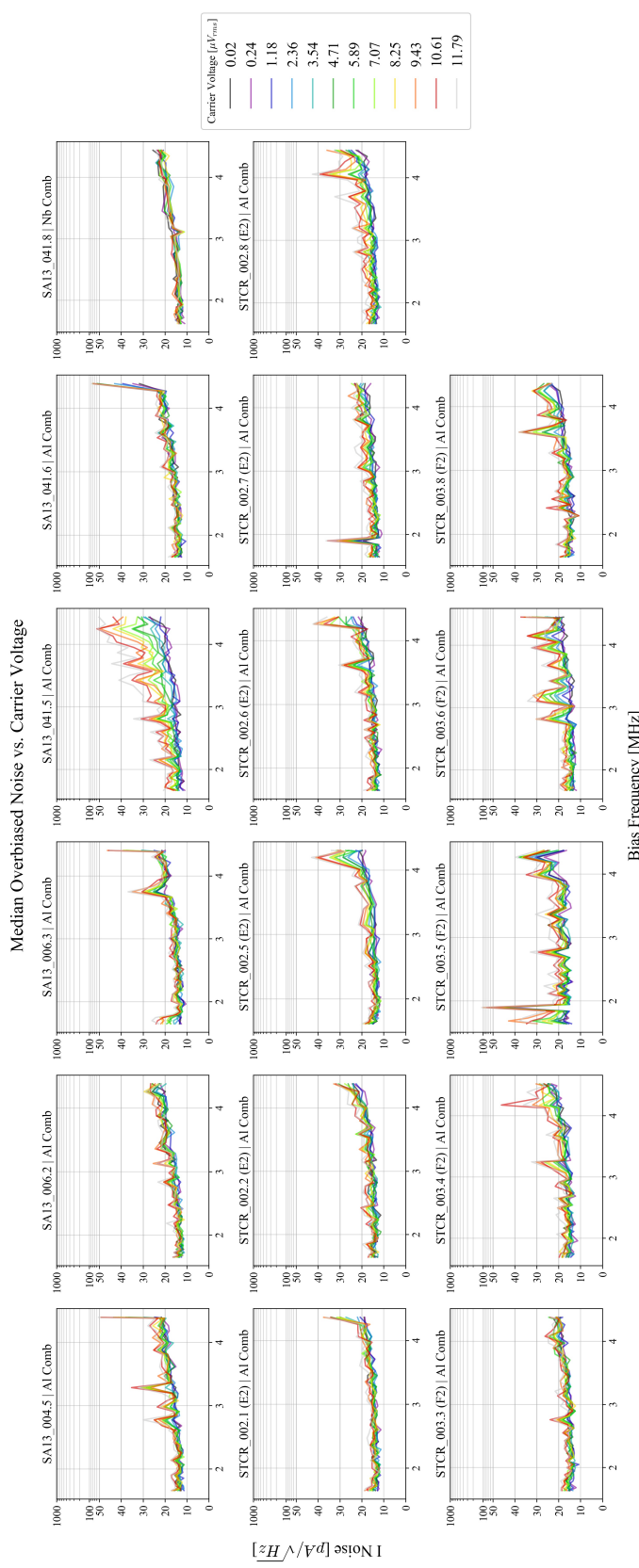


Figure 4.9: In phase (I) ADN measurement comparing NIST SA13a and Star Cryo-electronics SQUID designs.

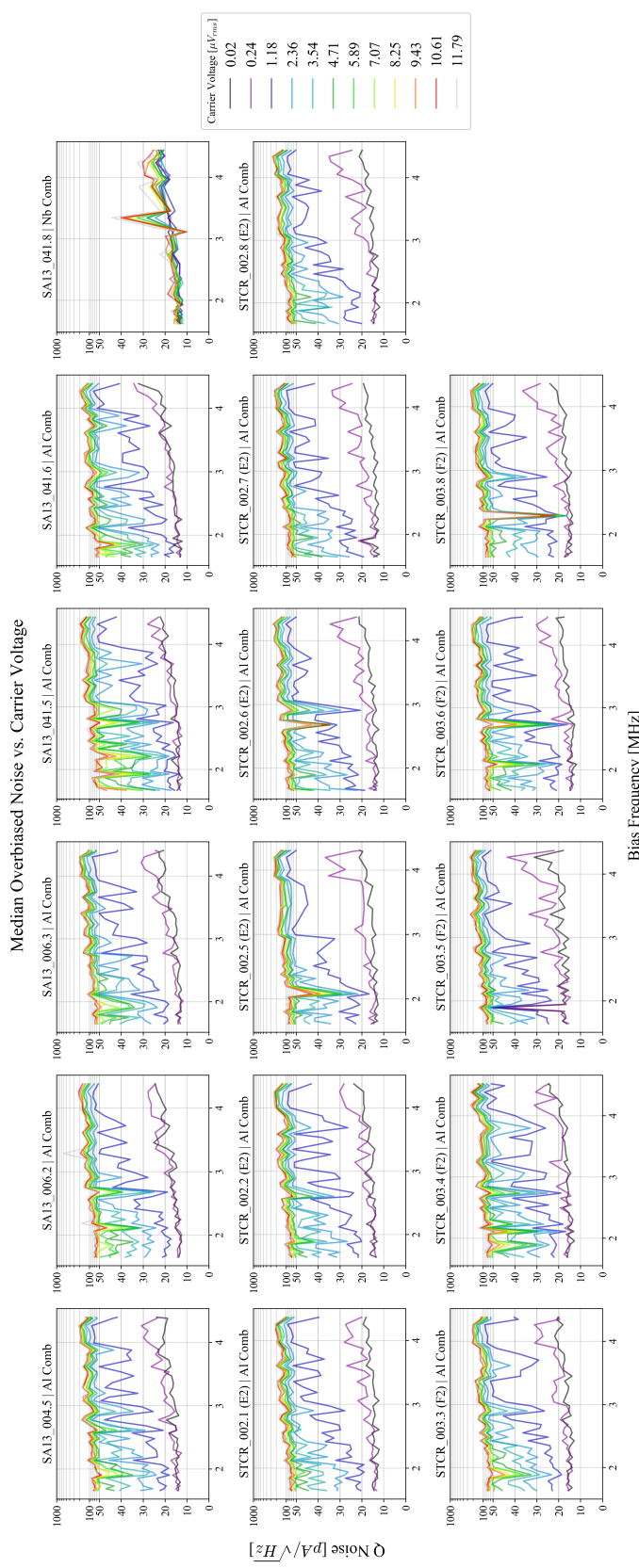


Figure 4.10: Quadrature phase (Q) ADN measurement comparing NIST SA13a and Star Cryoelectronics SQUID designs.

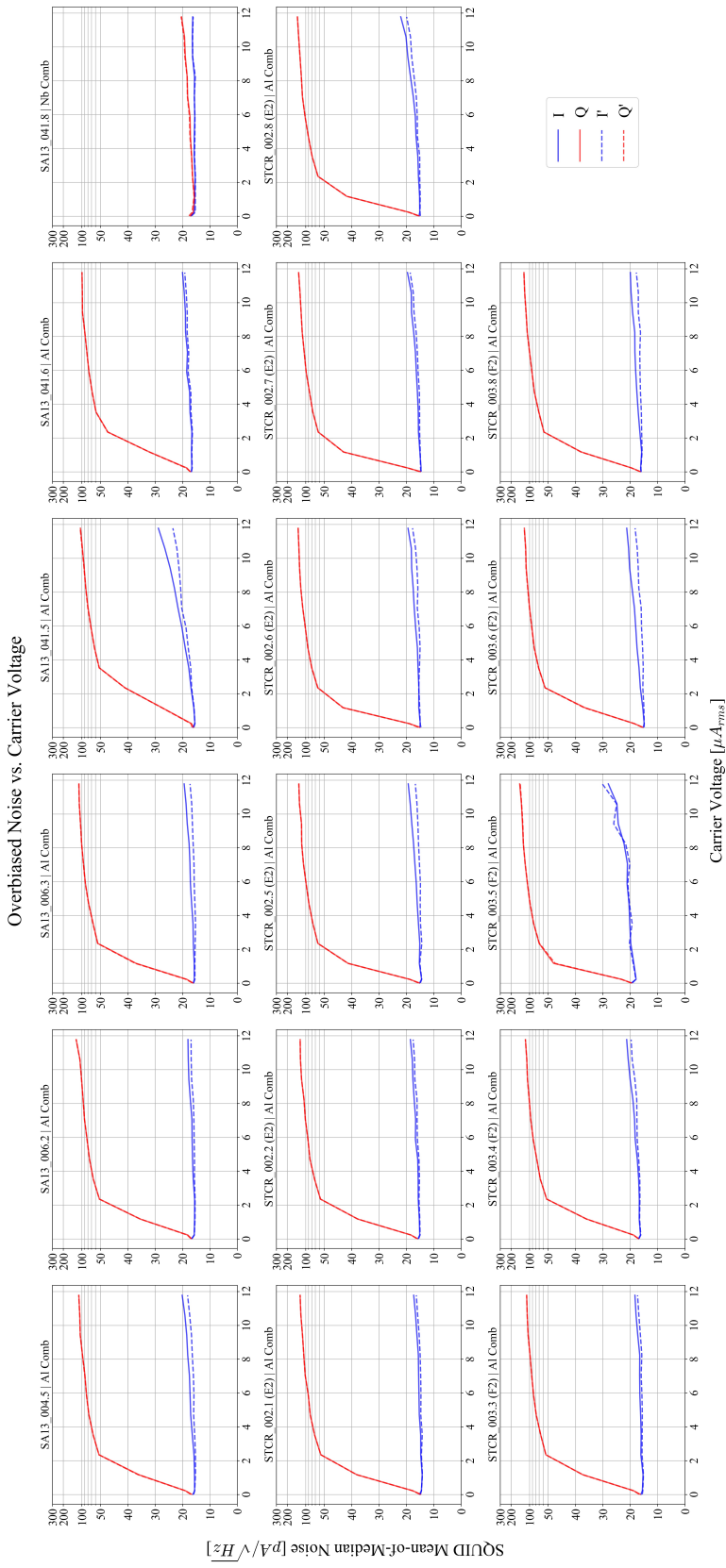


Figure 4.11: Mean-of-median ADN noise comparing NIST SA13a and Star Cryoelectronics SQUID designs. Also shown are the Γ and Q' phases, which are formed by rotating the I and Q phase by an angle θ resulting in the minimum variance (noise) in the I phase timestamp. This demonstrates that the weak rise in the I phase noise with carrier voltage may be due to leakage of the Q phase noise increase into the I phase.

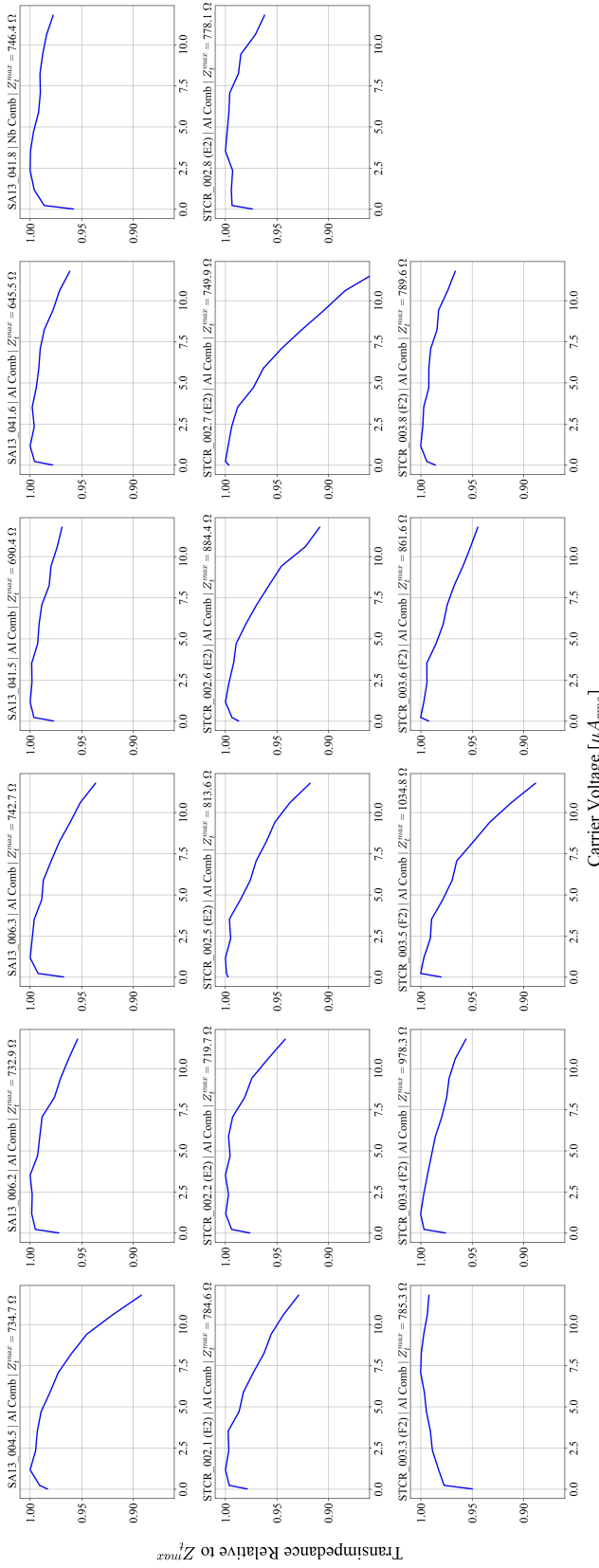


Figure 4.12: SQUID transimpedance during the ADN measurement normalized to the maximum transimpedance Z_t^{max} measured for the SQUID during the measurement. As discussed in Section 2.3.4, the SQUID tuning point is not chosen to solely optimize Z_t . The transimpedance increase should be interpreted as due to an RMS flux burden resulting from the detector bias tones, which moves the SQUID flux bias forward along the $V - \Phi$ curve. Eventually, Z_t^{max} is crossed and Z_t begins to drop. If the flux bias is pushed by an extreme amount towards a $V - \Phi$ peak/trough, nonlinearities increase significantly and the noise levels can rise dramatically.

In these ADN tests, each SQUID is able to bias and run 35 – 40 bolometer/resonator channels depending on wirebonding and fabrication yield, excepting SA13_041.8 which was attached to a prototype LC device fabricated with Nb wiring with only 19 channels. Figure 4.9 and 4.10 show the I and Q phase ADN measurements comparing the three candidate SQUID types. Additionally, Figure 4.11 shows the mean-of-median noise, i.e. the mean of the noise levels across each comb shown in Figures 4.9 and 4.10, to better show the trend with overbias voltage in both phases. Tracking the SQUID transimpedance Z_t while the carrier voltage is ramped, shown in Figure 4.12, is a final useful metric to attempt to distinguish SQUID performance. The I and Q phase ADN tests show no clear preference for a particular SQUID design. The Z_t as a function carrier voltage measurement does indicate slightly less gain degradation for the SA13a, than either of the Star Cryoelectronics device types.

The significant, rapid increase in the Q phase noise in the ADN tests is worth noting. Attempts have been made to explain this as stemming from a variety of sources, including: a kinetic inductance term in the LC combs, jitter in the 10 MHz signal used to clock the 300 K electronics, and improper choice of bias frequencies. More careful network analysis measurements and use of a very stable GPS-disciplined clock source¹ did not alleviate this effect. Original DfMUX system designs incorporated aluminum as the LC material. Aluminum is both known to have a large kinetic inductance and has a transition temperature of 1.2 K, which is relatively near the 600 mK temperature at which the ADN tests are performed – therefore exacerbating the kinetic inductance contribution.

¹<https://www.spectruminstruments.net/products/tm4/tm4.html>

For this reason LC devices using niobium as the superconductor (lower kinetic inductance and transition temperature of 9.3 K) were adopted for use in the POLARBEAR-2b and -2c receivers. This was not found to alleviate the carrier amplitude dependence of the Q noise and its source remains somewhat mysterious for the POLARBEAR-2 receivers.

As to the apparent lack of ADN on SA13_041.8, this can most likely be attributed to the fact that the comb operated by this SQUID has a 48% yield. Additionally, this SQUID was the only device on its SQUID card connected to a comb, minimizing the amount of crosstalk and IMD products which load the other SQUIDs whose neighbors are running full combs.

Comparing the demodulated noise levels at a typical overbias voltage, and at very low voltage serves as a useful summary of the ADN measurements shown in Figures 4.9, 4.10, and 4.12. At very low overbias voltages the effects of SQUID and other nonidealities are minimized and we obtain an accurate measurement of the ideal, readout-only contribution to the current noise (Figure 4.13). The typical overbias voltage measurement demonstrates the best possible realistic performance we can expect during operation (Figure 4.14). These comparisons show only a slight advantage to the Star Cryoelectronics E2 design with respect to minimum and realistic I phase noise, while the SA13a is the top performer in terms of realistic Q noise. As previously mentioned, the Q noise dependence on the overbias voltage is not well-understood and persists despite implementation of careful bias frequency selection, use of stable 10 MHz timing references, and implementation of niobium LC combs with a lower kinetic inductance. From both lab testing of POLARBEAR-2 detector arrays and performance on-sky of the POLARBEAR-1 instrument using the previous generation of

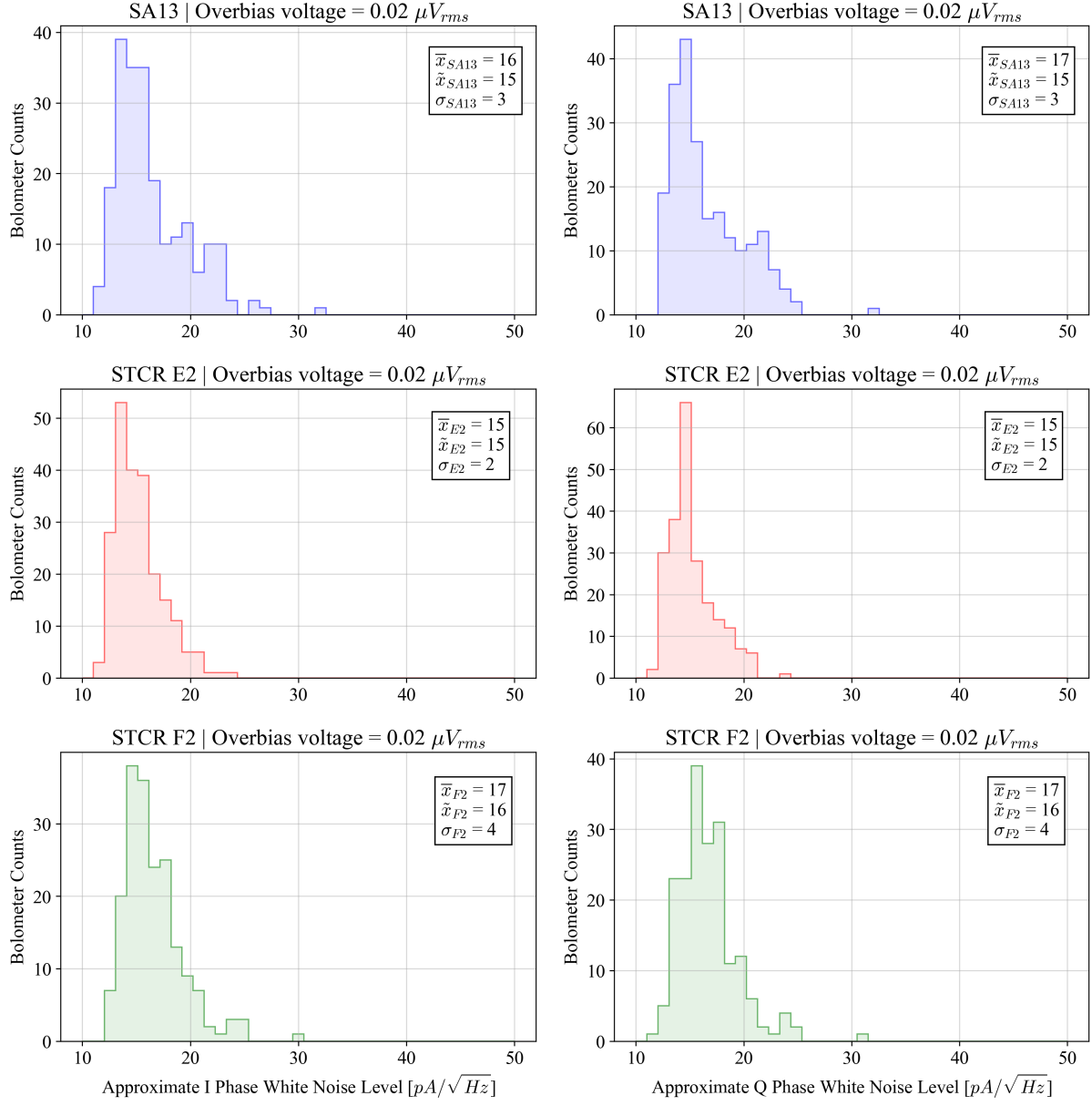


Figure 4.13: Comparison of the low carrier overbias voltage demodulated noise levels for the NIST SA13a and Star Cryoelectronics E2 and F2 SQUIDs. (*Left*) I phase noise. (*Right*) Q phase noise. In this test the I and Q phase noise are comparable because the Q phase carrier amplitude dependence has not set in at this low voltage, although it does begin to increase almost immediately as the carrier voltage is increased beyond $\sim 0.02 \mu V_{rms}$.

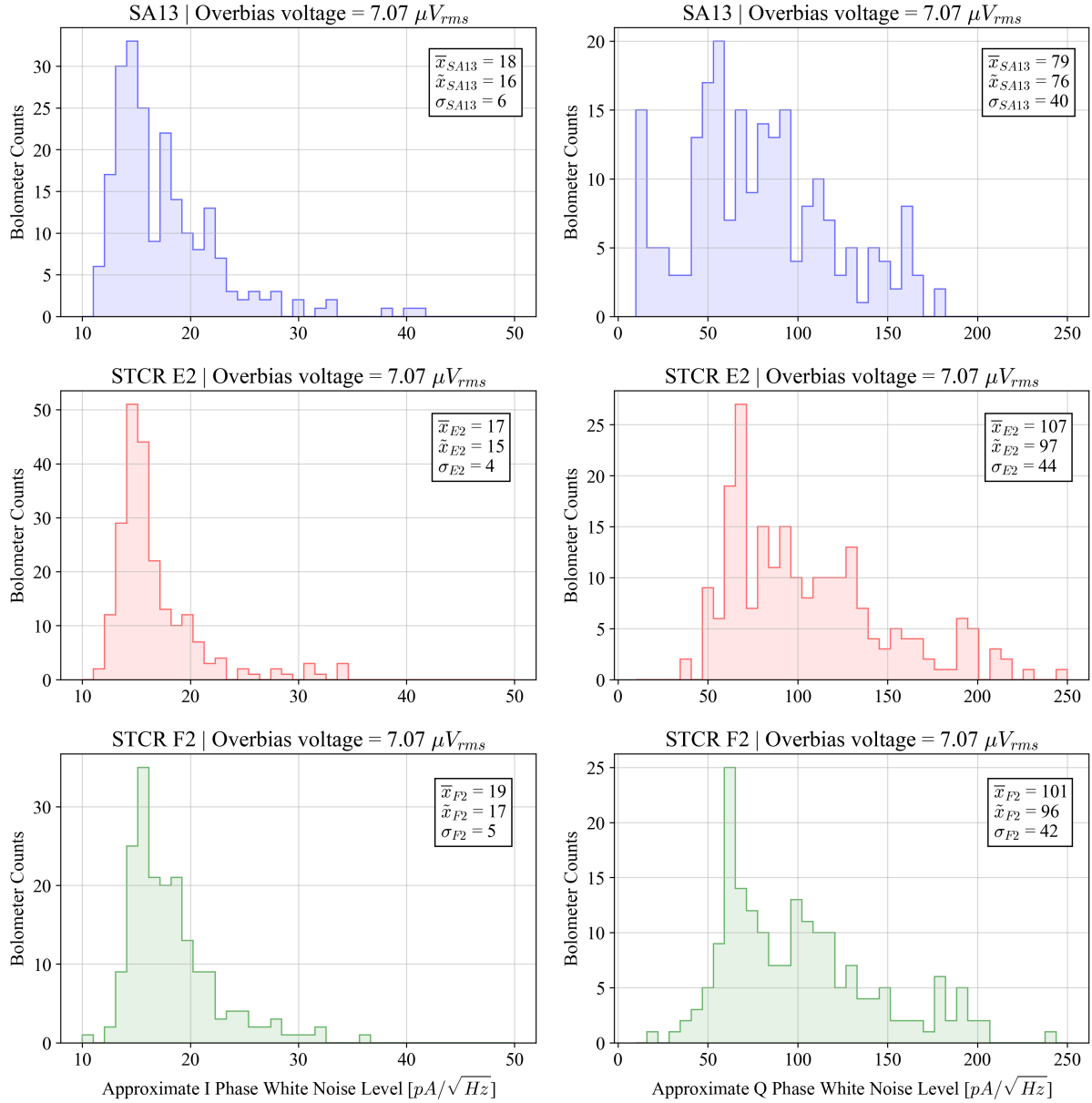


Figure 4.14: Comparison of the typical carrier overbias voltage demodulated noise levels for the NIST SA13a and Star Cryoelectronics E2 and F2 SQUIDs. (*Left*) I phase noise. (*Right*) Q phase noise.

DfMUX, we understand that the majority (and sometimes all) of the science signal lies in the I phase, so current implications are that the Q phase noise increase will not significantly affect observations.

4.2.3 Frequency Spectrum Effects from Bolometer Biasing

To attempt to quantify the amount of un-nulled current in the SQUID input coil during overbiasing we measured a raw SQUID voltage timestream after the carriers are turned on, Fourier transform, and convert to I_{in}^{rms} by dividing by the transimpedance. In order to minimize confusion due to too many channels being active, only five bolometers with bias frequencies around 3 MHz were biased. Here we present results from only one SQUID of each type. Figures 4.15, 4.16, and 4.17 show the results of this test with measurements of the noise floor, I_{in}^{rms} (obtained by integrating the entire ASD), and the number of un-nulled narrow lines in the ASD. The latter metric provides insight into the number of crosstalked and IMD tones which begin to appear and cannot be nulled by DAN as the carrier bias is ramped.

While the RMS values obtained in this test are not indicative of un-nulled input coil currents large enough to cause transimpedance degradation and nonlinearities (as discussed in Section 4.2.1), it should be emphasized that only 15 channels (out of a maximum of 8400 possible channels in a full POLARBEAR-2 focal plane) being run in this test. The ternary IMD products, the number of which scales as the cube of the number of tones, are generally the first order contribution because they are the first to routinely land below the bandwidth-limiting filtering (cutoff around 7 MHz). Typically these are non-negligible

only for tones within a comb, with nearest-neighbor LC chip/SQUID crosstalk the next leading source of tones participating in IMD product generation. The broadside coupling of nearest-neighbor LC chips leads to significant direct tone pickup between the SQUIDs running these LC combs, i.e. when biased, the resonant frequencies of chip A appear in the spectrum of chip B, and vice-versa. Less prominent but still apparent, is the appearance of lines in a given SQUID's spectrum corresponding to nearly all LC bias frequencies intrinsic to all other chips being run on a single SQUID card. Additionally, for every line corresponding to a crosstalked or IMD tone, we can see in Figures 4.15, 4.16, and 4.17, both the first and second harmonics in the ASDs, as well as a significant $1/f$ or $\lambda/2$ component in the spectra as the carrier voltage is increased.

To summarize, there are many mechanisms which can cause additional SQUID loading during operation, very few of which DAN is capable of nulling. In fact, if it is the case that a spurious tone can be nulled, this tone would participate in direct science signal contamination since the error signal DAN acts on is directly related to what we take as the CMB signal. In any event, RMS levels of un-nulled current approaching a significant fraction of a μA may be possible in the POLARBEAR-2 DfMUX readout system during observation. A summary of the metrics used in characterizing the These tests (i.e. Figures 4.15, 4.16, and 4.17) indicate that, at a typical overbias voltage of $\sim 7 \mu\text{V}_{rms}$, the SA13a design will experience a $\sim 50\%$ lower RMS flux burden than either Star Cryoelectronics device – as long as these results scale from the five bolometers biased in this test to a full comb during observation. All devices display a monotonically increasing RMS input coil current, noise floor, and number of significant peaks in the spectrum.

SA13_041.6 | SQUID Spectrum vs Overbias Amplitude (Bolos 20-24)

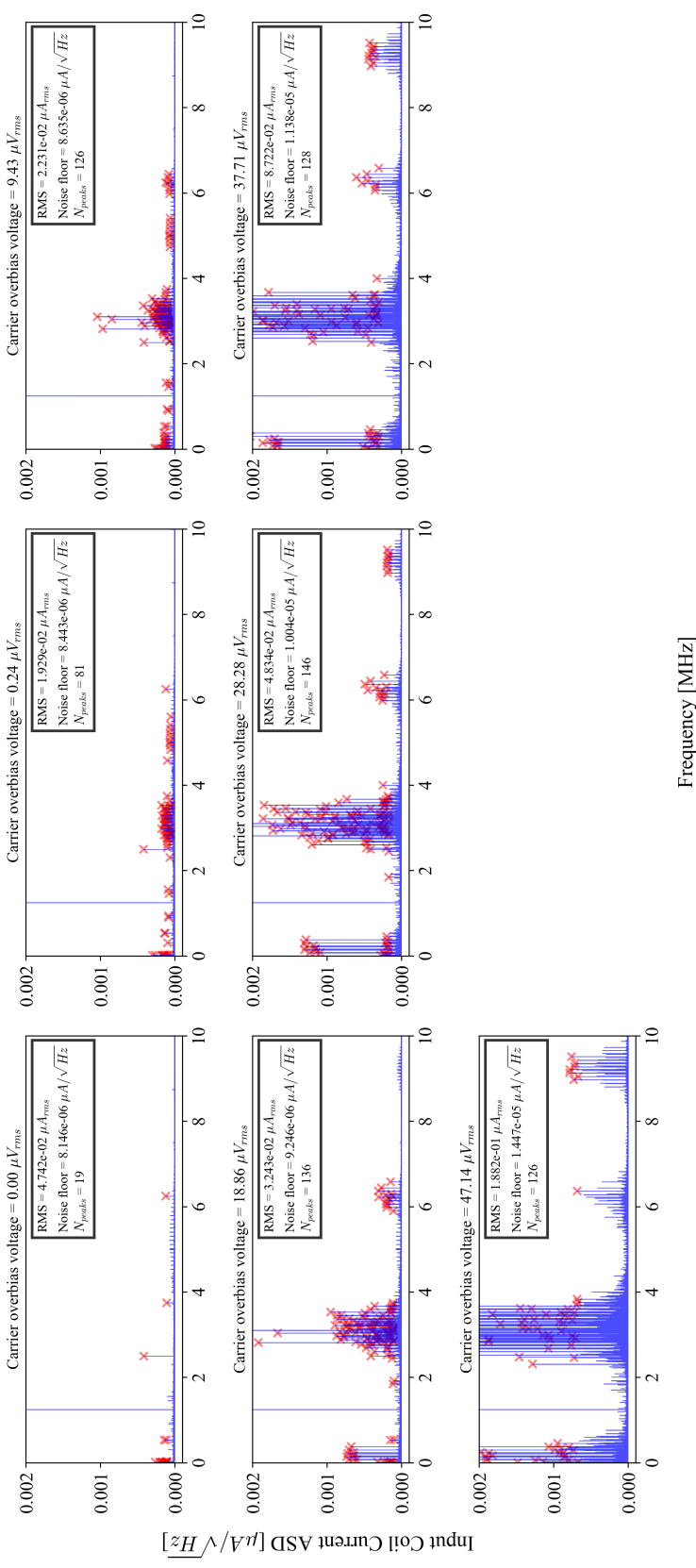


Figure 4.15: Analysis of the SQUID spectrum while overbiasing five bolometers on all evaluation devices. In this measurement a carrier voltage is applied to five bolometers with bias frequencies near 3 MHz and a timestream of the SQUID output voltage is sampled at 20 MHz, Fourier transformed, and converted to a current ASD with the measured Z_t . At each bias voltage the RMS value (calculated by integrating the complete spectrum), noise floor, and number of significant lines/peaks are quantified. For the latter calculation, only peaks which are separated by 100 Hz and whose height corresponds to 8σ significance, are counted.

STCR_002.8 | SQUID Spectrum vs Overbias Amplitude (Bolos 20-24)

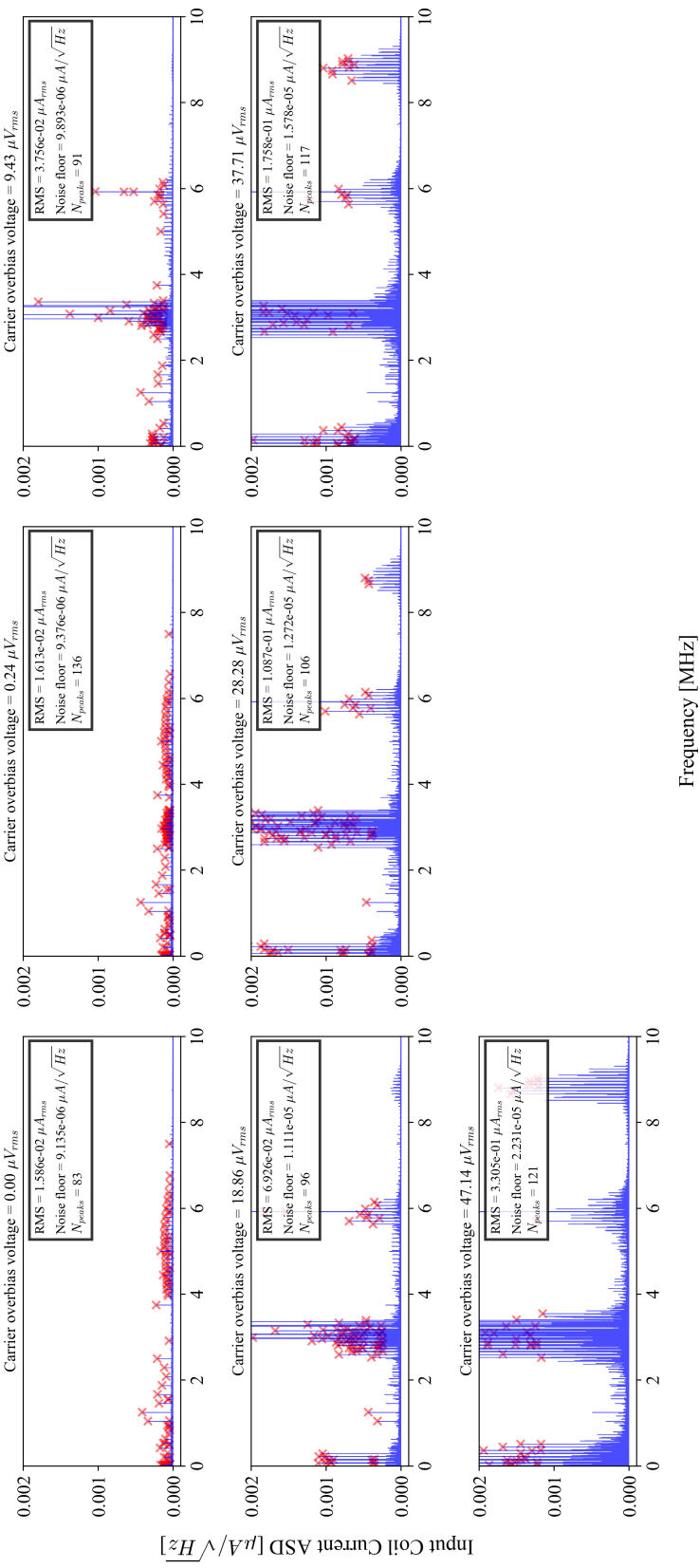


Figure 4.16: Analysis of the SQUID spectrum while overbiasing five bolometers on all evaluation devices. In this measurement a carrier voltage is applied to five bolometers with bias frequencies near 3 MHz and a timestream of the SQUID output voltage is sampled at 20 MHz, Fourier transformed, and converted to a current ASD with the measured Z_t . At each bias voltage the RMS value (calculated by integrating the complete spectrum), noise floor, and number of significant lines/peaks are quantified. For the latter calculation, only peaks which are separated by 100 Hz and whose height corresponds to 8σ significance, are counted.

STCR_003.4 | SQUID Spectrum vs Overbias Amplitude (Bolos 20-24)

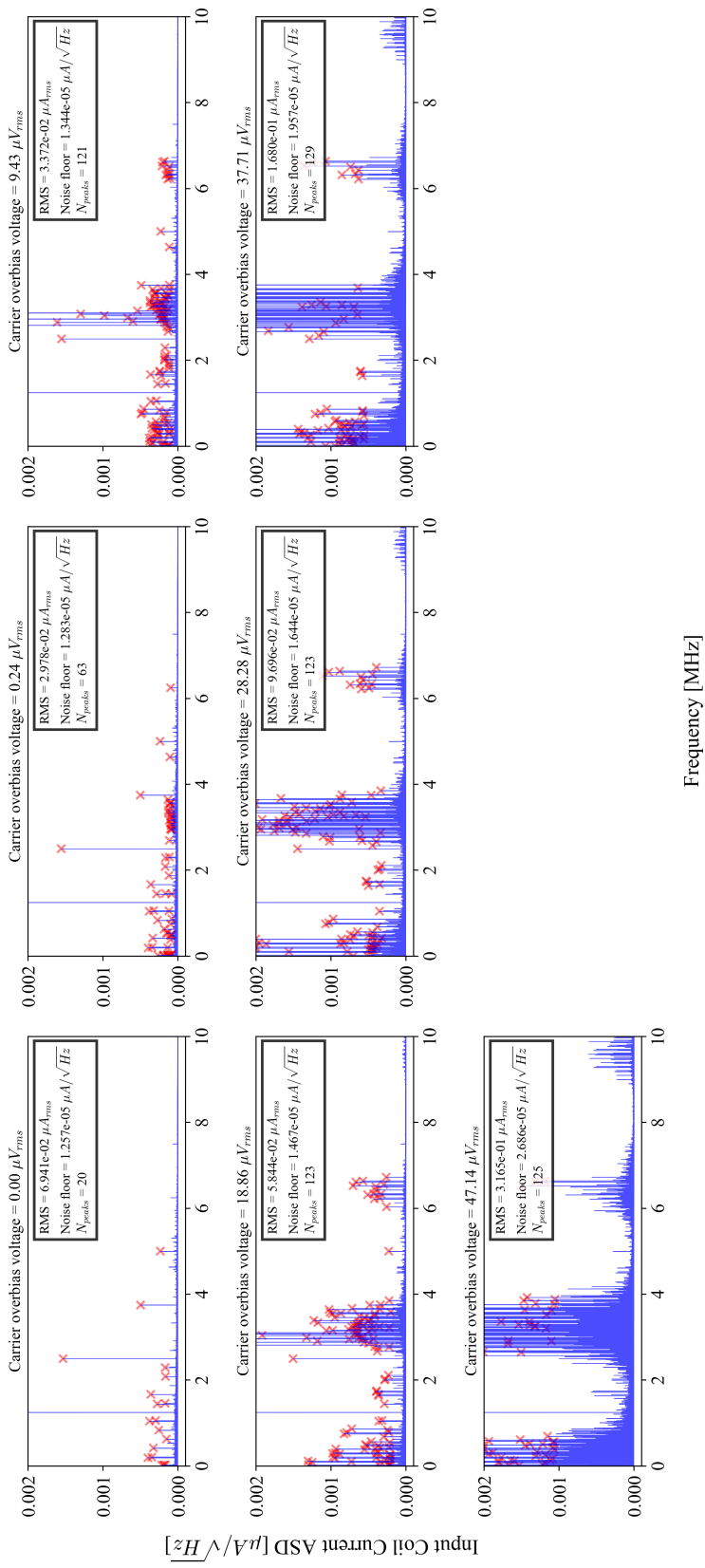


Figure 4.17: Analysis of the SQUID spectrum while overbiasing five bolometers on all evaluation devices. In this measurement a carrier voltage is applied to five bolometers with bias frequencies near 3 MHz and a timestream of the SQUID output voltage is sampled at 20 MHz, Fourier transformed, and converted to a current ASD with the measured Z_t . At each bias voltage the RMS value (calculated by integrating the complete spectrum), noise floor, and number of significant lines/peaks are quantified. For the latter calculation, only peaks which are separated by 100 Hz and whose height corresponds to 8σ significance, are counted.

4.2.4 Current Sharing Measurements

A final characterization comparing NIST SA13a and the Star Cryoelectronics designs was direct measurements of the current sharing enhancement factor Γ , since this was the primary motivation for initiating the search for a replacement SQUID design. Additionally, using the current sharing measurements we obtained estimates for the effective input coil inductance as, in addition to the design value of the on-chip coil, there are contributions from stray inductances due to wirebonds and traces on the SQUID card. Γ can be measured in two ways with the stage heated to 600 mK: (1) using the low carrier overbias voltage noise measurement, and (2) by taking a nuller network analysis measurement. For both methods we simply fit

$$\Gamma = \frac{|R_{bolo} + R_{bias} + i\omega L_{in,eff}|}{R_{bolo} + R_{bias}} \quad (4.1)$$

to the data, where $R_{bias} = 30 \text{ m}\Omega$ and $R_{bolo} = 1 \Omega$. Figure 4.18 shows the low amplitude overbias measurement.

The nuller network analysis measurement is complicated by the non-negligible output impedance of the SA13a and Star Cryoelectronics SQUIDs, which is much higher than for the SA4 (see Table 4.1). In combination with the 300 K to 4 K wiring parasitic capacitance, this forms a low pass filter (referred to as the “cold transfer function”) and can modify the total transfer function by more than 100%. This is demonstrated in Figure 4.19, and in the case of Al LC combs may be measured above the LC T_c of 1.2 K. Once the nuller network analysis is corrected by the measured cold transfer function, the current sharing may be measured by taking the value of the nuller network analysis at the previously-determined

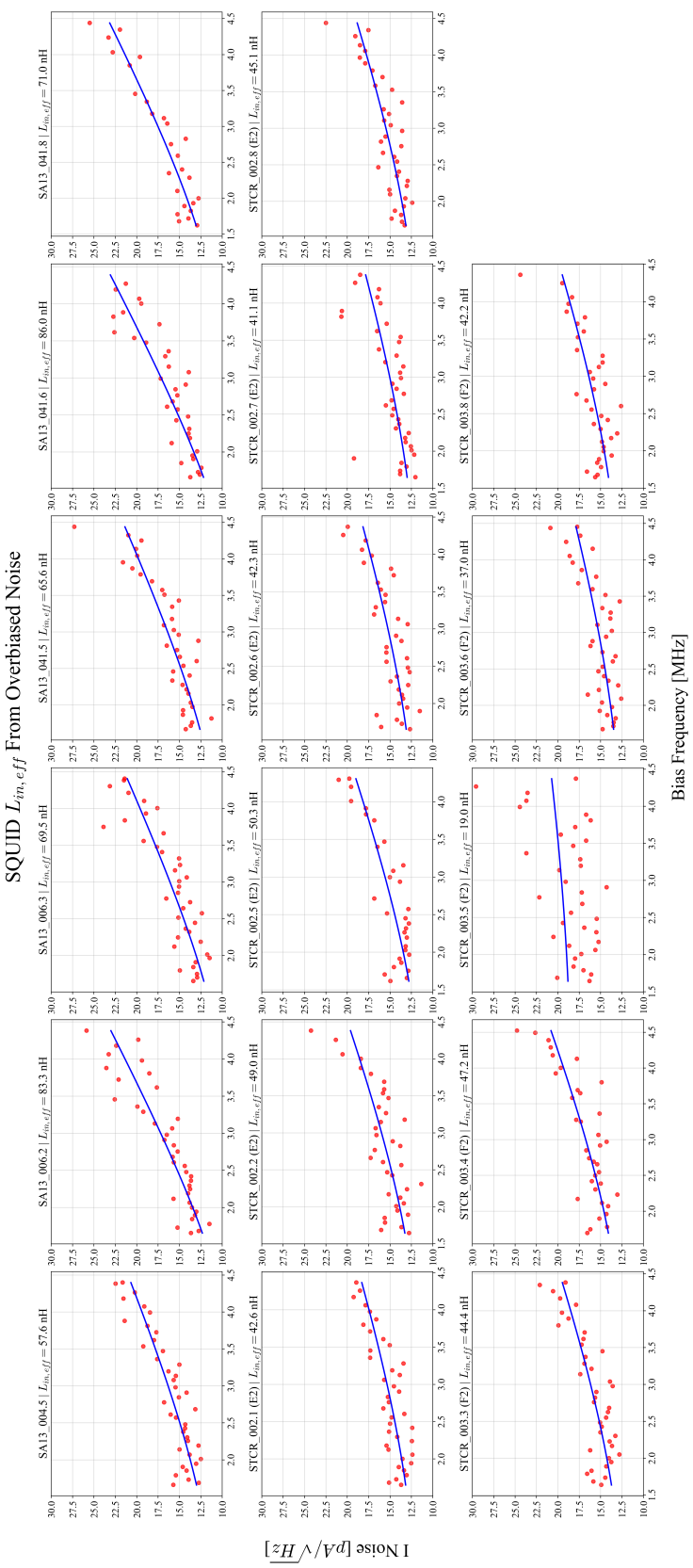


Figure 4.18: Effective SQUID input coil inductance measurement using current sharing noise enhancement with the low amplitude carrier overbias voltage. The mean SA13a value is $L_{in,S13a} = 72 \text{ nH}$, while the mean Star Cryoelectronics values are $L_{in,E2} = 45 \text{ nH}$ and $L_{in,F2} = 43 \text{ nH}$ (we omit STCR_003.5 as an outlier).

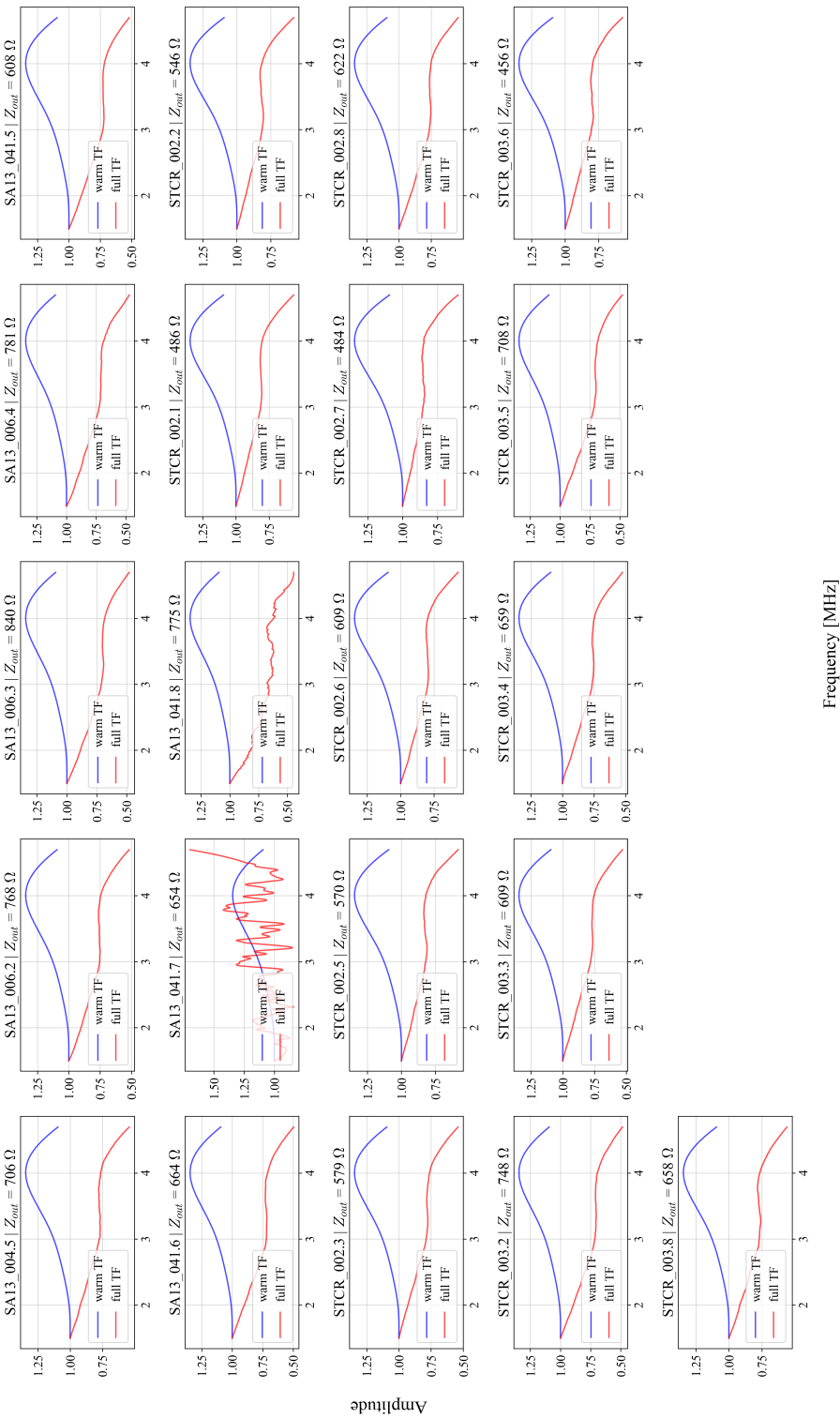


Figure 4.19: Comparison of the warm-only and full transfer functions for NIST SA13a and Star Cryoelectronics SQUIDs. Z_{out} of more than $\sim 100 \Omega$ clearly adds a significant modification to the full transfer function when compared to that measured only up to the cryostat input.

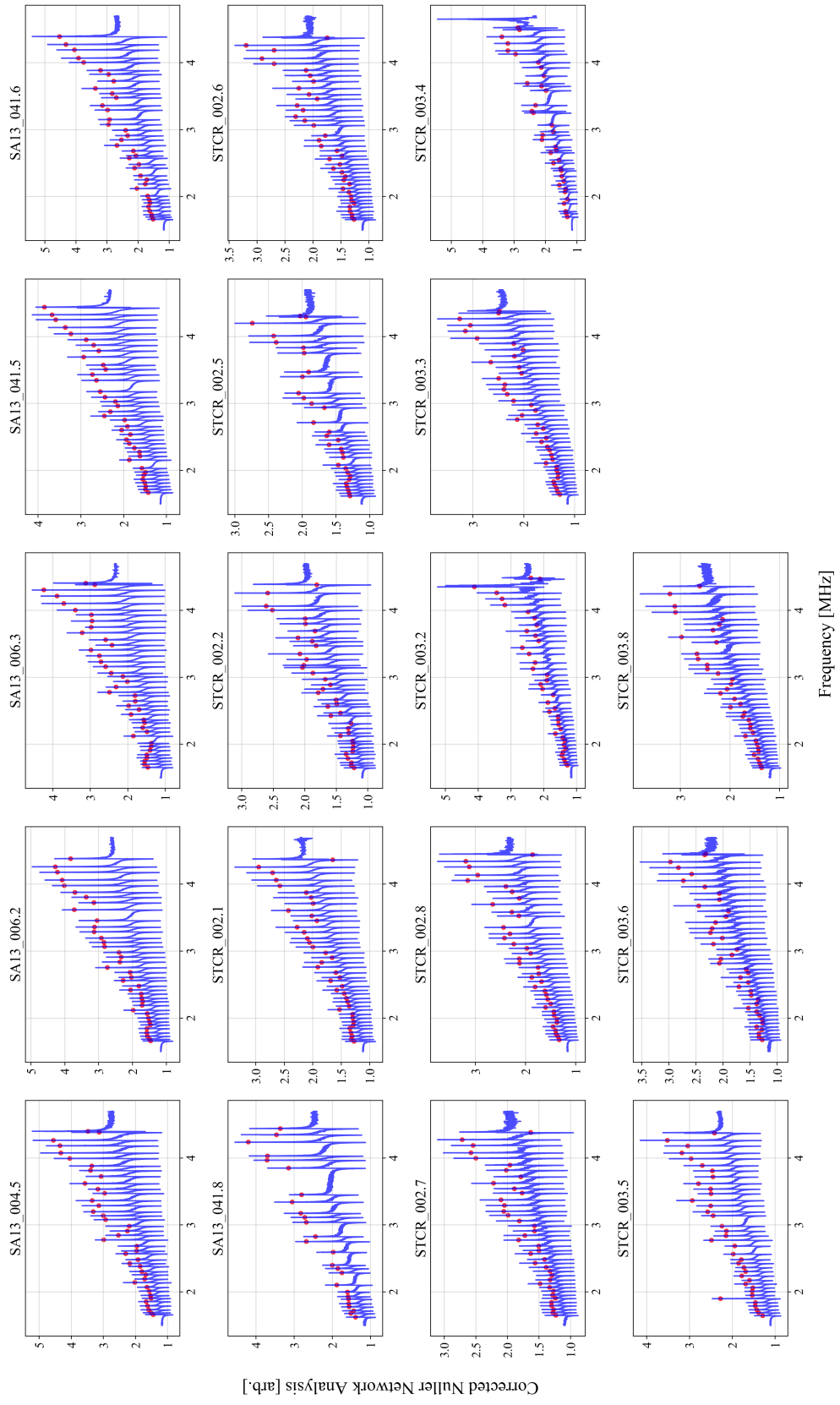


Figure 4.20: Nuller network analysis after correction for the cold transfer function, which is unique to each SQUID. Red points show the selected bias frequencies for each comb. The general trend upwards with frequency is due to current sharing.

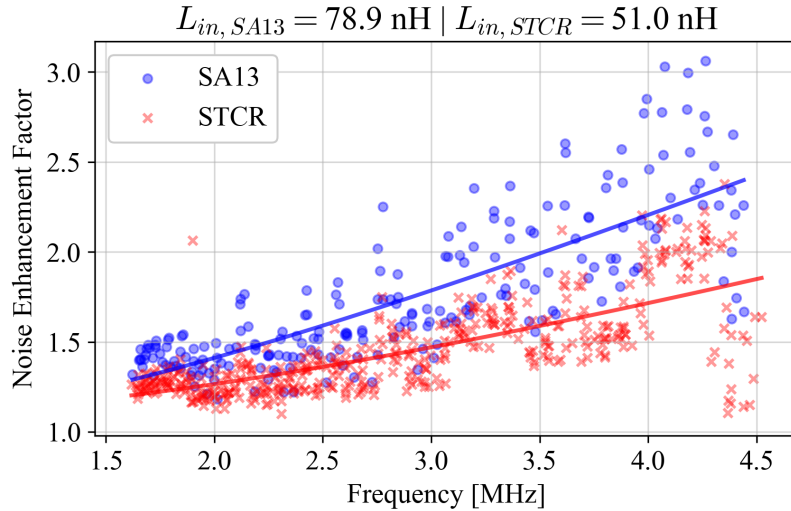


Figure 4.21: Channel-selected current sharing enhancement measurement via the corrected nuller network analysis. Data is split into channels operating on NIST SA13a and Star Cryoelectronics SQUIDs to provide an estimate to $L_{in,eff}$. The solid lines show the best fit to the noise enhancement factor Γ defined in Equation 4.1.

bias frequency for each channel. We then perform the same fit as with the low voltage overbias measurement. Figure 4.20 shows the corrected nuller network analysis, while Figure 4.21 shows the enhancement factor at each channel's bias frequency.

4.2.5 Conclusions and Device Selection

The last few sections summarized extensive device testing in order to select the best replacement for the originally planned NIST SA4 SQUIDs. The NIST SA13a and two Star Cryoelectronics variants were considered. No clear and significant advantage is given to any SQUID in terms of their linear dynamic range, overbiased noise performance, and susceptibility to loading once detector biases are activated. The largest benefits are actually summarized in Table 4.1, favoring the Star Cryoelectronics designs in terms of Z_t , Z_{out} ,

and L_{in} . Considering the estimates obtained for the effective input coil inductance it is not surprising that the low overbias voltage noise measurements favor the Star Cryoelectronics devices. This is the most faithful measurement of the readout-only noise contribution. Additionally, this leads to $\sim 50\%$ lower current sharing near the top of the readout band (4.5 MHz) for Star Cryoelectronics SQUIDs. A final item not discussed in the preceding sections is the existence of transient features/discontinuities in the $V - \Phi$ curves for the F2 SQUIDs, which are not present for the E2 type.

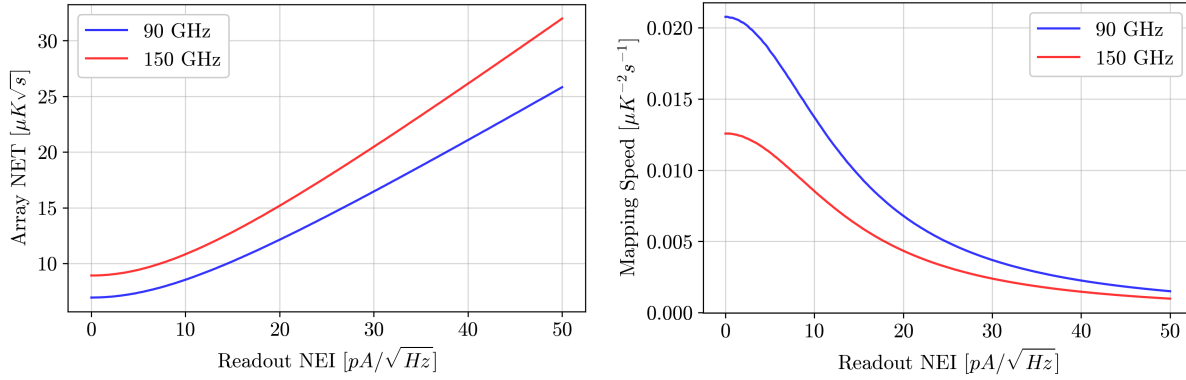


Figure 4.22: BoloCalc simulations for the POLARBEAR-2b NET and mapping speed as a function of the total readout (current) noise. Use of the SA4 SQUID design results in a typical noise level of 40 pA/ $\sqrt{\text{Hz}}$, while the DfMUX lower limit set by noise referral from the warm electronics is around 8 pA/ $\sqrt{\text{Hz}}$. Based on lab testing results, both the SA13a and Star Cryoelectronics SQUIDs display an expected noise level of ~ 15 pA/ $\sqrt{\text{Hz}}$.

Estimates for the achievable POLARBEAR-2b NET and mapping speed can be obtained using the BoloCalc simulation software package [111]. Additionally, these quantities can be obtained with respect to varying a parameter of interest. In this case we would like to know the effect on the total readout noise level in pA/ $\sqrt{\text{Hz}}$ as a result of current sharing and a given SQUID design and/or expected performance. Figure 4.22 shows the results of these simulations. Further reduction of the readout noise level is non-trivial, often

installation-specific, and would result in gains of only 10s of percent in sensitivity. In light of these results, the Star Cryoelectronics E2 devices were chosen for the POLARBEAR-2b receiver.

Chapter 5

Polarbear-2b Full Receiver

Integration and Final Commissioning

Always eat the mystery meat.

— Adapted from the teachings of Anthony Bourdain

In this chapter we present the latest work in final assembly and testing of the POLARBEAR-2b receiver before deployment to the Atacama site in Chile. From a hardware perspective, this involved integration of the backend and optics tube cryostats and building up the complete focal plane array of seven detector modules with their accompanying readout. Beyond simple cryogenic demonstration of sufficient cooling of critical components (lenses, the lyot, the cryogenic HWP, millikelvin stages, the SQUID stage etc.), a number of component-specific tests are required. Individual components whose failure can result in significant observational detector yield reduction (number of TESs which can be properly biased and read out) are the most critical to validate in lab. Additionally, verification of

the receiver focus and optical alignment must be demonstrated before deployment. For orientation purposes, Figure 5.1 shows the section view of the complete POLARBEAR-2b receiver with numerical labels for each component which are listed in Table 5.1.

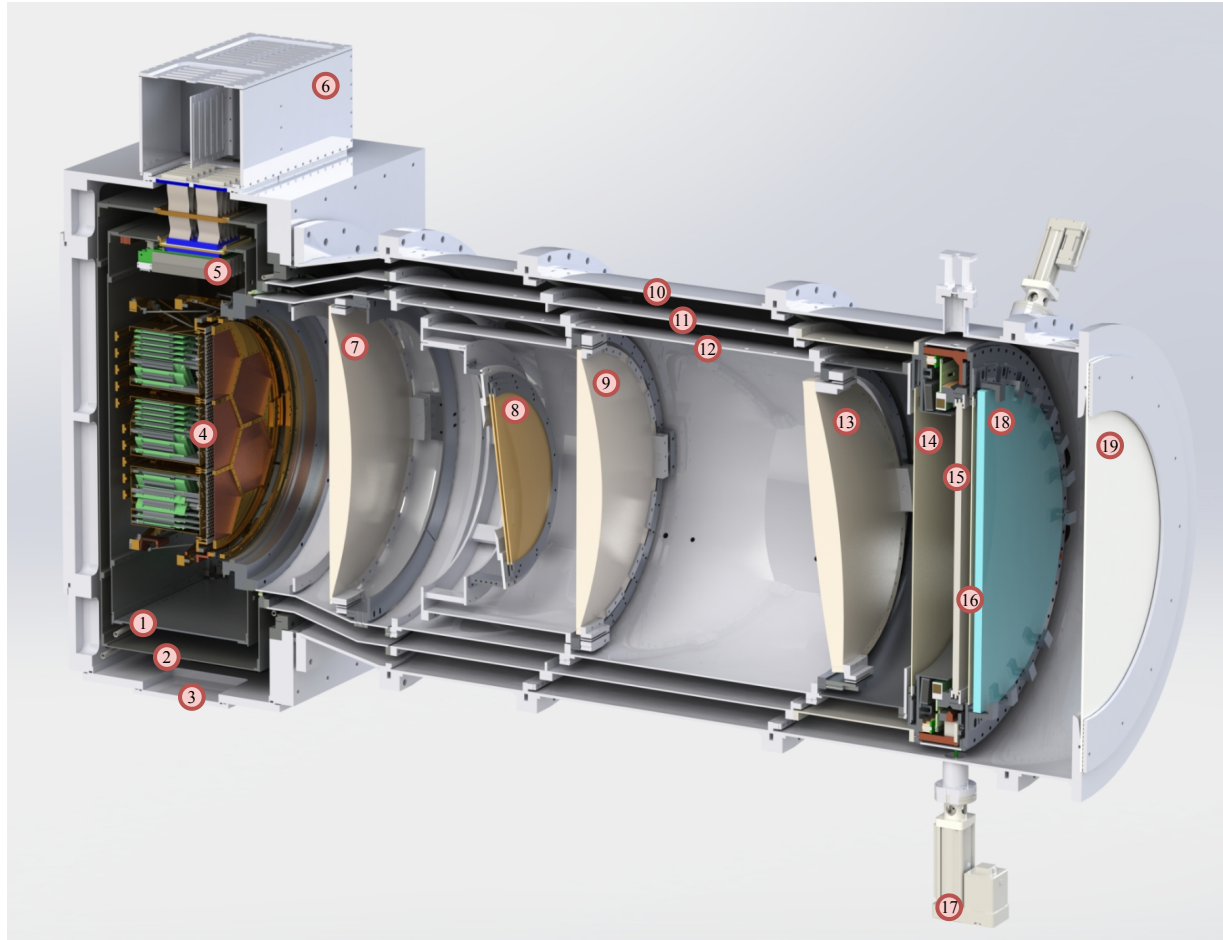


Figure 5.1: Section view of the POLARBEAR-2b receiver CAD with labels for key components. Table 5.1 gives the names of each labeled component. The POLARBEAR-2 lenses and 50 K IR-blocking filters are made of alumina ceramic.

Table 5.1: POLARBEAR-2b receiver components corresponding to labels in Figure 5.1.

Label	Component
1	Backend 4 K shell
2	Backend 50 K shell
3	Backend 300 K shell
4	FPT
5	SQUID card
6	SQUID controller electronics rf-tight enclosure
7	Collimator lens
8	Lyot stop
9	Aperture lens
10	Optics tube 300 K shell
11	Optics tube 50 K shell
12	Optics tube 4 K shell
13	Field lens
14	Detector side IR filter
15	CHWP rotor (sapphire)
16	Sky side IR filter
17	CHWP rotor gripper motor
18	Radio transmissive MLI (RTMLI)
19	Ultra-high molecular weight polyethylene (UHMWPE) window

5.1 Backend and Optics Tube Integration

Cryogenic validation of the the POLARBEAR-2b optics tube in its standalone configuration proved problematic for a variety of reasons. The primary symptom was elevated base temperatures indicating significant excess loading, mainly on the PTC first stage, beyond what was expected based on successful operation of the POLARBEAR-2a optics tube. This loading was most likely from underperformance of the MLI blankets at the edges where the tube sections of the 50 K radiation shields are mated. For integration with the backend we decided to add MLI “bridge” blankets (10 layers) to cover the bare mating

flanges and overlap the main 50-layer blankets on each tube by \sim 5 cm [112]. Figure 5.2 shows one such blanket installed during receiver assembly.

5.1.1 Dark Receiver Cryogenic Validation

The first integrated cooldown (run16b) was performed without the CHWP and a metal blankoff over the aperture, both at 50 K and 300 K, to establish a baseline for cryogenic performance without optical loading. Instead of the low pass MMF which will be located at the Lyot stop in the field, a piece of 1 cm thick nylon was installed as a stopgap attenuating filter to mitigate in-band detector loading and IR loading of the detector stage. Base temperatures for this run are listed in Table 5.2.

Load curves were measured in run16b for the field lens and Lyot using heaters on each elements, to allow measurement of the optical power load on each element once the receiver was optically coupled in run17b. These are shown in Figures 5.3 and 5.4. These also provide a measurement of the performance of the clamped 6N Al thermal straps which heatsink the lenses, shown in Figure 5.6 for the field lens. Temperatures of the optical elements in any CMB receiver are a factor in overall instrument sensitivity [111], so ensuring their base temperatures are sufficiently low is important. However, both the elevated readout noise levels (compared to the original design) and the fact that the sky temperature is \sim 15 K and the receiver optics are not lossy, the sensitivity of the POLARBEAR-2 receivers is largely independent of elevated optical element temperatures below \sim 10 K. This can be seen in Figure 5.5. Regardless, effort has been made to increase the efficacy of the heatstraps of all optical elements to lower temperatures when the receiver is deployed to

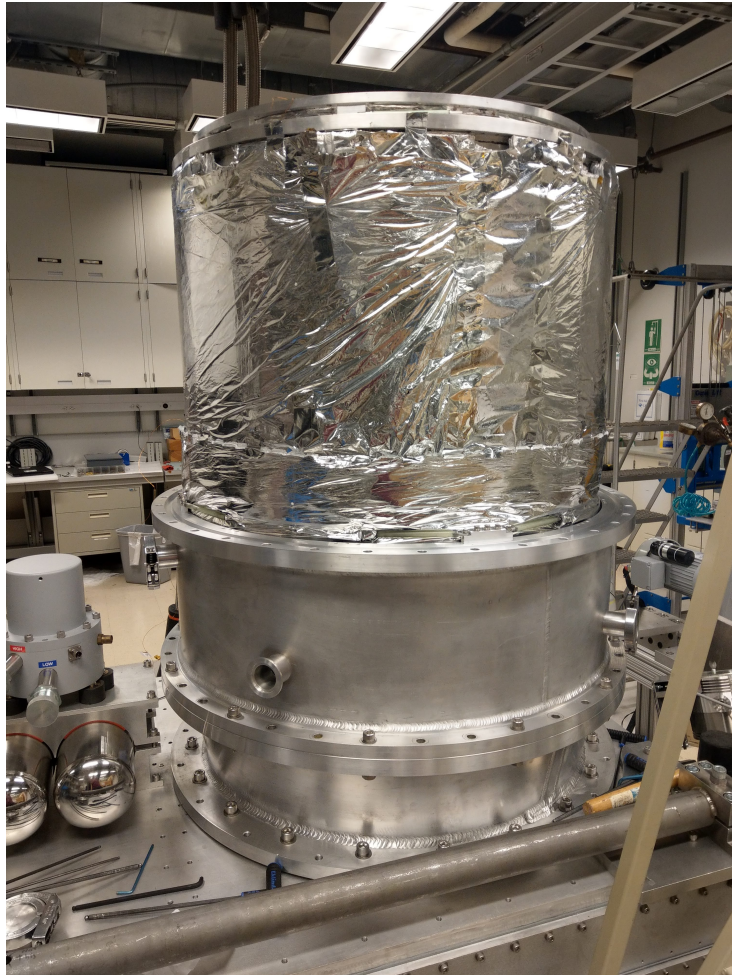


Figure 5.2: Photo of the POLARBEAR-2b receiver during assembly, showing the MLI bridge blanket installed on the lowest visible 50 K flange interface but not on the uppermost.

the site.

5.1.2 Cryo-optical Receiver Validation

With the largely successful dark, integrated cooldown of run16b the next step was to demonstrate so-called “cryo-optical” performance. The configuration for this run (run17b) is primarily the same as for run16b except that we install the CHWP and window to allow

Table 5.2: Integrated POLARBEAR-2b base temperatures for run16b and run17b. For run16b, the optics tube 4 K coldhead cooled below the coldest temperature in the thermometer calibration curve so we report an upper bound.

Key	Location	Run16b	Run17b
	UC Head	0.236	0.252
1	Bolostage	0.238	0.259
	IC Head	0.290	0.299
	He4 Head	0.835	0.840
	Booster Head	0.875	0.899
	Backend 4 K Coldhead	3.09	3.22
	4 K Mainplate	3.20	3.40
2	SQUID Bar	3.49	3.78
3	SQUID Card	3.55	3.84
	Backend 50 K Coldhead	35.3	38.3
4	Backend 50 K Front	51.9	57.8
5	Backend 4 K Front	3.65	3.9
	Optics Tube 4 K Coldhead	<3.4	3.42
	Optics Tube 50 K Coldhead	35.3	38.3
6	Collimator Lens	4.32	4.92
7	Optics Tube 4 K Bottom	4.33	5.13
8	Optics Tube 50 K Bottom	52.3	63.5
9	Lyot Stop	4.30	5.78
10	Aperture Lens	4.45	5.08
11	Field Lens	6.17	8.95
12	CHWP Solenoid		54.6
13	CHWP YBCO		58.1
14	CHWP 50 K Baseplate		50.9
15	CHWP Rotor		58.1
16	Sky Side Alumina IR Filter Baseplate		67.4
17	Sky Side Alumina IR Filter		67.3

optical power into the receiver. This configuration was meant to demonstrate adequate IR filtering at the sky side of the CHWP (50 K) by measuring the lens base temperatures. The majority of this filtering is achieved with radio transmissive MLI (RTMLI), and a 2 mm thick alumina plate mounted on the front of the CHWP. The POLARBEAR-2 RTMLI

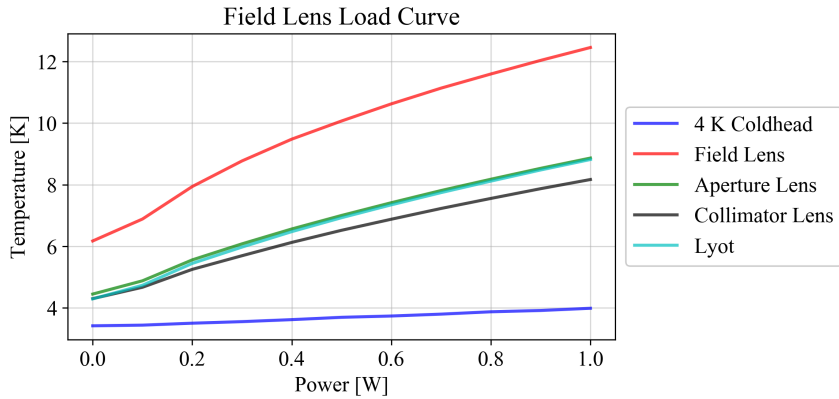


Figure 5.3: Run16b field lens load curve taken using a heater on the outer diameter of the lens. Temperatures of other optical elements are measured for completeness. The 4 K coldhead is that of the optics tube PTC. The backend temperatures are largely unaffected by the power deposited while taking optical element load curves.

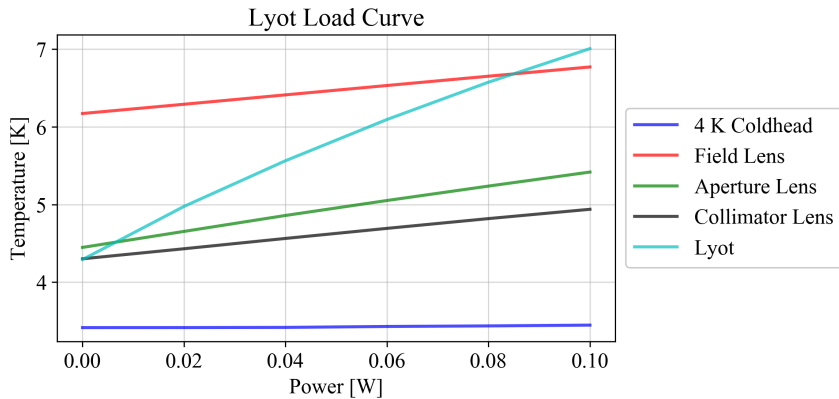


Figure 5.4: Run16b Lyot load curve taken using a heater on the outer diameter of the nylon disk. Temperatures of other optical elements are measured for completeness. The 4 K coldhead is that of the optics tube PTC. The backend temperatures are largely unaffected by the power deposited while taking optical element load curves.

consists of a series of 2 mm thick foam circles (8 – 10 pieces/layers) loosely mounted on top of the alumina sky side filter. RTMLI acts in a similar fashion as traditional MLI constructed from metalized plastic layers (discussed in Section 3.2.3), where each layer acts as an approximately isolated radiation shield with thermal endpoints of \sim 50 K and 300 K — with the key difference that the foam is transmissive to radio frequencies. For this run,

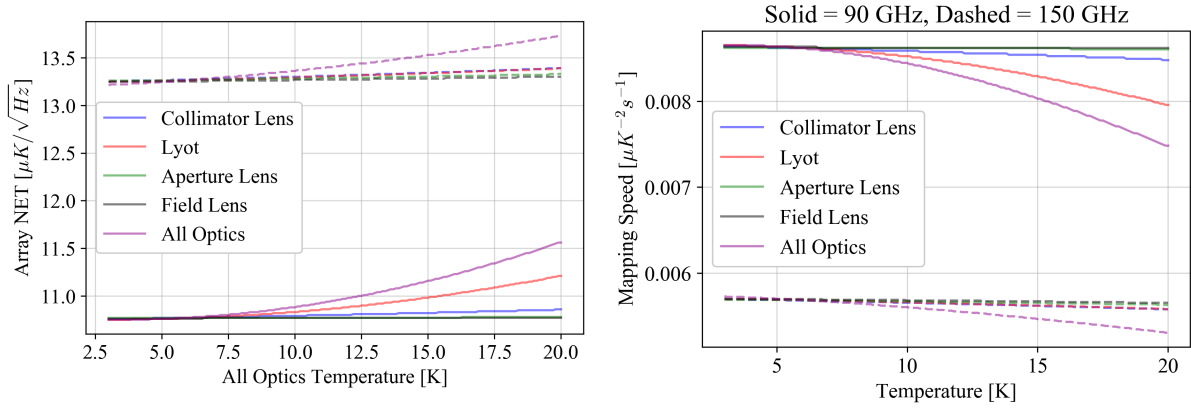


Figure 5.5: BoloCalc simulation of the POLARBEAR-2b sensitivity as a function of various optical element temperatures [111]. (*Left*) shows the array NET, while (*right*) shows mapping speed. By far the largest degradation is due to elevated temperatures at the Lyot, although this effect is still only a few percent if the Lyot climbs to ~ 10 K.



Figure 5.6: Photos of the POLARBEAR-2b field lens on its mounting ring. Heatsinking for all three lenses and both 50 K IR filters is achieved by clamping layers of 6N Al ribbons to the lens and their mounting rings.

the detector side alumina filter was not installed due to manufacturing delays.

Table 5.2 also shows the base temperatures for run17b and the cooldowns for the backend and optics tube are shown in Figures 5.7 and 5.8. Clearly, an appreciable amount of heating of the optical elements occurs once the receiver is optically coupled (~ 200 mW to the field lens based on Figure 5.3), however, as demonstrated in Figure 5.5, these

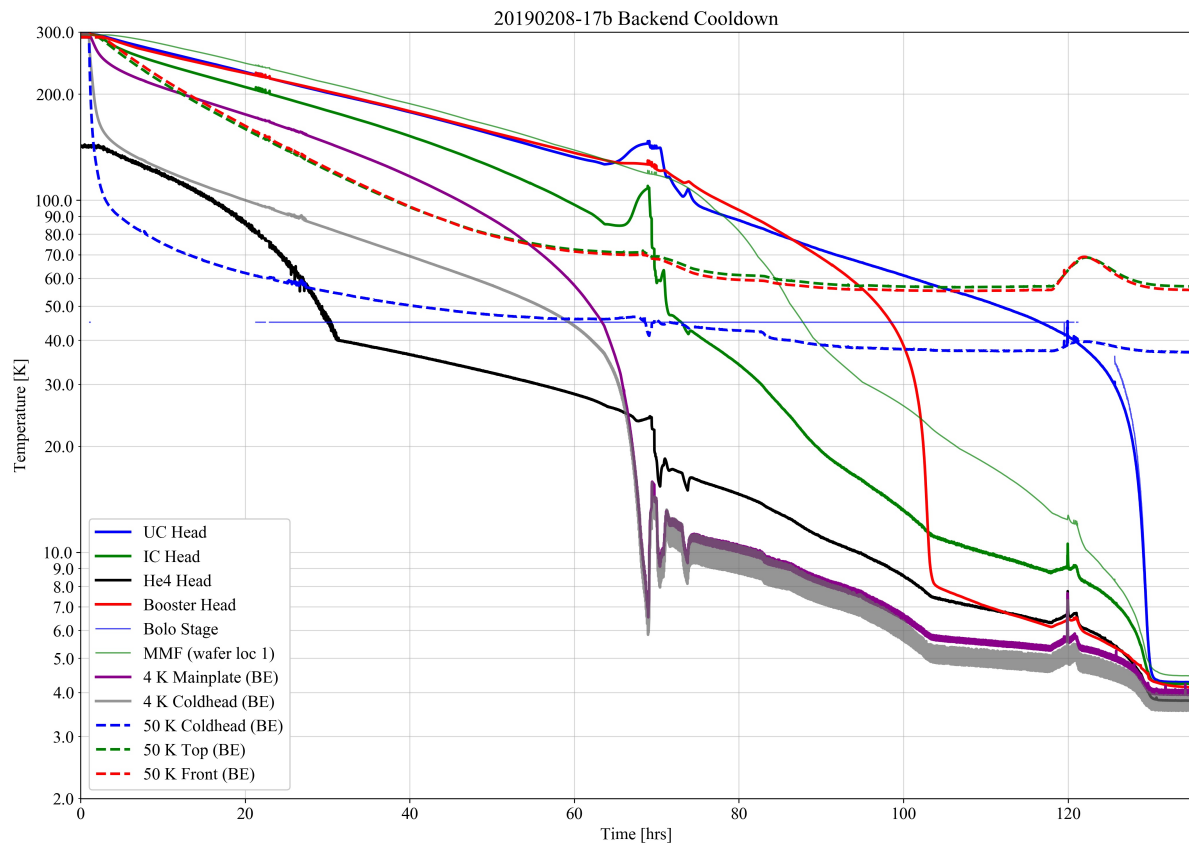


Figure 5.7: Cooldown plot of the POLARBEAR-2b backend during the cryo-optical validation run (run17b). Base temperatures were reached at ~ 127 hrs and are dominated, as expected, by cooling the FPT through the He10 fridge.

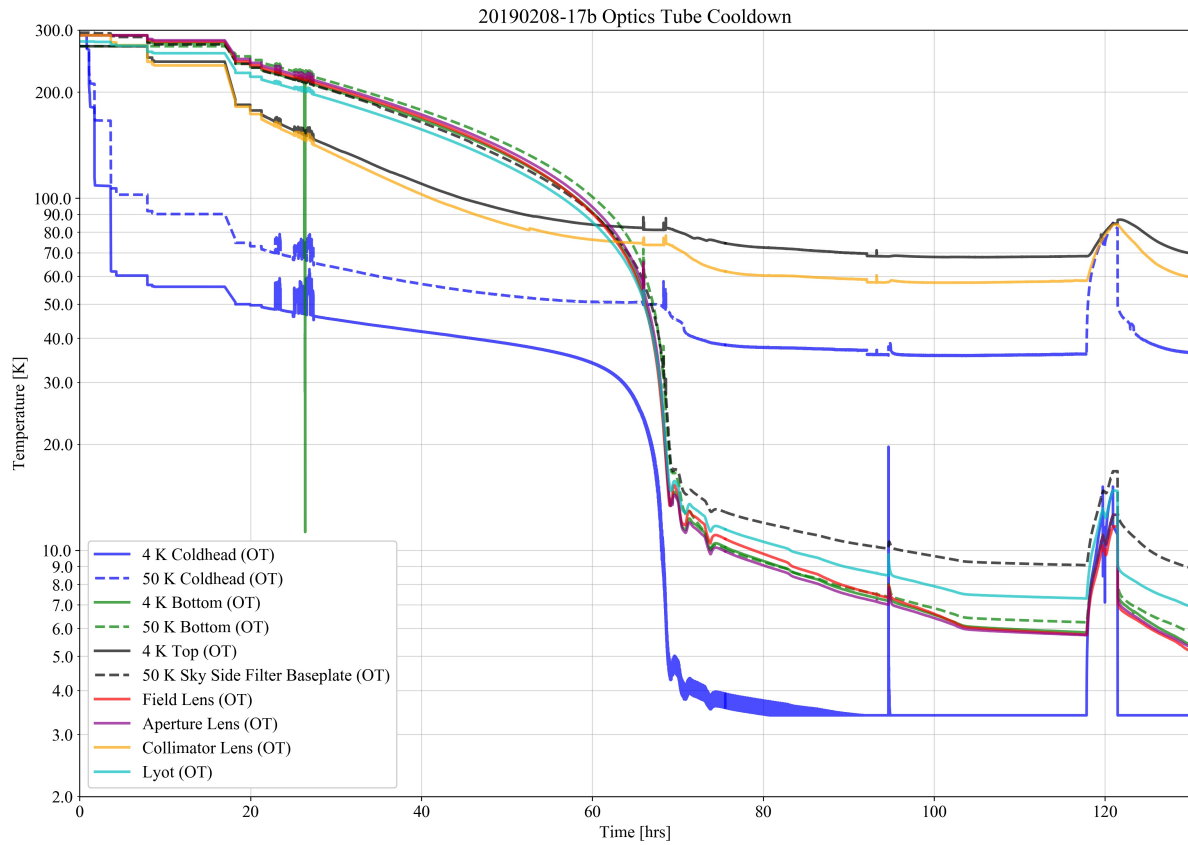


Figure 5.8: Cooldown plot of the POLARBEAR-2b optics tube during the cryo-optical validation run (run17b). Base temperatures were reached after ~ 90 hrs. The heating feature beginning just before 120 hrs was from deliberately turning off the optics tube PTC in order to raise the CHWP rotor above the YBCO T_c of 93 K in order to re-center the rotor using the gripper motors.

temperatures would result in percent-level or lower degradations in instrument sensitivity. Another potential cause for concern is the elevated UC head temperature, indicating $\sim 6 \mu\text{W}$ of additional loading. The focal plane in run16b contained only two detector modules (one partially populated with readout), while for run17b four complete modules were installed, so increased parasitic conductive loading via the readout striplines is expected, but this is less than $1 \mu\text{W}$. The model used to generate the optical loading estimates in Table 3.4 assumes all optics have anti reflection coatings and that the lyot MMF is installed. Without these two key components, the amount of IR which is transmitted from 300 K, through the optical stack, to the bolostage can be significantly higher than designed. A more accurate accounting of optical performance in the run17b configuration estimates $5 - 7 \mu\text{W}$ of loading, which is consistent based on the He-10 load curves in Figure 3.7. From the base temperatures of run17b it is clear that there is room for improvement of both the optical filtering, and the lens heatstraps. The former issue will be solved with the complete AR coated optics, while the latter has both been shown to negligibly affect performance and can easily be improved before final assembly in Chile.

Run17b was also meant to demonstrate operation of the CHWP [83] (i.e. proper cooling and spinning of the rotor), however, a failure in one of the gripper motors resulted in the inability to fully retract the gripper finger. This caused too much friction for the CHWP rotor driver to spin up and complete demonstration of the CHWP could not take place in run17b.

5.2 Final Lab Tests and Deployment

The remaining lab verifications for the POLARBEAR-2b receiver are primarily final checks and integration. This includes validation of CHWP operation, demonstration of optical alignment procedures during assembly that properly focus the receiver, testing and verification of properties of all seven detector modules for the deployed focal plane, and noise and performance checks of the readout system with the Star Cryoelectronics SQUIDs and complete focal plane (a complete focal plane was previously demonstrated in the POLARBEAR-2b backend using POLARBEAR-2a SA13 SQUIDs while screening device wafers for POLARBEAR-2a deployment). All items will be addressed in the final cooldown (run18b) of the POLARBEAR-2b receiver before deployment by the end of 2019.

Chapter 6

Conclusion

*If the business of physics is ever finished,
the world will be a much less interesting place in which to live.*

— John Gribbin

6.1 Current State of the Field

Since the discovery of the CMB in the mid 20th century, the precision to which we have measured the CMB has increased by approximately seven orders of magnitude, which has only recently been sufficient to detect the lensing B-mode signal and place upper bounds on r of 0.06 [34]. The spurious BICEP-2 large scale B-mode detection in 2014 [40] highlighted the need for foreground removal, and the measured amplitude of the lensing B-mode signal [9] mandates sophisticated delensing capabilities for further bounds on r to be possible. Current generation experiments such as AdvACT, BICEP-3/BICEP Array [113], [114], POLARBEAR-2 /Simons Array [4], [13], and SPT-3G possess $\mathcal{O}(10^4)$ detectors

and capabilities for observation at multiple frequencies. Figure 6.1 shows a comparison of current (and some past) CMB polarization experiments and their measurements of the B-mode signal.

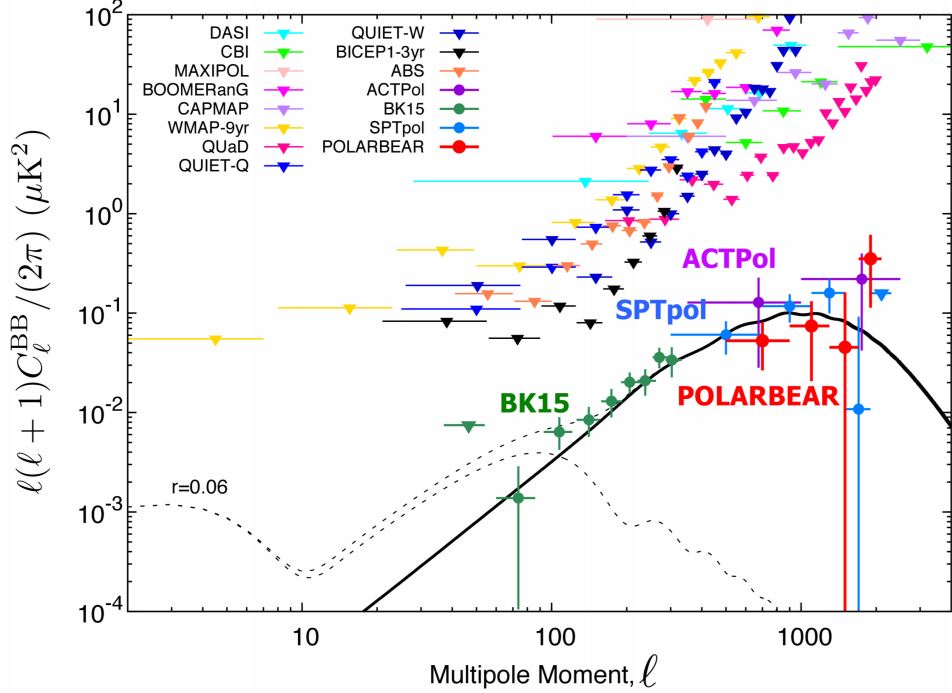


Figure 6.1: Current state of the field of CMB B-mode polarization measurements. Figure provided by Yuji Chinone.

6.2 The Simons Array

As mentioned in Section 2.7, the Simons Array is a third generation CMB polarization experiment which upgrades and expands the single POLARBEAR-1 instrument/telescope to an array of three telescopes – each containing an upgraded POLARBEAR-2 receiver. The Simons Array marks a factor of nearly 20 in terms of increasing the number of detectors over POLARBEAR-1, and expands from the single 150 GHz observing frequency to four

frequencies: 95, 150, 220, and 270 GHz. With these improvements to the focal planes of the POLARBEAR-2 receivers, the Simons Array is poised to make measurements of the CMB polarization map to unprecedented precision.

The first Simons Array receiver, POLARBEAR-2a, was deployed in December 2018 and is expected to begin CMB science observations in the coming months. The telescopes for POLARBEAR-2b and -2c have been deployed and are ready for the integration of their receivers. In this thesis, we presented work towards constructing and validating (in-lab) the POLARBEAR-2b receiver. We detailed the cryogenic design and validation of the backend cryostats for POLARBEAR-2b and -2c: demonstrating a millikelvin fridge hold time plus recycle time in excess of 72 hrs for both cryostats. We also discussed efforts in mitigating excess noise effects present in the DfMUX readout system (current sharing), and have shown that, with a suitable SQUID (the Star Cryoelectronics AR112-EB2 device) to replace the NIST SA4 SQUIDs used originally, the readout noise levels are $\sim 15 - 25 \text{ pA}/\sqrt{\text{Hz}}$ under biases typical during observation. This demonstrates sufficiently low readout noise levels which enable photon-noise-limited observations of the CMB are possible using the POLARBEAR-2b receiver. Finally, we presented initial results from integrating the POLARBEAR-2b backend and optics tube cryostats, which indicate acceptable performance of the cryogenics, the readout system/electronics, and detector arrays after full receiver integration. A final run is required in-lab to demonstrate successful operation of the CHWP, re-validate readout/detector performance with all detector modules and SQUIDs integrated (this was done in a previous run of only the POLARBEAR-2b backend during a run dedicated to performing quality control checks of detector modules deployed with POLARBEAR-2a),

and demonstrate proper optical alignment of the receiver optics. Once these requirements are met, the POLARBEAR-2b receiver will be deployed to the Atacama site in Chile, and science observations are expected to begin by the end of 2019. The POLARBEAR-2c receiver is currently undergoing similar integration and validation at UC Berkeley, and is scheduled for deployment early in 2020.

6.3 Future Experiments

In combination with a need for multiple observing frequencies to enable foreground subtraction, it is also clear that, depending on the science product, a combination of telescope aperture sizes is needed for future experiments hoping to place the best constraints or measurements of a variety of cosmological and fundamental physical parameters. One such example is $\sum m_\nu$, which cannot easily be constrained with large beam sizes since measurements of $\sum m_\nu$ come primarily from sub-degree scale features surrounding galaxies and galaxy clusters. The CMB Stage 4 experiment (CMB-S4) [115] marks an attempt at unifying many of the current field-leading collaborations' efforts in measurements of the CMB from the ground in order to drastically increase the overall program sensitivity. This experiment will combine data from numerous telescope sizes and designs, with a wide range of observation frequencies, and $\mathcal{O}(10^5 - 10^6)$ detectors.

The Simons Observatory (SO) [5] represents a first step towards such an effort and is a unification of the ACT and POLARBEAR/Simons Array collaborations. The SO experimental architecture contains both small aperture (large beam) and large aperture

telescope designs [6] to target science products at their optimal angular scales. Deployment of the first SO telescopes and receivers is expected to begin in just a few years [6].

In order to eliminate atmospheric limitations and obtain full-sky CMB maps, satellite-borne telescopes are necessary. LiteBIRD is one such experiment currently under development and partially funded [116]. The Simons Array is designated as a pathfinder for LiteBIRD, with the intention to use many of the devices and technologies of the POLARBEAR-2 receivers in LiteBIRD. The instrument will observe from the Earth-sun L2 Lagrange point for three years with 15 observing bands spanning 40 – 400 GHz and a total of 2,200 detectors. With a target launch date near the end of the 2020s, LiteBIRD expects to be able constrain r to be less than 10^{-3} . Finally, an exploratory study of a satellite beyond LiteBIRD, PICO, has recently been published [117].

6.4 Acknowledgment

Figure 6.1 was provided by Yuji Chinone.

Bibliography

- [1] L. Howe, C. Tsai, L. Lowry, K. Arnold, G. Coppi, J. Groh, X. Guo, B. Keating, A. Lee, A. May, L. Piccirillo, N. Stebor, and G. Teply, “Design and characterization of the POLARBEAR-2b and POLARBEAR-2c cosmic microwave background cryogenic receivers,” *Millimeter, Submillimeter, and Far-Infrared Detectors and Instrumentation for Astronomy IX*, vol. 10708, 2018.
- [2] S. Takakura, M. A. O. Aguilar-Faúndez, Y. Akiba, K. Arnold, C. Baccigalupi, D. Barron, D. Beck, F. Bianchini, D. Boettger, J. Borrill, K. Cheung, Y. Chinone, T. Elleflot, J. Errard, G. Fabbian, C. Feng, N. Goeckner-Wald, T. Hamada, M. Hasegawa, M. Hazumi, L. Howe, D. Kaneko, N. Katayama, B. Keating, R. Keskitalo, T. Kisner, N. Krachmalnicoff, A. Kusaka, A. T. Lee, L. N. Lowry, F. T. Matsuda, A. J. May, Y. Minami, M. Navaroli, H. Nishino, L. Piccirillo, D. Poletti, G. Puglisi, C. L. Reichardt, Y. Segawa, M. Silva-Feaver, P. Siritanasak, A. Suzuki, O. Tajima, S. Takatori, D. Tanabe, G. P. Teply, and C. Tsai, “Measurements of tropospheric ice clouds with a ground-based CMB polarization experiment, POLARBEAR,” *arXiv e-prints*, Sep. 2018.
- [3] The POLARBEAR Collaboration, D. Barron, K. Arnold, T. Elleflot, J. Groh, D. Kaneko, N. Katayama, A. Lee, L. Lowry, H. Nishino, A. Suzuki, S. Takatori, P. Ade, Y. Akiba, A. Ali, M. Aguilar, A. Anderson, P. Ashton, J. Avva, D. Beck, C. Baccigalupi, S. Beckman, A. Bender, F. Bianchini, D. Boettger, J. Borrill, J. Carron, S. Chapman, Y. Chinone, G. Coppi, K. Crowley, A. Cukierman, T. de Haan, M. Dobbs, R. Dunner, J. Errard, G. Fabbian, S. Feeney, C. Feng, G. Fuller, N. Galitzki, A. Gilbert, N. Goeckner-Wald, T. Hamada, N. Halverson, M. Hasegawa, M. Hazumi, C. Hill, W. Holzapfel, L. Howe, Y. Inoue, J. Ito, G. Jaehnig, O. Jeong, B. Keating, R. Keskitalo, T. Kisner, N. Krachmalnicoff, A. Kusaka, M. Le Jeune, D. Leon, E. Linder, A. Lowitz, A. Madurowicz, D. Mak, F. Matsuda, T. Matsumura, A. May, N. Miller, Y. Minami, J. Montgomery, T. Natoli, M. Navroli, J. Peloton, A. Pham, L. Piccirillo, D. Plambeck, D. Poletti, G. Puglisi, C. Raum, G. Rebeiz, C. Reichardt, P. Richards, H. Roberts, C. Ross, K. Rotermund, M. Silva-Feaver, Y. Segawa, B. Sherwin, P. Siritanasak, L. Steinmetz, R. Stompor, O. Tajima, S. Takakura, D. Tanabe, R. Tat, G. Teply, A. Tikhomirov, T. Tomaru, C. Tsai, C. Verges, B. Westbrook, N. Whitehorn, and A. Zahn, “Electrical characterization and tuning of the integrated POLARBEAR-2a focal plane and readout,” in *Millimeter,*

Submillimeter, and Far-Infrared Detectors and Instrumentation for Astronomy IX, vol. 10708, 2018.

- [4] The POLARBEAR Collaboration, M. Hasegawa, P. Ade, Y. Akiba, A. Ali, M. Aguilar, A. Anderson, K. Arnold, P. Ashton, J. Avva, D. Barron, D. Beck, C. Baccigalupi, S. Beckman, A. Bender, F. Bianchini, D. Boettger, J. Borrill, J. Carron, S. Chapman, Y. Chinone, G. Coppi, K. Crowley, A. Cukierman, T. de Haan, M. Dobbs, R. Dunner, T. Ellefot, J. Errard, G. Fabbian, S. Feeney, C. Feng, G. Fuller, N. Galitzki, A. Gilbert, J. Goeckner-Wald Groh, N., T. Hamada, N. Halverson, M. Hasegawa, M. Hazumi, C. Hill, W. Holzapfel, L. Howe, Y. Inoue, J. Ito, G. Jaehnig, D. Jeong O. Kaneko, N. Katayama, B. Keating, R. Keskitalo, T. Kisner, N. Krachmalnicoff, A. Kusaka, A. Lee, M. Le Jeune, D. Leon, E. Linder, A. Lowitz, L. Lowry, A. Madurowicz, D. Mak, F. Matsuda, T. Matsumura, A. May, N. Miller, Y. Minami, J. Montgomery, T. Natoli, M. Navroli, H. Nishino, J. Peloton, A. Pham, L. Piccirillo, D. Plambeck, D. Poletti, G. Puglisi, C. Raum, G. Rebeiz, C. Reichardt, P. Richards, H. Roberts, C. Ross, K. Rotermund, M. Silva-Feaver, Y. Segawa, B. Sherwin, P. Siritanasak, L. Steinmetz, R. Stompor, A. Suzuki, O. Tajima, S. Takakura, S. Takatori, D. Tanabe, R. Tat, G. Teply, A. Tikhomirov, T. Tomaru, C. Tsai, C. Verges, B. Westbrook, N. Whitehorn, and A. Zahn, “POLARBEAR-2: A new CMB polarization receiver system for the Simons Array,” in *Millimeter, Submillimeter, and Far-Infrared Detectors and Instrumentation for Astronomy IX*, vol. 10708, 2018, p. 1070802.
- [5] P. Ade, J. Aguirre, Z. Ahmed, S. Aiola, A. Ali, D. Alonso, M. A. Alvarez, K. Arnold, P. Ashton, J. Austermann, H. Awan, C. Baccigalupi, T. Baildon, D. Barron, N. Battaglia, R. Battye, E. Baxter, A. Bazarko, J. A. Beall, R. Bean, D. Beck, S. Beckman, B. Beringue, F. Bianchini, S. Boada, D. Boettger, J. R. Bond, J. Borrill, M. L. Brown, S. M. Bruno, S. Bryan, E. Calabrese, V. Calafut, P. Calisse, J. Carron, A. Challinor, G. Chesmore, Y. Chinone, J. Chluba, H. M. S. Cho, S. Choi, G. Coppi, N. F. Cothard, K. Coughlin, D. Crichton, K. D. Crowley, K. T. Crowley, A. Cukierman, J. M. D’Ewart, R. Dünner, T. De Haan, M. Devlin, S. Dicker, J. Didier, M. Dobbs, B. Dober, C. J. Duell, S. Duff, A. Duivenvoorden, J. Dunkley, J. Dusatko, J. Errard, G. Fabbian, S. Feeney, S. Ferraro, P. Fluxà, K. Freese, J. C. Frisch, A. Frolov, G. Fuller, B. Fuzia, N. Galitzki, P. A. Gallardo, J. T. G. Ghersi, J. Gao, E. Gawiser, M. Gerbino, V. Gluscevic, N. Goeckner-Wald, J. Golec, S. Gordon, M. Gralla, D. Green, A. Grigorian, J. Groh, C. Groppi, Y. Guan, J. E. Gudmundsson, D. Han, P. Hargrave, M. Hasegawa, M. Hasselfield, M. Hattori, V. Haynes, M. Hazumi, Y. He, E. Healy, S. W. Henderson, C. Hervias-Caimapo, C. A. Hill, J. C. Hill, G. Hilton, M. Hilton, A. D. Hincks, G. Hinshaw, R. Hložek, S. Ho, S. P. P. Ho, L. Howe, Z. Huang, J. Hubmayr, K. Huffenberger, J. P. Hughes, A. Iijas, M. Ikape, K. Irwin, A. H. Jaffe, B. Jain, O. Jeong, D. Kaneko, E. D. Karpel, N. Katayama, B. Keating, S. S. Kernasovskiy, R. Keskitalo, T. Kisner, K. Kiuchi, J. Klein, K. Knowles, B. Koopman, A. Kosowsky, N. Krachmalnicoff, S. E. Kuenstner, C. L. Kuo, A. Kusaka, J. Lashner, A. Lee, E. Lee, D. Leon, J. S. Leung, A. Lewis,

- Y. Li, Z. Li, M. Limon, E. Linder, C. Lopez-Caraballo, T. Louis, L. Lowry, M. Lungu, M. Madhavacheril, D. Mak, F. Maldonado, H. Mani, B. Mates, F. Matsuda, L. Maurin, P. Mauskopf, A. May, N. McCallum, C. McKenney, J. McMahon, P. D. Meerburg, J. Meyers, A. Miller, M. Mirmelstein, K. Moodley, M. Munchmeyer, C. Munson, S. Naess, F. Nati, M. Navaroli, L. Newburgh, H. N. Nguyen, M. Niemack, H. Nishino, J. Orlowski-Scherer, L. Page, B. Partridge, J. Peloton, F. Perrotta, L. Piccirillo, G. Pisano, D. Poletti, R. Puddu, G. Puglisi, C. Raum, C. L. Reichardt, M. Remazeilles, Y. Rephaeli, D. Riechers, F. Rojas, A. Roy, S. Sadeh, Y. Sakurai, M. Salatino, M. S. Rao, E. Schaan, M. Schmittfull, N. Sehgal, J. Seibert, U. Seljak, B. Sherwin, M. Shimon, C. Sierra, J. Sievers, P. Sikhosana, M. Silva-Feaver, S. M. Simon, A. Sinclair, P. Siritanasak, K. Smith, S. R. Smith, D. Spergel, S. T. Staggs, G. Stein, J. R. Stevens, R. Stompor, A. Suzuki, O. Tajima, S. Takakura, G. Teply, D. B. Thomas, B. Thorne, R. Thornton, H. Trac, C. Tsai, C. Tucker, J. Ullom, S. Vagnozzi, A. V. Engelen, J. V. Lanen, D. D. Winkle, E. M. Vavagiakis, C. Vergès, M. Vissers, K. Wagoner, S. Walker, J. Ward, B. Westbrook, N. Whitehorn, J. Williams, J. Williams, E. J. Wollack, Z. Xu, B. Yu, C. Yu, F. Zago, H. Zhang, and N. Zhu, “The Simons Observatory: Science goals and forecasts,” *Journal of Cosmology and Astroparticle Physics*, vol. 2019, no. 2, 2019.
- [6] The Simons Observatory Collaboration, N. Galitzki, A. Ali, K. S. Arnold, P. C. Ashton, J. E. Austermann, C. Baccigalupi, T. Baillod, D. Barron, J. A. Beall, S. Beckman, S. M. M. Bruno, S. Bryan, P. G. Calisse, G. E. Chesmore, Y. Chinone, S. K. Choi, G. Coppi, K. D. Crowley, K. T. Crowley, A. Cukierman, M. J. Devlin, S. Dicker, B. Dober, S. M. Duff, J. Dunkley, G. Fabbian, P. A. Gallardo, M. Gerbino, N. Goeckner-Wald, J. E. Golec, J. E. Gudmundsson, E. E. Healy, S. Henderson, C. A. Hill, G. C. Hilton, S.-P. P. Ho, L. A. Howe, J. Hubmayr, O. Jeong, B. Keating, B. J. Koopman, K. Kiuchi, A. Kusaka, J. Lashner, A. T. Lee, Y. Li, M. Limon, M. Lungu, F. Matsuda, P. D. Mauskopf, A. J. May, N. McCallum, J. McMahon, F. Nati, M. D. Niemack, J. L. Orlowski-Scherer, S. C. Parshley, L. Piccirillo, M. Sathyaranayana Rao, C. Raum, M. Salatino, J. S. Seibert, C. Sierra, M. Silva-Feaver, S. M. Simon, S. T. Staggs, J. R. Stevens, A. Suzuki, G. Teply, R. Thornton, C. Tsai, J. N. Ullom, E. M. Vavagiakis, M. R. Vissers, B. Westbrook, E. J. Wollack, Z. Xu, and N. Zhu, “The Simons Observatory: Instrument overview,” in *Millimeter, Submillimeter, and Far-Infrared Detectors and Instrumentation for Astronomy IX*, vol. 10708, Jul. 2018, p. 1070 804.
- [7] T. Elleflot, Y. Akiba, K. Arnold, J. Avva, D. Barron, A. N. Bender, A. Cukierman, T. de Haan, M. Dobbs, J. Groh, M. Hasegawa, M. Hazumi, W. Holzapfel, L. Howe, G. Jaehnig, B. Keating, A. Kusaka, A. T. Lee, L. Lowry, J. Montgomery, H. Nishino, C. Raum, K. M. Rotermund, M. Silva-Feaver, A. Suzuki, B. Westbrook, and N. Whitehorn, “Detector and readout assembly and characterization for the Simons Array,” *Journal of Low Temperature Physics*, vol. 193, no. 5, pp. 1094–1102, 2018.
- [8] The POLARBEAR Collaboration, B. Westbrook, P. A. R. Ade, M. Aguilar, Y. Akiba, K. Arnold, C. Baccigalupi, D. Barron, D. Beck, S. Beckman, A. N. Bender, F.

Bianchini, D. Boettger, J. Borrill, S. Chapman, Y. Chinone, G. Coppi, K. Crowley, A. Cukierman, T. de Haan, R. Dünner, M. Dobbs, T. Elleflot, J. Errard, G. Fabbian, S. M. Feeney, C. Feng, G. Fuller, N. Galitzki, A. Gilbert, N. Goeckner-Wald, J. Groh, N. W. Halverson, T. Hamada, M. Hasegawa, M. Hazumi, C. A. Hill, W. Holzapfel, L. Howe, Y. Inoue, G. Jaehnig, A. Jaffe, O. Jeong, D. Kaneko, N. Katayama, B. Keating, R. Keskitalo, T. Kisner, N. Krachmalnicoff, A. Kusaka, M. Le Jeune, A. T. Lee, D. Leon, E. Linder, L. Lowry, A. Madurowicz, D. Mak, F. Matsuda, A. May, N. J. Miller, Y. Minami, J. Montgomery, M. Navaroli, H. Nishino, J. Peloton, A. Pham, L. Piccirillo, D. Plambeck, D. Poletti, G. Puglisi, C. Raum, G. Rebeiz, C. L. Reichardt, P. L. Richards, H. Roberts, C. Ross, K. M. Rotermund, Y. Segawa, B. Sherwin, M. Silva-Feaver, P. Siritanasak, R. Stompor, A. Suzuki, O. Tajima, S. Takakura, S. Takatori, D. Tanabe, R. Tat, G. P. Teply, A. Tikhomirov, T. Tomaru, C. Tsai, N. Whitehorn, and A. Zahn, “The POLARBEAR-2 and Simons Array Focal Plane Fabrication Status,” *Journal of Low Temperature Physics*, Sep. 2018.

- [9] Collaboration, P. A. R. Ade, M. Aguilar, Y. Akiba, K. Arnold, C. Baccigalupi, D. Barron, D. Beck, F. Bianchini, D. Boettger, J. Borrill, S. Chapman, Y. Chinone, K. Crowley, A. Cukierman, R. Dünner, M. Dobbs, A. Ducout, T. Elleflot, J. Errard, G. Fabbian, S. M. Feeney, C. Feng, T. Fujino, N. Galitzki, A. Gilbert, N. Goeckner-Wald, J. C. Groh, G. Hall, N. Halverson, T. Hamada, M. Hasegawa, M. Hazumi, C. A. Hill, L. Howe, Y. Inoue, G. Jaehnig, A. H. Jaffe, O. Jeong, D. Kaneko, N. Katayama, B. Keating, R. Keskitalo, T. Kisner, N. Krachmalnicoff, A. Kusaka, M. Le Jeune, A. T. Lee, E. M. Leitch, D. Leon, E. Linder, L. Lowry, F. Matsuda, T. Matsumura, Y. Minami, J. Montgomery, M. Navaroli, H. Nishino, H. Paar, J. Peloton, A. T. P. Pham, D. Poletti, G. Puglisi, C. L. Reichardt, P. L. Richards, C. Ross, Y. Segawa, B. D. Sherwin, M. Silva-Feaver, P. Siritanasak, N. Stebor, R. Stompor, A. Suzuki, O. Tajima, S. Takakura, S. Takatori, D. Tanabe, G. P. Teply, T. Tomaru, C. Tucker, N. Whitehorn, and A. Zahn, “A Measurement of the Cosmic Microwave Background B-mode Polarization Power Spectrum at Subdegree Scales from Two Years of POLARBEAR Data,” *Astrophysical Journal*, vol. 848, 121, p. 121, Oct. 2017.
- [10] The POLARBEAR Collaboration, S. Takakura, M. Aguilar, Y. Akiba, K. Arnold, C. Baccigalupi, D. Barron, S. Beckman, D. Boettger, J. Borrill, S. Chapman, Y. Chinone, A. Cukierman, A. Ducout, T. Elleflot, J. Errard, G. Fabbian, T. Fujino, N. Galitzki, N. Goeckner-Wald, N. W. Halverson, M. Hasegawa, K. Hattori, M. Hazumi, C. Hill, L. Howe, Y. Inoue, A. H. Jaffe, O. Jeong, D. Kaneko, N. Katayama, B. Keating, R. Keskitalo, T. Kisner, N. Krachmalnicoff, A. Kusaka, A. T. Lee, D. Leon, L. Lowry, F. Matsuda, T. Matsumura, M. Navaroli, H. Nishino, H. Paar, J. Peloton, D. Poletti, G. Puglisi, C. L. Reichardt, C. Ross, P. Siritanasak, A. Suzuki, O. Tajima, S. Takatori, and G. Teply, “Performance of a continuously rotating half-wave plate on the POLARBEAR telescope,” *Journal of Cosmology and Astroparticle Physics*, vol. 2017, no. 05, p. 008, 2017.

- [11] The POLARBEAR Collaboration, D. Poletti, G. Fabbian, M. Le Jeune, J. Peloton, K. Arnold, C. Baccigalupi, D. Barron, S. Beckman, J. Borrill, S. Chapman, Y. Chinone, A. Cukierman, A. Ducout, T. Ellefot, J. Errard, S. Feeney, N. Goeckner-Wald, J. Groh, G. Hall, M. Hasegawa, M. Hazumi, C. Hill, L. Howe, Y. Inoue, A. H. Jaffe, O. Jeong, N. Katayama, B. Keating, R. Keskitalo, T. Kisner, A. Kusaka, A. T. Lee, D. Leon, E. Linder, L. Lowry, F. Matsuda, M. Navaroli, H. Paar, G. Puglisi, C. L. Reichardt, C. Ross, P. Siritanasak, N. Stebor, B. Steinbach, R. Stompor, A. Suzuki, O. Tajima, G. Teply, and N. Whitehorn, “Making maps of cosmic microwave background polarization for B-mode studies: the POLARBEAR example,” *Astronomy and Astrophysics*, vol. 600, A60, Apr. 2017.
- [12] The POLARBEAR Collaboration, Y. Inoue, P. Ade, Y. Akiba, C. Aleman, K. Arnold, C. Baccigalupi, B. Barch, D. Barron, A. Bender, D. Boettger, J. Borrill, S. Chapman, Y. Chinone, A. Cukierman, T. de Haan, M. A. Dobbs, A. Ducout, R. Dünner, T. Ellefot, J. Errard, G. Fabbian, S. Feeney, C. Feng, G. Fuller, A. J. Gilbert, N. Goeckner-Wald, J. Groh, G. Hall, N. Halverson, T. Hamada, M. Hasegawa, K. Hattori, M. Hazumi, C. Hill, W. L. Holzapfel, Y. Hori, L. Howe, F. Irie, G. Jaehnig, A. Jaffe, O. Jeong, N. Katayama, J. P. Kaufman, K. Kazemzadeh, B. G. Keating, Z. Kermish, R. Keskitalo, T. S. Kisner, A. Kusaka, M. Le Jeune, A. T. Lee, D. Leon, E. V. Linder, L. Lowry, F. Matsuda, T. Matsumura, N. Miller, K. Mizukami, J. Montgomery, M. Navaroli, H. Nishino, H. Paar, J. Peloton, D. Poletti, G. Puglisi, C. R. Raum, G. M. Rebeiz, C. L. Reichardt, P. L. Richards, C. Ross, K. M. Rotermund, Y. Segawa, B. D. Sherwin, I. Shirley, P. Siritanasak, N. Stebor, R. Stompor, J. Suzuki, A. Suzuki, O. Tajima, S. Takada, S. Takatori, G. P. Teply, A. Tikhomirov, T. Tomaru, N. Whitehorn, A. Zahn, and O. Zahn, “POLARBEAR-2: an instrument for CMB polarization measurements,” in *Millimeter, Submillimeter, and Far-Infrared Detectors and Instrumentation for Astronomy VIII*, ser. Proceedings of the International Society for Optics and Photonics, vol. 9914, Jul. 2016, p. 99141I.
- [13] The POLARBEAR Collaboration, N. Stebor, P. Ade, Y. Akiba, C. Aleman, K. Arnold, C. Baccigalupi, B. Barch, D. Barron, S. Beckman, A. Bender, D. Boettger, J. Borrill, S. Chapman, Y. Chinone, A. Cukierman, T. de Haan, M. Dobbs, A. Ducout, R. Dunner, T. Ellefot, J. Errard, G. Fabbian, S. Feeney, C. Feng, T. Fujino, G. Fuller, A. J. Gilbert, N. Goeckner-Wald, J. Groh, G. Hall, N. Halverson, T. Hamada, M. Hasegawa, K. Hattori, M. Hazumi, C. Hill, W. L. Holzapfel, Y. Hori, L. Howe, Y. Inoue, F. Irie, G. Jaehnig, A. Jaffe, O. Jeong, N. Katayama, J. P. Kaufman, K. Kazemzadeh, B. G. Keating, Z. Kermish, R. Keskitalo, T. Kisner, A. Kusaka, M. Le Jeune, A. T. Lee, D. Leon, E. V. Linder, L. Lowry, F. Matsuda, T. Matsumura, N. Miller, J. Montgomery, M. Navaroli, H. Nishino, H. Paar, J. Peloton, D. Poletti, G. Puglisi, C. R. Raum, G. M. Rebeiz, C. L. Reichardt, P. L. Richards, C. Ross, K. M. Rotermund, Y. Segawa, B. D. Sherwin, I. Shirley, P. Siritanasak, L. Steinmetz, R. Stompor, A. Suzuki, O. Tajima, S. Takada, S. Takatori, G. P. Teply, A. Tikhomirov, T. Tomaru, B. Westbrook, N. Whitehorn, A. Zahn, and O. Zahn, “The Simons Array CMB polarization experiment,” in *Millimeter, Submillimeter, and*

Far-Infrared Detectors and Instrumentation for Astronomy VIII, ser. Proceedings of the International Society for Optics and Photonics, vol. 9914, Jul. 2016, 99141H.

- [14] The POLARBEAR Collaboration, A. Suzuki, P. Ade, Y. Akiba, C. Aleman, K. Arnold, C. Baccigalupi, B. Barch, D. Barron, A. Bender, D. Boettger, J. Borrill, S. Chapman, Y. Chinone, A. Cukierman, M. Dobbs, A. Ducout, R. Dunner, T. Ellefot, J. Errard, G. Fabbian, S. Feeney, C. Feng, T. Fujino, G. Fuller, A. Gilbert, N. Goeckner-Wald, J. Groh, T. D. Haan, G. Hall, N. Halverson, T. Hamada, M. Hasegawa, K. Hattori, M. Hazumi, C. Hill, W. Holzapfel, Y. Hori, L. Howe, Y. Inoue, F. Irie, G. Jaehnig, A. Jaffe, O. Jeong, N. Katayama, J. Kaufman, K. Kazemzadeh, B. Keating, Z. Kermish, R. Keskitalo, T. Kisner, A. Kusaka, M. L. Jeune, A. Lee, D. Leon, E. Linder, L. Lowry, F. Matsuda, T. Matsumura, N. Miller, K. Mizukami, J. Montgomery, M. Navaroli, H. Nishino, J. Peloton, D. Poletti, G. Puglisi, G. Rebeiz, C. Raum, C. Reichardt, P. Richards, C. Ross, K. Rotermund, Y. Segawa, B. Sherwin, I. Shirley, P. Siritanasak, N. Stebor, R. Stompor, J. Suzuki, O. Tajima, S. Takada, S. Takakura, S. Takatori, A. Tikhomirov, T. Tomaru, B. Westbrook, N. Whitehorn, T. Yamashita, A. Zahn, and O. Zahn, “The POLARBEAR-2 and the Simons Array Experiments,” *Journal of Low Temperature Physics*, vol. 184, pp. 805–810, Aug. 2016.
- [15] S. P. Benz, S. B. Waltman, A. E. Fox, P. D. Dresselhaus, A. Rüfenacht, J. M. Underwood, L. Howe, R. E. Schwall, and C. J. Burroughs, “One-volt Josephson arbitrary waveform synthesizer,” *IEEE Transactions on Applied Superconductivity*, vol. 25, no. 1, pp. 1–8, 2015.
- [16] L. Howe, A. E. Fox, A. Rüfenacht, C. J. Burroughs, P. D. Dresselhaus, S. P. Benz, and R. E. Schwall, “NIST 10 V programmable Josephson voltage standard system using a low-capacity cryocooler,” *IEEE Transactions on Applied Superconductivity*, vol. 25, no. 3, pp. 1–4, 2015.
- [17] A. Rüfenacht, L. Howe, A. E. Fox, R. E. Schwall, P. D. Dresselhaus, C. J. Burroughs, and S. P. Benz, “Cryocooled 10 V programmable Josephson voltage standard,” *IEEE Transactions on Instrumentation and Measurement*, vol. 64, no. 6, pp. 1477–1482, 2015.
- [18] The POLARBEAR Collaboration, P. A. R. Ade, K. Arnold, M. Atlas, C. Baccigalupi, D. Barron, D. Boettger, J. Borrill, S. Chapman, Y. Chinone, A. Cukierman, M. Dobbs, A. Ducout, R. Dunner, T. Ellefot, J. Errard, G. Fabbian, S. Feeney, C. Feng, A. Gilbert, N. Goeckner-Wald, J. Groh, G. Hall, N. W. Halverson, M. Hasegawa, K. Hattori, M. Hazumi, C. Hill, W. L. Holzapfel, Y. Hori, L. Howe, Y. Inoue, G. C. Jaehnig, A. H. Jaffe, O. Jeong, N. Katayama, J. P. Kaufman, B. Keating, Z. Kermish, R. Keskitalo, T. Kisner, A. Kusaka, M. Le Jeune, A. T. Lee, E. M. Leitch, D. Leon, Y. Li, E. Linder, L. Lowry, F. Matsuda, T. Matsumura, N. Miller, J. Montgomery, M. J. Myers, M. Navaroli, H. Nishino, T. Okamura, H. Paar, J. Peloton, L. Pogosian, D. Poletti, G. Puglisi, C. Raum, G. Rebeiz, C. L. Reichardt, P. L. Richards, C. Ross, K. M. Rotermund, D. E. Schenck, B. D. Sherwin, M.

- Shimon, I. Shirley, P. Siritanasak, G. Smecher, N. Stebor, B. Steinbach, A. Suzuki, J.-i. Suzuki, O. Tajima, S. Takakura, A. Tikhomirov, T. Tomaru, N. Whitehorn, B. Wilson, A. Yadav, A. Zahn, and O. Zahn, “POLARBEAR constraints on cosmic birefringence and primordial magnetic fields,” *Physical Review Letters D*, vol. 92, no. 12, 123509, p. 123 509, Dec. 2015.
- [19] A. Rüfenacht, L. Howe, A. E. Fox, R. E. Schwall, P. D. Dresselhaus, C. J. Burroughs, and S. P. Benz, “Cryocooled 10 V programmable Josephson voltage standard,” in *Conference on Precision Electromagnetic Measurements*, IEEE, 2014, pp. 458–459.
- [20] L. Howe, C. J. Burroughs, P. D. Dresselhaus, S. P. Benz, and R. E. Schwall, “Cryogen-free operation of 10 V programmable Josephson voltage standards,” *IEEE Transactions on Applied Superconductivity*, vol. 23, no. 3, pp. 1 300 605–1 300 605, 2013.
- [21] S. Dodelson, *Modern cosmology*. 2003.
- [22] A. H. Guth, “Inflationary universe: A possible solution to the horizon and flatness problems,” *Physical Review D*, vol. 23, no. 2, p. 347, 1981.
- [23] E. Hubble, “A Relation between Distance and Radial Velocity among Extra-Galactic Nebulae,” *Proceedings of the National Academy of Science*, vol. 15, pp. 168–173, Mar. 1929.
- [24] Planck Collaboration, Ade, P. A. R., Aghanim, N., Arnaud, M., Ashdown, M., Aumont, J., Baccigalupi, C., Banday, A. J., Barreiro, R. B., Bartlett, J. G., Bartolo, N., Battaner, E., Battye, R., Benabed, K., Benoît, A., Benoit-Lévy, A., Bernard, J.-P., Bersanelli, M., Bielewicz, P., Bock, J. J., Bonaldi, A., Bonavera, L., Bond, J. R., Borrill, J., Bouchet, F. R., Boulanger, F., Bucher, M., Burigana, C., Butler, R. C., Calabrese, E., Cardoso, J.-F., Catalano, A., Challinor, A., Chamballu, A., Chary, R.-R., Chiang, H. C., Chluba, J., Christensen, P. R., Church, S., Clements, D. L., Colombi, S., Colombo, L. P. L., Combet, C., Coulais, A., Crill, B. P., Curto, A., Cuttaia, F., Danese, L., Davies, R. D., Davis, R. J., de Bernardis, P., de Rosa, A., de Zotti, G., Delabrouille, J., Désert, F.-X., Di Valentino, E., Dickinson, C., Diego, J. M., Dolag, K., Dole, H., Donzelli, S., Doré, O., Douspis, M., Ducout, A., Dunkley, J., Dupac, X., Efstathiou, G., Elsner, F., Enßlin, T. A., Eriksen, H. K., Farhang, M., Fergusson, J., Finelli, F., Forni, O., Frailis, M., Fraisse, A. A., Franceschi, E., Frejsel, A., Galeotta, S., Galli, S., Ganga, K., Gauthier, C., Gerbino, M., Ghosh, T., Giard, M., Giraud-Héraud, Y., Giusarma, E., Gjerløw, E., González-Nuevo, J., Górski, K. M., Gratton, S., Gregorio, A., Gruppuso, A., Gudmundsson, J. E., Hamann, J., Hansen, F. K., Hanson, D., Harrison, D. L., Helou, G., Henrot-Versillé, S., Hernández-Monteagudo, C., Herranz, D., Hildebrandt, S. R., Hivon, E., Hobson, M., Holmes, W. A., Hornstrup, A., Hovest, W., Huang, Z., Huffenberger, K. M., Hurier, G., Jaffe, A. H., Jaffe, T. R., Jones, W. C., Juvela, M., Keihänen, E., Keskitalo, R., Kisner, T. S., Kneissl, R., Knoche, J., Knox, L., Kunz, M., Kurki-Suonio, H., Lagache, G., Lähteenmäki, A., Lamarre, J.-M., Lasenby, A., Lattanzi, M., Lawrence, C. R., Leahy, J. P., Leonardi, R., Lesgourgues, J., Levrier, F., Lewis, A., Liguori,

M., Lilje, P. B., Linden-Vørnle, M., López-Caniego, M., Lubin, P. M., Macías-Pérez, J. F., Maggio, G., Maino, D., Mandolesi, N., Mangilli, A., Marchini, A., Maris, M., Martin, P. G., Martinelli, M., Martínez-González, E., Masi, S., Matarrese, S., McGehee, P., Meinholt, P. R., Melchiorri, A., Melin, J.-B., Mendes, L., Mennella, A., Migliaccio, M., Millea, M., Mitra, S., Miville-Deschénes, M.-A., Moneti, A., Montier, L., Morgante, G., Mortlock, D., Moss, A., Munshi, D., Murphy, J. A., Naselsky, P., Nati, F., Natoli, P., Netterfield, C. B., Nørgaard-Nielsen, H. U., Noviello, F., Novikov, D., Novikov, I., Oxborrow, C. A., Paci, F., Pagano, L., Pajot, F., Paladini, R., Paoletti, D., Partridge, B., Pasian, F., Patanchon, G., Pearson, T. J., Perdereau, O., Perotto, L., Perrotta, F., Pettorino, V., Piacentini, F., Piat, M., Pierpaoli, E., Pietrobon, D., Plaszczynski, S., Pointecouteau, E., Polenta, G., Popa, L., Pratt, G. W., Prézeau, G., Prunet, S., Puget, J.-L., Rachen, J. P., Reach, W. T., Rebolo, R., Reinecke, M., Remazeilles, M., Renault, C., Renzi, A., Ristorcelli, I., Rocha, G., Rosset, C., Rossetti, M., Roudier, G., Rouillé d'Orfeuil, B., Rowan-Robinson, M., Rubiño-Martín, J. A., Rusholme, B., Said, N., Salvatelli, V., Salvati, L., Sandri, M., Santos, D., Savelainen, M., Savini, G., Scott, D., Seiffert, M. D., Serra, P., Shellard, E. P. S., Spencer, L. D., Spinelli, M., Stolyarov, V., Stompor, R., Sudiwala, R., Sunyaev, R., Sutton, D., Suur-Uski, A.-S., Sygnet, J.-F., Tauber, J. A., Terenzi, L., Toffolatti, L., Tomasi, M., Tristram, M., Trombetti, T., Tucci, M., Tuovinen, J., Türler, M., Umana, G., Valenziano, L., Valiviita, J., Van Tent, F., Vielva, P., Villa, F., Wade, L. A., Wandelt, B. D., Wehus, I. K., White, M., White, S. D. M., Wilkinson, A., Yvon, D., Zacchei, A., and Zonca, A., "Planck 2015 results - XIII. cosmological parameters," *A&A*, vol. 594, A13, 2016.

- [25] B. Ryden, *Introduction to cosmology*. 2003.
- [26] A. R. Liddle and D. H. Lyth, *Cosmological Inflation and Large-Scale Structure*. Jun. 2000, p. 414.
- [27] J. C. Mather, E. S. Cheng, D. A. Cottingham, R. E. Eplee Jr., D. J. Fixsen, T. Hewagama, R. B. Isaacman, K. A. Jensen, S. S. Meyer, P. D. Noerdlinger, S. M. Read, L. P. Rosen, R. A. Shafer, E. L. Wright, C. L. Bennett, N. W. Boggess, M. G. Hauser, T. Kelsall, S. H. Moseley Jr., R. F. Silverberg, G. F. Smoot, R. Weiss, and D. T. Wilkinson, "Measurement of the cosmic microwave background spectrum by the COBE FIRAS instrument," *The Astrophysical Journal*, vol. 420, pp. 439–444, Jan. 1994.
- [28] D. Fixsen, "The temperature of the cosmic microwave background," *The Astrophysical Journal*, vol. 707, no. 2, p. 916, 2009.
- [29] Planck Collaboration, Y. Akrami, F. Argüeso, M. Ashdown, J. Aumont, C. Bacigalupi, M. Ballardini, A. J. Banday, R. B. Barreiro, N. Bartolo, S. Basak, K. Benabed, J.-P. Bernard, M. Bersanelli, P. Bielewicz, L. Bonavera, J. R. Bond, J. Borrill, F. R. Bouchet, F. Boulanger, M. Bucher, C. Burigana, R. C. Butler, E. Calabrese, J.-F. Cardoso, L. P. L. Colombo, B. P. Crill, F. Cuttaia, P. de Bernardis, A. de Rosa, G. de Zotti, J. Delabrouille, E. Di Valentino, C. Dickinson, J. M. Diego,

S. Donzelli, A. Ducout, X. Dupac, G. Efstathiou, F. Elsner, T. A. Enßlin, H. K. Eriksen, Y. Fantaye, F. Finelli, M. Frailis, E. Franceschi, A. Frolov, S. Galeotta, S. Galli, K. Ganga, R. T. Génova-Santos, M. Gerbino, T. Ghosh, J. González-Nuevo, K. M. Górski, S. Gratton, A. Gruppuso, J. E. Gudmundsson, W. Handley, F. K. Hansen, D. Herranz, E. Hivon, Z. Huang, A. H. Jaffe, W. C. Jones, A. Karakci, E. Keihänen, R. Keskitalo, K. Kiiveri, J. Kim, T. S. Kisner, N. Krachmalnicoff, M. Kunz, H. Kurki-Suonio, J.-M. Lamarre, A. Lasenby, M. Lattanzi, C. R. Lawrence, J. P. Leahy, F. Levrier, M. Liguori, P. B. Lilje, V. Lindholm, M. López-Caniego, Y.-Z. Ma, J. F. Macías-Pérez, G. Maggio, D. Maino, N. Mandolesi, A. Mangilli, M. Maris, P. G. Martin, E. Martínez-González, S. Matarrese, N. Mauri, J. D. McEwen, P. R. Meinhold, A. Melchiorri, A. Mennella, M. Migliaccio, D. Molinari, L. Montier, G. Morgante, A. Moss, P. Natoli, L. Pagano, D. Paoletti, B. Partridge, G. Patanchon, L. Patrizii, M. Peel, F. Perrotta, V. Pettorino, F. Piacentini, G. Polenta, J.-L. Puget, J. P. Rachen, B. Racine, M. Reinecke, M. Remazeilles, A. Renzi, G. Rocha, G. Roudier, J. A. Rubiño-Martín, L. Salvati, M. Sandri, M. Savelainen, D. Scott, D. S. Seljebotn, C. Sirignano, G. Sirri, L. D. Spencer, A.-S. Suur-Uski, J. A. Tauber, D. Tavagnacco, M. Tenti, L. Terenzi, L. Toffolatti, M. Tomasi, T. Trombetti, J. Valiviita, F. Vansyngel, B. Van Tent, P. Vielva, F. Villa, N. Vittorio, B. D. Wandelt, R. Watson, I. K. Wehus, A. Zacchei, and A. Zonca, “Planck 2018 results. II. Low Frequency Instrument data processing,” *arXiv e-prints*, Jul. 2018.

- [30] Planck Collaboration, N. Aghanim, Y. Akrami, M. Ashdown, J. Aumont, C. Baccigalupi, M. Ballardini, A. J. Banday, R. B. Barreiro, N. Bartolo, S. Basak, K. Benabed, J.-P. Bernard, M. Bersanelli, P. Bielewicz, J. R. Bond, J. Borrill, F. R. Bouchet, F. Boulanger, M. Bucher, C. Burigana, E. Calabrese, J.-F. Cardoso, J. Carron, A. Challinor, H. C. Chiang, L. P. L. Colombo, C. Combet, F. Couchot, B. P. Crill, F. Cuttaia, P. de Bernardis, A. de Rosa, G. de Zotti, J. Delabrouille, J.-M. Delouis, E. Di Valentino, J. M. Diego, O. Doré, M. Douspis, A. Ducout, X. Dupac, G. Efstathiou, F. Elsner, T. A. Enßlin, H. K. Eriksen, E. Falgarone, Y. Fantaye, F. Finelli, M. Frailis, A. A. Fraisse, E. Franceschi, A. Frolov, S. Galeotta, S. Galli, K. Ganga, R. T. Génova-Santos, M. Gerbino, T. Ghosh, J. González-Nuevo, K. M. Górski, S. Gratton, A. Gruppuso, J. E. Gudmundsson, W. Handley, F. K. Hansen, S. Henrot-Versillé, D. Herranz, E. Hivon, Z. Huang, A. H. Jaffe, W. C. Jones, A. Karakci, E. Keihänen, R. Keskitalo, K. Kiiveri, J. Kim, T. S. Kisner, N. Krachmalnicoff, M. Kunz, H. Kurki-Suonio, G. Lagache, J.-M. Lamarre, A. Lasenby, M. Lattanzi, C. R. Lawrence, F. Levrier, M. Liguori, P. B. Lilje, V. Lindholm, M. López-Caniego, Y.-Z. Ma, J. F. Macías-Pérez, G. Maggio, D. Maino, N. Mandolesi, A. Mangilli, P. G. Martin, E. Martínez-González, S. Matarrese, N. Mauri, J. D. McEwen, A. Melchiorri, A. Mennella, M. Migliaccio, M.-A. Miville-Deschénes, D. Molinari, A. Moneti, L. Montier, G. Morgante, A. Moss, S. Mottet, P. Natoli, L. Pagano, D. Paoletti, B. Partridge, G. Patanchon, L. Patrizii, O. Perdereau, F. Perrotta, V. Pettorino, F. Piacentini, J.-L. Puget, J. P. Rachen, M. Reinecke, M. Remazeilles, A. Renzi, G. Rocha, G. Roudier, L. Salvati, M. Sandri, M. Save-

lainen, D. Scott, C. Sirignano, G. Sirri, L. D. Spencer, R. Sunyaev, A.-S. Suur-Uski, J. A. Tauber, D. Tavagnacco, M. Tenti, L. Toffolatti, M. Tomasi, M. Tristram, T. Trombetti, J. Valiviita, F. Vansyngel, B. Van Tent, L. Vibert, P. Vielva, F. Villa, N. Vittorio, B. D. Wandelt, I. K. Wehus, and A. Zonca, “Planck 2018 results. III. High Frequency Instrument data processing and frequency maps,” *arXiv e-prints*, Jul. 2018.

- [31] W. Hu and S. Dodelson, “Cosmic microwave background anisotropies,” *Annual Review of Astronomy and Astrophysics*, vol. 40, no. 1, pp. 171–216, 2002.
- [32] A. Lewis and A. Challinor, “CAMB: Code for anisotropies in the microwave background,” *Astrophysics Source Code Library*, 2011.
- [33] E. E. Flanagan and S. A. Hughes, “The basics of gravitational wave theory,” *New Journal of Physics*, vol. 7, no. 1, p. 204, 2005.
- [34] The BICEP/Keck Collaboration, : P. A. R. Ade, Z. Ahmed, R. W. Aikin, K. D. Alexander, D. Barkats, S. J. Benton, C. A. Bischoff, J. J. Bock, H. Boenish, R. Bowens-Rubin, J. A. Brevik, I. Buder, E. Bullock, V. Buza, J. Connors, J. Cornelison, B. P. Crill, M. Crumrine, M. Dierickx, L. Duband, C. Dvorkin, J. P. Filippini, S. F. J. Grayson, G. Hall, M. Halpern, S. Harrison, S. R. Hildebrandt, G. C. Hilton, H. Hui, K. D. Irwin, J. Kang, K. S. Karkare, E. Karpel, J. P. Kaufman, B. G. Keating, S. Kefeli, S. A. Kernasovskiy, J. M. Kovac, C. L. Kuo, K. Lau, N. A. Larsen, E. M. Leitch, M. Lueker, K. G. Megerian, L. Moncelsi, T. Namikawa, B. Netterfield, H. T. Nguyen, R. O’Brient, R. W. Ogburn IV, S. Palladino, C. Pryke, B. Racine, S. Richter, R. Schwarz, A. Schillaci, C. D. Sheehy, A. Soliman, T. St. Germaine, Z. K. Staniszewski, B. Steinbach, R. V. Sudiwala, G. P. Teply, K. L. Thompson, J. E. Tolan, C. Tucker, A. D. Turner, C. Umita, A. G. Vieregg, A. Wandui, A. C. Weber, D. V. Wiebe, J. Willmert, C. L. Wong, W. L. K. Wu, H. Yang, K. W. Yoon, and C. Zhang, “Measurements of Degree-Scale B-mode Polarization with the BICEP/Keck Experiments at South Pole,” *arXiv e-prints*, Jul. 2018.
- [35] U. Seljak, “Gravitational lensing effect on cosmic microwave background anisotropies: A power spectrum approach,” *arXiv e-prints*, 1995.
- [36] M. Zaldarriaga and U. Seljak, “Gravitational lensing effect on cosmic microwave background polarization,” *Physical Review D*, vol. 58, no. 2, 1998.
- [37] L. Cayon, E. Martinez-Gonzalez, and J. L. Sanz, “Gravitational lensing and the cosmic microwave background,” *The Astrophysical Journal*, vol. 403, pp. 471–475, 1993.
- [38] L. Knox and Y.-S. Song, “Limit on the detectability of the energy scale of inflation,” *Physical Review Letters*, vol. 89, no. 1, p. 011 303, 2002.
- [39] M. Zaldarriaga and U. Seljak, “Reconstructing projected matter density power spectrum from cosmic microwave background,” *Physical Review D*, vol. 59, no. 12, p. 123 507, 1999.

- [40] BICEP2 Collaboration, P. A. R. Ade, R. W. Aikin, D. Barkats, S. J. Benton, C. A. Bischoff, J. J. Bock, J. A. Brevik, I. Buder, E. Bullock, C. D. Dowell, L. Duband, J. P. Filippini, S. Fliescher, S. R. Golwala, M. Halpern, M. Hasselfield, S. R. Hildebrandt, G. C. Hilton, V. V. Hristov, K. D. Irwin, K. S. Karkare, J. P. Kaufman, B. G. Keating, S. A. Kernasovskiy, J. M. Kovac, C. L. Kuo, E. M. Leitch, M. Lueker, P. Mason, C. B. Netterfield, H. T. Nguyen, R. O'Brient, R. W. Ogburn, A. Orlando, C. Pryke, C. D. Reintsema, S. Richter, R. Schwarz, C. D. Sheehy, Z. K. Staniszewski, R. V. Sudiwala, G. P. Teply, J. E. Tolan, A. D. Turner, A. G. Vieregg, C. L. Wong, and K. W. Yoon, “Detection of B-Mode Polarization at Degree Angular Scales by BICEP2,” *Physical Review Letters*, vol. 112, no. 24, 241101, p. 241 101, Jun. 2014.
- [41] P. A. R. Ade, N. Aghanim, Z. Ahmed, R. W. Aikin, K. D. Alexander, M. Arnaud, J. Aumont, C. Baccigalupi, A. J. Banday, D. Barkats, R. B. Barreiro, J. G. Bartlett, N. Bartolo, E. Battaner, K. Benabed, A. Benoît, A. Benoit-Lévy, S. J. Benton, J.-P. Bernard, M. Bersanelli, P. Bielewicz, C. A. Bischoff, J. J. Bock, A. Bonaldi, L. Bonavera, J. R. Bond, J. Borrill, F. R. Bouchet, F. Boulanger, J. A. Brevik, M. Bucher, I. Buder, E. Bullock, C. Burigana, R. C. Butler, V. Buza, E. Calabrese, J.-F. Cardoso, A. Catalano, A. Challinor, R.-R. Chary, H. C. Chiang, P. R. Christensen, L. P. L. Colombo, C. Combet, J. Connors, F. Couchot, A. Coulais, B. P. Crill, A. Curto, F. Cuttaia, L. Danese, R. D. Davies, R. J. Davis, P. de Bernardis, A. de Rosa, G. de Zotti, J. Delabrouille, J.-M. Delouis, F.-X. Désert, C. Dickinson, J. M. Diego, H. Dole, S. Donzelli, O. Doré, M. Douspis, C. D. Dowell, L. Duband, A. Ducout, J. Dunkley, X. Dupac, C. Dvorkin, G. Efstathiou, F. Elsner, T. A. Enßlin, H. K. Eriksen, E. Falgarone, J. P. Filippini, F. Finelli, S. Fliescher, O. Forni, M. Frailis, A. A. Fraisse, E. Franceschi, A. Frejsel, S. Galeotta, S. Galli, K. Ganga, T. Ghosh, M. Giard, E. Gjerløw, S. R. Golwala, J. González-Nuevo, K. M. Górska, S. Gratton, A. Gregorio, A. Gruppuso, J. E. Gudmundsson, M. Halpern, F. K. Hansen, D. Hanson, D. L. Harrison, M. Hasselfield, G. Helou, S. Henrot-Versillé, D. Herranz, S. R. Hildebrandt, G. C. Hilton, E. Hivon, M. Hobson, W. A. Holmes, W. Hovest, V. V. Hristov, K. M. Huffenberger, H. Hui, G. Hurier, K. D. Irwin, A. H. Jaffe, T. R. Jaffe, J. Jewell, W. C. Jones, M. Juvela, A. Karakci, K. S. Karkare, J. P. Kaufman, B. G. Keating, S. Kefeli, E. Keihänen, S. A. Kernasovskiy, R. Keskitalo, T. S. Kisner, R. Kneissl, J. Knoche, L. Knox, J. M. Kovac, N. Krachmalnicoff, M. Kunz, C. L. Kuo, H. Kurki-Suonio, G. Lagache, A. Lähteenmäki, J.-M. Lamarre, A. Lasenby, M. Lattanzi, C. R. Lawrence, E. M. Leitch, R. Leonardi, F. Levrier, A. Lewis, M. Liguori, P. B. Lilje, M. Linden-Vørnle, M. López-Caniego, P. M. Lubin, M. Lueker, J. F. Macías-Pérez, B. Maffei, D. Maino, N. Mandolesi, A. Mangilli, M. Maris, P. G. Martin, E. Martínez-González, S. Masi, P. Mason, S. Matarrese, K. G. Megerian, P. R. Meinhold, A. Melchiorri, L. Mendes, A. Mennella, M. Migliaccio, S. Mitra, M.-A. Miville-Deschénes, A. Moneti, L. Montier, G. Morgante, D. Mortlock, A. Moss, D. Munshi, J. A. Murphy, P. Naselsky, F. Nati, P. Natoli, C. B. Netterfield, H. T. Nguyen, H. U. Nørgaard-Nielsen, F. Noviello, D. Novikov, I. Novikov, R.

O'Brient, R. W. Ogburn, A. Orlando, L. Pagano, F. Pajot, R. Paladini, D. Paoletti, B. Partridge, F. Pasian, G. Patanchon, T. J. Pearson, O. Perdereau, L. Perotto, V. Pettorino, F. Piacentini, M. Piat, D. Pietrobon, S. Plaszczynski, E. Pointecouteau, G. Polenta, N. Ponthieu, G. W. Pratt, S. Prunet, C. Pryke, J.-L. Puget, J. P. Rachen, W. T. Reach, R. Rebolo, M. Reinecke, M. Remazeilles, C. Renault, A. Renzi, S. Richter, I. Ristorcelli, G. Rocha, M. Rossetti, G. Roudier, M. Rowan-Robinson, J. A. Rubiño Martín, B. Rusholme, M. Sandri, D. Santos, M. Savelainen, G. Savini, R. Schwarz, D. Scott, M. D. Seiffert, C. D. Sheehy, L. D. Spencer, Z. K. Staniszewski, V. Stolyarov, R. Sudiwala, R. Sunyaev, D. Sutton, A.-S. Suur-Uski, J.-F. Sygnet, J. A. Tauber, G. P. Teply, L. Terenzi, K. L. Thompson, L. Toffolatti, J. E. Tolan, M. Tomasi, M. Tristram, M. Tucci, A. D. Turner, L. Valenziano, J. Valiviita, B. Van Tent, L. Vibert, P. Vielva, A. G. Vieregg, F. Villa, L. A. Wade, B. D. Wandelt, R. Watson, A. C. Weber, I. K. Wehus, M. White, S. D. M. White, J. Willmert, C. L. Wong, K. W. Yoon, D. Yvon, A. Zacchei, and A. Zonca, “Joint analysis of BICEP2/Keck Array and Planck data,” *Phys. Rev. Lett.*, vol. 114, p. 101301, 10 2015.

- [42] “The am atmospheric model (v. 10.0),” 2018.
- [43] Y.-P. Li, Y. Liu, S.-Y. Li, H. Li, and X. Zhang, “Tibet’s Ali: A New Window to Detect the CMB Polarization,” *arXiv e-prints*, Sep. 2017.
- [44] C.-Z. Liu, D. Wu, F.-J. Lu, H. Xu, H. Li, Y.-J. Zhang, Z.-W. Li, S.-Y. Li, X. Zhang, Y. Liu, Y.-P. Li, Y. Cai, M. Li, Y.-Q. Yao, G.-B. Zhao, Z.-H. Fan, and C.-L. Kuo, “Probing primordial gravitational waves: Ali CMB Polarization Telescope,” *National Science Review*, vol. 6, no. 1, pp. 145–154, Feb. 2018.
- [45] D. Samtleben, S. Staggs, and B. Winstein, “The cosmic microwave background for pedestrians: A review for particle and nuclear physicists,” *Annu. Rev. Nucl. Part. Sci.*, vol. 57, pp. 245–283, 2007.
- [46] T. Hoang and A. Lazarian, “Radiative torque alignment: Essential physical processes,” *Monthly Notices of the Royal Astronomical Society*, vol. 388, no. 1, pp. 117–143, 2008.
- [47] Polarbear Collaboration, P. A. R. Ade, Y. Akiba, A. E. Anthony, K. Arnold, M. Atlas, D. Barron, D. Boettger, J. Borrill, S. Chapman, Y. Chinone, M. Dobbs, T. Elleflot, J. Errard, G. Fabbian, C. Feng, D. Flanigan, A. Gilbert, W. Grainger, N. W. Halverson, M. Hasegawa, K. Hattori, M. Hazumi, W. L. Holzapfel, Y. Hori, J. Howard, P. Hyland, Y. Inoue, G. C. Jaehnig, A. H. Jaffe, B. Keating, Z. Kermish, R. Keskitalo, T. Kisner, M. Le Jeune, A. T. Lee, E. M. Leitch, E. Linder, M. Lungu, F. Matsuda, T. Matsumura, X. Meng, N. J. Miller, H. Morii, S. Moyerman, M. J. Myers, M. Navaroli, H. Nishino, A. Orlando, H. Paar, J. Peloton, D. Poletti, E. Quealy, G. Rebeiz, C. L. Reichardt, P. L. Richards, C. Ross, I. Schanning, D. E. Schenck, B. D. Sherwin, A. Shimizu, C. Shimmin, M. Shimon, P. Siritanasak, G. Smecher, H. Spieler, N. Stebor, B. Steinbach, R. Stompor, A. Suzuki, S. Takakura, T. Tomaru, B. Wilson, A. Yadav, and O. Zahn, “A Measurement of the Cosmic

Microwave Background B-mode Polarization Power Spectrum at Sub-degree Scales with POLARBEAR,” *The Astrophysical Journal*, vol. 794, 171, p. 171, Oct. 2014.

- [48] A. T. Lee, P. L. Richards, S. W. Nam, B. Cabrera, and K. D. Irwin, “A superconducting bolometer with strong electrothermal feedback,” *Applied Physics Letters*, vol. 69, no. 12, pp. 1801–1803, 1996.
- [49] T. M. Lanting, “Multiplexed readout of superconducting bolometers for cosmological observations,” PhD thesis, 2006.
- [50] W. Holmes, J. M. Gildemeister, P. L. Richards, and V. Kotsubo, “Thermal Transport Measurements of Low Stress Silicon Nitride Membranes,” in *APS March Meeting Abstracts*, Mar. 1998, G26.01.
- [51] D. R. Barron, “Precision measurements of cosmic microwave background polarization to study cosmic inflation and large scale structure,” PhD thesis, UC San Diego, 2015.
- [52] K. S. Arnold, “Design and deployment of the POLARBEAR cosmic microwave background polarization experiment,” PhD thesis, 2010.
- [53] J. C. Mather, “Bolometer noise: Nonequilibrium theory,” *Applied optics*, vol. 21, no. 6, pp. 1125–1129, 1982.
- [54] J. Zmuidzinas, “Thermal noise and correlations in photon detection,” *Applied optics*, vol. 42, no. 25, pp. 4989–5008, 2003.
- [55] J. Clarke and A. I. Braginski, *The SQUID handbook: Applications of SQUIDs and SQUID systems*. John Wiley & Sons, 2006.
- [56] P. Richards, “Bolometric detectors for measurements of the cosmic microwave background,” *Journal of superconductivity*, vol. 17, no. 5, pp. 545–550, 2004.
- [57] J. Bardeen, L. N. Cooper, and J. R. Schrieffer, “Theory of superconductivity,” *Physical review*, vol. 108, no. 5, p. 1175, 1957.
- [58] W. Meissner and R. Ochsenfeld, “Ein neuer effekt bei eintritt der supraleitfähigkeit,” *Naturwissenschaften*, vol. 21, no. 44, pp. 787–788, 1933.
- [59] M. A. Dobbs, M. Lueker, K. A. Aird, A. N. Bender, B. A. Benson, L. E. Bleem, J. E. Carlstrom, C. L. Chang, H.-M. Cho, J. Clarke, T. M. Crawford, A. T. Crites, D. I. Flanigan, T. de Haan, E. M. George, N. W. Halverson, W. L. Holzapfel, J. D. Hrubes, B. R. Johnson, J. Joseph, R. Keisler, J. Kennedy, Z. Kermish, T. M. Lanting, A. T. Lee, E. M. Leitch, D. Luong-Van, J. J. McMahon, J. Mehl, S. S. Meyer, T. E. Montroy, S. Padin, T. Plagge, C. Pryke, P. L. Richards, J. E. Ruhl, K. K. Schaffer, D. Schwan, E. Shirokoff, H. G. Spieler, Z. Staniszewski, A. A. Stark, K. Vanderlinde, J. D. Vieira, C. Vu, B. Westbrook, and R. Williamson, “Frequency multiplexed superconducting quantum interference device readout of large bolometer arrays for cosmic microwave background measurements,” *Review of Scientific Instruments*, vol. 83, no. 7, 073113-073113-24, pp. 073113–073113–24, Jul. 2012.

- [60] M. Dobbs, E. Bissonnette, and H. Spieler, “Digital frequency domain multiplexer for mm-wavelength telescopes,” in *Real-Time Conference, 2007 15th IEEE-NPSS*, IEEE, 2007, pp. 1–6.
- [61] D. Drung, C. Hinnrichs, and H.-J. Barthelmess, “Low-noise ultra-high-speed dc SQUID readout electronics,” *Superconductor Science and Technology*, vol. 19, no. 5, S235, 2006.
- [62] G. Stiehl, H.-M. Cho, G. C. Hilton, K. D. Irwin, J. Mates, C. D. Reintsema, and B. L. Zink, “Time-division SQUID multiplexers with reduced sensitivity to external magnetic fields,” *IEEE Transactions on Applied Superconductivity*, vol. 21, no. 3, pp. 298–301, 2011.
- [63] D. Drung, C. Abmann, J. Beyer, A. Kirste, M. Peters, F. Rueder, and T. Schurig, “Highly sensitive and easy-to-use SQUID sensors,” *IEEE Transactions on Applied Superconductivity*, vol. 17, no. 2, pp. 699–704, 2007.
- [64] K. D. Irwin and K. W. Lehnert, “Microwave SQUID multiplexer,” *Applied physics letters*, vol. 85, no. 11, pp. 2107–2109, 2004.
- [65] J. A. B. Mates, “The microwave SQUID multiplexer,” *Ph. D thesis*, 2011.
- [66] K. D. Irwin, “SQUID multiplexers for transition-edge sensors,” *Physica C: Superconductivity*, vol. 368, no. 1-4, pp. 203–210, 2002.
- [67] Z. D. Kermish, P. Ade, A. Anthony, K. Arnold, D. Barron, D. Boettger, J. Borrill, S. Chapman, Y. Chinone, M. A. Dobbs, J. Errard, G. Fabbian, D. Flanigan, G. Fuller, A. Ghribi, W. Grainger, N. Halverson, M. Hasegawa, K. Hattori, M. Hazumi, W. L. Holzapfel, J. Howard, P. Hyland, A. Jaffe, B. Keating, T. Kisner, A. T. Lee, M. Le Jeune, E. Linder, M. Lungu, F. Matsuda, T. Matsumura, X. Meng, N. J. Miller, H. Morii, S. Moyerman, M. J. Myers, H. Nishino, H. Paar, E. Quealy, C. L. Reichardt, P. L. Richards, C. Ross, A. Shimizu, M. Shimon, C. Shimmin, M. Sholl, P. Siritanasak, H. Spieler, N. Stebor, B. Steinbach, R. Stompor, A. Suzuki, T. Tomaru, C. Tucker, and O. Zahn, “The POLARBEAR experiment,” in *Millimeter, Submillimeter, and Far-Infrared Detectors and Instrumentation for Astronomy VI*, ser. Proceedings of the SPIE, vol. 8452, Sep. 2012, p. 84521C.
- [68] L. Bleem, P. Ade, K. Aird, J. Austermann, J. Beall, D. Becker, B. Benson, J. Britton, J. Carlstrom, C. L. Chang, H. Cho, T. de Haan, T. Crawford, A. Crits, A. Datesman, M. Dobbs, W. Everett, A. Ewall-Wice, E. George, N. Halverson, N. Harrington, J. Henning, G. Hilton, W. Holzapfel, S. Hoover, J. Hubmayr, K. Irwin, R. Keisler, J. Kennedy, A. Lee, E. Leitch, D. Li, M. Lueker, D. P. Marrone, J. McMahon, J. Mehl, S. Meyer, J. Montgomery, T. Montroy, T. Natoli, J. Nibarger, M. Niemack, V. Novosad, S. Padin, C. Pryke, C. Reichardt, J. Ruhl, B. Saliwanchik, J. Sayre, K. Schafer, E. Shirokoff, K. Story, K. Vanderlinde, J. Vieira, G. Wang, R. Williamson, V. Yefremenko, K. W. Yoon, and E. Young, “An Overview of the SPTpol Experiment,” *Journal of Low Temperature Physics*, vol. 167, pp. 859–864, Jun. 2012.

- [69] R. W. Ogburn, P. A. R. Ade, R. W. Aikin, M. Amiri, S. J. Benton, C. A. Bischoff, J. J. Bock, J. A. Bonetti, J. A. Brevik, E. Bullock, B. Burger, G. Davis, C. D. Dowell, L. Duband, J. P. Filippini, S. Fliescher, S. R. Golwala, M. Gordon, M. Halpern, M. Hasselfield, G. Hilton, V. V. Hristov, H. Hui, K. Irwin, J. P. Kaufman, B. G. Keating, S. A. Kernasovskiy, J. M. Kovac, C. L. Kuo, E. M. Leitch, M. Lueker, T. Montroy, C. B. Netterfield, H. T. Nguyen, R. O'Brient, A. Orlando, C. L. Pryke, C. Reintsema, S. Richter, J. E. Ruhl, M. C. Runyan, R. Schwarz, C. D. Sheehy, Z. K. Staniszewski, R. V. Sudiwala, G. P. Teply, K. Thompson, J. E. Tolan, A. D. Turner, A. G. Vieregg, D. V. Wiebe, P. Wilson, and C. L. Wong, “BICEP2 and Keck array operational overview and status of observations,” in *Millimeter, Submillimeter, and Far-Infrared Detectors and Instrumentation for Astronomy VI*, ser. Proceedings of the SPIE, vol. 8452, Sep. 2012, 84521A.
- [70] D. S. Swetz, P. A. R. Ade, M. Amiri, J. W. Appel, E. S. Battistelli, B. Burger, J. Chervenak, M. J. Devlin, S. R. Dicker, W. B. Doriese, R. Dünner, T. Essinger-Hileman, R. P. Fisher, J. W. Fowler, M. Halpern, M. Hasselfield, G. C. Hilton, A. D. Hincks, K. D. Irwin, N. Jarosik, M. Kaul, J. Klein, J. M. Lau, M. Limon, T. A. Marriage, D. Marsden, K. Martocci, P. Mauskopf, H. Moseley, C. B. Netterfield, M. D. Niemack, M. R. Nolta, L. A. Page, L. Parker, S. T. Staggs, O. Stryzak, E. R. Switzer, R. Thornton, C. Tucker, E. Wollack, and Y. Zhao, “Overview of the Atacama Cosmology Telescope: Receiver, Instrumentation, and Telescope Systems,” *The Astrophysical Journal Supplementary Series*, vol. 194, 41, p. 41, Jun. 2011.
- [71] W. B. Doriese, K. M. Morgan, D. A. Bennett, E. V. Denison, C. P. Fitzgerald, J. W. Fowler, J. D. Gard, J. P. Hays-Wehle, G. C. Hilton, K. D. Irwin, Y. I. Joe, J. A. B. Mates, G. C. O’Neil, C. D. Reintsema, N. O. Robbins, D. R. Schmidt, D. S. Swetz, H. Tatsuno, L. R. Vale, and J. N. Ullom, “Developments in time-division multiplexing of x-ray transition-edge sensors,” *Journal of Low Temperature Physics*, vol. 184, no. 1, pp. 389–395, 2016.
- [72] K. Irwin, M. Niemack, J. Beyer, H. Cho, W. Doriese, G. Hilton, C. Reintsema, D. Schmidt, J. Ullom, and L. Vale, “Code-division multiplexing of superconducting transition-edge sensor arrays,” *Superconductor Science and Technology*, vol. 23, no. 3, p. 034 004, 2010.
- [73] A. N. Bender, J.-F. Cliche, T. de Haan, M. A. Dobbs, A. J. Gilbert, J. Montgomery, N. Rowlands, G. M. Smecher, K. Smith, and A. Wilson, “Digital frequency domain multiplexing readout electronics for the next generation of millimeter telescopes,” in *Millimeter, Submillimeter, and Far-Infrared Detectors and Instrumentation for Astronomy VII*, International Society for Optics and Photonics, vol. 9153, 2014, 91531A.
- [74] S. Stanchfield, P. Ade, J. Aguirre, J. A. Brevik, H.-M. Cho, R. Datta, M. Devlin, S. R. Dicker, B. Dober, S. M. Duff, D. Egan, P. Ford, G. Hilton, J. Hubmayr, K. Irwin, K. Knowles, P. Marganian, B. S. Mason, J. A. B. Mates, J. McMahon, M. Mello, T. Mroczkowski, C. Romero, J. Sievers, C. Tucker, L. R. Vale, M. Vissers,

- S. White, M. Whitehead, J. Ullom, and A. Young, “High Resolution Imaging with MUSTANG-2 on the GBT,” in *American Astronomical Society Meeting Abstracts #231*, ser. American Astronomical Society Meeting Abstracts, vol. 231, Jan. 2018, p. 322.05.
- [75] S. W. Henderson, Z. Ahmed, J. Austermann, D. Becker, D. A. Bennett, D. Brown, S. Chaudhuri, H.-M. Cho, J. M. D’Ewart, B. Dober, S. M. Duff, J. E. Dusatko, S. Fatigoni, J. C. Frisch, J. D. Gard, M. Halpern, G. C. Hilton, J. Hubmayr, K. D. Irwin, E. D. Karpel, S. S. Kernasovskiy, S. E. Kuenstner, C.-L. Kuo, D. Li, J. A. B. Mates, C. D. Reintsema, S. R. Smith, J. Ullom, L. R. Vale, D. D. Van Winkle, M. Vissers, and C. Yu, “Highly-multiplexed microwave SQUID readout using the SLAC Microresonator Radio Frequency (SMuRF) Electronics for Future CMB and Sub-millimeter Surveys,” *arXiv e-prints*, pp. 1–16, 2018.
- [76] A. E. Lowitz, A. N. Bender, M. A. Dobbs, and A. J. Gilbert, “Digital frequency multiplexing with sub-kelvin SQUIDs,” in *Millimeter, Submillimeter, and Far-Infrared Detectors and Instrumentation for Astronomy IX*, International Society for Optics and Photonics, vol. 10708, 2018, p. 107081D.
- [77] K. Bandura, A. N. Bender, J. F. Cliche, T. de Haan, M. A. Dobbs, A. J. Gilbert, S. Griffin, G. Hsyu, D. Ittah, J. M. Parra, J. Montgomery, T. Pinsonneault-Marotte, S. Siegel, G. Smecher, Q. Y. Tang, K. Vanderlinde, and N. Whitehorn, “ICE: a scalable, low-cost FPGA-based telescope signal processing and networking system,” *arXiv e-prints*, 2016.
- [78] T. de Haan, G. Smecher, and M. Dobbs, “Improved performance of tes bolometers using digital feedback,” in *Millimeter, Submillimeter, and Far-Infrared Detectors and Instrumentation for Astronomy VI*, International Society for Optics and Photonics, vol. 8452, 2012, 84520E.
- [79] J. Montgomery, “Development of multiplexed bolometer readout electronics for mm-wave space astronomy,” PhD thesis, McGill University Libraries, 2015.
- [80] A. N. Bender, P. A. R. Ade, Z. Ahmed, A. J. Anderson, J. S. Avva, K. Aylor, P. S. Barry, R. Basu Thakur, B. A. Benson, L. S. Bleem, S. Bocquet, K. Byrum, J. E. Carlstrom, F. W. Carter, T. W. Cecil, C. L. Chang, H.-M. Cho, J. F. Cliche, T. M. Crawford, A. Cukierman, T. de Haan, E. V. Denison, J. Ding, M. A. Dobbs, S. Dodelson, D. Dutcher, W. Everett, A. Foster, J. Gallicchio, A. Gilbert, J. C. Groh, S. T. Guns, N. W. Halverson, A. H. Harke-Hosemann, N. L. Harrington, J. W. Henning, G. C. Hilton, G. P. Holder, W. L. Holzapfel, N. Huang, K. D. Irwin, O. B. Jeong, M. Jonas, A. Jones, T. S. Khaire, L. Knox, A. M. Kofman, M. Korman, D. L. Kubik, S. Kuhlmann, C.-L. Kuo, A. T. Lee, E. M. Leitch, A. E. Lowitz, S. S. Meyer, D. Michalik, J. Montgomery, A. Nadolski, T. Natoli, H. Ngyuen, G. I. Noble, V. Novosad, S. Padin, Z. Pan, J. Pearson, C. M. Posada, W. Quan, S. Raghunathan, A. Rahlin, C. L. Reichardt, J. E. Ruhl, J. T. Sayre, E. Shirokoff, G. Smecher, J. A. Sobrin, A. A. Stark, K. T. Story, A. Suzuki, K. L. Thompson, C. Tucker, L. R. Vale, K. Vanderlinde, J. D. Vieira, G. Wang, N. Whitehorn, W. L. K. Wu,

- V. Yefremenko, K. W. Yoon, and M. R. Young, “Year two instrument status of the SPT-3G cosmic microwave background receiver,” in *Millimeter, Submillimeter, and Far-Infrared Detectors and Instrumentation for Astronomy IX*, ser. Society of Photo-Optical Instrumentation Engineers (SPIE) Conference Series, vol. 10708, Jul. 2018, p. 1070 803.
- [81] J Errard, Y Akiba, K Arnold, M Atlas, C Baccigalupi, D Barron, D Boettger, J Borrill, S Chapman, Y Chinone, A Cukierman, J Delabrouille, M Dobbs, A Ducout, T Ellefot, G Fabbian, C Feng, S Feeney, A Gilbert, N. W. Halverson, M Hasegawa, K Hattori, M Hazumi, C Hill, W. L. Holzapfel, Y Hori, Y Inoue, G. C. Jaehnig, A. H. Jaffe, O Jeong, N Katayama, J Kaufman, B Keating, Z Kermish, R Keskitalo, T Kisner, M. L. Jeune, A. T. Lee, E. M. Leitch, D Leon, E Linder, F Matsuda, T Matsumura, N. J. Miller, M. J. Myers, M Navaroli, H Nishino, T Okamura, H Paar, J Peloton, D Poletti, G Puglisi, G Rebeiz, C. L. Reichardt, P. L. Richards, C Ross, K. M. Rotermund, D. E. Schenck, B. D. Sherwin, P Siritanasak, G Smecher, N Stebor, B Steinbach, R Stompor, A Suzuki, O Tajima, S Takakura, A Tikhomirov, T Tomaru, N Whitehorn, B Wilson, A Yadav, and O Zahn, “Modeling atmospheric emission for CMB ground-based observations,” *arXiv e-prints*, 2015.
- [82] C. A. Hill, S. Beckman, Y Chinone, N. Goeckner-Wald, M. Hazumi, B. Keating, A. Kusaka, A. T. Lee, F. Matsuda, R. Plambeck, A. Suzuki, and S. Takakura, “Design and development of an ambient-temperature continuously-rotating achromatic half-wave plate for CMB polarization modulation on the POLARBEAR-2 experiment,” July 2016, vol. 9914, 2016, 99142U.
- [83] C. A. Hill, A. Kusaka, P. Barton, B. Bixler, A. G. Droster, M. Flament, S. Ganjam, A. Jadbabaie, O. Jeong, A. T. Lee, A. Madurowicz, F. T. Matsuda, T. Matsumura, A. Rutkowski, Y. Sakurai, D. R. Sponseller, A. Suzuki, and R. Tat, “A Large-Diameter Cryogenic Rotation Stage for Half-Wave Plate Polarization Modulation on the POLARBEAR-2 Experiment,” *Journal of Low Temperature Physics*, vol. 193, no. 5-6, pp. 851–859, 2018.
- [84] P. A. R. Ade, R. W. Aikin, D. Barkats, S. J. Benton, C. A. Bischoff, J. J. Bock, J. A. Brevik, I. Buder, E. Bullock, C. D. Dowell, L. Duband, J. P. Filippini, S. Fliescher, S. R. Golwala, M. Halpern, M. Hasselfield, S. R. Hildebrandt, G. C. Hilton, V. V. Hristov, K. D. Irwin, K. S. Karkare, J. P. Kaufman, B. G. Keating, S. A. Kernasovskiy, J. M. Kovac, C. L. Kuo, E. M. Leitch, M. Lueker, P. Mason, C. B. Netterfield, H. T. Nguyen, R. O’Brient, R. W. Ogburn, A. Orlando, C. Pryke, C. D. Reintsema, S. Richter, R. Schwarz, C. D. Sheehy, Z. K. Staniszewski, R. V. Sudiwala, G. P. Teply, J. E. Tolan, A. D. Turner, A. G. Vieregg, C. L. Wong, and K. W. Yoon, “Detection of *B*-Mode Polarization at Degree Angular Scales by BICEP2,” *Phys. Rev. Lett.*, vol. 112, p. 241 101, 24 2014.
- [85] M. J. Mortonson and U. Seljak, “A joint analysis of Planck and BICEP2 *B* modes including dust polarization uncertainty,” *Journal of Cosmology and Astroparticle Physics*, vol. 2014, no. 10, p. 035, 2014.

- [86] K. Arnold, N. Stebor, P. Ade, Y. Akiba, A. E. Anthony, M. Atlas, D. Barron, A. Bender, D. Boettger, J. Borrill, S. Chapman, Y. Chinone, A. Cukierman, M. Dobbs, T. Elleflot, J. Errard, G. Fabbian, C. Feng, A. Gilbert, N. Goeckner-Wald, N. W. Halverson, M. Hasegawa, K. Hattori, M. Hazumi, W. Holzapfel, Y. Hori, Y. Inoue, G. C. Jaehnig, A. H. Jaffe, N. Katayama, B. Keating, Z. Kermish, R. Keskitalo, T. Kisner, M. Le Jeune, A. Lee, E. Leitch, E. Linder, F. Matsuda, T. Matsumura, X. Meng, N. J. Miller, H. Morii, M. J. Myers, M. Navaroli, H. Nishino, T. Okamura, H. Paar, J. Peloton, D. Poletti, C. Raum, G. Rebeiz, C. L. Reichardt, P. L. Richards, C. Ross, K. M. Rotermund, D. E. Schenck, B. D. Sherwin, I. Shirley, M. Sholl, P. Siritanasak, G. Smecher, B. Steinbach, R. Stompor, A. Suzuki, J. Suzuki, S. Takada, S. Takakura, T. Tomaru, B. Wilson, A. Yadav, and O. Zahn, “The Simons Array: expanding POLARBEAR to three multi-chroic telescopes,” *SPIE Astronomical Telescopes + Instrumentation*, no. August 2014, 91531F, 2014.
- [87] M. Levi, C. Bebek, T. Beers, R. Blum, R. Cahn, D. Eisenstein, B. Flaugher, K. Honscheid, R. Kron, O. Lahav, and the DESI collaboration, “The DESI Experiment, a whitepaper for Snowmass 2013,” *arXiv e-prints*, 2013.
- [88] P. A. Ade, G. Pisano, C. Tucker, and S. Weaver, “A review of metal mesh filters,” in *Millimeter and Submillimeter Detectors and Instrumentation for Astronomy III*, International Society for Optics and Photonics, vol. 6275, 2006, 62750U.
- [89] M. A. Green, S. S. Chouhan, C Wang, and A. F. Zeller, “Second stage cooling from a cryomech PT415 cooler at second stage temperatures up to 300 K with cooling on the first-stage from 0 to 250 W,” *IOP Conference Series: Materials Science and Engineering*, vol. 101, no. 1, p. 012 002, 2015.
- [90] F. Pobell, *Matter and methods at low temperatures*. Springer, 2007, vol. 2.
- [91] E. S. Cheng, S. S. Meyer, and L. A. Page, “A high capacity 0.23 k 3he refrigerator for balloon-borne payloads,” *Review of scientific instruments*, vol. 67, no. 11, pp. 4008–4016, 1996.
- [92] A. N. Bender, J.-F. Cliche, T. de Haan, M. A. Dobbs, A. Gilbert, J. Montgomery, N. Rowlands, G. M. Smecher, K. Smith, and A. Wilson, “Digital frequency domain multiplexing readout electronics for the next generation of millimeter telescopes,” *SPIE Astronomical Telescopes + Instrumentation*, vol. 9153, Jul. 2014.
- [93] J. R. Howell, M. P. Menguc, and R. Siegel, *Thermal radiation heat transfer*. CRC press, 2010.
- [94] S. Bapat, K. Narayankhedkar, and T. Lukose, “Performance prediction of multilayer insulation,” *Cryogenics*, vol. 30, no. 8, pp. 700–710, 1990.
- [95] C. Keller, “Thermal performance of multilayer insulations final report,” 1971.
- [96] M. Runyan and W. Jones, “Thermal conductivity of thermally-isolating polymeric and composite structural support materials between 0.3 and 4 K,” *Cryogenics*, vol. 48, pp. 448–454, Jul. 2008.

- [97] N. Kellaris, M. Daal, M. Epland, M. Pepin, O. Kamaev, P. Cushman, E. Kramer, B. Sadoulet, N. Mirabolfathi, S. Golwala, and M. Runyan, “Sub-kelvin thermal conductivity and radioactivity of some useful materials in low background cryogenic experiments,” *Journal of Low Temperature Physics*, vol. 176, no. 3, pp. 201–208, 2014.
- [98] M. Barucci, E. Gottardi, I. Peroni, and V. Guido, “Low temperature thermal conductivity of kapton and upilex,” *Cryogenics*, vol. 40, pp. 145–147, Feb. 2000.
- [99] .
- [100] A. L. Woodcraft, “Recommended values for the thermal conductivity of aluminium of different purities in the cryogenic to room temperature range, and a comparison with copper,” *Cryogenics*, vol. 45, no. 9, pp. 626–636, 2005.
- [101] W. H. Krueger and S. Pollack, “The initial oxidation of aluminum thin films at room temperature,” *Surface Science*, vol. 30, no. 2, pp. 263–279, 1972.
- [102] G. L. Pollack, “Kapitza resistance,” *Reviews of Modern Physics*, vol. 41, no. 1, p. 48, 1969.
- [103] R. Berman, “Some experiments on thermal contact at low temperatures,” *Journal of Applied Physics*, vol. 27, no. 4, pp. 318–323, 1956.
- [104] L. J. Salerno and P. Kittel, “Thermal contact conductance,” *Journal of Materials Processing Technology*, vol. 135, no. 2-3, pp. 204–210, 2003.
- [105] E. T. Swartz and R. O. Pohl, “Thermal boundary resistance,” *Reviews of modern physics*, vol. 61, no. 3, p. 605, 1989.
- [106] I. Didschuns, A. L. Woodcraft, D. Bintley, and P. C. Hargrave, “Thermal conductance measurements of bolted copper to copper joints at sub-kelvin temperatures,” *Cryogenics*, vol. 44, no. 5, pp. 293–299, 2004.
- [107] E. Gmelin, M. Asen-Palmer, M. Reuther, and R. Villar, “Thermal boundary resistance of mechanical contacts between solids at sub-ambient temperatures,” *Journal of Physics D: Applied Physics*, vol. 32, no. 6, R19, 1999.
- [108] P. Siritanasak, C. Aleman, K. Arnold, A. Cukierman, M. Hazumi, K. Kazem-zadeh, B. Keating, T. Matsumura, A. T. Lee, C. Lee, E. Quealy, D. Rosen, N. Stebor, and A. Suzuki, “The Broadband Anti-reflection Coated Extended Hemispherical Silicon Lenses for POLARBEAR-2 Experiment,” *Journal of Low Temperature Physics*, vol. 184, pp. 553–558, Aug. 2016.
- [109] S. T. P. Boyd, J. A. Hall, A. Suzuki, and R. Cantor, “Series SQUID Array Amplifiers Optimized for MHz Frequency-Domain Multiplexed Detector Readout,” *Journal of Low Temperature Physics (poster)*, p. 100, 2017.
- [110] M. Silva-Feaver, K. Arnold, D. Barron, E. V. Denison, M. Dobbs, J. Groh, G. Hilton, J. Hubmayr, K. Irwin, A. Lee, and L. R. Vale, “Comparison of NIST SA13a and SA4b SQUID Array Amplifiers,” *Journal of Low Temperature Physics*, vol. 193, no. 3, pp. 600–610, 2018.

- [111] C. A. Hill, S. M. M. Bruno, S. M. Simon, A. Ali, K. S. Arnold, P. C. Ashton, D. Barron, S. Bryan, Y. Chinone, G. Coppi, K. T. Crowley, A. Cukierman, S. Dicker, J. Dunkley, G. Fabbian, N. Galitzki, P. A. Gallardo, J. E. Gudmundsson, J. Hubmayr, B. Keating, A. Kusaka, A. T. Lee, F. Matsuda, P. D. Mauskopf, J. McMahon, M. D. Niemack, G. Puglisi, M. S. Rao, M. Salatino, C. Sierra, S. Staggs, A. Suzuki, G. Teply, J. N. Ullom, B. Westbrook, Z. Xu, and N. Zhu, “BoloCalc: a sensitivity calculator for the design of Simons Observatory,” *arXiv e-prints*, vol. 1070842, no. July, 2018.
- [112] J. A. Sobrin, P. A. R. Ade, Z. Ahmed, A. J. Anderson, J. S. Avva, R. Basu Thakur, A. N. Bender, B. A. Benson, J. E. Carlstrom, F. W. Carter, T. W. Cecil, C. L. Chang, J. F. Cliche, A. Cukierman, T. de Haan, J. Ding, M. A. Dobbs, D. Dutcher, W. Everett, A. Foster, J. Gallichio, A. Gilbert, J. C. Groh, S. T. Guns, N. W. Halverson, A. H. Harke-Hosemann, N. L. Harrington, J. W. Henning, W. L. Holzapfel, N. Huang, K. D. Irwin, O. B. Jeong, M. Jonas, T. S. Khaire, A. M. Kofman, M. Korman, D. L. Kubik, S. Kuhlmann, C. L. Kuo, A. T. Lee, A. E. Lowitz, S. S. Meyer, D. Michalik, J. Montgomery, A. Nadolski, T. Natoli, H. Nguyen, G. I. Noble, V. Novosad, S. Padin, Z. Pan, J. Pearson, C. M. Posada, W. Quan, A. Rahlin, J. E. Ruhl, J. T. Sayre, E. Shirokoff, G. Smecher, A. A. Stark, K. T. Story, A. Suzuki, K. L. Thompson, C. Tucker, K. Vanderlinde, J. D. Vieira, G. Wang, N. Whitehorn, V. Yefremenko, K. W. Yoon, and M. Young, “Design and characterization of the SPT-3G receiver,” *arXiv e-prints*, Aug. 2018.
- [113] H. Hui, P. A. R. Ade, Z. Ahmed, R. W. Aikin, K. D. Alexander, D. Barkats, S. J. Benton, C. A. Bischoff, J. J. Bock, R. Bowens-Rubin, J. A. Brevik, I. Buder, E. Bullock, V. Buza, J. Connors, J. Cornelison, B. P. Crill, M. Crumrine, M. Dierickx, L. Duband, C. Dvorkin, J. P. Filippini, S. Fliescher, J. Grayson, G. Hall, M. Halpern, S. Harrison, S. R. Hildebrandt, G. C. Hilton, K. D. Irwin, J. Kang, K. S. Karkare, E. Karpel, J. P. Kaufman, B. G. Keating, S. Kefeli, S. A. Kernasovskiy, J. M. Kovac, C. L. Kuo, K. Lau, N. A. Larsen, E. M. Leitch, M. Lueker, K. G. Megerian, L. Moncelsi, T. Namikawa, C. B. Netterfield, H. T. Nguyen, R. OBrient, R. W. Ogburn, S. Palladino, C. Pryke, B. Racine, S. Richter, R. Schwarz, A. Schillaci, C. D. Sheehy, A. Soliman, T. S. Germaine, Z. K. Staniszewski, B. Steinbach, R. V. Sudiwala, G. P. Teply, K. L. Thompson, J. E. Tolan, C. Tucker, A. D. Turner, C. Umita, A. G. Vieregg, A. Wandui, A. C. Weber, D. V. Wiebe, J. Willmert, C. L. Wong, W. L. K. Wu, E. Yang, K. W. Yoon, and C. Zhang, “BICEP Array: a multi-frequency degree-scale CMB polarimeter,” *arXiv e-prints*, no. July, 2018.
- [114] J. A. Grayson, P. A. R. Ade, Z. Ahmed, K. D. Alexander, M. Amiri, J. A. Grayson, P. A. R. Ade, Z. Ahmed, K. D. Alexander, M. Amiri, D. Barkats, C. A. Bischoff, J. J. Bock, H. Boenish, I. Buder, G. C. Hilton, V. V. Hristov, H. Hui, K. D. Irwin, J. Kang, K. S. Karkare, and E. Karpel, “BICEP3 performance overview and planned Keck Array upgrade,” no. July, 2016.
- [115] K. N. Abazajian, P. Adshead, Z. Ahmed, S. W. Allen, D. Alonso, K. S. Arnold, C. Baccigalupi, J. G. Bartlett, N. Battaglia, B. A. Benson, C. A. Bischoff, J. Borrill,

V. Buza, E. Calabrese, R. Caldwell, J. E. Carlstrom, C. L. Chang, T. M. Crawford, F.-Y. Cyr-Racine, F. De Bernardis, T. de Haan, S. di Serego Alighieri, J. Dunkley, C. Dvorkin, J. Errard, G. Fabbian, S. Feeney, S. Ferraro, J. P. Filippini, R. Flauger, G. M. Fuller, V. Gluscevic, D. Green, D. Grin, E. Grohs, J. W. Henning, J. C. Hill, R. Hlozek, G. Holder, W. Holzapfel, W. Hu, K. M. Huffenberger, R. Keskitalo, L. Knox, A. Kosowsky, J. Kovac, E. D. Kovetz, C.-L. Kuo, A. Kusaka, M. Le Jeune, A. T. Lee, M. Lilley, M. Loverde, M. S. Madhavacheril, A. Mantz, D. J. E. Marsh, J. McMahon, P. D. Meerburg, J. Meyers, A. D. Miller, J. B. Munoz, H. N. Nguyen, M. D. Niemack, M. Peloso, J. Peloton, L. Pogosian, C. Pryke, M. Raveri, C. L. Reichardt, G. Rocha, A. Rotti, E. Schaan, M. M. Schmittfull, D. Scott, N. Sehgal, S. Shandera, B. D. Sherwin, T. L. Smith, L. Sorbo, G. D. Starkman, K. T. Story, A. van Engelen, J. D. Vieira, S. Watson, N. Whitehorn, and W. L. Kimmy Wu, “CMB-S4 Science Book, First Edition,” *arXiv e-prints*, Oct. 2016.

- [116] T. Matsumura, Y. Akiba, K. Arnold, J. Borrill, R. Chendra, Y. Chinone, A. Cukierman, T. de Haan, M. Dobbs, A. Dominjon, T. Ellefot, J. Errard, T. Fujino, H. Fuke, N. Goeckner-wald, N. Halverson, P. Harvey, M. Hasegawa, K. Hattori, M. Hattori, M. Hazumi, C. Hill, G. Hilton, W. Holzapfel, Y. Hori, J. Hubmayr, K. Ichiki, J. Inatani, M. Inoue, Y. Inoue, F. Irie, K. Irwin, H. Ishino, H. Ishitsuka, O. Jeong, K. Karatsu, S. Kashima, N. Katayama, I. Kawano, B. Keating, A. Kibayashi, Y. Kibe, Y. Kida, K. Kimura, N. Kimura, K. Kohri, E. Komatsu, C. L. Kuo, S. Kuromiya, A. Kusaka, A. Lee, E. Linder, H. Matsuhara, S. Matsuoka, S. Matsuura, S. Mima, K. Mitsuda, K. Mizukami, H. Morii, T. Morishima, M. Nagai, T. Nagasaki, R. Nagata, M. Nakajima, S. Nakamura, T. Namikawa, M. Naruse, K. Natsume, T. Nishibori, K. Nishijo, H. Nishino, T. Nitta, A. Noda, T. Noguchi, H. Ogawa, S. Oguri, I. S. Ohta, C. Otani, N. Okada, A. Okamoto, A. Okamoto, T. Okamura, G. Rebeiz, P. Richards, S. Sakai, N. Sato, Y. Sato, Y. Segawa, S. Sekiguchi, Y. Sekimoto, M. Sekine, U. Seljak, B. Sherwin, K. Shinozaki, S. Shu, R. Stompor, H. Sugai, H. Sugita, T. Suzuki, A. Suzuki, O. Tajima, S. Takada, S. Takakura, K. Takano, Y. Takei, T. Tomaru, N. Tomita, P. Turin, S. Utsunomiya, Y. Uzawa, T. Wada, H. Watanabe, B. Westbrook, N. Whitehorn, Y. Yamada, N. Yamasaki, T. Yamashita, M. Yoshida, T. Yoshida, and Y. Yotsumoto, “LiteBIRD: Mission Overview and Focal Plane Layout,” *Journal of Low Temperature Physics*, vol. 184, no. 3, pp. 824–831, 2016.
- [117] S. Hanany and Inflation Probe Mission Study Team, “The Probe of Inflation and Cosmic Origins,” in *American Astronomical Society Meeting Abstracts #231*, ser. American Astronomical Society Meeting Abstracts, vol. 231, Jan. 2018, p. 121.01.